



HAL
open science

Surface evolution of corroding magnesium : new analytical approaches to understand corrosion mechanisms and protection strategies

Alina Maltseva

► **To cite this version:**

Alina Maltseva. Surface evolution of corroding magnesium : new analytical approaches to understand corrosion mechanisms and protection strategies. Theoretical and/or physical chemistry. Université Paris sciences et lettres, 2018. English. NNT : 2018PSLEEC002 . tel-02389064

HAL Id: tel-02389064

<https://pastel.hal.science/tel-02389064>

Submitted on 2 Dec 2019

HAL is a multi-disciplinary open access archive for the deposit and dissemination of scientific research documents, whether they are published or not. The documents may come from teaching and research institutions in France or abroad, or from public or private research centers.

L'archive ouverte pluridisciplinaire **HAL**, est destinée au dépôt et à la diffusion de documents scientifiques de niveau recherche, publiés ou non, émanant des établissements d'enseignement et de recherche français ou étrangers, des laboratoires publics ou privés.

THÈSE DE DOCTORAT

de l'Université de recherche Paris Sciences et Lettres
PSL Research University

Préparée à Ecole Nationale Supérieure de Chimie de Paris

Evolution de surface lors de la corrosion du magnésium:
nouvelles approches analytiques pour comprendre les mécanismes
de corrosion et de protection

Ecole doctorale n°388

CHIMIE PHYSIQUE ET CHIMIE ANALYTIQUE

Spécialité Physico-chimie

Soutenue par Alina MALTSEVA
le 26 septembre 2018

Dirigée par Polina VOLOVITCH
et Grégory LEFEVRE

COMPOSITION DU JURY :

Mme. COURTY Alexa
Université Pierre et Marie Curie, France,
Président du jury

M. WILLIAMS Geraint
Swansea University, Royaume-Uni, Rapporteur

M. FERON Damien
INSTN, CEA, France, Rapporteur

Mme. VOLOVITCH Polina
Chimie ParisTech, Université PSL, France,
Examineur

M. LEFEVRE Grégory
IRCP, France, Examineur

Mme. LAMAKA Sviatlana
Helmholtz-Zentrum Geesthacht, Allemagne,
Examineur



PhD thesis

Surface evolution of corroding magnesium:
new analytical approaches to understand
corrosion mechanisms and protection
strategies

Acknowledgements

Time flies, three years of PhD passed so fast... I should note that it was a great time, full of interesting work, new discoveries, and bright impressions!

First of all, I would like to express my sincere gratitude to my supervisors, **Polina Volovitch** and **Grégory Lefèvre**. Without them my doctoral thesis would not be possible. Polina, thanks a lot for your help and support, for teaching me, spending hours, days and even nights in reviewing my presentations, posters and writing! Grégory, *Merci Beaucoup* for your help, fruitful discussions and patience.

I would like to thank my reviewers, **Geraint Williams** and **Damien Ferron**, who found a time to evaluate my thesis manuscript, besides the precious vacation time and a huge amount of work. Thanks to the jury members, **Sviatlana Lamaka** and **Alexa Courty**, for coming to my PhD thesis defense and interesting questions. I am also grateful to invited persons taking part of jury commission, **Viacheslav Shkirskiy** and **Patrick Chapon** for the participation in the discussion, their valuable comments and wise advices.

I also want to say thanks to **Michel Cassir**, the director of our group, **Armelle Ringuede**, **Kevin Ogle**, **Virginie Lair**, **Valerie Albin**, who welcomed and helped me since my first days at the lab.

It is not enough space in this section to express my gratitude to **Dr. Slava!** Thank you for your warm support, for the huge help in work (the software deserves the highest praise) and everyday life! You were always ready to prepare the hot drinks at the moments of sadness and encourage me with your very special jokes☺!

I can not forget my lab mates, who shared with me everyday life during these happy 3 years.

Xuejie and Peng, many thanks for sharing office, meals, jokes with me, for providing me the best Chinese tea and the advanced-level Chinese vocabulary. 谢谢! Muchas gracias, **Dieguito**, for your emotional support, soulful crous-coffee-breaks, lessons of Spanish, for providing me the good music and encouraging smile☺! *Merci beaucoup*, **Thomas, Cyril, Perrine!** You were the first persons with whom I started to speak French, thanks a lot for your patience to my “Je n’ai pas compris, tu peux répéter, s’il te plait ?” Thank you to the chief of the lab upstairs, **Abdelilah**, for

your kindness! Many thanks to interns who helped me a lot with experimental work, **Ksenia, Elvina, Dima!** Of course, thanks a lot to my lab-mates not mentioned yet: **Katrinka, Romain, Junsoo, Andrey, Haitam, Aurélie, Manel, Arturo, Oumaïma,** etc...

Special thanks to the members of “Crystal band” with whom we organized small concerts in our school. **Jean-François, Sacha, Philippe, Diana, Gilles and Franz,** thank you for the good music you played, I evolved a lot as a musician with your help!

Here I should put the long list of my **Russian friends** and express my БОЛЬШОЕ СПАСИБО for inspiring and supporting me with your “берешь и делаешь” at every moment of my life!

Finally, I would like to thank all **my family**, who was always with me, calling me almost every day, supporting me on the conferences and thesis defense!

CURRICULUM VITAE

Alina Maltseva, 3rd year PhD student

E-mail: alina.maltseva@chimieparistech.psl.eu

Address: 11 Rue Pierre et Marie Curie, 75005 Paris



Research interests: physical and analytical chemistry, corrosion science, in situ vibrational spectroscopy, local electrochemical methods

Quantitative results: 1 article published, 2 articles submitted, 5 international conferences (1 oral, 4 posters, 3 Poster-Prizes) + 1 oral presentation accepted

EDUCATION

2015 – present **PhD student in physical and analytical chemistry**, PSL Research University, Chimie ParisTech, Institut de Recherche de Chimie Paris, *I2E team*

PhD project: Surface films on corroding magnesium: new analytical approaches to understand corrosion mechanism and protection strategies

Scientific supervisors: Dr. Polina Volovitch and Dr. Grégory Lefèvre

2015 **Master in Chemistry, Diploma with Honors**, Lomonosov Moscow State University, Moscow, Laboratory of Kinetics and Catalysis, Division of Physical Chemistry

RELEVANT SKILLS AND EXPERIENCE

Techniques, expert level: Raman spectroscopy, GD-OES

Techniques, user level: IR spectroscopy, UV-VIS spectroscopy, XRD, SEM, EDX, XPS, chromatography, nitrogen adsorption, acidity measurements, NMR characterization

Teaching activity:

2018	supervisor of M1-M2 internship students practical works for M1 students (ENSCP)
2017	GD-OES training for PhD students in ENSCP
2016	theoretical lecture and practical classes (6h) in Raman spectroscopy for PhD and Master students in ENSCP
2012-2015	private lessons in chemistry for high school students

Language: English (advanced), French (fluent), Russian (mother-tongue)

AWARDS

June 2018 1st Poster Prize, The 1st International Surface Fest, Bordeaux, France

July 2016 1st Poster Prize, The 1st international summer school “Multifunctional Smart coatings and surfaces”, University of Aveiro, Portugal

June 2016 2nd Poster Prize, 10th International Symposium on Electrochemical Impedance Spectroscopy (EIS'16), Toxa, Galicia, Spain

PUBLICATIONS

- V. Shkirskiy, A. Maltseva, K. Ogle, P. Volovitch, Environmental effects on selective dissolution from ZnAlMg alloy under low frequency alternating current perturbations, *Electrochimica Acta* <http://dx.doi.org/10.1016/j.electacta.2017.03.210>
- V. Shkirskiy, M. Uebel, A. Maltseva, G. Lefèvre, P. Volovitch and M. Rohwerder, New Insights on the Mechanism of Cathodic Driven Coating Delamination: Suppressed Cation Migration along Zn/Polymer Interface in Atmospheric CO₂ (submitted to Nature publishing journal *Materials Degradation*)
- Y. Yan, O. Gharbi, A. Maltseva, X. Chen, Z. Zeng, S. Xu, W. Xu, P. Volovitch, M. Ferry, N. Birbilis, Investigating the structure of the surface film on a corrosion resistant Mg-Li(-Al-Y-Zr) alloy (submitted to *Corrosion*)

CONFERENCE ABSTRACTS

- **A. Maltseva**, S. Lamaka, G. Lefèvre, P. Volovitch, Inhibition Mechanisms of Mg Corrosion by Selected Carboxylates: Contribution of in situ Raman Spectroscopy and Glow Discharge Optical Emission Spectroscopy, June 2018, Bordeaux, France (**poster**)
- **A. Maltseva**, V. Shkirskiy, G. Lefèvre, P. Volovitch, Corrosion products films on high purity Mg, European Corrosion Congress 2017, Prague, Czech Republic, September 2017 (**oral**)
- **A. Maltseva**, V. Shkirskiy, G. Lefèvre, P. Volovitch, Corrosion products films on low alloyed Mg: Raman spectroscopy, Ecole thématique CNRS organisée par le Groupe Français de Spectroscopies Vibratoires (GFSV), Ile de Porquerolles, France, Octobre 2016 (**poster**)
- **A. Maltseva**, A. Michot Mignucci, C. de Faria Barros, K. Ogle, S. Gaiaschi, P. Chapon, N. Birbilis, P. Volovitch, Corrosion product films on high purity Mg alloys, 8th International GD Day, Synchrotron SOLEIL, Gif sur Yvette, France, September 2016 (**poster**)
- **P. Volovitch**, A. Maltseva, C. de Faria Barros, V. Shkirskiy, G. Lefèvre, Effect of pH on growth and barrier properties of brucite film on Mg, 67th Annual meeting of the ISE, the Hague, Nederland, 21-26 August 2016 (lecture, abstract book <http://www.ise-online.org/annmeet/folder/67th-AM-abstracts.pdf> p. 405), August 2016
- **A. Maltseva**, V. Shkirskiy, K. Ogle, P. Volovitch, Selective dissolution from ZnMgAl alloy under low frequency AC perturbations and its consequence for the interpretation of electrochemical signal, 1st International Summer School of Multifunctional Smart Coating and Surfaces, Aveiro, Portugal, July 2016 (**poster**)
- **A. Maltseva**, V. Shkirskiy, K. Ogle, P. Volovitch, Selective dissolution from ZnMgAl alloy under low frequency AC perturbations and its consequence for the interpretation of electrochemical signal, 10th International Symposium on Electrochemical Impedance Spectroscopy EIS'16, Toxa, Spain, June 2015 (**poster**)

Résumé de la thèse

La réactivité des alliages de Mg est fortement influencée par la formation et la stabilité du film de surface, rendant primordiale leur compréhension au niveau fondamental pour concevoir une stratégie anticorrosion. Ces films sont considérés comme à l'origine de la barrière de protection à la corrosion. Néanmoins, des inhomogénéités locales dues à une formation non-uniforme, une rupture, ou une accumulation d'impuretés métalliques plus nobles que le magnésium, peuvent conduire à une corrosion localisée et accélérer la dégradation du matériau. Ainsi, ce travail a pour but d'abord de développer des méthodologies permettant d'une part une investigation in situ de l'évolution locale du film d'oxy-hydroxyde (composition, distribution spatiale, morphologie, cinétique de croissance et de rupture), et d'autre part une analyse ex situ de la distribution élémentaire en profondeur. Par la suite, la réactivité de Mg est corrélée à la composition du film et son évolution caractérisée par les méthodes développées.

La spectroscopie Raman confocale a été adaptée pour cartographier in situ la cinétique de l'évolution du film de surface lors des étapes initiales de corrosion de Mg grâce à une cellule en circulation. L'approche proposée a été appliquée pour visualiser les zones de croissance de $\text{Mg}(\text{OH})_2$, qui a été décrite par différentes lois cinétiques selon l'environnement et la localisation sur la surface. L'analyse in situ a été complétée par la spectroscopie infrarouge en mode réflexion totale atténuée (ATR-IR) et la spectroscopie à décharge lumineuse (GD-OES).

La GD-OES a été utilisée pour évaluer l'enrichissement du film, en explorant les limites analytiques propres aux surfaces corrodées. L'interprétation brute des profils de concentration obtenus avec un plasma d'argon pouvait mener à des conclusions erronées, et une procédure a été proposée pour obtenir des résultats plus fiables tenant compte de la modification du plasma durant la pulvérisation du film d'oxy-hydroxyde à cause de la présence d'hydrogène.

Ces développements analytiques ont contribué à la compréhension des corrélations entre la composition de la solution, l'évolution du film de surface et la réactivité de Mg. Dans des solutions de NaCl, au niveau des zones n'évoluant pas en microscopie optique, la cinétique de croissance de $\text{Mg}(\text{OH})_2$ était parabolique (limitée par la diffusion) à pH 13 mais linéaire (limitée par des réactions de surface) à pH 7-10.5. Une brutale accélération était observée près des sites de corrosion (filaments noirs). L'apparition de cette accélération coïncide avec l'observation des premiers filaments de la zone étudiée. Les spectres Raman ont été analysés pour obtenir des informations sur la taille des cristaux et la morphologie du film. Un mécanisme de formation de $\text{Mg}(\text{OH})_2$ a été proposé, basé sur la dissolution-précipitation d'une solution sursaturée, qui était cohérent avec l'effet du pH sur l'évolution de la cinétique et la taille des cristaux.

En présence d'inhibiteurs, deux tendances différentes ont été observées pour la croissance de $\text{Mg}(\text{OH})_2$. Pour le fumarate, la croissance est ralentie par rapport à une solution de NaCl 0,1 M. La présence de salicylate ou de 2,5-pyridinedicarboxylate (PDCA) n'a pas d'effet sur la croissance pendant environ 40 minutes, puis la cinétique rejoint celle observée pour le fumarate. Une analyse fine des spectres révèle une interaction spécifique entre le salicylate et le fer ou $\text{Mg}(\text{OH})_2$ formé dans les zones cathodiques. Ceci est cohérent avec l'inhibition cathodique reportée dans la littérature, mais qui n'est pas observée sur du Mg de haute pureté (faible teneur en Fe). Le fumarate et le PDCA conduisent à la formation de films homogènes, cohérents avec l'inhibition de la réactivité anodique. Tous les films formés en présence d'inhibiteurs contenaient des cristaux de $\text{Mg}(\text{OH})_2$ de taille réduite par rapport à des solutions sans inhibiteurs, bloquant l'accès aux Cl^- (d'après le GD-OES), diminuant la corrosion localisée.

Thesis abstract

The reactivity of Mg alloys is strongly affected by formation and stability of surface films making their fundamental understanding critical for intelligent anticorrosion strategy. These films are regarded as a source of the initial barrier corrosion protection. However, any local inhomogeneity caused by a non-uniform film formation, or film breakdown or accumulation of more noble than Mg metallic impurities can result in localized corrosion and accelerated material degradation. Thus, this work aims firstly to develop methodologies which permit both, in situ investigation of local oxide/hydroxide layer evolution (chemical composition, spatial distribution, morphology, growth and breakdown kinetics), and ex situ observation of elemental distribution within the layer depth. Secondly, to correlate environmental composition, surface film evolution and Mg reactivity with help of these methodologies.

In-situ confocal Raman spectroscopy was adapted to map the local kinetics of surface film evolution at initial stages of Mg corrosion in thin layer cell. Proposed approach was applied to visualize zones with $\text{Mg}(\text{OH})_2$ growth described by different kinetic laws and to compare kinetics trends in different environments as well as in different locations on the surface. The in-situ surface analysis was completed by ex-situ Attenuated Total Reflectance Fourier-Transform Infrared Spectroscopy (ATR-FTIR) and Glow Discharge Optical Emission Spectroscopy (GD OES).

GD OES was used to survey the film enrichment. Analytical limits related to the application of GD OES to corroded surfaces were explored. It was evidenced that simple interpretation of depth profiles obtained in Ar plasma can be misleading and a correction procedure was proposed that takes into account plasma modifications during the sputtering of oxide/hydroxide layer because of the presence of H.

Developed analytical approaches contributed to understanding of the correlations between solution composition, the surface film evolution and the reactivity. In NaCl solutions, on the areas, which did not evolve in optical images during immersion, $\text{Mg}(\text{OH})_2$ growth kinetics was parabolic (diffusion limited) at pH 13 but linear (surface reaction limited) at pH 7-10.5. A jump in the kinetics curve was observed near local corrosion sites (black filaments). The time of this jump in kinetics curve coincided with the first visual observation of the filament in studied zone. The spectra were also tentatively analyzed in order to extract information about the in-situ evolution of the crystal size and morphology. Proposed $\text{Mg}(\text{OH})_2$ evolution mechanism, described as a dissolution-precipitation from supersaturated solution, was coherent with the observed pH effect on the kinetics trends and crystal size.

In presence of inhibitors, two different trends in the brucite growth kinetics were observed. For fumarate the growth was slower compared to 0.1 M NaCl solution. The presence of salicylate and 2,5-pyridinedicarboxylate (PDCA) did not affect the growth kinetics for approximately 40 minutes, and then the slope of kinetics curve became similar to observed in fumarate solution. Deep spectra analysis revealed the nature of specific interactions of salicylate with Fe and $\text{Mg}(\text{OH})_2$ rapidly formed at cathodic areas. This is coherent with cathodic inhibition reported in the literature and the absence of the inhibition for high purity Mg (low Fe content). Fumarate and PDCA form homogenous surface films that is coherent with inhibition of anodic reactivity. All the films formed in the presence of inhibitors contained $\text{Mg}(\text{OH})_2$ nanocrystals with a reduced size compared to the films formed w/o inhibitors, and blocked Cl^- access to the surface (from GD-OES), reducing probability of localized corrosion.

Résumé de la thèse

L'origine et les objectifs de l'étude doctorale

Les alliages à base de magnésium (Mg) sont des matériaux intéressants pour une large gamme d'applications comme l'industrie automobile, aéronautique, électronique ou la médecine [1], du fait de leur rapport résistance masse élevé, leur biocompatibilité, l'abondance de Mg. La réactivité élevée de ces matériaux en environnement aqueux peut être considéré comme problématique (corrosion) ou au contraire avantageux (implants résorbables, batteries). Le contrôle de la réactivité en milieu aqueux est donc primordial pour assurer de bonnes propriétés en service. Une compréhension fine de la réactivité de Mg est un point-clé pour développer une stratégie efficace de son contrôle.

Il est communément accepté que la chimie et la morphologie des films de surface et des produits de corrosion a un effet significatif sur la réactivité des substrats métalliques. Dans le cas des alliages de Mg, le film natif d'oxyde s'hydrate spontanément en milieu aqueux, formant $\text{Mg}(\text{OH})_2$ (brucite), un minéral dont la solubilité est inférieure à MgO . De nombreuses études indiquent une structure duplex à la surface de Mg corrodé [2–5]: une fine couche interne de MgO (inférieure au micron) et une couche externe de $\text{Mg}(\text{OH})_2$. Ce film d'oxyhydroxyde peut être considéré comme protecteur lors des étapes initiales de la corrosion [6,7].

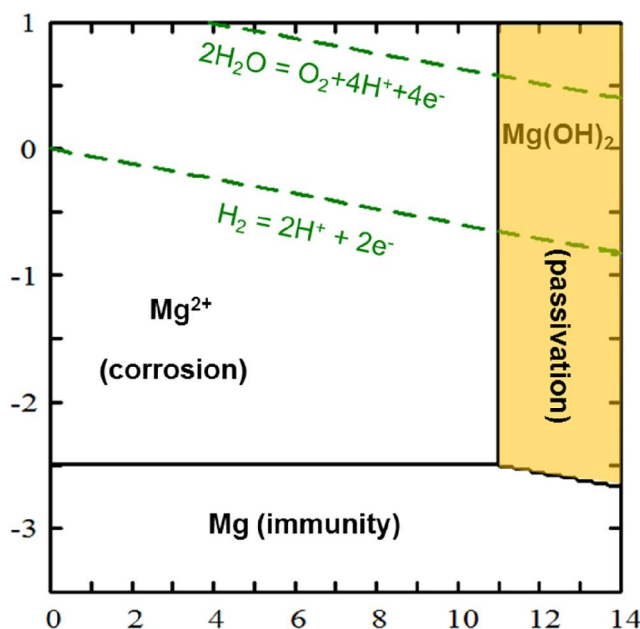


Fig. 1 Diagramme E-pH (Pourbaix) du magnésium pur en solution aqueuse à 25 °C [8].

Selon le diagramme E-pH (Fig. 1), Mg(OH)_2 est stable en milieu très alcalin et peut passiver Mg. Néanmoins, en milieu faiblement alcalin ou neutre, ce film n'est thermodynamiquement pas stable et peut perdre ses propriétés de protection. Le film peut se rompre du fait de plusieurs facteurs, comme la modification de l'environnement chimique local (pH, anions, ...). La présence d'inhomogénéités, causée par la croissance non-uniforme ou la rupture du film, peut conduire à des couplages micro-galvaniques accélérant la dégradation de Mg [9,10]. La corrosion localisée peut également être favorisée par l'enrichissement de la surface en impuretés métalliques plus nobles que Mg (Fe, Ni, Cu) qui sont présentes à de faibles concentrations (ppm) après les procédés de mise en forme [3,11–13]. Ces deux mécanismes de corrosion localisée sont illustrés dans la Fig. 2.

Ainsi, du fait de l'importance du film de surface sur la réactivité de Mg, ces deux aspects, l'évolution du film duplex en milieu aqueux et l'enrichissement de surface par des impuretés métalliques, doivent être compris. De nombreuses données obtenues de façon ex situ sur la morphologie et la composition chimique de surfaces de Mg corrodées ont été publiées [14], mais la surface analysée ex situ peut être différente de l'interface en présence de solution. Pour cette raison, des méthodes in situ pourraient apporter des données pertinentes, notamment sur la cinétique, pour aider à comprendre la croissance et la rupture du film. Peu d'observations de ce type ont été publiées, et aucune n'a pour l'instant permis d'apporter des informations à des échelles macroscopique et microscopique simultanément [7,15].

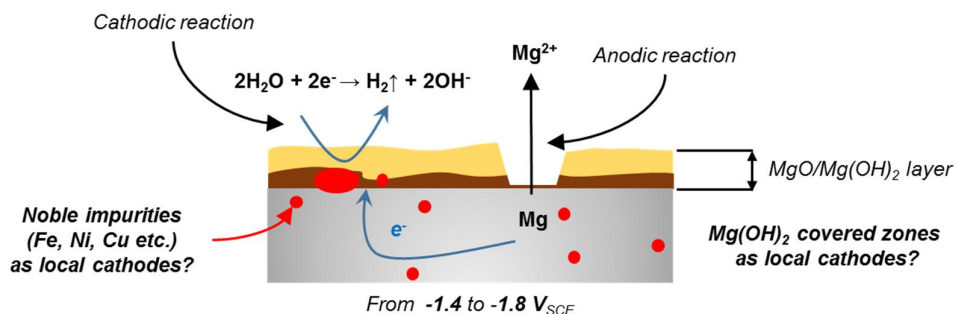


Fig. 2. Schéma de la réactivité de Mg: effet du film d'oxy-hydroxyde sur la corrosion localisée

Considérant l'évolution non-uniforme d'une surface de Mg se corrodant, **le premier objectif** de cette thèse était de développer une méthodologie pour cartographier in situ la cinétique de l'évolution du film d'oxy-hydroxyde en milieu aqueux sur des surfaces assez étendues et avec une résolution latérale élevée. Cette méthodologie pourra être étendue à différents phénomènes pour lesquels une mesure in situ d'une évolution locale peut être intéressant.

Le second objectif était de trouver une technique peu coûteuse, rapide, simple (comparée à des méthodes analytiques sous vide comme l'XPS, le ToF SIMS, ...) pour vérifier l'enrichissement de la surface par des impuretés métalliques et des ions provenant de l'électrolyte, dont les limites seront testées. La méthodologie proposée pour Mg pourra alors être utilisée pour la corrosion d'autres métaux.

Le troisième objectif de ce travail était de corrélérer composition de l'environnement, l'évolution de la surface corrodée et la réactivité de Mg à l'aide de l'approche analytique développée.

Les résultats devraient contribuer à la compréhension fondamentale des mécanismes de la corrosion de Mg, en particulier l'effet de la composition de la solution. Cela peut également aider à un choix de stratégies anticorrosion. Parmi différents facteurs pouvant être pris en compte, nous avons sélectionné l'effet du pH, des ions chlorure et de plusieurs inhibiteurs organiques

Malgré les nombreux inhibiteurs proposés pour le Mg et ses alliages [16,17], les mécanismes d'inhibition sont mal compris. Les conclusions sur les mécanismes basés sur des mesures électrochimiques sont limitées par l'attribution d'un additif particulier au type anodique / cathodique / mixte ou au type adsorption / précipitation. La caractérisation in situ de l'évolution de la surface en présence d'inhibiteurs serait un élément essentiel pour comprendre les mécanismes d'inhibition.

Ainsi, ce travail a pour but d'abord de développer des méthodologies permettant d'une part une investigation in situ de l'évolution locale du film d'oxy-hydroxyde (composition, distribution spatiale, morphologie, cinétique de croissant et de rupture), et d'autre part une analyse ex situ de la distribution élémentaire en profondeur. Par la suite, la réactivité de Mg est corrélée à la composition du film et son évolution caractérisée par les méthodes développées.

L'approche analytique

La cartographie à résolution micrométrique fournie par la microscopie confocale Raman (CRM) semble être une méthode prometteuse pour l'analyse in situ des produits de corrosion avec une bonne résolution latérale. La spectroscopie Raman est sensible aux vibrations des espèces OH^- et CO_3^{2-} , ainsi elle peut être utilisée en routine pour l'identification des produits de corrosion dans les solutions aqueuses [18–21]. L'intensité de la lumière diffusée Raman provenant d'un échantillon est proportionnelle au nombre de liaisons actives dans le volume analysé [22], cela permet une analyse semi-quantitative et le suivi de la cinétique de croissance en utilisant la procédure de normalisation des spectres. En principe, des informations sur la forme et la morphologie des cristaux peuvent également être obtenues à l'aide des spectres Raman [23].

Bien que la spectroscopie Raman in situ soit couramment utilisée pour l'identification des produits de corrosion, les mesures cinétiques in situ de la croissance ou de la dégradation du film, en particulier dans un mode de cartographie, n'ont jamais été publiées.

Dans ce travail, la spectroscopie Raman confocale a été adaptée pour cartographier in situ l'évolution du film de surface (composition chimique, morphologie, cinétique de croissance et de rupture). Cette technique était utilisée pour étudier l'effet du pH, des ions chlorure et de plusieurs inhibiteurs organiques dans les mécanismes de développement du film de surface.

De toute évidence, la spectroscopie Raman a des limites; la plus importante est que certains composés sont inactifs. Ainsi, il est impossible d'étudier directement l'évolution de

MgO, en particulier s'il est enrichi par des inclusions métalliques ou des espèces agressives telles que Cl⁻.

Dans cette perspective, le profil de profondeur élémentaire ex situ de matériaux corrodés peut fournir une information complémentaire. Parmi d'autres techniques d'analyse de surface, la spectrométrie d'émission optique à décharge luminescente (GD-OES) offre une combinaison unique de pulvérisation rapide (le temps d'une mesure varie entre 2 et 10 minutes pour les échantillons de Mg) ; une capacité multi-élément et une simplicité expérimentale sans nécessité d'un ultra-vide ou d'une préparation de surface spéciale [24]. Son application aux surfaces corrodées reste toutefois difficile en raison de l'interprétation des données analytiques de couches poreuses qui reste inexplorée, compliquée par une modification importante du plasma lors de la pulvérisation des couches d'oxy-hydroxyde [25,26].

Dans cette thèse, les limites analytiques liées à l'application de GD-OES sur les surfaces corrodées sont explorées et la technique est appliquée pour suivre la distribution de profondeur élémentaire dans la couche d'oxy-hydroxyde sur Mg corrodé et ses alliages. Cette technique a significativement contribué à la compréhension du mécanisme d'inhibition de Mg.

Le résumé et la structure de la thèse de doctorat

Cette thèse est organisée en 4 parties principales: **Introductory section**, **Methodology**, **Results section** et **Concluding remarks**.

La partie introductive présente les questions scientifiques à travers une revue bibliographique. Cette partie contient 3 chapitres. 1) “**Introduction**”, qui présente un aperçu global et le résumé de la thèse; 2) “**Surface films on corroded Mg**” qui détaille l'état des connaissances concernant les films de surface, leur stabilité et leur rôle dans la réactivité de Mg; 3) “**Corrosion inhibition of Mg**” qui représente l'état de l'art dans les approches pour la protection anti-corrosion de Mg.

Les mécanismes proposés pour la réactivité et la protection de Mg sont analysés dans les **Chapitres 2 et 3**. En marge de la partie introductive, chaque chapitre dans la partie **Results section** contient une étude bibliographique.

La 2ème partie, **Experimental section**, décrit les méthodologies principales utilisées dans ce travail, notamment La spectroscopie Raman in situ et la spectroscopie à décharge

luminescente. La **Chapitre 4** présente les principes des deux techniques, leurs avantages et leurs limites.

La 3ème partie de la thèse est la plus importante et elle est composée des 3 chapitres présentés sous la forme des publications préparées pour la soumission dans différents journaux.

La **Chapitre 5 “pH effect on MgO/Mg(OH)₂ film evolution on corroding Mg by in-situ Kinetic Raman Mapping (KRM)”** décrit la mise au point de la méthodologie de cartographie Raman in situ (KRM) et démontre sa capacité à décrire l’effet de la composition de la solution (pH, présence de Cl⁻) sur l’évolution locale du film superficiel aux stades initiaux de la corrosion de Mg en couche mince. L'utilisation d'une procédure de normalisation spécifique pour l'évolution du pic de brucite A_{1g} (3652 cm⁻¹) lors de l'immersion permet d'extraire la cinétique de croissance du film d'une surface suffisamment grande avec une résolution spatiale d'environ 10 μm. Sur les zones n'ayant pas évolué sur les images optiques pendant l'immersion, la cinétique de croissance de la brucite était parabolique (limitée par la diffusion) à pH 13 mais linéaire (limitée par des réactions de surface) à pH 7-10,5 (Fig. 3a). Un saut de la courbe de cinétique a été observé à des endroits particuliers de la surface (Fig. 3b).

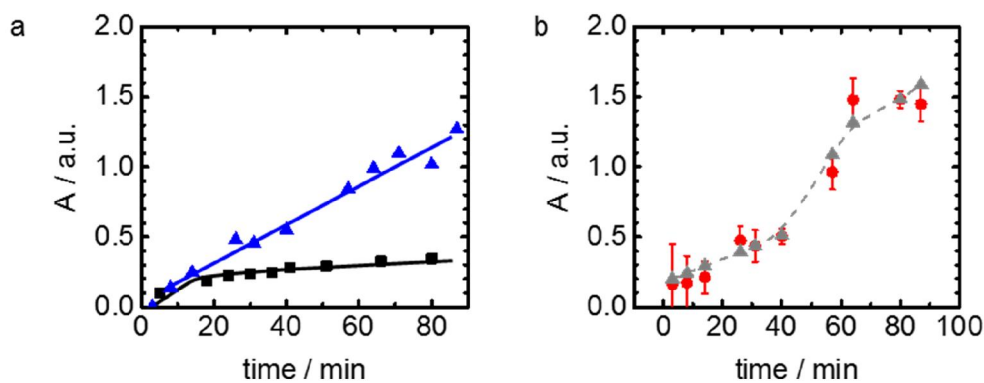


Fig. 3. Exemples de la cinétique de croissance de Mg (OH)₂ localisée in situ sur Mg immergé dans une solution de 10 mM NaCl à différents pH: a) zones "intactes" à pH 9 (triangles bleus) et pH 13 (carrés noirs); et b) dans un filament noir à pH 9, résultats expérimentaux (cercles rouges) et simulation théorique de la précipitation de Mg (OH)₂ suite à une augmentation instantanée du pH.

Le traitement statistique des données montre que ce type de cinétique est associé à la proximité des filaments noirs (Fig. 4a) et que le temps de la forte augmentation de la cinétique coïncide avec la première observation visuelle du filament dans la zone étudiée (Fig. 4b). Dans la Fig. 4b, le code couleur reflète le temps du saut dans la courbe de croissance de Mg

(OH)₂. La fraction de surface avec un film "rompu" en fonction du temps a également été tracée, montrant une cinétique de dégradation linéaire.

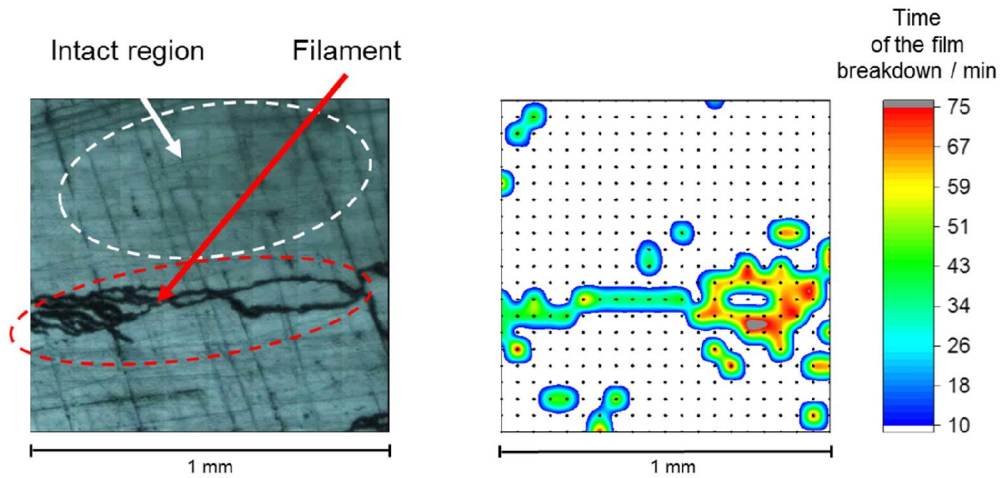


Fig. 4 (a) Exemple de l'apparence d'une surface de Mg surface après 80 minutes en contact avec une solution de NaCl 0,1 M ; (b) cartographie cinétique (temps du saut dans la courbe de croissance pour chaque point) pour la même zone.

Les spectres ont également été analysés afin d'extraire des informations sur l'évolution in situ de la taille et de la morphologie des cristaux. L'augmentation de l'alcalinité a favorisé l'apparition de pics de "satellites" dans les spectres Raman (exemple dans Fig. 5c). Les bandes à 3675 cm⁻¹ et 3710 cm⁻¹ ont été attribuées aux vibrations des groupes de surface Mg-OH avec des plans cristallographiques orientés différemment, (0001) et (10-10) respectivement [27]. La présence de « satellites » peut donc être considérée comme une preuve de la surface spécifique élevée et de la taille plus petite des cristaux de Mg(OH)₂ à pH élevé, cela a été confirmé par microscopie électronique à balayage ex situ (Fig. 5). Une cinétique similaire de croissance (pic de brucite et pics satellites) a été obtenue à pH 13 après environ 10 minutes de période d'induction, ce qui indique que la morphologie cristalline atteint l'équilibre à ce moment.

L'effet du pH sur la cinétique de croissance, la taille et la morphologie des cristaux est cohérent avec le modèle de dissolution-précipitation de la formation de Mg(OH)₂. À cet égard, une croissance de Mg(OH)₂ à proximité des filaments pourrait s'expliquer par une dégradation du film de surface dans ces endroits entraînant la libération d'ions Mg²⁺ et / ou OH⁻ excédentaires, provoquant une précipitation supplémentaire de la brucite (Fig. 6)

Un calcul simple de la cinétique de croissance du film autour des filaments en utilisant une précipitation de la solution sursaturée donne des résultats qui correspondent bien au saut observé (la cinétique simulée est représentée par la courbe grise dans la Fig. 3b).

L'enrichissement de la surface par des impuretés métalliques est en focus du **Chapitre 6 “On the application of Glow Discharge Optical Emission Spectroscopy (GD OES) for depth profiling of corroded materials: example of pH effect on Fe and Mn enrichment on corroding Mg”**.

Malgré la simplicité expérimentale, l'interprétation des données de GD OES n'est pas toujours évidente, surtout pour l'estimation de l'enrichissement de la couche de surface par des impuretés au niveau du ppm provenant du volume de métal. Le problème principal est que l'hydrogène atomique dans le plasma, provenant de l'échantillon (couche d'hydroxyde externe), peut modifier de manière significative la vitesse de pulvérisation, les limites de détection et le rendement d'émission de certaines bandes d'émission. Cela entraîne une interprétation ambiguë des variations d'intensité d'éléments dans la couche d'oxy-hydroxyde par rapport au volume de métal. Les effets de H sur les paramètres analytiques de GD OES, les conséquences de ces effets pour l'interprétation des profils de profondeur des surfaces corrodées, et la manière d'obtenir des profils qualitatifs sont discutés dans le travail.

La Fig. 7a présente un exemple de profil de profondeur GD OES obtenu dans un plasma d'Ar sur Mg pur (pureté commerciale : 280 ppm de Fe, 50 ppm de Mn, 10 ppm d'Al) après 12 h d'immersion dans de l'eau à pH 9. Interprétation brute des résultats obtenus dans le plasma Ar peut conduire à une conclusion erronée à propos de l'appauvrissement en Mn de la couche d'oxy-hydroxyde. Ainsi, le traitement de données proposé (correction H) conduit à conclure que l'appauvrissement apparent en Mn résulte de l'effet de H dans le plasma. La correction H ainsi que les expériences dans le plasma Ar/H₂ ont montré dans ces conditions que la surface était enrichie par Mn dans les conditions étudiées. Le GD OES a également démontré que H n'influence pas le comportement du Cl et que la couche d'oxyde-hydroxyde est enrichie en Cl.

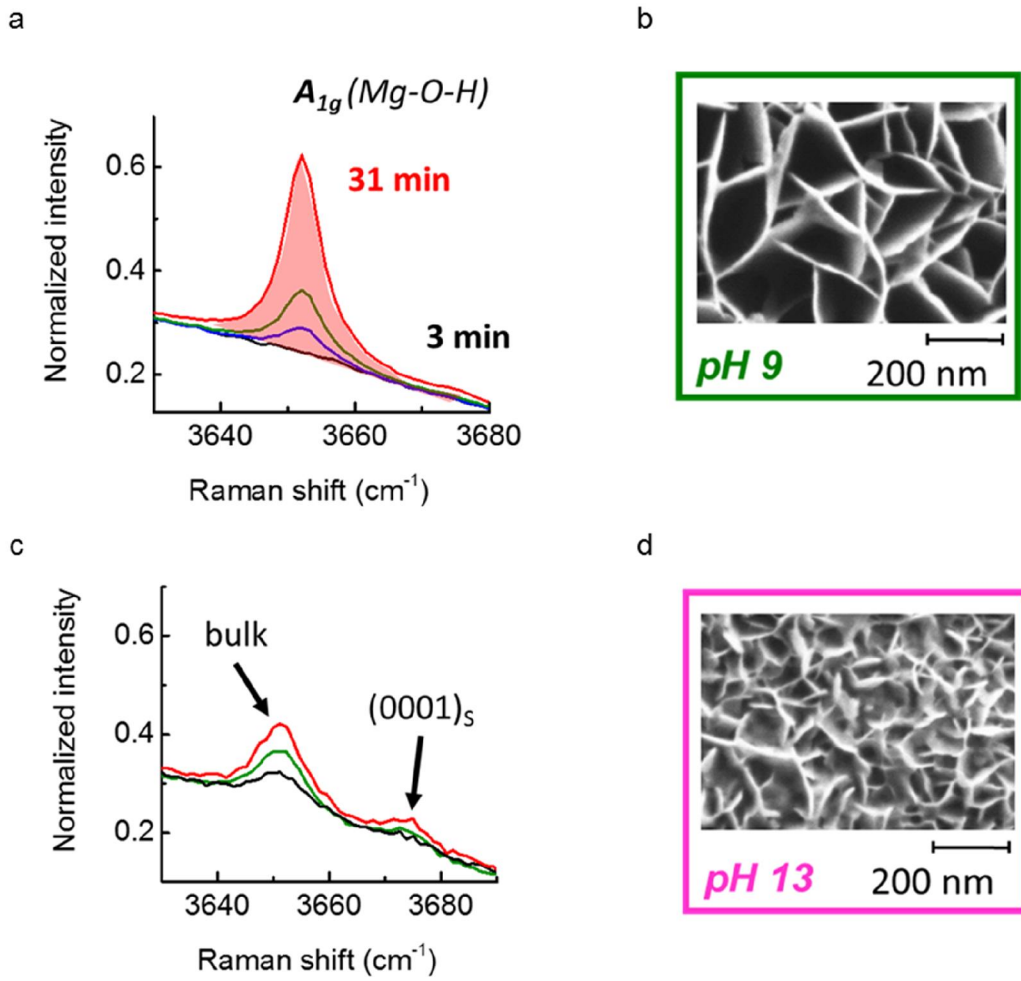


Fig. 5. Exemples de spectres Raman in situ de Mg en contact avec la solution de 0,1 M NaCl à pH 9 (a) et 13 (b) et images MEB ex situ des surfaces correspondantes après immersion.

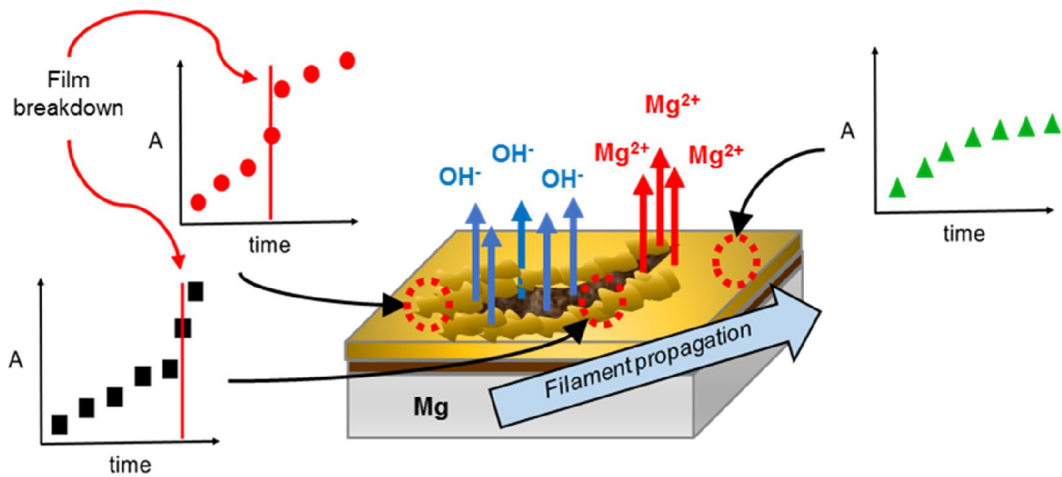


Fig. 6. Schéma de croissance de $Mg(OH)_2$ dans un environnement aqueux contenant Cl^- , à proximité de filament et dans la zone intacte.

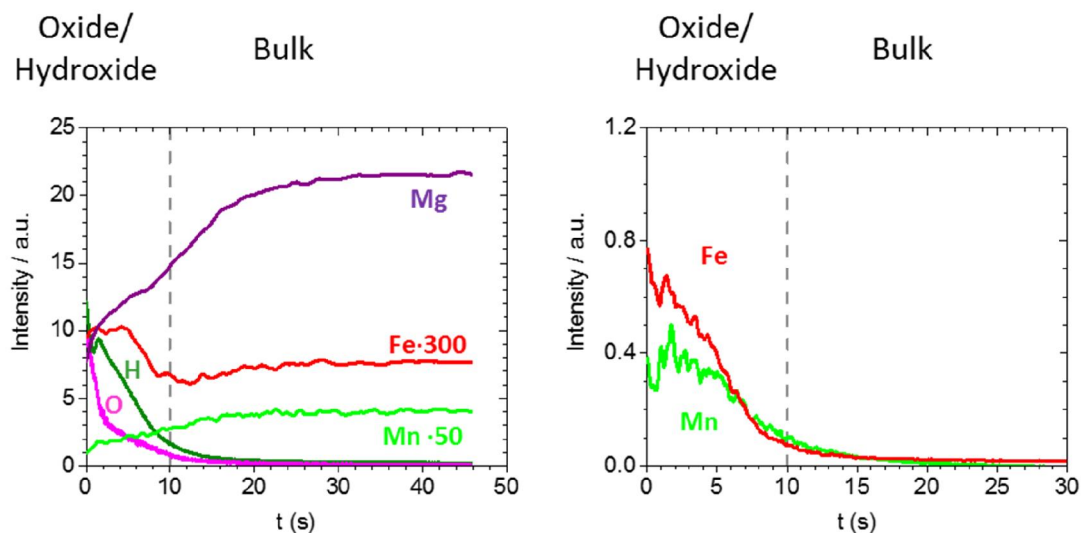


Fig. 7. Profils de profondeur élémentaires GD OES obtenus pour Mg pur (280 ppm Fe, 50 ppm Mn, 10 ppm Al) après 12 h d'immersion dans l'eau à pH 9: (a) données brutes; (b) profil de Fe et Mn après la correction H.

L'utilisation de Ar / H₂ à la place du gaz conventionnel peut éviter certains artefacts liés à la vitesse de pulvérisation de l'oxyde et du métal et à des modifications significatives du plasma entre ces deux couches. Malheureusement, la limite de détection du Fe est significativement dégradée en présence de H₂, il n'a donc pas été possible de confirmer l'enrichissement en ppm du film d'oxyde dans le plasma Ar/H₂.

Le Chapitre 7 “Mechanisms of Mg corrosion inhibition by selected organic inhibitors” illustre l'application des méthodes analytiques proposées pour explorer les mécanismes d'inhibition de la corrosion par plusieurs molécules organiques, à savoir les sels de sodium des acides salicylique, 2,5-pyridine-dicarboxylique (PDCA) et fumarique (Fig. 8).

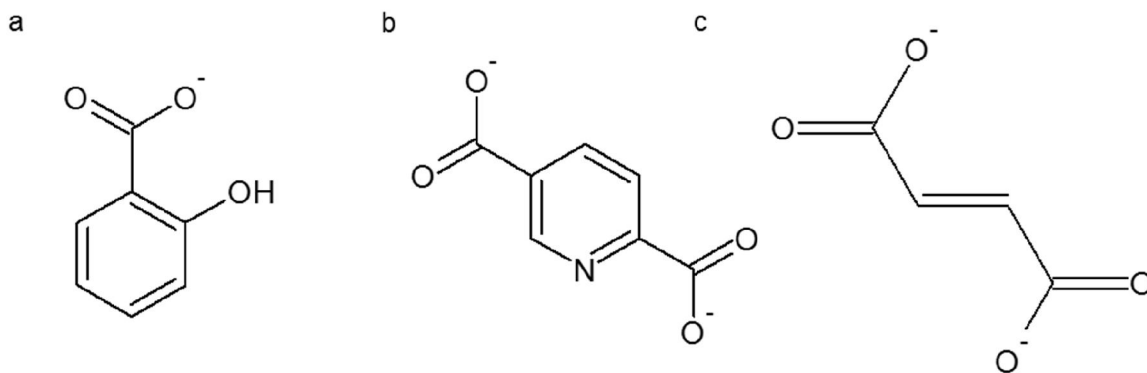


Fig. 8. Formule développée des inhibiteurs de corrosion Mg étudiés dans ce travail: (a) salicylate, (b) 2,5-pyridinedicarboxylate, (c) fumarate.

Les deux méthodologies établies aux chapitres 6 et 7 sont utilisées et complétées par d'autres techniques afin de comparer la formation de film dans une solution de 0,1 M NaCl

avec et sans inhibiteurs sur deux types de Mg pur. La différence principale entre les compositions de Mg était la quantité d'impuretés de Fe, 342 et 50 ppm respectivement pour le Mg commercial et de haute pureté. Tous les inhibiteurs retardent efficacement la corrosion de Mg, à l'exception du salicylate, qui inhibe uniquement la corrosion de Mg avec une teneur de Fe élevée.

Tout d'abord, les profils de profondeur ex situ GD-OES après l'immersion de Mg dans des solutions de NaCl 0,1 M avec et sans inhibiteurs Fig. 9 ont confirmé que tous les inhibiteurs étaient incorporés dans le film oxyde / hydroxyde (signal de C est assez fort) et diminué efficacement la quantité de Cl⁻ adsorbé.

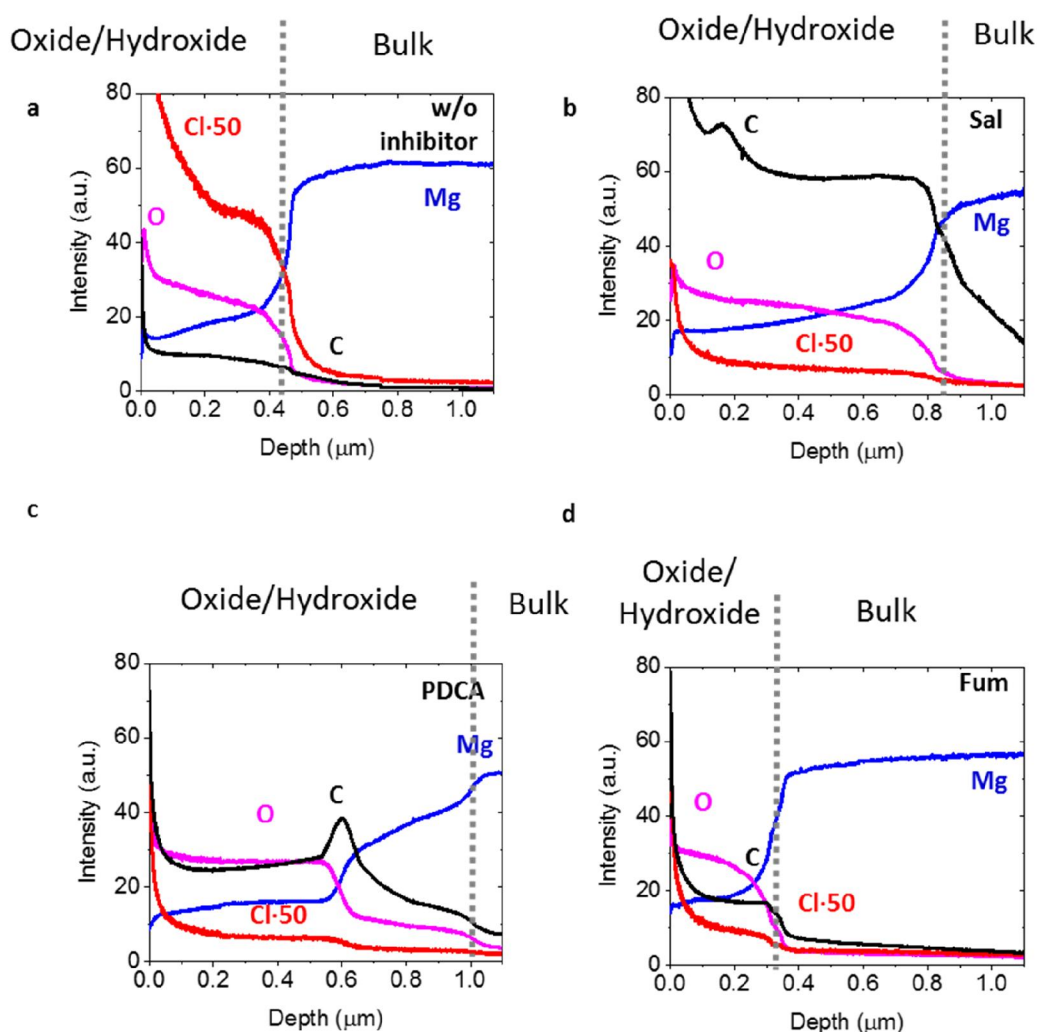


Fig. 9. Profils de profondeur élémentaire GD OES (Ar/H₂ plasma) de Mg pur (pureté commerciale) après 2 h d'immersion dans la solution de 0,1 M NaCl sans inhibiteurs (a) et en présence d'inhibiteur: salicylate de sodium (b), PDCA (c) ou fumarate de sodium.

La spectroscopie Raman in situ a révélé deux tendances différentes de la cinétique de croissance de $Mg(OH)_2$ en présence d'inhibiteurs (Fig. 10). Pour le fumarate, la croissance a été plus lente par rapport à une solution de 0,1 M NaCl. Pour le salicylate et le PDCA, la croissance a évolué en 2 périodes. Initialement, elle était similaire à l'évolution de la croissance en absence des inhibiteurs. Après environ 40 minutes d'immersion, la croissance était plus lente et ressemblait à la solution de fumarate. En présence de tous les inhibiteurs, les pics satellites étaient visibles, révélant une taille de cristal plus petite que dans les solutions sans inhibiteurs.

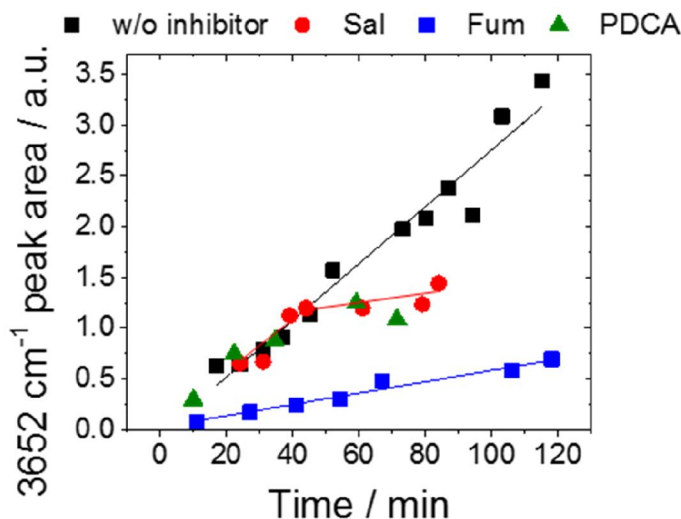


Fig. 10. Cinétique de croissance typique de $Mg(OH)_2$ dans la solution de 0,1 M NaCl en absence d'inhibiteur (carrés noirs) et en présence de sels de sodium des acides fumariques (carrés bleus, Fum) salicyliques (cercles rouges) et 2,5-pyridindicarboxylique (triangles verts, PDCA).

L'interaction des inhibiteurs avec le film de surface a également été analysée. Pour le Mg de pureté commerciale, les pics Raman caractéristiques et les positions des bandes IR des groupes $-COO^-$ et $-OH$ du salicylate ont été décalés par rapport à la position observée dans le spectre de la solution (Fig. 11). Ceci a été interprété comme une interaction spécifique du salicylate avec la surface de Mg . Pour le fumarate, aucune interaction spécifique n'a été observée. Pour le PDCA, aucun décalage dans la position des pics dans les spectres Raman n'a été enregistré pendant les 40 premières minutes, puis le fond de fluorescence élevé est apparu, gênant le signal Raman. Cela pourrait s'expliquer par la formation d'un ensemble spécifique de molécules organiques possédant une chaîne de liaisons doubles et simples alternées, appelée conjugaison [28]. L'analyse ex situ par spectroscopie IR a confirmé les légers décalages des positions des pics caractéristiques des vibrations des cycles aromatiques pour le PDCA.

Trois types d'interaction des molécules organiques avec la surface de Mg ont été proposés pour les inhibiteurs étudiés. L'adsorption physique du fumarate, la chimisorption du salicylate sur Mg(OH)₂ ou sur les particules contenant du Fe, et la formation de polymère de coordination à l'interface entre des couches d'oxy-hydroxy dans le cas du PDCA, sont les mécanismes les plus probables de l'évolution de surface. En ce qui concerne les mécanismes d'inhibition, l'interaction spécifique du salicylate avec Fe est cohérente avec l'inhibition cathodique rapportée dans la littérature [29] ainsi que l'absence d'effet d'inhibition pour le Mg de haute pureté. Le fumarate et le PDCA forment des films de surface homogènes plus cohérents avec l'inhibition de la réactivité anodique. Tous les films de surface formés en présence d'inhibiteurs contiennent des nanocristaux de Mg(OH)₂ de taille réduite par rapport aux films formés sans inhibiteurs et bloquent l'accès de Cl⁻ à la surface, réduisant la possibilité de la corrosion localisée. Les mécanismes proposés pour la formation des films en présence des inhibiteurs et ses conséquences sur la réactivité sont résumés dans la Fig. 12.

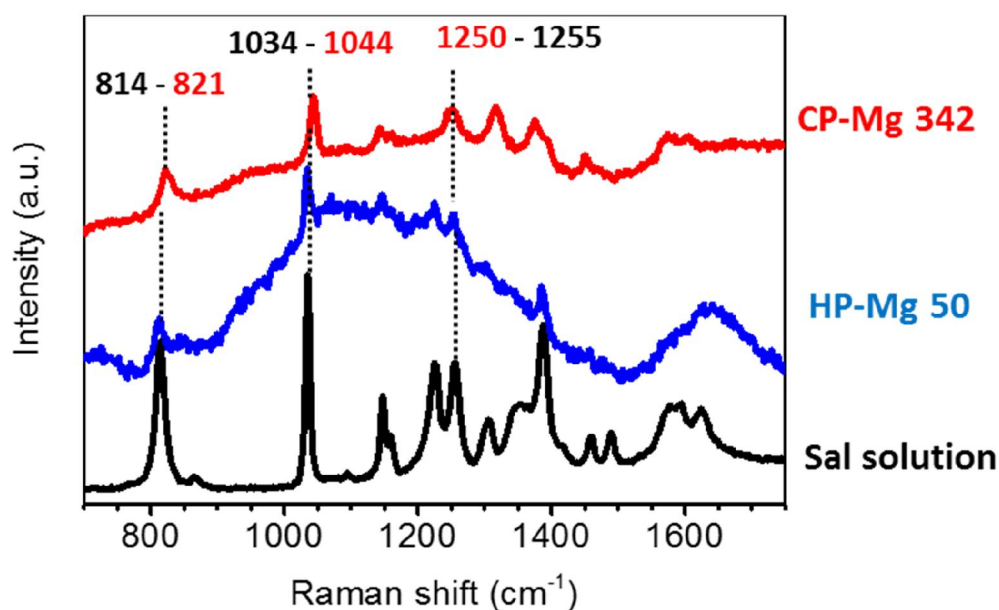


Fig. 11. Spectres Raman in situ de Mg de pureté commerciale (CP-Mg342) et de Mg de haute pureté (HP-Mg50) en contact avec une solution de 0,1 M NaCl + 0,05 M salicylate de Na comparés aux spectres Raman de la solution de salicylate de Na.

Le Chapitre 8 “**Conclusions and perspectives**” présente la conclusion générale ainsi que les perspectives issues de ce travail.

Dans l’annexes, les résultats supplémentaires illustrant l’application des méthodologies développées dans plusieurs systèmes présentant un intérêt potentiel sont inclus. Parmi eux, l’effet de Li sur la chimie des films de surface des alliages de MgLi

corrodés ; l'effet de l'auto-assemblage des molécules organiques de monocouches sur la cinétique de croissance du film.

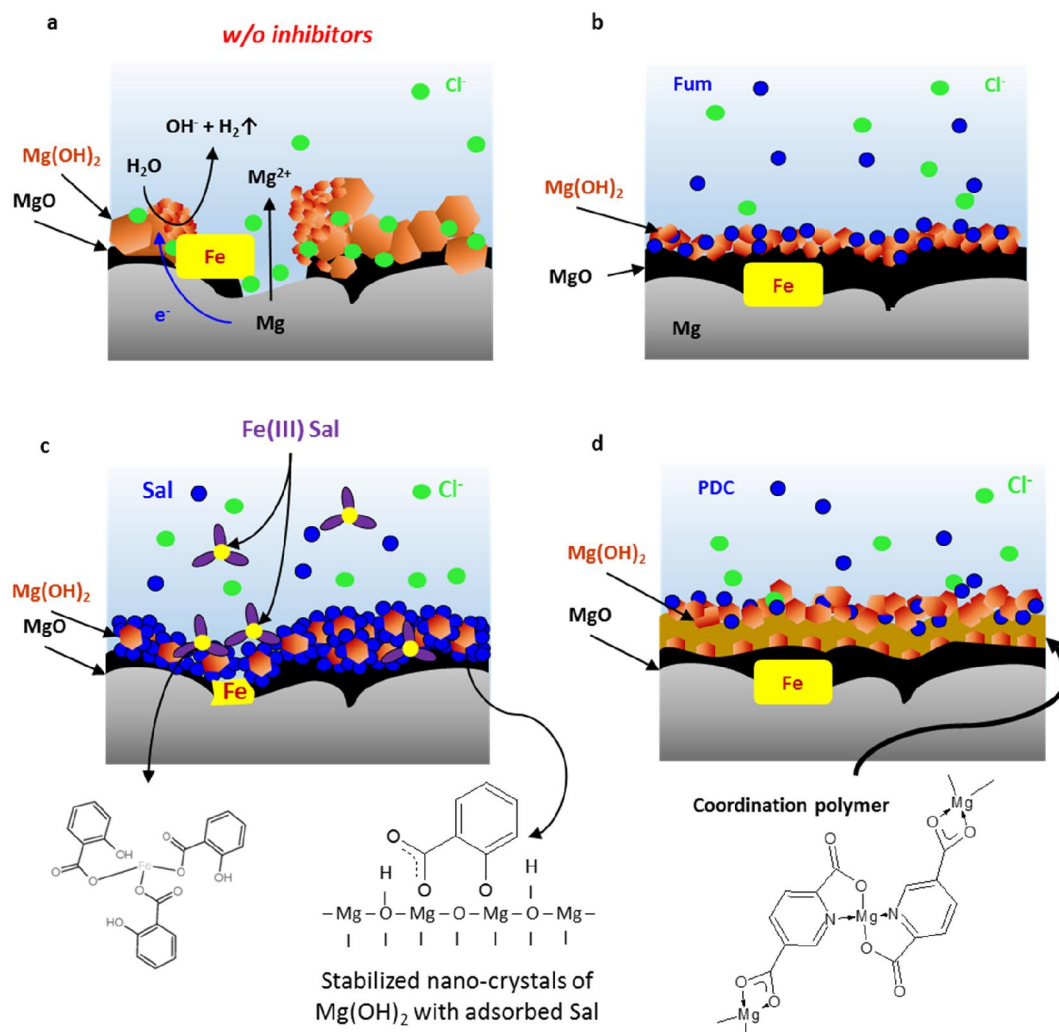


Fig. 12. Représentation schématique de la réactivité de Mg en l'absence d'inhibiteurs (a) et mécanismes d'inhibition de la corrosion de Mg en présence de (b) fumarate - adsorption physique, (c) salicylate - stabilisation de nano cristaux de Mg(OH)₂ ; adsorption spécifique de Sal, (d) 2,5-pyridinedicarboxylate - précipitation du polymère de coordination.

Contents

CONTENTS	15
INTRODUCTORY SECTION	17
Introduction	19
Context and objectives of the study	19
Analytical approach of the work	22
Summary and structure of the manuscript	23
Surface films on corroded Mg	33
Basics of Mg reactivity	33
Corrosion products in Mg reactivity	35
Impurities incorporation in corrosion products	42
Strategies for Mg inhibition	49
Phase film formation inhibitors for Mg	51
Adsorption-type inhibitors for Mg	51
EXPERIMENTAL APPROACH	57
Methodologies	59
Raman spectroscopy	59
Glow Discharge Optical Emission Spectroscopy (GD OES)	68
RESULTS SECTION	73
The effect of pH on the Mg(OH)₂ film evolution on corroding Mg by in situ Kinetic Raman Mapping (KRM)	75
Abstract	76
Introduction	76
Experimental details	79
Results	81
Discussion	88
Conclusions	91

Supplementary 1	92
Supplementary 2	92
Supplementary 3	93
On the application of Glow Discharge Optical Emission Spectroscopy (GD-OES) for depth profiling of corroded materials: example of pH effect on Fe and Mn enrichment on corroding Mg	95
Abstract	96
Introduction	96
Experimental and calculation details	98
Results	100
Discussion	105
Conclusions	108
Inhibition Mechanisms of Mg Corrosion by Selected Carboxylates	109
Introduction	110
Experimental details	111
Results	114
Discussion	125
Conclusions	130
Conclusions and Perspectives	131
Development of new analytical approaches for investigation of Mg corrosion and protection mechanisms	131
Understanding the solution chemistry effects on the evolution of oxide/hydroxide films on corroding Mg: corrosion and protection mechanisms	132
Perspectives	139
BIBLIOGRAPHY	141
APPENDICES	163
Investigating the surface film on a corrosion resistant Mg-Li(-Al-Y-Zr) alloy	165
On the application of in situ Raman spectroscopy to investigation of effect of self-assembling monolayers on the film growth kinetics	193
Environmental effects on selective dissolution from ZnAlMg alloy under low frequency alternating current perturbations	195

Introductory section

This part of the PhD thesis defines the context of the study and the scientific questions, which should be answered.

Chapter 1

Introduction

Context and objectives of the study

Magnesium (Mg) based alloys are attractive materials for a wide range of applications such as automotive, aerospace, electronics, medicine [1] due to their high strength to weight ratio, biocompatibility, high abundance of Mg, etc. High reactivity of these materials in aqueous environments can be considered as a harmful (for corrosion / durability) or an advantageous (resorbable implants, battery applications) property. The control of this aqueous reactivity becomes critical to ensure good service properties and service life. Deep understanding of the mechanisms of Mg reactivity is the key to the development of efficient strategies for its control.

It is commonly accepted that the chemistry and morphology of the surface films and corrosion products significantly affect the reactivity of metallic substrates. In case of Mg alloys, the natural oxide film spontaneously hydrates in aqueous environments forming $\text{Mg}(\text{OH})_2$ (brucite), a mineral with a lower solubility than MgO . Numerous works have reported the bi-layered structure of the film on corroded Mg surfaces [2–5]: a thin inner MgO layer and a thick (up to μm) outer layer of $\text{Mg}(\text{OH})_2$. This oxide-hydroxide film can be considered as protective at initial stages of corrosion [6,7]. According to the E-pH diagram (Fig. 1), at a strong alkaline pH $\text{Mg}(\text{OH})_2$ is stable and hence could passivate Mg, however, at neutral and slightly alkaline pH, $\text{Mg}(\text{OH})_2$ film is not thermodynamically stable and could not hence be protective. Film breakdown can be due to numerous factors [8], including modification of local chemical environment (pH, anions, etc.).

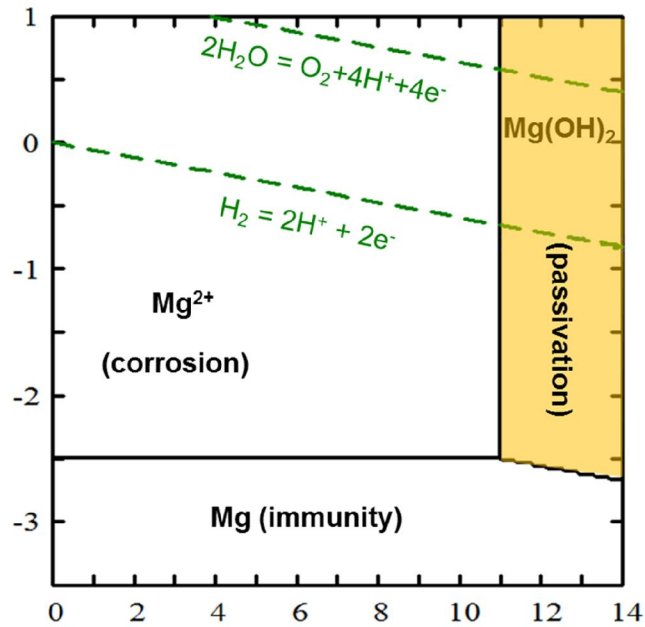


Fig. 1 Potential-pH (Pourbaix) diagram for pure magnesium in water at 25 °C [9].

Any inhomogeneity, caused by either the non-uniform growth or breakdown of the film can result in micro-galvanic coupling contributing to accelerated Mg degradation [10,11]. Localized corrosion can be also enhanced by the surface enrichment of more noble than Mg metallic impurities (Fe, Ni, Cu,) which are always present in Mg matrix at ppm level after casting process [3,12–14]. These two mechanisms of localized corrosion are schematically shown in Fig. 2.

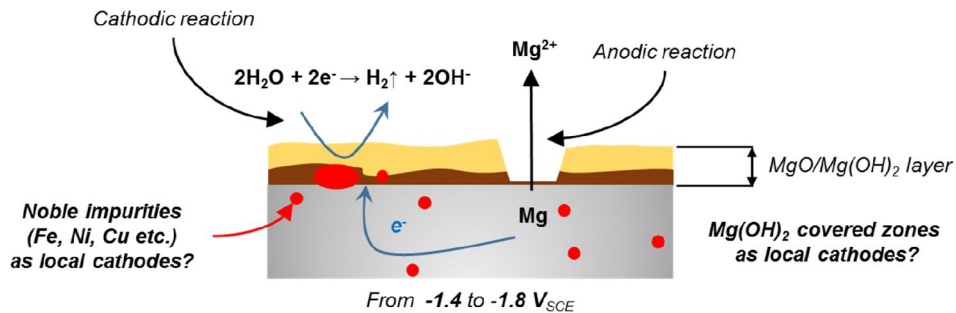


Fig. 2. Schematic representation of the effect of surface film on the enhanced localized corrosion.

Thus, considering the effect of surface films on the reactivity of Mg, these two aspects, the oxide/hydroxide evolution in aqueous environment and the surface enrichment by more noble than Mg inclusions should be understood. Numerous ex situ data about morphology and chemical composition of corroded Mg surfaces were published [15], however the surface analyzed ex situ can be very different from the surface reacting in aqueous solution. In this respect, in situ methods

could bring more valuable data. In particular, the kinetic information could be helpful for understanding the film growth and breakdown mechanisms. Very limited in-situ observations related to the evolution of Mg surface films were communicated [7,16] and neither of them was able to obtain simultaneously global and local information.

Taking into account non-uniform surface evolution of corroding Mg, **the first objective** of this PhD was hence to develop a methodology able to survey in-situ the kinetics of the oxide/hydroxide film evolution in aqueous solutions on significantly large surfaces and with sufficient lateral resolution (mapping mode). From the methodological point of view such a technic should be easily extended to multiple processes for which in-situ measurement with local resolution can be of interest.

The second objective of the PhD was to find a relatively non-expensive and simple way to verify the surface enrichment by different metallic impurities and ions coming from the electrolyte and test the limits of the chosen method. The proposed analytical techniques developed for Mg corroded surfaces could be also used for other corroded materials.

Once the analytical approaches are found and tested, **the third objective** was to correlate environmental composition, evolution of the surface film and Mg reactivity with help of these methodologies.

The results should contribute to fundamental understanding of Mg corrosion mechanisms, in particular the effect of solution composition on the evolution of the surface films. It can also help for a comprehensive choice of anticorrosion strategies. Among different factors which could be taken into account, we selected the effects of solution pH, concentration of Cl⁻ ions and the presence of selected organic inhibitors. Despite the numerous inhibitors proposed for Mg and its alloys [17,18], there is a lack of understanding of the inhibition mechanisms. The mechanistic speculations based on electrochemical measurements are limited by attributing of particular additive to anodic/cathodic/mixed inhibitor type or adsorption/precipitation type. In-situ characterization of the surface evolution in the presence of inhibitors can help to understand the inhibition mechanisms.

To conclude, this work aims firstly, to develop methodologies which permit both, in situ investigation of local oxide/hydroxide layer evolution (chemical composition, spatial distribution, morphology, growth and breakdown kinetics), and ex situ observation of elemental distribution within the layer depth. Secondly, to correlate environmental composition, surface film evolution and Mg reactivity with help of these methodologies.

Analytical approach of the work

Mapping at micrometric resolution provided by **Confocal Raman Microscopy (CRM)** seems to be a promising method for in-situ analysis of corroding surfaces with high lateral resolution. Raman spectroscopy is sensitive to OH^- and CO_3^{2-} vibrations that allows its routine use for identification of corrosion products in aqueous solutions [19–22]. The intensity of Raman scattered light from a sample is proportional to the number of Raman active bonds in the analyzed volume [23] making possible a semi-quantitative analysis and monitoring of film growth kinetics using the spectra normalization procedure. In principle, information on crystal shapes and morphology can be obtained from Raman spectra as well [24].

Although in-situ Raman spectroscopy in corrosion field is commonly used for identification of corrosion products, in-situ kinetic measurements of the film growth or breakdown and in particular in a mapping mode have never been published in this area.

In this work, for the first time, Confocal Raman Microscopy was adapted to map in-situ on large surfaces ($\sim\text{mm}^2$) and with high lateral resolution (\sim tens of μm) the local evolution (chemical composition, morphology, and growth kinetics and disruption kinetics) of surface films during aqueous corrosion of Mg. This technique was used to study the effect of pH, Cl⁻ concentration, inhibitors on the surface film formation and evolution.

Obviously, Raman spectroscopy has its own limitations; the most significant being that some compounds are Raman inactive. Thus, it is impossible to survey directly what happens with MgO, in particular if it is enriched by metallic inclusions or aggressive species such as Cl⁻. In this regard, ex situ elemental depth profiling of corroded material can provide a complementary information. Among others surface-sensitive analytical techniques, **Glow Discharge Optical Emission Spectrometry (GD-OES)** offers a unique combination of a fast sputtering rate (time of one measurement varies between 2 and 10 minutes for Mg samples), high depth resolution, excellent sensitivity, multi-element capability and experimental simplicity with no requirement for an ultrahigh vacuum or special surface preparation [25]. Its application to corroded surfaces is however, still challenging because of formation of porous layers and unexplored analytical data interpretation complicated by a significant plasma modification when sputtering the oxide/hydroxide layers [26,27].

In the PhD, the analytical limits related to the application of GD OES to corroded surfaces are explored and the techniques is successfully applied to monitor the elemental depth-distribution within the oxide/hydroxide layer on corroded Mg and its alloys. This technique significantly contributed to understanding of the Mg inhibition mechanism.

Summary and structure of the manuscript

The manuscript is composed of four main parts: **Introductory section**, **Methodology**, **Results section** and **Concluding remarks**.

The **Introductory section** defines the context and the scientific questions, which should be answered. This part contains 3 chapters: 1) “**Introduction**”, which explain the context of the study and gives the summary of the dissertation; 2) “**Surface films on corroded Mg**” which reviews the existing knowledge about the surface films, their stability and their role for Mg reactivity; and 3) “**Corrosion inhibition of Mg**” representing state of the art in mechanistic approaches for Mg anticorrosion protection. The most important works are listed and the proposed in the literature mechanisms of Mg reactivity as well as inhibition strategies are analyzed in **Chapters 2 and 3**. It should be noted that in addition to this section, each chapter in the Results part includes a short introductory bibliographic section.

The second part, **Experimental section**, describes the main techniques used in this work, namely in situ Raman Spectroscopy and Glow Discharge Optical Emission Spectroscopy. **Chapter 4** presents the principles of both techniques, their advantages and limitations.

The third part, **Results section**, present the most important results obtained during the PhD study and their discussion. This part consists of 3 chapters presented in the form of publications prepared for submission to different journals.

Chapter 5 “pH effect on MgO/Mg(OH)₂ film evolution on corroding Mg by in-situ Kinetic Raman Mapping (KRM)” develops in-situ kinetics Raman mapping (KRM) methodology and demonstrates its applicability to describe the effect of solution composition (pH, presence of Cl⁻) on the local evolution of surface films at initial stages of Mg corrosion in thin layer cell. The use of a specific normalizing procedure for the evolution of A_{1g} brucite peak (3652 cm⁻¹) during immersion in different locations allows extracting film growth kinetics from sufficiently large surface with about 10 μm spatial resolution within the same experiment. On the areas, which did not evolve in optical images during immersion, brucite growth kinetics was

parabolic (diffusion limited) at pH 13 but linear (surface reaction limited) at pH 7-10.5 (Fig. 3a). A jump in the kinetics curve was observed in particular locations on the surface (Fig. 3b).

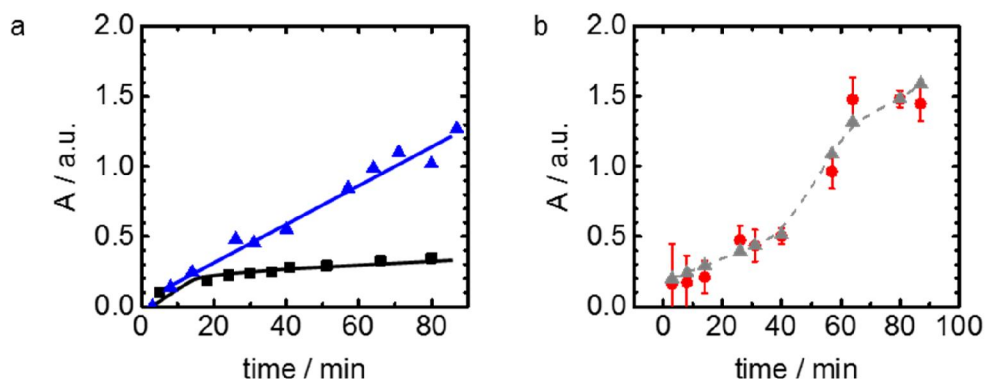


Fig. 3. Examples of localized in-situ $\text{Mg}(\text{OH})_2$ growth kinetics on corroding Mg immersed in 10 mM NaCl at different pH: a) “intact” areas at pH 9 (blue triangles) and pH 13 (black squares); and b) in black filament at pH 9, experimental results (red circles) and theoretical simulation of enhanced $\text{Mg}(\text{OH})_2$ precipitation due to spontaneous pH increase.

Statistical data treatment shows that this type of kinetics is associated with the proximity of black filaments (Fig. 4a) and the time of the steep increase in kinetics curve coincides with the first visual observation of filament in studied zone (Fig. 4b). On Fig. 4b the color code reflects the time of the jump in the $\text{Mg}(\text{OH})_2$ growth kinetics curve. Fraction of the surface with “broken” film as a function of time was also plotted showing the linear breakdown kinetics.

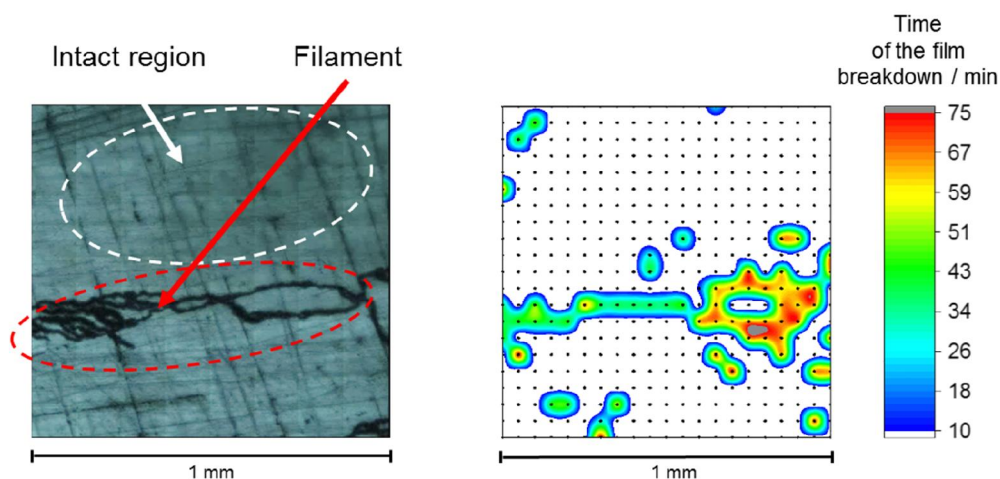


Fig. 4 (a) Example of Mg surface appearance at 80 minutes of contact with 0.1 M NaCl solution; (b) kinetic map (time of sharp growth rate increase for each point) for the same surface.

The spectra were also tentatively analyzed in order to extract information about the in-situ evolution of the crystal size and morphology. Alkalinity increase favored the appearance of “satellites” peaks in Raman spectra (example in Fig. 5c). Bands at 3675 cm^{-1} and 3710 cm^{-1} were

attributed to the vibrations of surface Mg-OH groups with different crystallographic oriented planes, (0001) and (10-10) respectively [28]. The presence of “satellites” hence can be considered as an evidence of high surface area and smaller Mg(OH)₂ crystal size at high pH, which was confirmed by ex-situ Scanning Electron Microscopy (SEM) (Fig. 5). Similar kinetics of the bulk and satellite peaks growth were obtained at pH 13 after about 10 minutes of induction period indicating that the crystal morphology reaches equilibrium at this time.

pH effect on the kinetics of the brucite film growth and the crystals size and morphology is coherent with dissolution-precipitation model of its formation. In this regard, enhanced growth of Mg(OH)₂ in proximity of filaments could be explained by surface film breakdown in this locations resulting in the injection of the excess Mg²⁺ and/ or OH⁻ ions and causing additional brucite precipitation as schematically present in Fig. 6.

A simple calculation of film growth kinetics around the filaments using a precipitation from supersaturated solution gives results which fit well with the observed jump (simulated kinetics is shown by the grey curve in Fig. 3b).

Surface enrichment by metal impurities is in the center of **Chapter 6 “On the application of Glow Discharge Optical Emission Spectroscopy (GD OES) for depth profiling of corroded materials: example of pH effect on Fe and Mn enrichment on corroding Mg”**. Despite its experimental simplicity, the results interpretation of GD OES is not always evident, especially for the estimation of the surface layer enrichment by ppm-level impurities from the metal bulk. The problem is that atomic H in plasma, coming from the sample (outer hydroxide layer), can significantly modify not only the sputtering rate but also detection limits and emission yields for particular emission lines. This causes the ambiguous interpretation of elements intensities changes in oxide/hydroxide layer compared to metal bulk. The effects of H on the analytical parameters of GD OES, the consequences of these effects for the interpretation of depth profiles of corroded surfaces and the way to obtain simply interpretable qualitative profiles are discussed in the work.

Fig. 7a shows an example of a GD OES depth profile obtained in Ar plasma on commercially pure Mg (280 ppm Fe, 50 ppm Mn, 10 ppm Al) after 12 h of immersion in water at pH 9. Raw interpretation of the results obtained in Ar plasma can lead to a wrong conclusion about the depletion of the oxide/hydroxide layer in Mn. Thus, the proposed data treatment (H-correction), shows that the apparent Mn depletion is a result of H effect in plasma. The H correction as well as the experiments in Ar/H₂ plasma demonstrated that the surface was enriched by Mn in studied conditions. GD OES has also demonstrated that H does not influence Cl behavior and that the oxide-hydroxide layer is enriched by Cl.

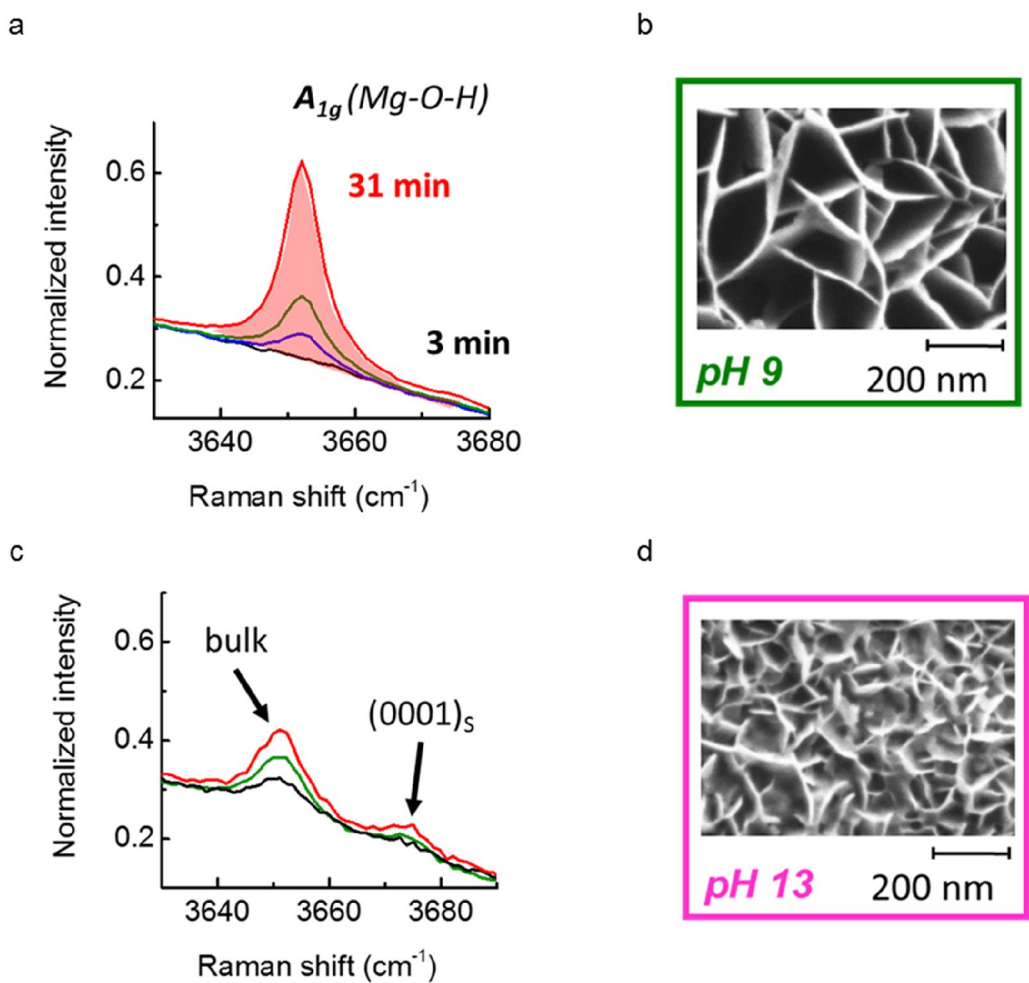


Fig. 5. Examples of in-situ Raman spectra Mg surface in contact with 0.1 M NaCl at pH 9 (a) and 13 (b) and ex-situ SEM images of the corresponding surfaces after immersion.

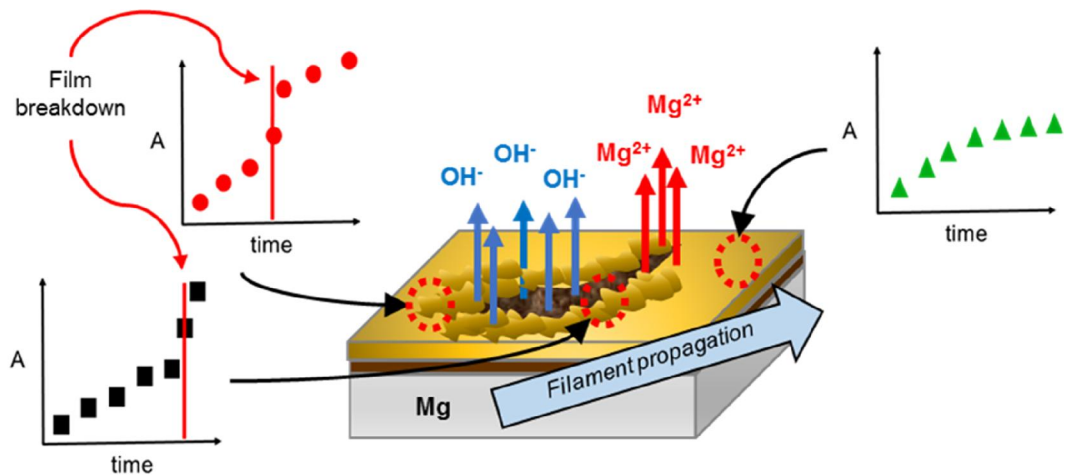


Fig. 6. Schematic representation of $Mg(OH)_2$ growth in Cl^- containing solution around filament and in intact region.

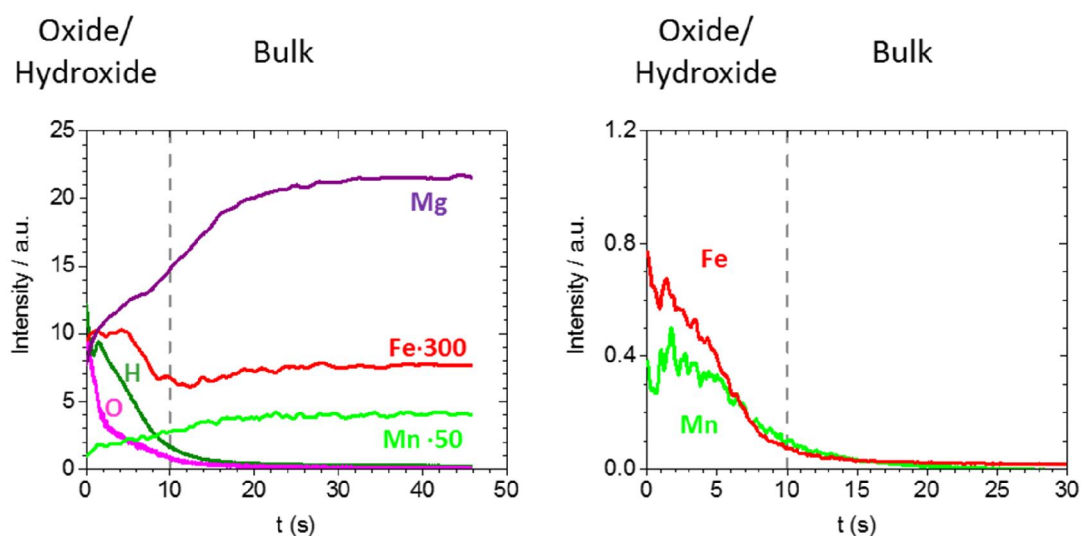


Fig. 7 Elemental GD OES depth profiles obtained for commercially pure Mg (280 ppm of Fe, 50 ppm of Mn, 10 ppm of Al) after 12 h of immersion in water at pH 9: (a) raw data; (b) Fe and Mn profile after H-correction.

Working in Ar/H₂ in place of conventional Ar gas can prevent some artefacts related to the different sputtering rates of corrosion products and the metal and significant plasma modifications between these two layers. Unfortunately, detection limit for Fe is significantly degraded in presence of H, thus, it was not possible to confirm the ppm-level enrichment of the oxide film in Ar/H₂ plasma, however the results of theoretical H-correction taking into account the measured in Ar/H₂ plasma interferences of H signal on the Fe background signal can at least help to verify for the cases with higher Fe content if the enrichment can be considered by GD OES.

Chapter 7 “Inhibition mechanisms of Mg corrosion selected carboxylates” applies the proposed analytical methods to explore the mechanisms of Mg corrosion inhibition by several organic molecules, namely sodium salts of salicylic, 2,5-pyridine-dicarboxylic (PDCA) and fumaric acids (see Fig. 8)

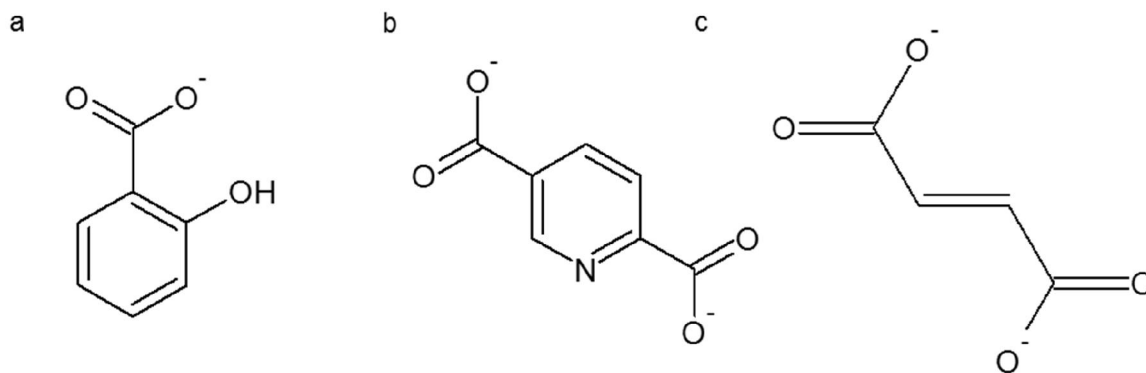


Fig. 8. Structural formula of Mg corrosion inhibitors studied in this work: (a) salicylate, (b) 2,5-pyridinedicarboxylate, (c) fumarate.

Both methodologies established in **Chapters 6 and 7** were used and completed by other techniques in order to compare the film formation in 0.1 M NaCl solution with and without inhibitors on two types of pure Mg. The principal difference between the Mg compositions was amount of Fe impurities, 342 and 50 ppm for commercial and high purity Mg respectively. All of inhibitors efficiently retarded Mg corrosion, except salicylate, which inhibited only Mg with higher content of Fe inclusions and, conversely, accelerated corrosion for high purity Mg.

First of all, ex-situ GD-OES depth profiles after immersion of Mg in 0.1 M NaCl solutions with and w/o the inhibitors (Fig. 8) confirmed that all inhibitors were incorporated into the oxide/hydroxide film (strong C signal) and efficiently decreased the quantity of adsorbed Cl^- , which is known as a film destabilizing agent responsible for the initial pitting.

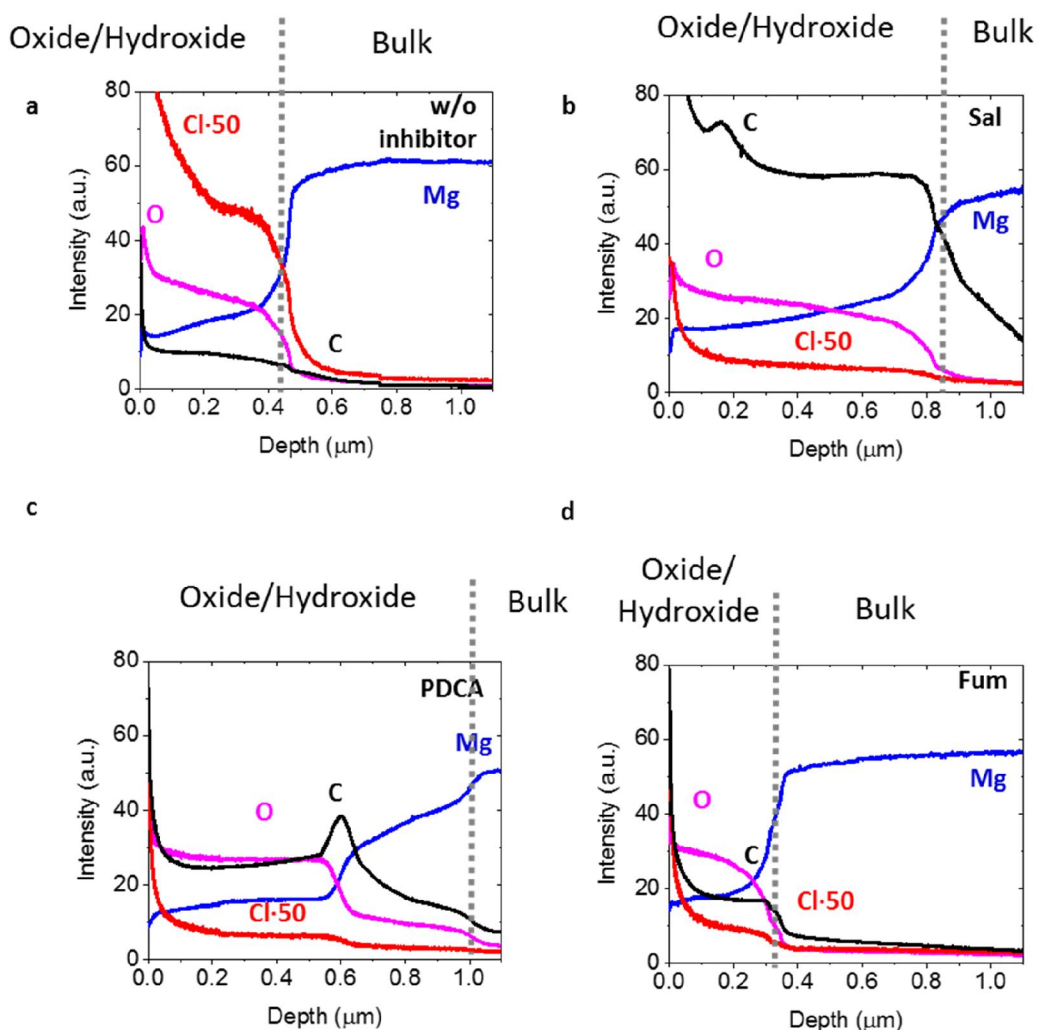


Fig. 9. Elemental GD OES depth profiles obtained in Ar/H₂ plasma for commercial purity Mg (ppm impurities level) after 2 h of immersion in 0.1 M NaCl without inhibitors (a) and with addition of a selected inhibitor: sodium salicylate (b), PDCA (c) or sodium fumarate (d).

In situ Raman spectroscopy revealed two different trends in $\text{Mg}(\text{OH})_2$ growth kinetics in presence of inhibitors (Fig. 10). For fumarate, the growth was slower as compared with 0.1 M NaCl solution. For salicylate and PDCA the growth rate evolved in 2 periods. Initially, it was similar to the growth rate evolution w/o inhibitors. After approximately 40 minutes of the surface contact with the solution, the growth was slower and looked similar to fumarate solution. In presence of all inhibitors the satellite peaks were visible, revealing smaller crystal size than in solutions w/o the inhibitors.

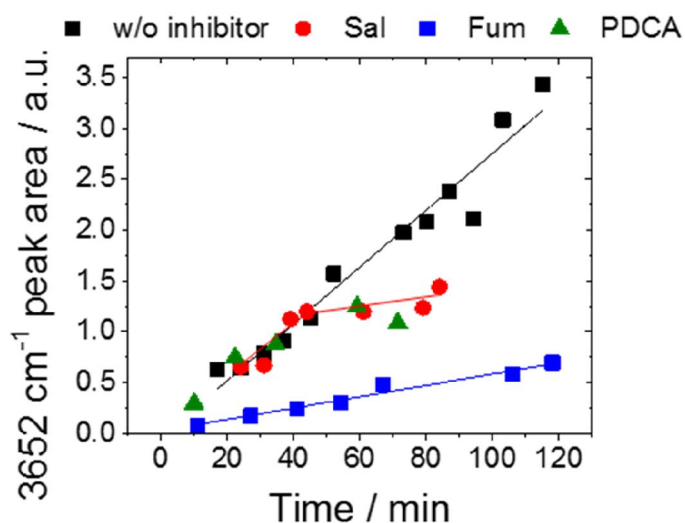


Fig. 10. Typical localized $\text{Mg}(\text{OH})_2$ growth kinetics on corroding Mg immersed in 0.1 M NaCl w/o inhibitors (black squares), with addition of 0.05 M sodium salts of fumaric (blue squares, Fum) salicylic (red circles) and 2,5-pyridindicarboxylic (green triangles, PDCA) acids.

The interaction of the inhibitors with the surface film was also analyzed. On the corroding Mg of commercial purity, the characteristic Raman shifts and IR bands positions of $-\text{COO}^-$ and $-\text{OH}$ groups of salicylate were shifted as compared with the positions observed for the unbounded inhibitor (Fig. 11). This was interpreted as a specific interaction of salicylate with the surface. For fumarate, no specific interaction was observed. For PDCA no shifts in bands position in Raman spectra were registered during the first 40 minutes, and then the high fluorescence background appeared hindering the Raman signal. This could be explained by formation of a specific network of the organic molecules which has a chain of alternating double and single bonds, called conjugation [29]. Ex situ analysis by IR spectroscopy confirmed slight shifts of the peaks positions characteristic for aromatic ring vibrations for PDCA.

Three different types of interaction of the organic molecules with the Mg surface were proposed for the studied inhibitors. Physical adsorption of fumarate, chemisorption of salicylate on $\text{Mg}(\text{OH})_2$ or Fe-containing particles on cathodic areas and coordinated polymer formation at the interface between more and less hydrated oxide/hydroxide layers in case of PDCA are the most

probable mechanisms of the surface modification. Concerning the inhibition mechanisms, specific interaction of salicylate with Fe is coherent with cathodic inhibition reported in the literature [30] as well as with the absence of the inhibition effect for high purity Mg. Fumarate and PDCA form homogenous surface films which is coherent with the inhibition of anodic reactivity. All the surface films formed in the presence of inhibitors contain $Mg(OH)_2$ nanocrystals with a reduced size as compared with the films formed w/o inhibitors and block Cl^- access to the surface, reducing the possibility of localized corrosion due to the film breakdown. The proposed mechanisms of the films formation in the presence of the inhibitors and its consequence for the reactivity are summarized in Fig. 12.

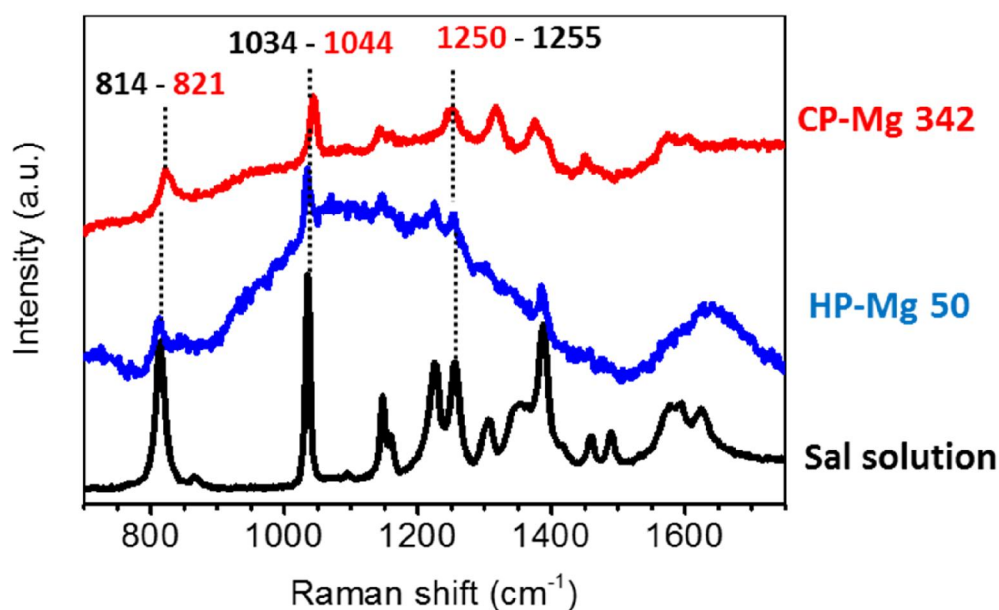


Fig. 11. Examples of in-situ Raman spectra of commercial purity Mg (CP-Mg342) and high purity Mg (HP-Mg50) in contact with 0.1 M NaCl + 0.05 M Na salicylate solution compared with Raman spectrum of sodium salicylate solution.

The **Chapter 8, “Conclusions and perspectives”**, summarizes the main findings, their importance for corrosion mechanisms and the perspectives open by the proposed analytical approach.

In **Appendices**, some additional results obtained during the PhD and illustrating the application of developed methodologies to several systems with potential applied interest are included. Among them, the effect of Li alloying in the chemistry of the surface films and the effect of self assembling monolayers on the film growth kinetics.

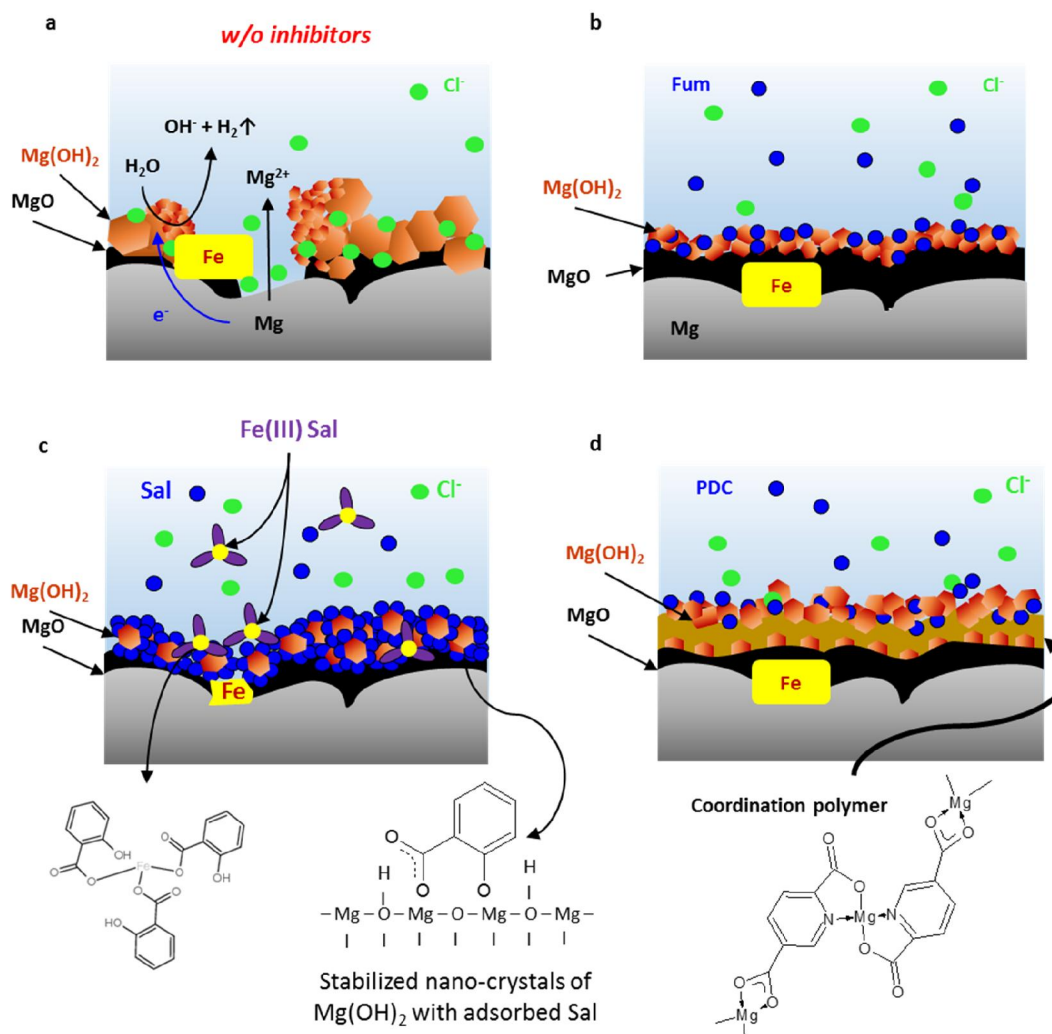


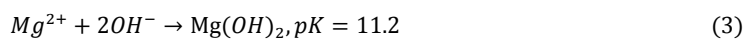
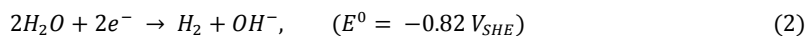
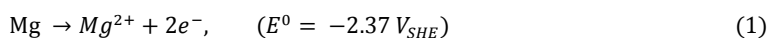
Fig. 12. Schematic representation of Mg reactivity in absence of inhibitors (a) and Mg corrosion inhibition mechanisms for (b) fumarate – physical adsorption, (c) salicylate – dissolution of Fe-rich inclusions and stabilization of Mg(OH)₂ crystals due to specific adsorption of Sal, (d) 2,5-pyridinedicarboxylate – precipitation of coordination polymer.

Chapter 2

Surface films on corroded Mg

Basics of Mg reactivity

The high rate of Mg aqueous corrosion is usually associated with two key factors. Firstly, the electrochemical nature of the metal: the highly electronegative potential of Mg (1) implies that the water reduction is the cathodic half-reaction (2), therefore Mg corrosion proceeds even in the absence of oxygen. Secondly, surface films naturally formed on Mg (3) have poor protective properties because of their high solubility (see section “Composition of corrosion products”).



Perhaps, the main topic concerning the mechanism of Mg corrosion in the last decades was so-called Enhanced Hydrogen Evolution (hydrogen evolution rate, HER). The fact that H₂ evolution (cathodic reaction, (2)) occurred even when anodic potentials or currents were imposed,

first reported by Beetz in 1866 [31], intrigued several generations of scientists. In this regard, Mg behavior is unusual when compared to other metals, where typically a cathodic reaction becomes progressively suppressed under anodic polarization. The enhanced hydrogen evolution is accompanied by the mass loss that is notably higher than those one calculated from Faraday's law for a 2 electron transfer process. The term Negative Difference Effect is also used for this phenomenon, where the difference means subtracting the hydrogen evolution rate measured in the absence of external polarization from that observed when an anodic potential is applied.

It should be noted that existence of anomalous HER makes complicated the quantitative estimation of amounts of Mg dissolved under anodic polarization using just electrochemical methods: a certain amount of the electrons generated by the Mg oxidation reaction do not flow through the potentiostat to the counter electrode but rather are consumed by the HER on the Mg electrode surface, thereby remaining undetected. Taking into account that Mg has the most negative electrochemical potential between all metallic engineering materials, it is supposed to be polarized anodically in contact with them in real applications. Thus, understanding of the origins of anomalous HER has potential scientific and technological interests, being the key for elaboration of intelligent anticorrosion strategy.

Numerous theories, summarized elsewhere [32,33], were proposed to explain this aspect in Mg behavior, among them:

- 1) the existence of uni-positive cation Mg^+ and its further oxidation to Mg^{2+} , that leads to the water reduction in the solution [34–37];
- 2) “chunk effect” of non-faradaic mass loss via metal spalling [38];
- 3) formation and dissolution of hydrides [39];
- 4) surface enrichment by noble impurities [12];
- 5) formation and dissolution of partially protective films,
etc...

Noble inclusions and corrosion products are assumed to play a crucial role in Mg degradation in aqueous environments even though precise mechanism is still under discussion. Therefore, further bibliography review is focused on these two aspects.

Corrosion products in Mg reactivity

Composition of corrosion products

Mg reacts with atmospheric oxygen forming a surface film of MgO with a thickness of a few nm [15]. This layer ensures corrosion protection in the dry air at ambient temperature.



MgO has a thermodynamic tendency to interact with water with formation of Mg(OH)₂ even at low water vapor concentration (>1ppm H₂O) [5,15,16,40].

In aqueous environments MgO dissolves easily ($K_{sp}(\text{MgO}) \sim 10^{-6}$, [15]), that leads to the formation of Mg(OH)₂ (brucite) precipitates [41]. Thus, the typical surface film that is usually observed on Mg surface after immersion tests has a bilayer structure consisting of a thin, inner MgO-based layer, and a porous Mg(OH)₂ outer region [2–5,42], as shown in Fig. 13 and Fig. 14. The outer precipitated brucite usually presents a platelet-like or needles morphology(Fig. 15).

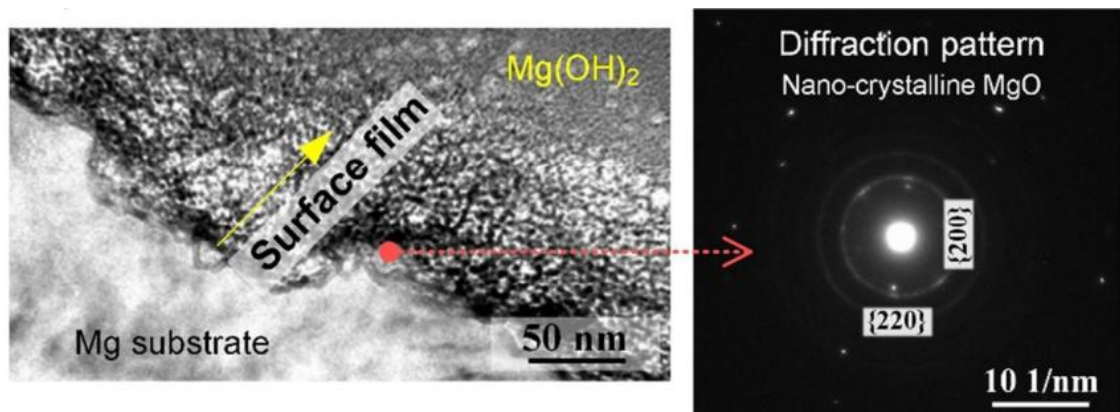


Fig. 13. TEM micrograph and a diffraction pattern detecting nanocrystalline MgO at the interface region, after exposure to pure water for 48 h [4].

This layer is considered in the literature as “quasi-passive”, because it can provide corrosion protection at the early stages of immersion [6,7]. However, MgO and Mg(OH)₂ are both relatively soluble in water ($K_{sp}(\text{Mg(OH)}_2) \sim 10^{-11}$ [15]). At pH higher than ≈ 10.5 the outer hydroxide film is thermodynamically stable [43], whereas its disruption occurs in neutral solutions containing chloride, sulphate, or nitrate anions [7,8]. This phenomenon is often explained by formation of other compounds with higher solubility constant.

For instance, different chloride containing compounds such as $\text{MgCl}_2 \cdot 6\text{H}_2\text{O}$, $\text{Mg}_3(\text{OH})_5\text{Cl} \cdot 4\text{H}_2\text{O}$ and $5(\text{Mg}(\text{OH})_2) \cdot \text{MgCl}_2$ were identified by infrared spectroscopy, X-ray diffraction and Auger electron spectroscopy on magnesium corroded in NaCl solution [8]. Presence of elemental Cl extending to the inner MgO-base film region was reported in several works [2,44]. Some authors have postulated the presence of carbonates on the surface layer after humid air exposure [45,46] or after aqueous corrosion [47].

Particular attention should be paid to local Mg corrosion. The appearance of so-called “dark zones” on the surface, which can be in form of threadlike filaments or shallow excavated disks (Fig. 16) was mentioned in many works [3,11,48–56]. The shape of dark zones was noticed to be dependent on the impurities content and Cl^- concentration in the solution [57]. The black color of the corroded area can be explained by cracking of the surface and detaching of small Mg particles [38,58]. As observed in [6], the black corroded zones are highly rough compared to the intact (uniformly covered by $\text{Mg}(\text{OH})_2$ layer) Mg. It has been noted that morphological changes of hydroxide layer take place after the initial surface film breakdown, which is transformed from a compact thin film to a much thicker film with high porosity [44]. Dark zones are considered to be consisting of irregular granular features of Mg metal and/or magnesium (hydr)oxide [3,14].

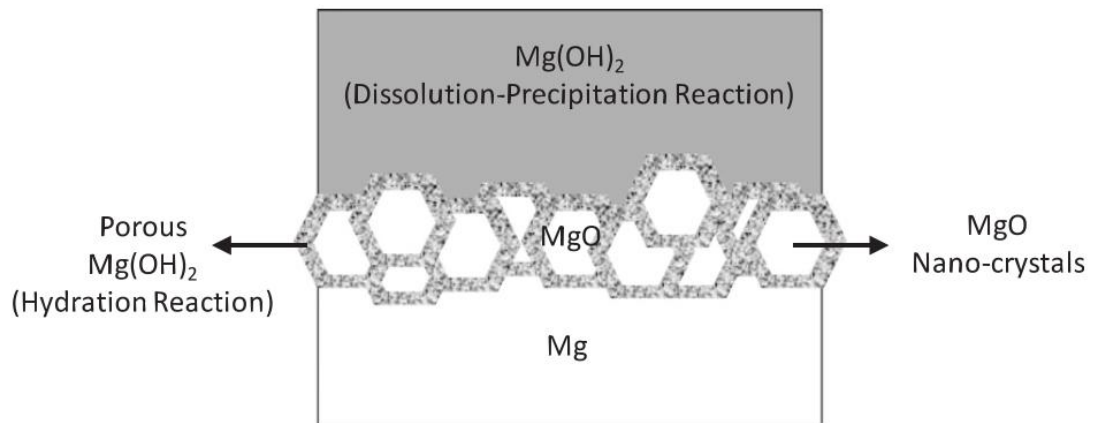


Fig. 14. Schematic of the diffuse bi-layer structure of the surface film formed on mechanically polished Mg after aging at E_{corr} in pure H_2O at room temperature for 48 h [4].

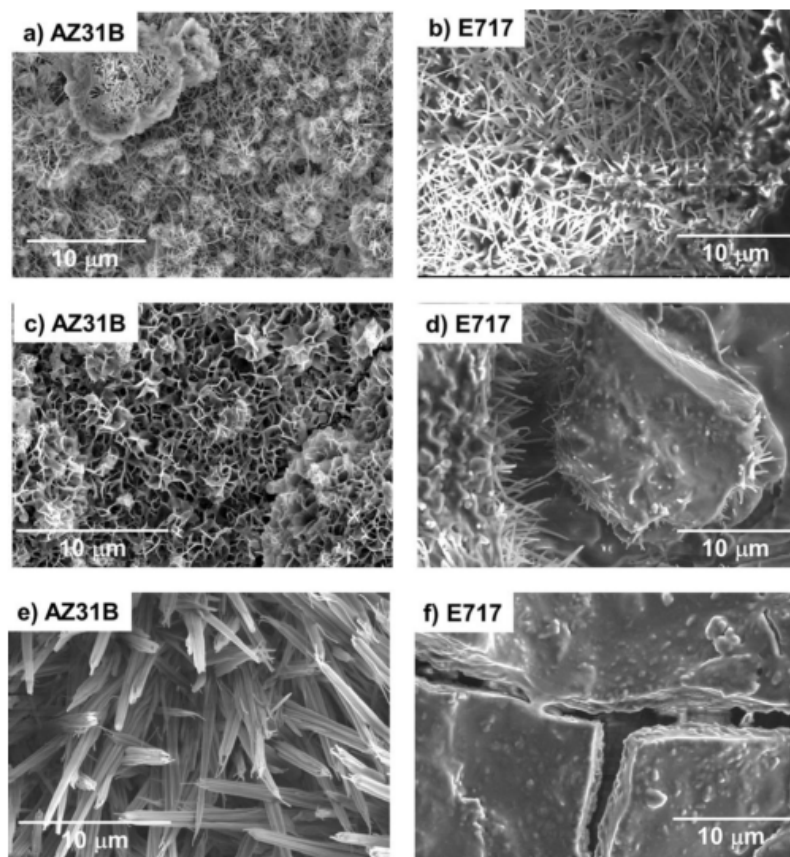


Fig. 15. Surface secondary mode SEM images of AZ31B (a,c,e) and E717 (b,d,f) after 24 h in D2O with 5 wt% NaCl showing wide morphological variation of $Mg(OH)_2$ -base surface products formed. (Illustration was taken from [2])

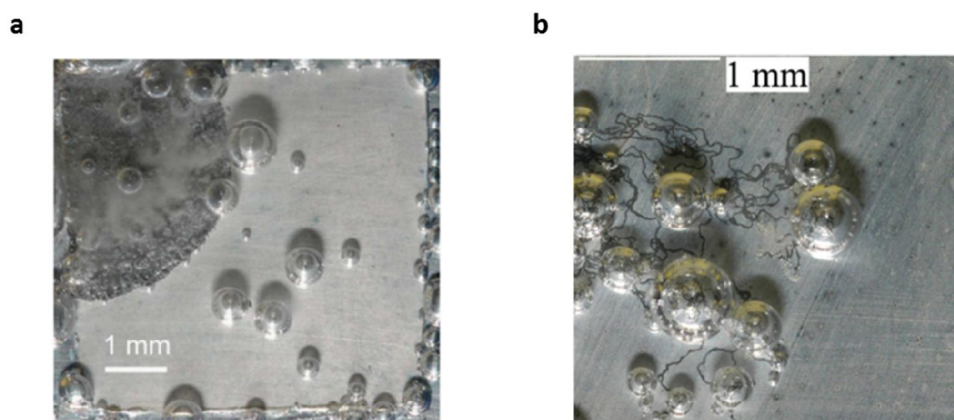


Fig. 16. Photographic images of a commercial purity magnesium surface freely corroding in aerated (a) 5% w/v and (b) 0.01 M NaCl (aq) at pH 6.5 taken at 38 min and 64 min following immersion respectively. (Illustrations are taken from [11,49]).

Influence of corrosion products on HER

It has been shown in many works that Mg corrosion products provide enhanced catalytic activity towards the HER [10,48,59,60]. When Mg dissolves at the open circuits potential (OCP), dark regions progressively appear on the initially silvery surface, eventually covering it completely. Williams et al. [11] studied the HE on pure Mg during anodic polarization using the Scanning Vibrating Electrode Technique (SVET). They found that the circumference of the expanding dark corrosion zone is an intense net local anode, while its center was shown to be cathodic (Fig. 17). Application of an anodic (or cathodic) polarization resulted in faster (or slower) propagation of the active anodic region with respect to the propagation dark regions [61].

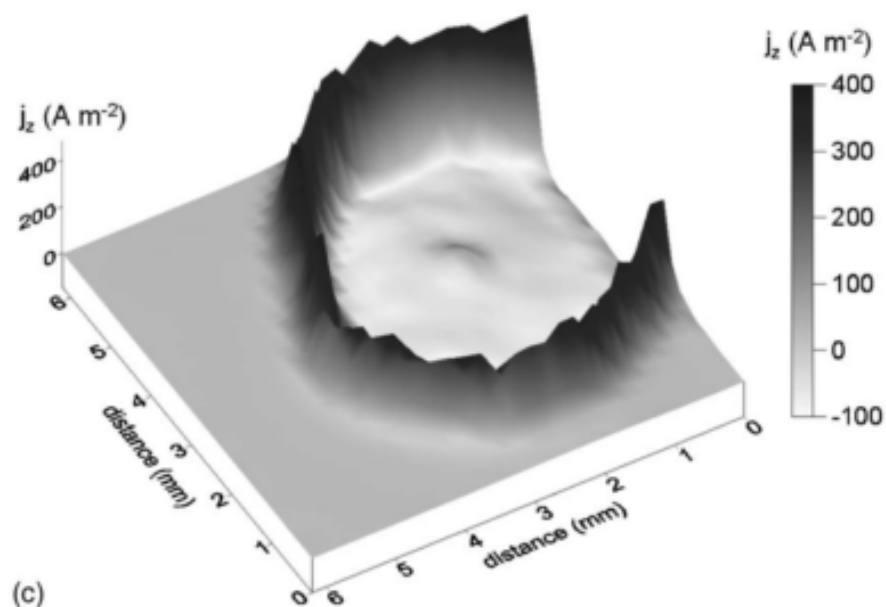


Fig. 17. Surface plots showing the distribution of normal current density j_z above a CP magnesium sample freely corroding in aerated 5 g per 100 ml aqueous NaCl solution at 20°C. Data were obtained from SVET scans carried out after 36 min of immersion. (Figure from [11]).

Not only dark zones were reported as cathodically active. The evolution of anomalous H₂ was recently studied by Fajardo et al. [62] on HP Mg in an acidic citric acid buffered solution where the typical dark corrosion product known for neutral and alkaline solutions was not found. These authors observed anomalous HE even in the absence of a dark corrosion product.

The kinetics of the hydrogen evolution reaction (HER) were examined on pristine Mg and Mg(OH)₂ coated Mg [10]. The kinetics of the HER measured by scanning electrochemical microscopy (SECM) was ~3 times and ~4-6 times more fast on Mg(OH)₂ coated Mg than on the

pristine surface at corrosion potential and under cathodic polarization at -1.9 . V_{SCE} respectively (Fig. 18).

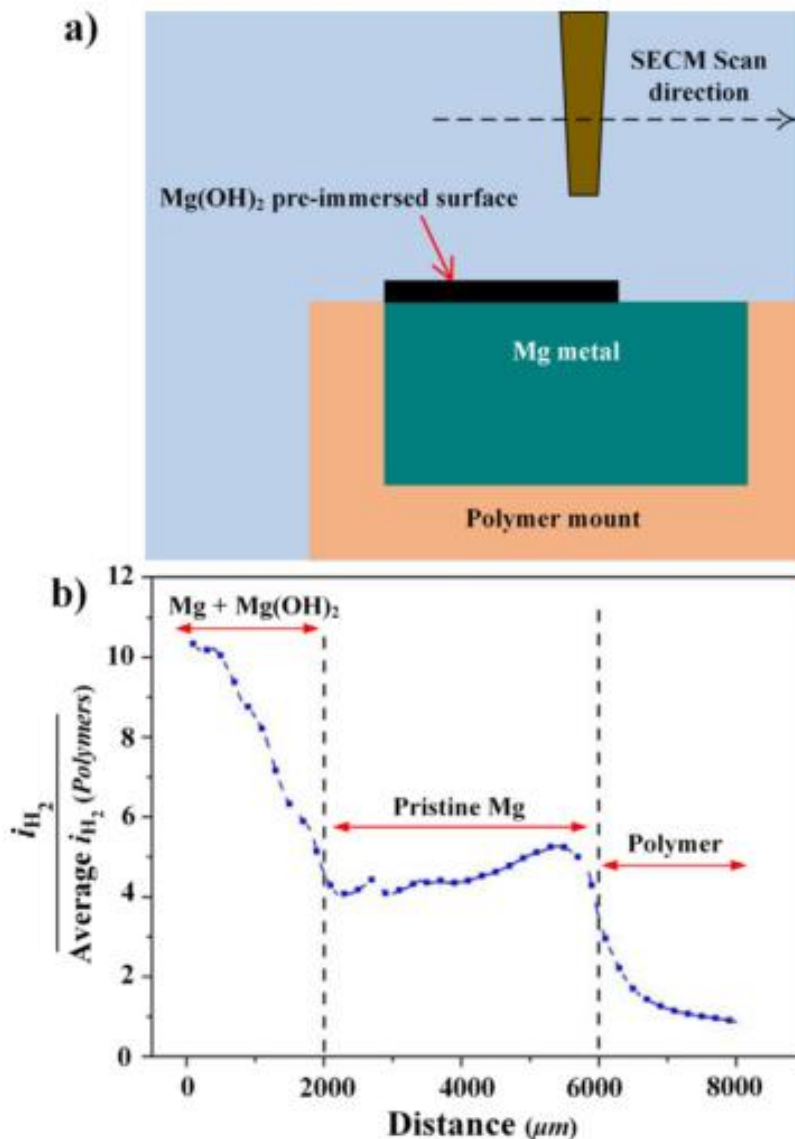


Fig. 18. Catalytic activity towards the HER associated with the film determined by SECM. (a) Schematic representation of the setup used for the SECM experiments, and (b) normalized H₂ oxidation currents measured during a line scan from the Mg(OH)₂ coated Mg surface, through the pristine Mg surface, and to the polymer surface [10].

Nevertheless, up to now, there is no comprehensive explanation in the literature of the origins of the reactivity of Mg corrosion products. Sometimes this theory raises the criticism because all of corrosion products usually formed on Mg (MgO, Mg(OH)₂, hydroxy-carbonates etc) are insulators, thus, in principle, they are unlikely act as cathodes, except if they contain significant quantity of the defects or form very thin layer enough to allow electron tunneling. Moreover, the rate of HE measured using H₂ collection methods is often constant with time, rather

than increasing with time. Instead, the HE rate correlates with the anodic current density applied or the rate of corroded area production, not with the number of corroded areas. These observations are not consistent with the notion that the dark corrosion regions are the primary source of anomalous HE.

Alternative mechanism suggested by Salleh et al. [10] is based on the enhancement of the self-dissociation of water on corrosion products, arising from the disruption in the local ionic equilibrium as Mg^{2+} ions precipitate as $Mg(OH)_2$ in supersaturated conditions (Fig. 19). DFT calculations performed by other researchers also suggested that the presence of adsorbed OH^- groups or hydroxylation of the Mg surface (akin to $Mg(OH)_2$ on the Mg surface) activate water dissociation upon Mg [63].

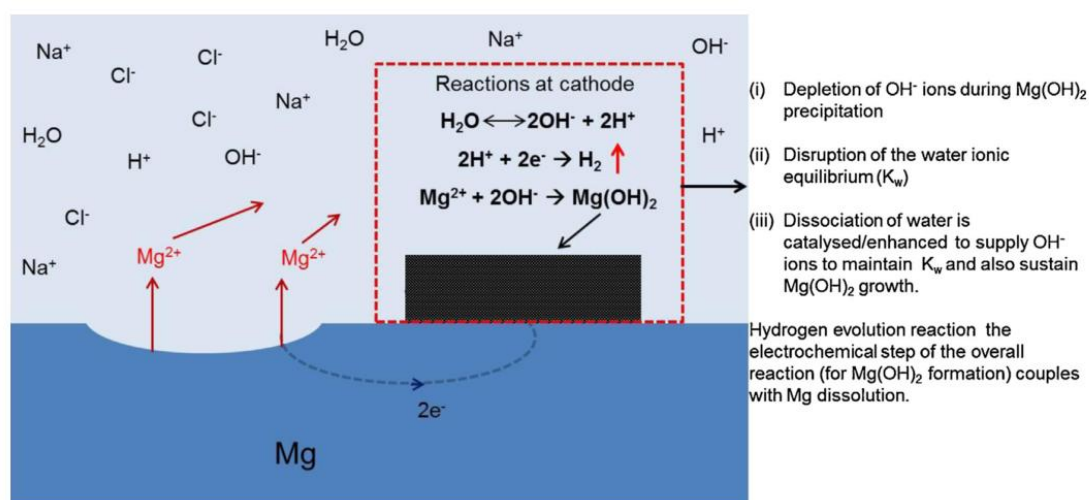


Fig. 19. Schematic representation of HER governed by precipitation of $Mg(OH)_2$ presented in [10]. In super-saturated conditions, the sites of $Mg(OH)_2$ formation consume Mg^{2+} ions and OH^- ions. There is a rapid depletion of OH^- ions in the system, resulting in the disruption of the ionic equilibrium of water. Water dissociation immediately takes place in the system, supplying the necessary OH^- ions to complete $Mg(OH)_2$ formation. The protons released during water dissociation, undergo HER coupled to Mg dissolution.

Indeed, idea of enhanced precipitation of $Mg(OH)_2$ in dark zones follows logically from the assumptions of changes in local concentrations of Mg^{2+} and OH^- due to the enhanced anodic reactivity on the edges of these zones. Local release of ions, measured in situ by Scanning Ion-selective Electrode Technique (SIET), was reported by Lamaka et al [64], however nobody have shown formation of surface film on Mg in situ, with good spatial resolution. Some in situ studies of the film formation on Mg were performed by in situ ellipsometry [7], but this method can be applied only to very thin films (less than 170 nm), it doesn't provide the local information and hence not applicable to the initial stages of corrosion and understanding of black filaments. Moreover, it does not provide any information about the chemical evolution of the films.

Dynamically formed oxide/hydroxide surface films can influence Mg reactivity: protect it from corrosion due to barrier properties, or accelerate degradation promoting the cathodic hydrogen evolution. Up to now, there are plenty of in situ studies reporting the local currents and ion flux distribution during Mg corrosion, however, there is no information about the local film growth and evolution kinetics, in particular nothing is reported about the evolution of its morphology and chemical composition in situ.

Kinetics analysis

Multiple phenomena can be involved in the formation of the oxide films on metals in aqueous environment: the direct growth of the oxide layer, the dissolution of the oxide film and the precipitation of dissolving species from the solution [65]. Different kinetics models were established to describe each of these processes.

The direct growth of the compact oxide layer on metal surface (solid-state diffusion) was described by models based on Wagner theory [66]: Cabrera-Mott [67], Fehler-Mott [68] models were initially established for the thermal oxidation of metals in the air; Point Defect Model (PDM) assume the oxidation in aqueous environment [69,70]. All of these models predict logarithmic (5) or reciprocal logarithmic (6) kinetics laws for the film thickness (x) of thin passive layers

$$x = k_1 + k_2 \ln t \quad (5)$$

$$\frac{1}{x} = k'_1 - k'_2 \ln t \quad (6)$$

where k are constants.

For the thick oxide layers the parabolic law (Eq. (7)) describes formation of a coherent, impenetrable layer, it assumes the diffusion of cations or anions as the rate-controlling step [71,72].

$$x = (k_p t)^{1/2} \quad (7)$$

The linear law (8) describes surface-controlled reactions. This kinetics law is expected if the oxide film is porous or cracked [73] it implies that the oxidant has an unrestricted access to the growth site, via oxide pores [74].

$$x = kt \quad (8)$$

To describe precipitation from supersaturated solutions, different approximations, depending on the mechanism (nucleation controlled, polynuclear growth or mononuclear growth) can be used [75]. Generally, experimental data of reaction degree (α) as a function of time can be fitted by power function (9) for $\alpha \rightarrow 0$ or exponential function for $\alpha \rightarrow 1$.

$$\alpha \cong k''t^b \quad (9)$$

$$\alpha \cong 1 - \exp(-Kt) \quad (10)$$

where k, K, b are constants.

Attribution of the experimental kinetics data to one of the equations listed above is ambiguous for the aqueous corrosion. Thus, it has been clearly demonstrated on the example of mild steel that corrosion products formation cannot be described only by precipitation from the bulk solution, the formation rate is directly related to corrosion rate and the conditions at the metal surface [76]. Other factors such as multilayered growth [77], local corrosion [78] etc. can influence the growth kinetics.

Very limited data about the kinetics of Mg(OH)₂ growth were found in literature. Hara et al reported kinetics of Mg(OH)₂ growth on pure Mg and Mg alloys in NaCl and Na₂SO₄ neutral solutions [7] in two-stages: linear growth law for the first 1 to 5 minutes and the following decrease of the growth rate.

Impurities incorporation in corrosion products

Beside MgO and Mg(OH)₂, the surface film can contain other elements, coming from the Mg alloy matrix or from the environment, that can eventually influence the corrosion performance. Diversity of existing Mg-alloys with different alloying elements and the role of each element in Mg reactivity is out of scope of this work. Instead, the following literature review is focused on minor impurities that can be present in pure Mg as a consequence of casting process. Speaking about environment, most of corrosion tests are usually performed in chloride-containing solutions, because Cl⁻ is known as a corrosion accelerator for many metals. In particular, it causes pitting corrosion and other types of localized corrosion on metals that form passive films. Therefore, one sub-section will be dedicated to Cl⁻ influence on Mg reactivity and corrosion products formation.

Role of more noble than Mg impurities

Since Mg has the lowest electrochemical potential of all of the structural metals and hence a lower potential than the potential of the majority of alloying elements present in Mg and its alloys, almost any metallic impurity or alloying element will be more noble than Mg. Among all the known impurities, iron (Fe) is definitely one of the most prevalent due to its low solubility in Mg and its presence at virtually every production step, e.g. tools and casting pots [79]. The effect of

more noble impurities on its corrosion performance has been known for a long time. McNulty and Hanawalt argued that iron-rich second-phase particles constitute the principal cathodic hydrogen evolution reaction (HER) site on Mg [12]. They also demonstrated a “tolerance limit” for iron of 100–320 ppm, above which HER rate increased dramatically. Recently, it was reported that the shape of corrosion front (dark corroded zones) depends on the Fe-content: at fixed Cl⁻ concentration, disc-form corrosion is observed on samples having ≥ 280 ppm Fe, but filiform-like corrosion predominates at ≤ 80 ppm Fe [57].

It is usually assumed that as the result of preferential dissolution of Mg during open circuit corrosion or under anodic polarization, impurities present in the bulk material, such as Fe, may accumulate in/under the dark corrosion film formed on the surface. As a result, the concentration of impurities at the surface could become substantially higher than the concentration in the bulk metal. Sites of enriched noble elements with higher exchange current density for the HER than that of Mg would lead to enhanced rates of HE even at potentials for which Mg is anodically polarized.

The precise location of more noble inclusions in the corroded film is not clear. Taheri et al. detected small Fe-rich particles embedded **in the outer hydroxide layer** formed on a HP-Mg electrode after anodic polarization (Fig. 20,[3]).

Cain et al. [13] studied the enrichment of transition metals on dissolving Mg using Rutherford Backscattered Spectroscopy (RBS) and revealed direct evidence of Fe enrichment in the corrosion oxide/hydroxide film but, more importantly, **under the film on the metal surface of a Mg anode**.

The kinetics of the hydrogen evolution reaction (HER) were compared for the pristine Fe and Mg(OH)₂ coated Fe. It was demonstrated that Mg(OH)₂ layer does not inhibit the HER on the Fe surface, at potentials close to the Mg’s OCP. This implies that Fe impurity particles, which are entrapped under corrosion products (Mg(OH)₂), even it is supposed to be poorly conductive, can still sustain the HER at high rates upon them [10]. Thus, approximate mechanism could be presented such as in work of Taheri et al. (see Fig. 21) [3].

Höche et al. used an original approach combining magnetic field, X-ray diffraction and TEM [80] to show Fe enrichment on corroded Mg surface. The proposed mechanism for anomalous HE was based on the idea of iron re-deposition. Authors assumed that Fe impurities present in the Mg specimen would leave the surface by non-Faradaic release associated with the dissolution of the surrounding Mg matrix, and then redeposit on the Mg surface after dissolution at their own open circuit potential in the electrolyte.

This idea was further explored by Lamaka et al. [81] who formulated the novel strategy of Mg inhibition based on suppression of iron re-deposition. Authors proposed that addition of Fe-

complexing agents in the solution should bind Fe ions, hence, preventing Fe re-deposition and enhanced HE. Indeed, HE estimated by hydrogen collection measurements at the OCP showed that most of the Fe complexing agents efficiently lowered the corrosion rate of Mg [18], which is a strong support for the role of noble impurities in the corrosion mechanisms of Mg alloys.

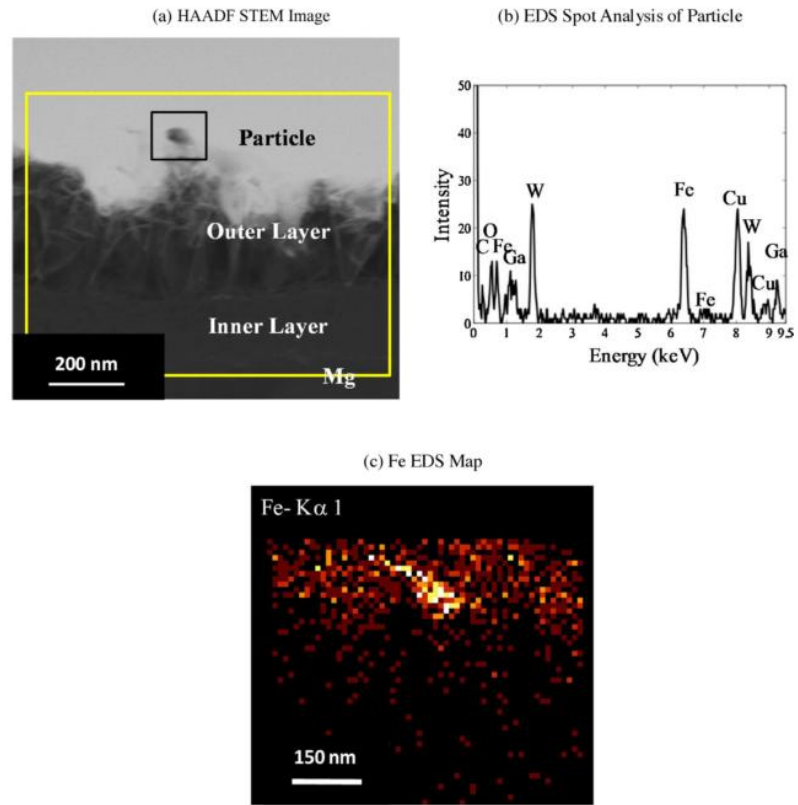


Fig. 20. TEM examination of FIB prepared lamella from a localized dark region of the Mg surface in cross-section: (a) HAADF STEM image showing impurity particle embedded in surface along with spot analysis area (black frame) and two dimension map (yellow frame), (b) EDS spot analysis of particle embedded in columnar outer layer, (c) two dimension EDS map for Fe. (Figure from [3]).

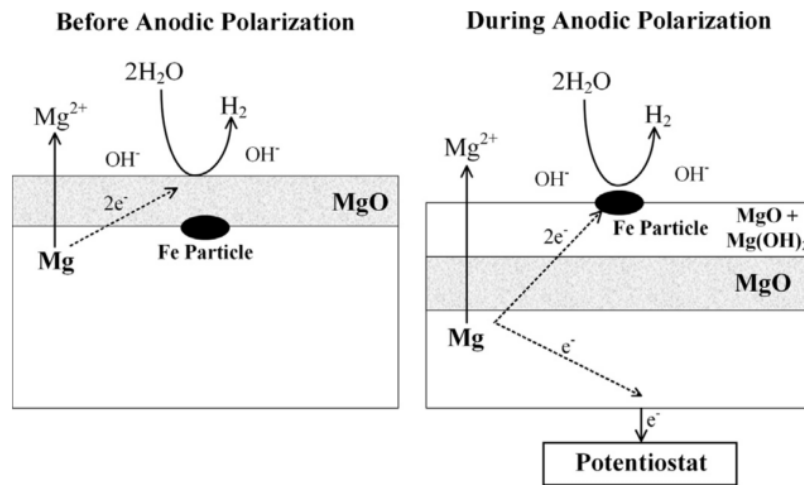


Fig. 21. Schematic model based on the effect of impurity enrichment on α -Mg surface for the anomalous HE [3].

The same idea of iron re-deposition was supported by Mercier et al. [82]. Authors provided 3D Time-of-Flight Secondary Ion Mass Spectrometry (ToF-SIMS) chemical images of pristine and corroded Mg surface. Significant segregation of Fe, Mn, Al metallic impurities at grain boundaries (GBs) of the initial Mg surface after chemical etching and homogeneous distribution of these elements after polarization performed in 0.1 M NaCl electrolyte at $E_{\text{OCP}}+0.5$ V were reported. It was assumed, that during polarization of Mg a significant dissolution of magnesium can occur at grain boundaries generating the release of noble metallic impurities localized at/near grain boundaries, leading to intergranular corrosion. Dissolution of the metallic impurities was followed by a re-deposition during the corrosion process (Fig. 22).

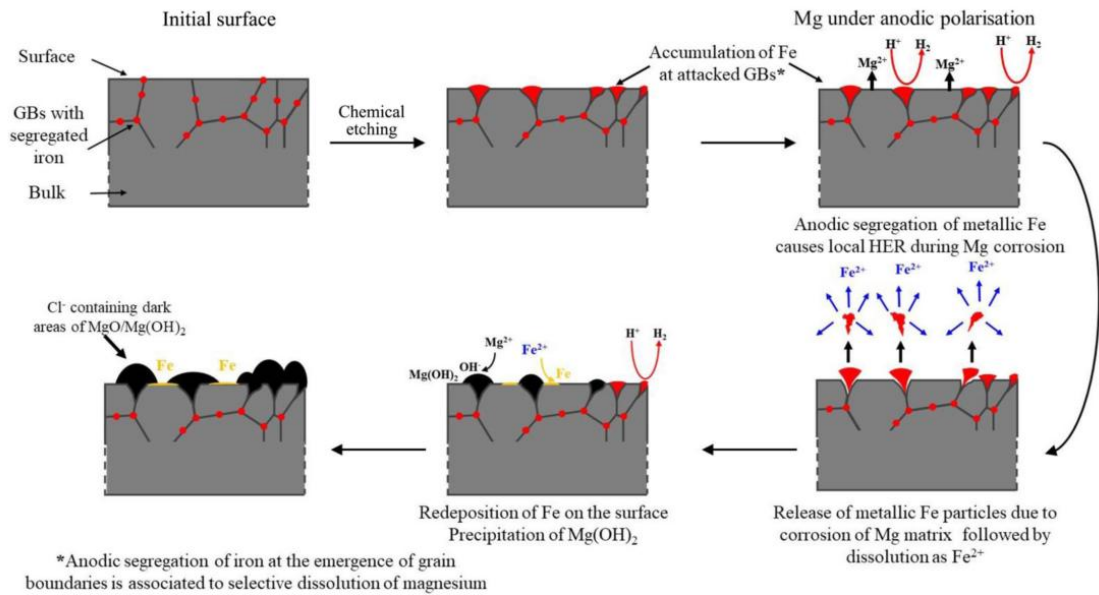


Fig. 22. Proposed in [82] mechanisms of Mg corrosion at grain boundaries and HER including the role of the segregation of metallic impurities (Fe) at grain boundaries (GBs).

Even if the enrichment of more noble impurities was shown to influence corrosion behavior of Mg, it should be noted that it still cannot fully explain the phenomenon of anomalous HE. The main criticism arises from the question how such an extensive amount of hydrogen can be cathodically generated on the noble inclusions, since they constitute only a minor fraction of the total surface area of the Mg substrate. In particular, it is true for magnesium of relatively high purity where the concentration of impurities is at the ppm level. It was shown that at anodic polarization HE was very large for both high purity Mg (99,98%) and ultra high purity Mg (99,9999%), independent of Fe content [60]. In work of Birbilis et al. [83], even though the concentration of surface impurities was shown to appreciably increase after anodic dissolution, enrichment efficiency was less than 1 %.

Role of Cl⁻ concentration

It has been shown in several studies, where combination of anodic polarization and electrochemical impedance spectroscopy were used, that increasing chloride concentration ($[Cl^-]$) leads to higher rates of Mg corrosion [84–86]. Cl^- concentration influenced the shape of corrosion front (dark zones), namely disc-form corrosion features appeared in concentrated NaCl electrolyte, whereas filiform corrosion was observed on the same Mg samples at lower Cl^- concentration [57]. Williams et al. [52] have shown quantitatively the relationship between corrosion resistance and $[Cl^-]$. Breakdown potential (E_b) values were measured as a function of $[Cl^-]$ for commercial purity Mg and AZ31 alloy specimens immersed in aqueous sodium chloride electrolytes at pH 7 and

shown to obey a linear relationship $E_b = A + B \log_{10} [Cl^-]$, where A and B are constants. It was proposed that the relationship of E_b with $[Cl^-]$ derives from the chloride ion influence on the solubility product (K_{sp}) of magnesium hydroxide, where K_{sp} is known to be a function of $\log_{10} [Cl^-]$. From the literature explanations of the E_b vs $\log_{10} [Cl^-]$ relationship observed for other metals, it would seem that the point defect model best represents Cl^- -induced Mg passivity breakdown, since the non-acidic nature of the Mg^{2+} cation is inconsistent with assumption of low pH within pits made by alternative theories. Presence of elemental Cl extending to the inner MgO-base film region was reported in several works [2,44].

The Fe in Mg matrix as well as Cl^- in the corrosive environment both accelerate corrosion rate leading to their incorporation into the corrosion products. Detection of these species remains a challenging task. For example, some authors detected Fe-rich particles in the outer hydroxide layer, another authors reported evenly distributed Fe, most likely in an oxidized state. The methods used in cited works are either sensitive not enough for the trace impurities level (case of scanning electron microscopy, electron dispersive spectroscopy, X-ray diffraction) or not convenient for routine studies of isolated impurities in corrosion products of micrometric thickness (photoelectron spectroscopy, transmission electron microscopy, etc.). Thus, another experimental approach, which is suitable for routine depth profiling of thick (several μm) corrosion products, could bring a new perspective and help to clarify the role of inclusions in the oxide/hydroxide films on corroding Mg in its corrosion mechanisms.

Chapter 3

Strategies for Mg inhibition

Classification of corrosion inhibitors

A corrosion inhibitor is a chemical compound, which being present in corrosive environment even at low concentrations can effectively slow down corrosion rates. Application of inhibitors is one of the most used methods of anticorrosion protection. They can be embedded in conversional coatings or added directly in the corrosive environment, like in case of engine coolant. In the past decades, numerous chemicals have already been identified as excellent corrosion inhibitors for aluminum, steel, copper and their alloys [30,87–89]. However, only a limited number of compounds have been reported until recently to be effective for Mg alloys, since Mg is chemically active with respect to the most engineering metallic materials. In further sections, principles of inhibitors classification will be presented, and examples of reported inhibiting systems will be listed, according to the existing classifications.

Depending on their effect on the anodic or cathodic partial reactions in the corrosion process, the inhibitors can be classified as **anodic, cathodic, or mix-type**. Anodic inhibitors particularly alter the anodic reactions in a chemical cell, forcing the metallic surface into the passivation region by modifying of the surface potential or forming a covering film on anodic areas. Cathodic inhibitors either slow the cathodic reaction by itself or selectively interact with cathodic areas to increase the surface impedance and limit the diffusion of reducible species to these areas. Mix-type inhibitors are film-forming compounds that reduce both the cathodic and the anodic reaction rates. Attribution of an inhibitor to one of these categories is usually based on

the observation of potentiodynamic polarization curves, see examples in Fig. 23. For Mg, almost all reported inhibitors are either anodic or mixed-type. Reports on cathodic inhibitors for Mg are rare.

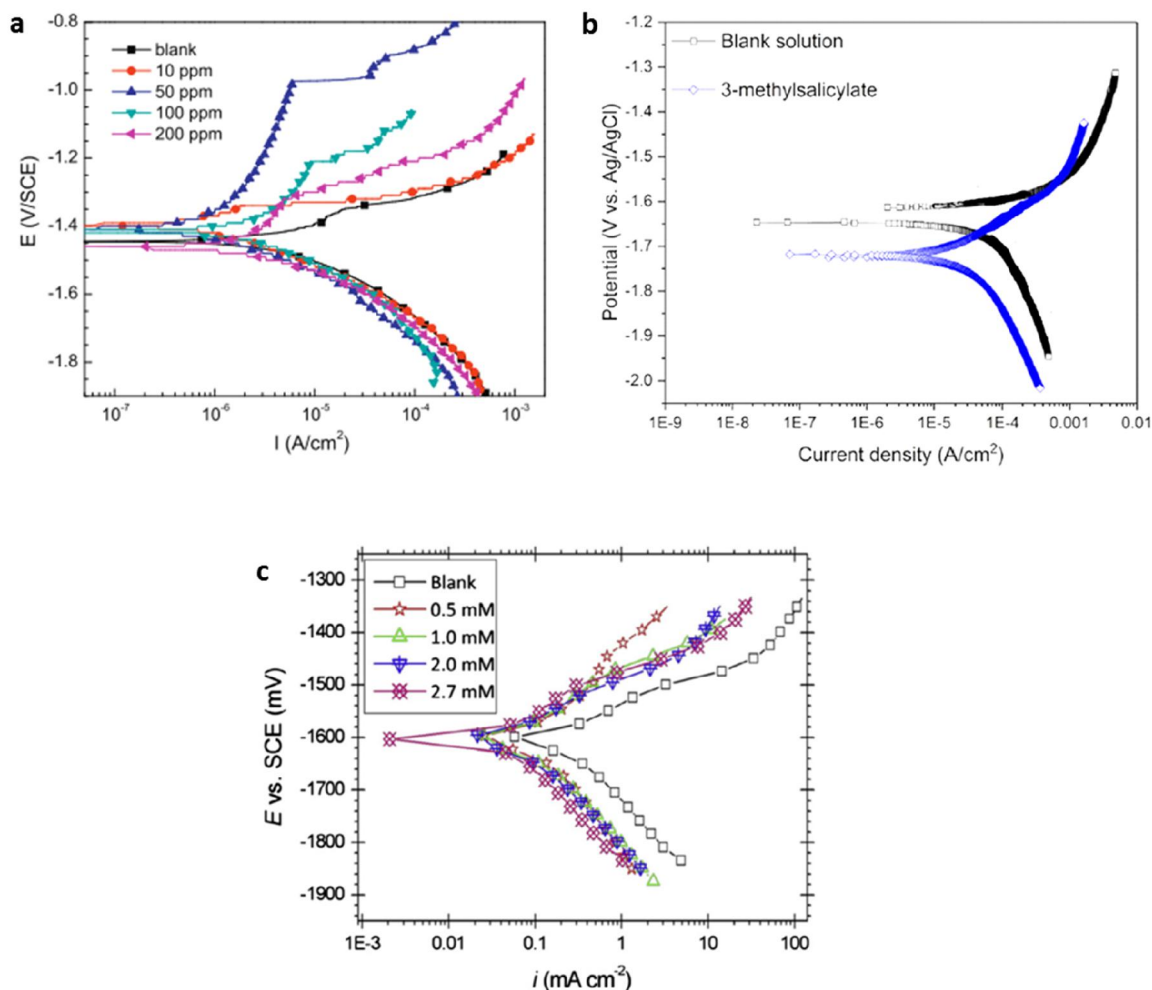


Fig. 23. Examples of polarization curves for (a) anodic [90], (b) cathodic [30] and (c) mix-type [91] inhibitors. (a) AZ91D magnesium alloy in 0.05 wt.% NaCl blank solution and the solutions containing various concentrations of paeonol; (b) CP-Mg immersed in 0.5 wt.% NaCl solution in absence and presence of 50 mM 3-methylsalicylate; (c) ZE41 alloy in 0.2 M Na_2SO_4 – 0.1 M NaCl solutions containing different concentrations of palmitate at 30 °C.

Recently, a new inhibition approach for Mg has been proposed by Lamaka et al. [81]. The main idea was based on the suppression of detrimental effect of noble inclusions (mostly, Fe) which are always present in magnesium based engineering materials and acting as local cathodes. Authors assumed that initial corrosion process leads to the detachment of iron particles from magnesium substrate, its further self-corrosion occurs with formation of $Fe^{2+/3+}$. These species can be reduced to metallic iron and re-precipitated on Mg substrate creating local cathodes that causes acceleration of corrosion process [80]. The prevention of the last step due to the complexing of

$\text{Fe}^{2+/3+}$ is the general principle of proposed inhibition approach, which has been further extended by testing of more than 150 chemical compounds [18]. According to the proposed mechanism, these inhibitors are expected to provide cathodic or mix-type behavior which was illustrated on the example of sodium 3-methylsalicylate (cathodic type, Fig. 23b) and sodium salts of fumaric and 2,5-pyridinedicarboxylic acids [30] (mix type). The detailed action of each of these inhibitors was not however studied.

In recent review on corrosion inhibitors for Mg [17], inhibiting systems were divided into three groups according to the mechanism of their action: **passivation, precipitation and adsorption** groups. Sometimes these categories can be mixed. For example, in theory, passivation-type and precipitation-type inhibition mechanisms have different film formation processes. The former film is converted from the substrate while the latter is deposited from the environment solution. However, on Mg, due to the spontaneous increase of the Mg surface alkalinity and the presence of the naturally formed surface oxides, it is difficult to tell whether a surface film results from a surface conversion or an environmental deposition. Therefore, these types of inhibitors are reviewed as a group of **phase film formation inhibitors**.

Phase film formation inhibitors for Mg

Fluoride [90,92], chromate and phosphate [93], molybdate and tungstate [17] are precipitation-type corrosion inhibitors for Mg alloys. F⁻ reacted with Mg and formed a protective fluoride-containing film on the Mg surface. Molybdate and tungstate salts mainly inhibited the cathodic reactions of Mg alloys through forming a protective layer on the cathodic active sites. It has also been demonstrated that organic sodium aminopropyltriethoxysilicate (APTS-Na) and inorganic zinc nitrate [92,94], sodium phosphate [95] also have a great inhibition effect on Mg alloys. As explained by Kartsonakis and Chen et al., the inhibition by most inorganic substances can be correlated with the formation of chemical conversion films that seal the intrinsic defects in magnesium hydroxide or oxide layers [92].

Adsorption-type inhibitors for Mg

This category includes mainly organic compounds. First of all, it should be noted that the term “adsorption” includes so-called “chemical adsorption” (formation of covalent bonds) and “physical adsorption” (electrostatic interaction). The generally accepted free energy threshold for

physisorption and chemisorption, respectively are 20 kJ mol^{-1} and 40 kJ mol^{-1} [96]. The fully occupied outmost orbital (2p) restricts Mg accepting electrons from donative molecules forming stable chemical bonds, thus chemical adsorption on Mg surface is not expected [97]. Thus, speaking about adsorption inhibitors for Mg, authors usually mean adsorption on $\text{Mg}(\text{OH})_2$ film and often the interpretation like “hydroxide film, doped by organic molecules” can be seen in articles [90,98,99], see **Error! Reference source not found.** This model is supported by SEM images demonstrating formation of a dense surface layer in the presence of inhibitors (Fig. 25) and the fact that organic molecules are detected by EDS analysis which should not be enough sensitive for molecular thickness layers.

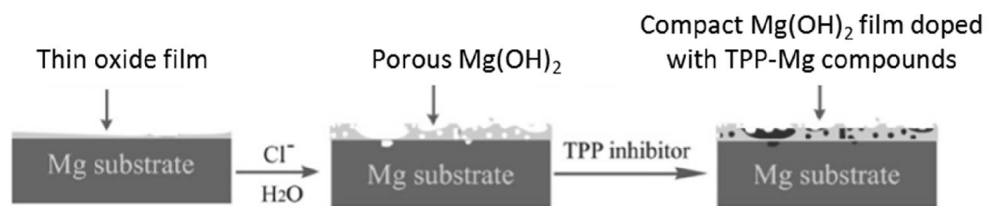


Fig. 24. Schematic illustration of the surface film formation on AZ91D Mg alloy in presence of TTP[99]

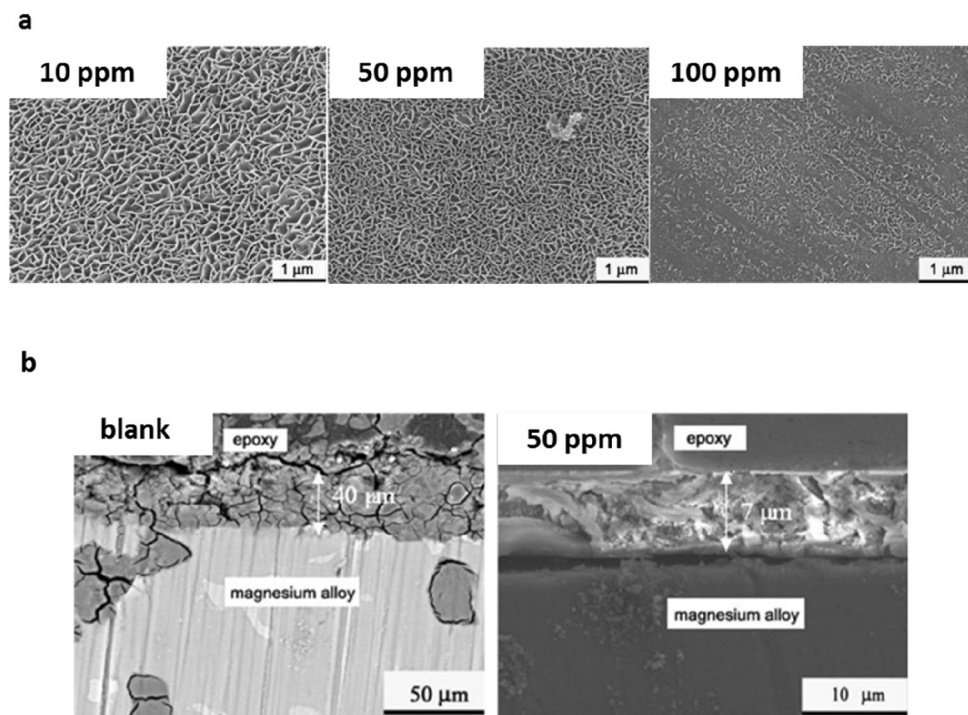


Fig. 25. (a) SEM images of AZ91 D magnesium alloy after 3 days of immersion in solution with various paeonol concentrations. (b) The cross-section morphologies of AZ91 D magnesium after 3 days of immersion in blank solution and the solution containing 50 wt.ppm paeonol [90].

Tested adsorption inhibitors for Mg alloys mainly include sodium dodecylbenzenesulfonate (SDBS) [98], sodium benzoate [98], derivatives of lactobionic-acid (LTA) [100], 6-ring organic compounds containing N-heteroatom [100], amino acids (phenylalanine, cysteine, tyrosine, etc.) [101], anionic surfactants (sodium salt of N-lauroylsarcosine, N-lauroyl-N-methyltaurine, sodium lauryl sulphate) [102], tetraphenylporphyrin [97], pyrazine and piperazine [103], long chain alkyl carboxylates (stearate, palmitate and myristate) [91], 2-Hydroxy-4-methoxy-acetophenone [90].

Normally, attribution of the inhibitor to an adsorption type is made on the basis of the following experimental results:

- 1) Clear dependence of the inhibition efficiency on the inhibitor concentration: increasing of the concentration leads to increasing of the inhibition efficiency until a “saturation concentration”, when all the adsorption sites are occupied by adsorbed molecules [97]. In some cases corrosion resistance may decrease after saturation concentration, probably due to dissolution of surface film by the excess of inhibitor [102].
- 2) The surface coverage (θ) of adsorbed inhibitors follows Langmuir (11), Temkin (12) or Frumkin (13) isotherms [99],

$$\theta = \frac{KC}{1 + KC} \quad (11)$$

$$\theta = K_1 \ln(K_2 C) \quad (12)$$

$$KC = \frac{\theta}{1 + \theta} e^{-2A_F \theta} \quad (13)$$

where C is the concentration of the inhibitor in the solution; K, K_1 and K_2 – constants and A_F - parameter associated with the interaction of adsorbed molecules. Usually Langmuir equation is used for fitting, see examples in [91,98,99,101].

- 3) In case of chemical adsorption - changes in geometry and distribution of electron density of adsorbed inhibitors. This could be detected by surface analysis techniques such as UV-absorption spectroscopy [30,97], XPS analysis [94,97], vibrational spectroscopy [97,104] etc.

Example of a chemisorption-type inhibiting mechanism evidenced by UV-absorption spectra can be found in [99]. Authors studied inhibition of AZ91D magnesium alloy in 0.05 wt.% NaCl solution by 5,10,15,20-Tetraphenylporphyrin (TPP). For the synthesized TPP powder, due to the presence of the conjugate large ring, porphyrin compounds have a very strong absorption band at 300–340 nm. This absorption Soret belt (also called B belt) is caused by the $\alpha_{1\mu}(\pi) \rightarrow e_g(\pi^*)$

transition of porphyrin. There are also other four weak absorption Q belt peaks at 517.4, 554.6, 594.2 and 648.7 nm, which are caused by the porphyrin $\alpha_{2u}(\pi) \rightarrow e_g(\pi^*)$ transitions. After exposure to TPP-containing solution, the Q belt of the surface film formed on the Mg alloy surface, disappears, which was attributed to the formation of Mg-porphyrin complex, as shown in Fig. 27. The four N atoms of the porphyrin ring chelate with the central metal Mg ions, which improves the molecular symmetry and the energy levels. Therefore, the Soret belt undergoes red shift (416.0 nm) and the Q belt becomes invisible, suggesting the formation of Mg-porphyrin complex. These observations indicate that the dissolved Mg^{2+} ions could directly bind with TPP molecules via an N atom and form a protective TPP-Mg film on the Mg alloy surface (**Error! Reference source not found.**).

Vibrational spectroscopy is a power tool for investigation of molecule interactions with the surface. Particularly, fourier transform infrared spectroscopy (FTIR) is known to be sensitive to small concentrations (order of 10^{-4} M), and is widely used for adsorption studies[105–107], it was applied to studies of corrosion inhibition mechanisms on Zn [108]. However, FTIR application for Mg corrosion inhibition is poorly presented in the literature, some reported interpretation of FTIR spectra was found to be wrong, the most informative spectrum regions were not discussed [90,104]

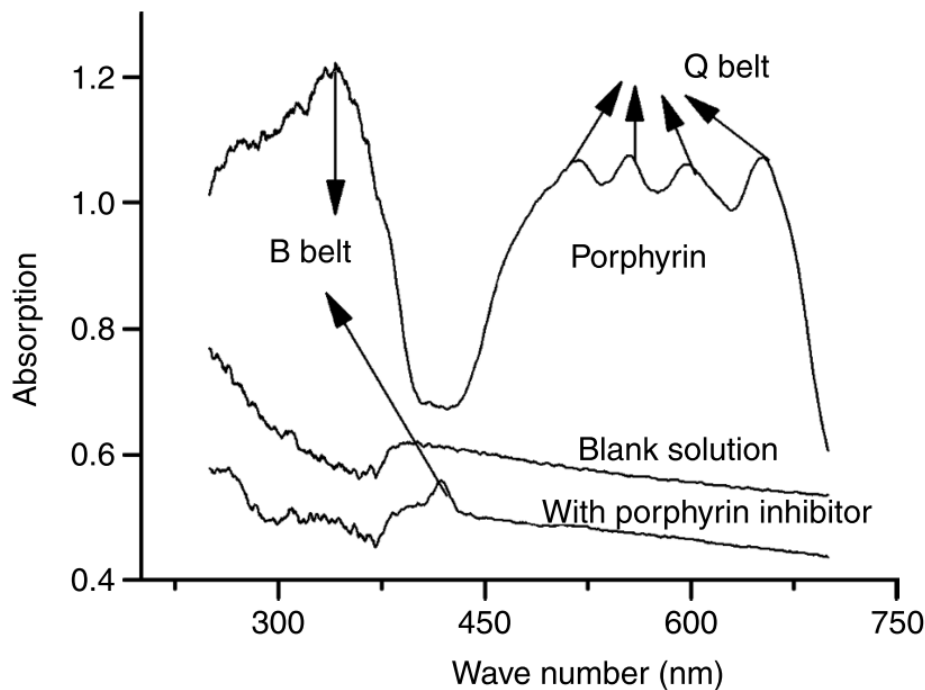


Fig. 26. Ultra-violet absorption spectra of the synthesized TPP powder and the Mg surface films after 7 days of immersion in the blank solution and blank + 5 ppm TPP solution at 60°C [99].

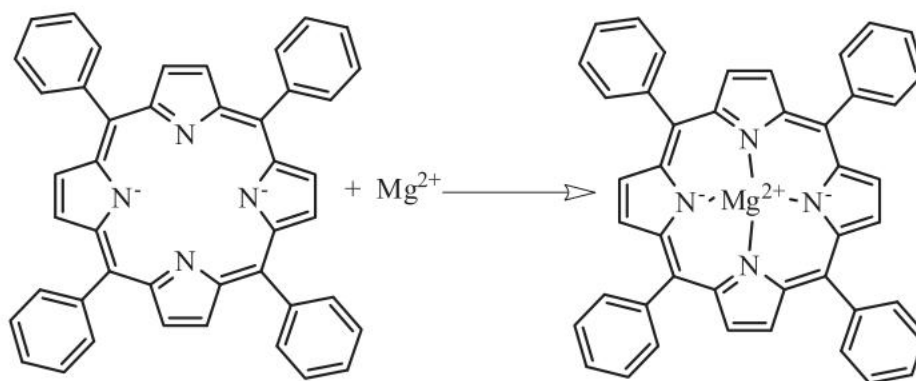


Fig. 27. Formation of porphyrin complex with Mg^{2+} [99].

Inhibitors action on Mg corrosion mechanisms are commonly categorized according to the observed in polarization curves reduce of the rates of anodic, cathodic or both reactions. The mechanisms of the interaction between the inhibitor and the reacting surface are poorly documented, the confusion exists between the passivation, precipitation, phase film formation, and adsorption mechanisms until detailed surface analysis is provided. All the reported in the literature results about the chemistry and morphology of the surface film in presence of the inhibitors are obtained by ex-situ characterization which could be misleading if the film can be transformed in dry condition, under vacuum or under high energy beam conditions used in the conventional ex-situ characterizations applied in the most works.

Experimental approach

This section describes the principles of two main techniques used in this work for analysis of corrosion surfaces, namely in situ Raman Spectroscopy and Glow Discharge Optical Emission Spectroscopy and justifies their implication.

(information summarized from [109–111])

Chapter 4

Methodologies

Raman spectroscopy

Principle of Raman spectroscopy

Raman spectroscopy being a non-contact, non-destructive, and relatively fast technique, offers the possibility to characterize a material in-situ and access how external perturbations (mechanical stress, thermal cycling, electrochemical cycling, corroding atmosphere, ...) may affect its behavior. It relies on inelastic (Raman) scattering of monochromatic coherent light, usually from a laser in the visible, near infrared, or near ultraviolet range. The laser light interacts with electronic and vibrational levels of atomic bonds: theory predicts both elastic (so called Rayleigh scattering) and inelastic (Stokes and Anti-Stokes) contributions in the scattered electric field (Fig. 28). The latter occurs only if vibrations change bond polarizability. The energy shift provides information about the vibrational modes in the system. Raman scattering is complementary to infrared absorption with the advantage of much narrower peaks.

Raman scattering and Fluorescence emission are two competing phenomena (Fig. 28). When the energy of the excitation photon is close enough to transition energy between two electronic states, one then deals with resonance fluorescence. If it occurs, the high background appears on Raman spectra, that hiding informative Raman features. The simplest way to avoid fluorescence background is to use the excitation light with lower energy (in contrast to Raman

scattering, fluorescence phenomena depends on the excitation wavelength). Often, for organic compounds or biological objects it is not enough to change the laser wavelength, more sophisticated approaches, described in a recent review [112], can be used.

Information from Raman spectra

The basic information which can be obtained from Raman spectra is summarized in (Fig. 29).

Identification of chemical compounds

Positions of Raman peaks strongly depend on the atoms mass, bond lengths and the angles between atom-sharing bonds. Thus, they are used as fingerprints for identification of particular substances.

Qualitative estimation of the grain size

It is noted elsewhere [24] that Raman spectra of crystals can be influenced by their size and shape: absolute scattering intensity, relative intensities and band shapes can be affected. However, these effects take place only for nano-size material, 5 – 50 nm [113].

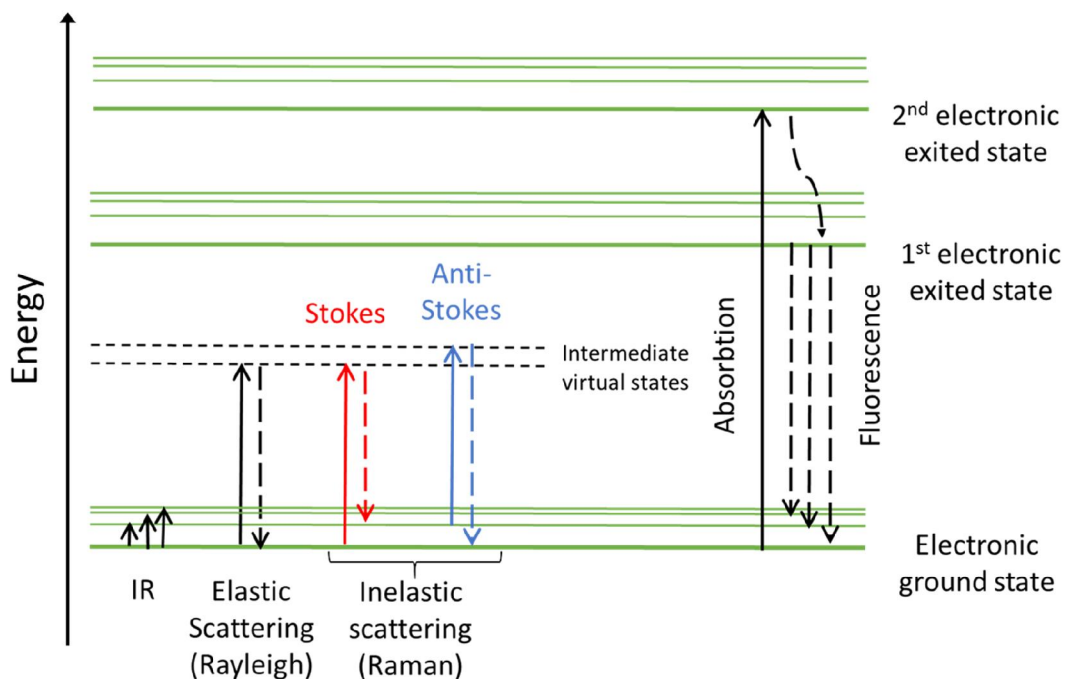


Fig. 28. Jablonski Diagram of Quantum Energy transitions for Rayleigh, Raman Scattering and Fluorescence.

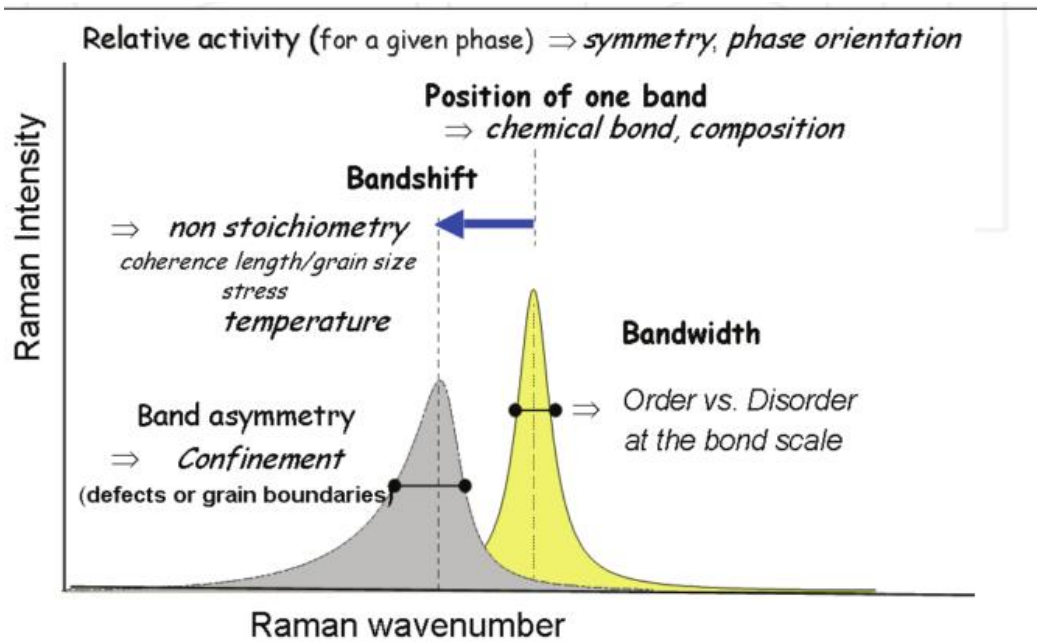


Fig. 29. The basics of the information to be extracted from a Raman spectrum [110]

When the particle size is below than ~ 30 nm (D , see Fig. 30), contribution of atoms at the particle surface or atoms having their chemical bonding perturbed by the vicinity of the surface in spectrum becomes more important than the contribution of the bulk atoms. Vacancy concentration is maximal close to the surface and where adsorbed species can be present: hydroxylation, water, etc.

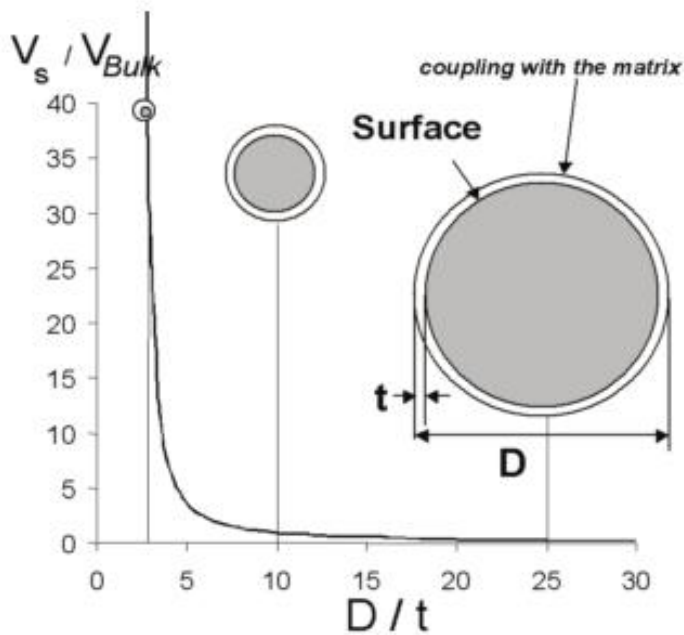


Fig. 30. Schematic of the relative contribution of skin/bulk matter for a particle as a function of its size: for a nanosized grain less than 1-10 nm in diameter the contribution of the surface atoms is very

Examples of the contribution of surface-active groups can be found in the theoretical work of Zeitler et al. [28]. Authors provided molecular simulations to describe Mg–O–H vibrations, they have found that the surface O–H bond stretch frequency is higher than the bulk (internal) frequency, which may be attributed to hydrogen bonding between layers in the bulk resulting in weaker hydroxyl bonds.

The direct estimation of the grain size from Raman spectra is impossible without modeling. Two models described in [24] are widely used for this purpose: the Phonon Confinement Model (PCM) and Elastic Sphere Model (ESM).

Quantitative analysis

It was mentioned in [110], that the scattering intensity varies by orders of magnitude depending on the bond polarizability (the more covalent the bonds, the higher the number of electrons involved and the higher the Raman peak intensity), the crystal symmetry and the exciting wavelength. As polarizability (α second rank tensor) changes drastically from one bond to another, Raman intensity may not be used to measure the relative amounts of different phases without preliminary calibration. Consequently, minor phases or even traces could have a stronger Raman signature than some major phases.

For liquid or gaseous phases, it is common to provide calibration and present the spectral parameter (intensity, area or bandwidth) as a function of concentration, as it is shown in Fig. 31. In case of an ideal solid sample and a perfectly focused laser beam, the intensity of Raman scattered light from a sample is proportional to the number of molecules in the sample volume being probed by the Raman instrument [23]. However, the real sample with uneven surface and physical defects could provide light penetration, reflection, scattering and/or diffusion. Consequently, the volume from which Raman signals are generated is different from the focal volume. In order to provide quantitative (or semi-quantitative) analysis the normalization of spectra and a deep data analysis must be performed. Depending on particular applications, different ways of spectra normalization which are described elsewhere [23,109], can be used. In case of solid samples, it is common to analyze material in terms of layer thickness [114,115] or provide semi quantitative analysis using the ratio between different components [113,116].

Despite the complexity of the quantitative data treatment in Raman spectroscopy [23], it has been possible to extract the kinetics of the chemical evolution from Raman spectra [117] in case of phase transformations of polymers [118] or inorganic compounds [119–121], as well as to use Raman spectroscopy in biological applications [122,123].

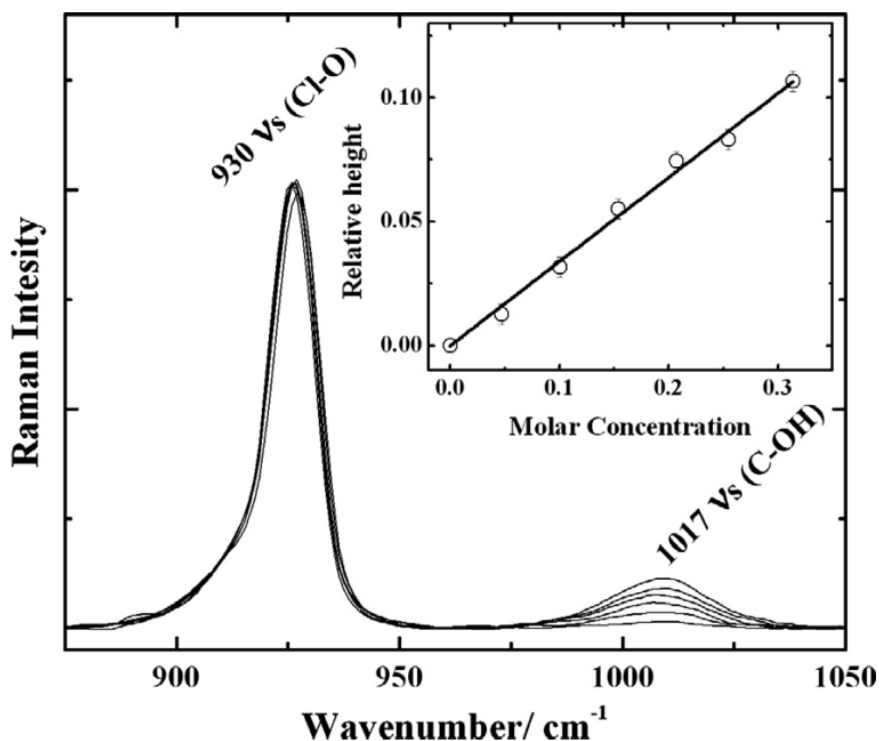


Fig. 31. Raman spectra of different aqueous solutions of NaClO₄ (0.3 M) and NaHCO₃ (0.1–0.6 M), respectively. The inset shows the calibration curve obtained from the spectra shown at different molar concentrations of the bicarbonate ion [120].

Confocal Raman Mapping

By coupling an optical microscope with a conventional Raman spectrometer, the technique becomes a microprobe with a spatial resolution of less than 1 μm , determined by the wavelength of the radiation and the numerical aperture of the microscope objective. The principle of the Raman mapping is that numerous spectra can be recorded on a representative sample area. Using selected parameter(s) extracted from each spectrum (peak intensity, wavenumber shift but also grain size, defect concentration, etc.), it is possible to build a map of the investigated area. Raman mapping provides a way to represent a sample in two or even three dimensions with information-rich content: chemical nature, molecular orientation, crystallinity ratios and polymorph content, strain and stress, all being accessible from the Raman spectra available for each pixel of the Raman map.

Technical details

This sub-section is dedicated to the technical details for the experiment design of Raman mapping. First of all, the objective of the experiment must be clear: the size of analyzed features should be known, the analyzed area must be chosen in order to be representative of the different topological features but limiting the number of spectra to be collected and processed to build Raman map. As soon as these parameters are known, the excitation wavelength, microscope

objective, mapping step and acquisition time should be chosen according to the required sampling volume and map resolution.

Sampling volume

The microscope objective should be chosen for the resulting probing to match the sample details of interest. From a practical point of view, microscope objectives are usually characterized by the numerical aperture NA

$$NA = n \sin \theta \quad (14)$$

In Eq. (14), θ is the maximum collection angle for the backscattered light and n is the refractive index in the medium between the sample and the microscope lens. The numerical aperture is a key parameter because it sets the resolution of the microscope, defined as the shortest spacing for two points on a sample surface to be resolved with λ wavelength observation.

The sampling volume of a single measurement is often approximated by the laser focal cylinder dimensions. The laser beam waist diameter (d) and the depth of focus ($\Delta\zeta$) can be estimated by equations numbered (3) and (16) in [109] which are repeated below:

$$d \sim \frac{2n\lambda}{\pi NA} \quad (15)$$

$$\Delta\zeta \sim \frac{2n^2\lambda}{\pi NA^2} \quad (16)$$

However, it is important to realize that actual volume from which the Raman signal is collected can be different due to the imperfection of optical components, the sample and medium properties (finite penetration of the light in the sample or parasite refractions, Fig. 32). The presence of several phase boundaries between sample and lenses causes the light refraction and, as a consequence, the change of focus position and lateral and axis resolution. Therefore, the experimental evaluation of actual values is usually provided. The lateral diameter is measured by scanning the laser spot over a material with a very sharp edge or feature, and measuring the response. The depth of focus can be measured by focusing the laser beam just above a silicon wafer, and measuring the 520.5 cm^{-1} band intensity as the wafer is raised vertically through the beam focus. The full width at half-maximum (FWHM) of the silicon signal gives the waist length of the focal volume (Fig. 33). Its shape and volume will, however, be distorted if the beam is focused into a material with a different refractive index [124].

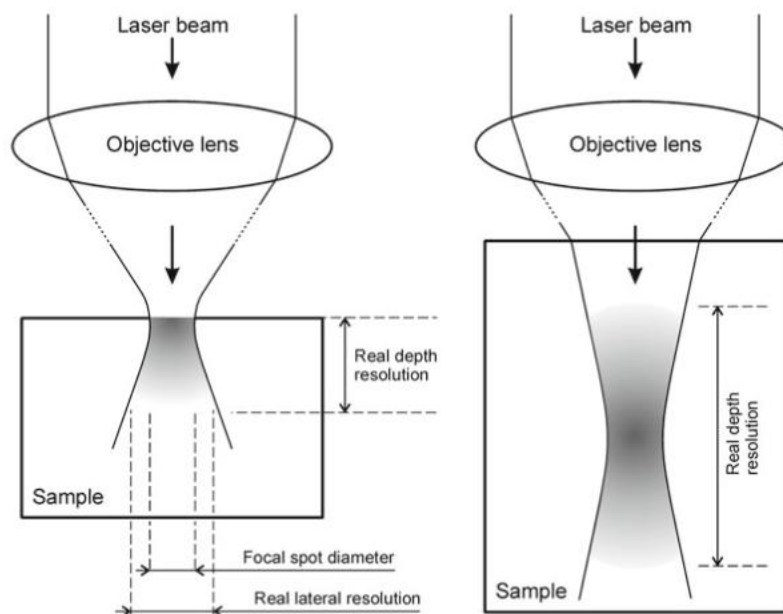


Fig. 32. Simplified sketches (not to scale) of the beam path of a confocal Raman spectrometer. The analyzed volume areas are shown gray. Left, beam focused at the sample surface; right, beam focused inside the sample. Note that in the latter case the focus quality is decreased appreciably, resulting in an enlarged focal-spot diameter and dramatically decreased depth resolution [109].

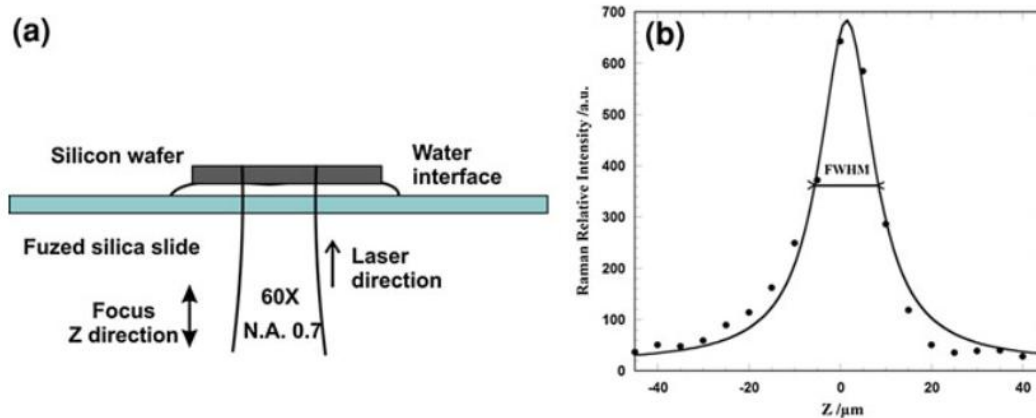


Fig. 33. (a) Setup to measure the longitudinal dimension of the beam waist in a liquid sample. (b) variation of the Raman signal of silicon (520cm^{-1}) in function of the Z position of the objective. The FWHM is ~ 14.5 microns [109].

Data treatment

Preprocessing

The first step of data treatment is preprocessing. One goal is to separate and eliminate undesirable spectral features such as spikes from cosmic ray, broad backgrounds from fluorescence or stray light, and the baseline from dark signal.

Darksignal is the photon counts that come from the detector itself, and is a function of the exposure time and temperature. It is a detector (type and unit) specific constant (plus random noise). Subtracting a constant (e.g. the minimum intensity) from the spectrum can remove the dark signal. This is often called “offset correction.”

Cosmic rays are generated from high energy particles from the outer space. A cosmic ray can be identified by appearing at random. Live correction compares two repeated spectra point-to-point, and removes the points with a sudden and significant intensity increase. Alternatively, a cosmic ray can be identified by a delta-function like increase/decrease of intensity instead of the gradual increase/decrease of a Raman band (Lorentzian/Gaussian curve).

Fluorescence bands are much stronger and nearly always much broader than Raman bands. It is better to select the excitation wavelength that avoids or minimizes the fluorescence. When it is not entirely applicable, and the level of fluorescence is tolerable, it can be corrected by fitting and subtracting the baseline (e.g. polynomial functions). Baseline fitting is however an example where an artifact can be introduced during data processing. A Raman mapping is a collection of numerous, and often heterogeneous spectra. Baseline may vary in each and every spectrum. The quality of fitting can vary a lot. Over- or under-correction, therefore, can introduce an artificial feature.

Smoothing must be performed only when necessary, because it always changes the spectral features, significantly or insignificantly. It is better to reduce signal to noise ratio (S/N) by increasing the acquisition time for more Raman signals, whenever possible.

There are many ways to normalize spectra. The most widely used ones are:

- 1) Normalize with respect to the sum of intensity: $I_i^{norm} = I_i / \sum I_i$
- 2) Normalize with respect to the total spectrum area: $I_i^{norm} = I_i / \sum I_i \Delta S_i$
- 3) Normalize with respect to the maximum intensity:

$$I_i^{norm} = (I_i - I_{min}) / (I_{max} - I_{min})$$

- 4) Normalize with respect to the variance of the spectrum intensity (standard normal variate, SNV): $I_i^{norm} = (I_i - \mu) / \sigma$, where $\mu = \sum I_i / n$ and $\sigma = \sqrt{\sum (I_i - \mu)^2 / n}$

In these equations I_i is the i^{th} intensity at the spectral point of the spectrum, ΔS_i is the spectral pixel width at the i^{th} spectral point of the spectrum (spectral axis of a Raman spectrum is unevenly spaced)

Normalization for a qualitative analysis (e.g. classification, identification) scales spectral intensity to be expressed in a similar scale. Unit area normalization (#2) or height normalization (#4) are often sufficient. Normalization for a quantitative analysis aims to separate and remove

intensity variation from the other factors than the variation of the chemical composition. For liquid phases, absolute Raman intensity depends on the path length of the laser beam in the solution, thus it must be normalized with respect to the path length. For the solid samples, situation is more complicated because of penetration, reflection, scattering, and/or diffusion on uneven surface with physical defects. The spectral intensity is affected by the analyzed volume as well as the chemical composition, and it is not trivial to estimate the analyzed volume with high accuracy. Thus, the normalization should be performed carefully and be individual in every particular case.

Spectral analysis and map building

Univariate analysis uses one variable at a time, including peak position (absolute or shift), peak height (absolute, relative or normalized), band width (absolute or broadening) or area (absolute, relative or normalized).

Multivariate analysis treats a spectrum as a vector, and a Raman map as a matrix.

One type of multivariate analyses is performed by comparing each element of a spectrum with the corresponding element of another spectrum. Another type of multivariate analyses is based on the covariance. Principal component analysis (PCA) is the best known example.

Application of Raman spectroscopy in corrosion science

Corrosion of metal results in the reaction of the metal with some species present in the environment and the formation of new bonds at the metal surface. Since Raman spectroscopy is sensitive to these changes, it has found the widespread application in corrosion studies.

Firstly, it can be used for the identification of corrosion products and their spatial distribution on the surface [110,125–133]. As an example of the application of Raman spectroscopy for Mg corrosion, one can see the Raman study of the chemical composition of different surface treatment systems (Zn based conversion coatings) on AM60 Mg alloy [134], calcium phosphate/chitosan composite coatings on micro-arc oxidized AZ91D Mg alloy [135], and cerium conversion coatings on Mg [136].

Secondly, in situ approach allows to follow chemical reactions on metal/liquid interface. In situ Raman spectroscopy was used to study the dissolution of phosphate layers on zinc coated steel [121], delamination of organic coatings [137–139], inhibition [140–143].

An example from Mg corrosion application is the work of Samaniego et al. [144] who used in situ Raman spectroscopy to study the mechanism of Mg corrosion. The authors aimed to reproduce experiments of Petty et al. [34], who noticed formation of reducing species in the solution being in contact with corroding Mg. The work of Petty et al. was often cited as an evidence of existence of Mg^+ in the solution. Samaniego et al. with help of in situ Raman analysis demonstrated that SO_4^{2-} contained in the solution was reduced to SO_2 on the surface of Mg at open

circuit potential and under anodic and cathodic polarization. The existence of these species was not considered by Petty, who attributed the reduction properties of solution after contact with Mg to Mg^+ existence.

Raman spectroscopy is a powerful tool for in-situ analysis of the liquid/solid interface evolution. It is often used in corrosion studies as an instrument for identification of corrosion products and analysis of their spatial distribution. It is also possible to use it for semi-quantitative characterization and kinetics measurements. The perspective direction in methodology development is combining Raman mapping with kinetics measurements in order to survey system evolution locally, with micrometric resolution and in more quantitative manner.

Glow Discharge Optical Emission Spectroscopy (GD OES)

Principle of GD OES

(Information summarized from [111], <http://www.horiba.com>)

Glow Discharge Optical Emission Spectroscopy (GD OES) provides rapid, direct bulk analysis and depth profiling analysis of solids: metals, glasses and ceramics. The radio frequency (RF) pulsed source allows measuring all types of solid samples conductive or non, even fragile or heat sensitive with optimum performances. Thin and thick films with thickness ranging from one nanometer to over 100 microns can be analyzed with this technique. Sputtering rates change from 0.1 nm/s up to 100 nm/s, depending on the sample material and the excitation conditions used [111], it ensures fast analysis. GD-OES is highly sensitive for many chemical elements relevant to corrosion studies including the light elements as C, H, N, O etc.

Principle of GD sputtering is shown in Fig. 34. In a glow discharge, the cathode (analyzed sample) is bombarded by positive ions formed from the noble gas (Ar in our case). This bombardment induces surface erosion called cathodic sputtering: material is removed layer by layer from the sample surface. The sputtered atoms migrate into the plasma where they are excited through collisions with electrons or metastable carrier gas atoms. The characteristic spectrum emitted by these excited atoms is measured by a specific detection technique, usually optical emission or mass spectrometer, with which the GD chamber is coupled. In the present work an Optical Atomic Emission Spectrometer was coupled with GD for the chemical analysis of the formed plasma giving the technique name GD OES. The intensities are recorded as function of time.

Based on a calibration method, establish beforehand, these qualitative results can be transformed in a quantitative depth profiles.

Thanks to recently developed Differential Interferometry Profiling device (DiP), a direct measurement of the depth as a function of time, with a nanometric precision, can be performed simultaneously with the GD analysis (Fig. 34). In DiP the laser beam is separated into two spots. The reference spot is directed to the intact surface of the sample, while the depth sensing one is directed to the center of the GD sputtered area. The interference between the two reflected beams is measured as the sample is sputtered, giving a direct measurement of the crater depth.

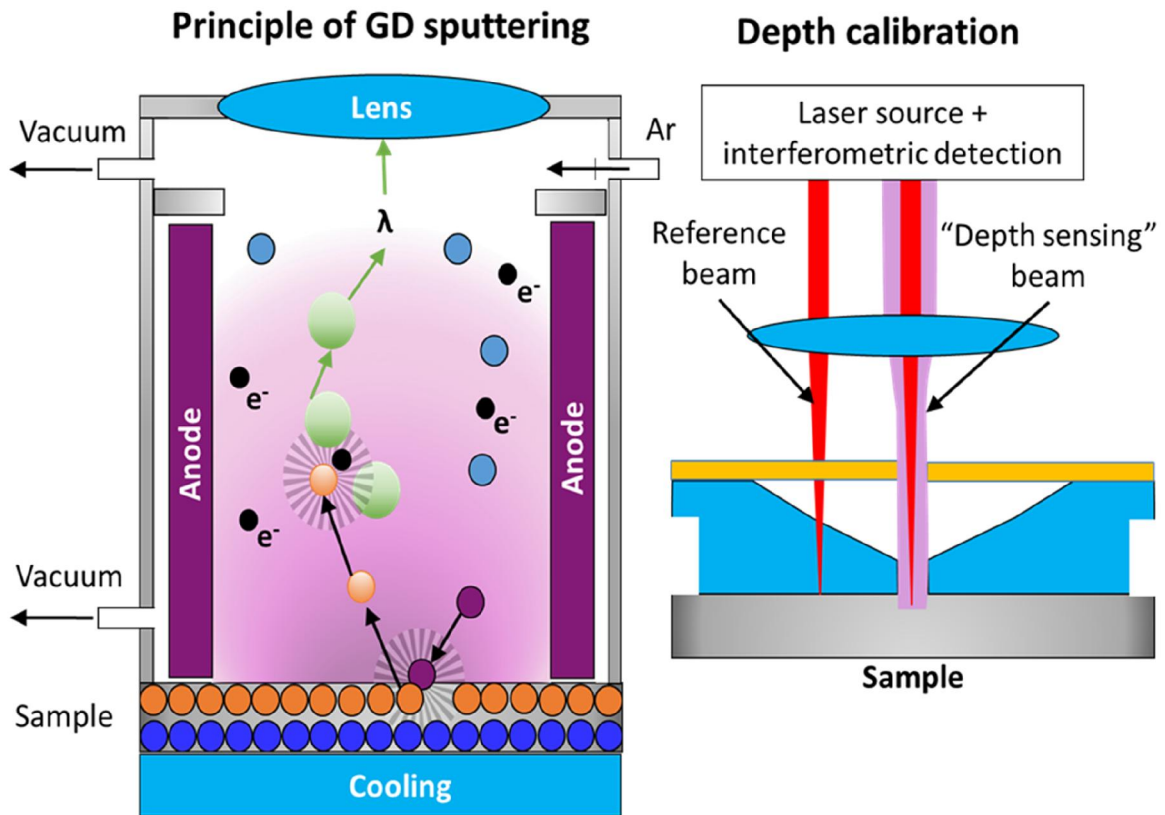


Fig. 34. Principle of GD OES profiling with DIP (Fig. from Horiba Scientific).

Compared to other surface analytical techniques used for elemental depth profiling, GD-OES has advantages related to vary large depth resolution, short analysis time, simplicity of sample preparation and no need of high vacuum (see Table 1).

Table 1. Comparison between RF GD-OES and other surface analytical methods used for chemical depth profiling (Secondary Ion Mass Spectrometry (SIMS), X-ray Photoelectron Spectrometry (XPS), Auger Electron Spectroscopy (AES))

	GD-OES	SIMS	XPS/AES
Detection limit*	20 ppm (10^{18} atoms/cm ³)	Up to 1 ppm ($5 \cdot 10^{16}$ atoms/cm ³)	1000 ppm ($5 \cdot 10^{19}$ atoms/cm ³)
Area analyzed	φ 2 mm φ 4 mm φ 7 mm	Tens of μm ² or larger	φ 10 μm or larger (XPS) φ Tens of nm or larger (AES)
Depth resolution	Approx. 1 nm	A few nm or greater	A few nm or greater
Depth profile analysis time**	Up to 1 min.	20 to 30 min.	3 hours or longer

*The detection limit varies with elements.

** time approximated for a thin-film measurement with a thickness of a few hundred nanometers

GD OES analysis of corroded metals is not a trivial task. Normally, this kind of samples are assumed as multilayered structures (corrosion products films, conversion coatings and metal bulk), where each layer has different properties (conductivity, porosity etc) and provides its own sputtering rate and matrix effects. Some chemical elements present in corrosion products (C, O, H) can significantly modify the processes in plasma, which can result in modifications of emission yields and detection limits of other elements, complicating the data analysis in particular for minors.

Influence of H in discharge gas on GD OES results

Bengtson and Hånström [145] have observed that small amounts of hydrogen (<0.1% partial pressure) added to an argon glow discharge can significantly alter the analyte emission yields. The effects appeared to be unique for each spectral line, i.e., enhancement has been observed for certain lines but quenching was found for other lines of the same element. Moreover, the effects seemed to be similar when hydrogen was introduced in gaseous form and when it was sputtered from the sample. Effects of water which have similar effects to those one for hydrogen was reported as well [146–149]. A theoretical review regarding the possible mechanisms taking place in an argon glow discharge containing hydrogen has been published by Bogaerts and Gijbels

[150]. The results showed that matrix correction algorithms for hydrogen are needed for accurate quantification in the analysis of surface layers containing hydrogen.

Hodoroaba et al. have measured the changes in intensity of a number of emission lines as a function of the amount of hydrogen in the plasma [26,151,152]. Payling et al. [153] suggested the approach to provide H-correction in order to obtain the correct quantitative depth profiles of sample, containing significant amount of hydrogen. Authors used the term “inverse relative emission yield” R_i , the coefficient which allows to correlate measured ($I_{meas.}$) and corrected intensity of particular analytical line (17)

$$R_i = I_{corr.}/I_{meas.} \quad (17)$$

To calculate this coefficient, authors used results of Hodoraba (dependencies of emission yields of analytical lines on hydrogen intensities), normalized them so that the general form of the effect on the inverse relative emission yield could be explored. For emission lines that increase with hydrogen content, they divided the intensities by the value at zero hydrogen and then normalized the intensities to have the same average slope. For emission lines that decrease with hydrogen content, they divided the intensities by the value at zero hydrogen but then plotted the inverse intensities, normalized to have the same average slope. The general trend of these results is that the effect of hydrogen on the inverse relative emission yield can be described by either of the following equations:

$$R_i \approx 1/(1 + h_i I_H) \quad (18)$$

$$R_i \approx 1 + h_i I_H \quad (19)$$

where I_H is the hydrogen intensity, and Eq.(18) and (19) refer to emission lines whose intensities increase or decrease with hydrogen, respectively.

The interpretation of elemental GD-OES depth profiles obtained on corroded surface is not trivial due to possible matrix effects (namely, H-effect) of the oxide/hydroxide films. Thus, further development of this analytical approach is required.

Results section

Chapter 5

The effect of pH on the $\text{Mg}(\text{OH})_2$ film evolution on corroding Mg by in situ Kinetic Raman Mapping (KRM)

This chapter develops in-situ kinetics Raman mapping (KRM) methodology and demonstrates its applicability to describe the effect of solution composition (pH, presence of Cl^-) on the local evolution of surface films at initial stages of Mg corrosion in thin layer cell.

(The results of this chapter are presented in the form of the article in preparation for JACS)

Abstract

The effect of pH on the local surface film evolution at initial stages of Mg corrosion in a thin layer cell was studied by in-situ Raman spectroscopy adapted for kinetic Raman mapping (KRM). The local film growth and breakdown kinetics were mapped with different lateral resolution for surfaces up to several mm² using the water signal as an internal standard to normalize the area of A_{1g} (Mg-OH) brucite peak (Raman shift 3652 cm⁻¹). On the areas, which did not evolve in optical images during immersion, brucite growth kinetics was parabolic (diffusion limited) at pH 13 but linear (surface reaction limited) at pH 7-10.5. A threshold-like kinetics of the brucite growth was observed locally, in proximity of dark corroded zones. This type of kinetics curve correlated with a following development of black filaments in the corresponding locations. High local alkalinity favored the appearance of 3675 cm⁻¹ and/or 3710 cm⁻¹ “satellites” peaks in Raman spectra. They were attributed to surface vibrations from (0001) and (10-10) brucite surfaces respectively and tentatively used to extract an information about the in-situ evolution of the crystal size and morphology. The attributed sizes and morphologies ranked for different surface conditions and locations were in a good agreement with the ex-situ scanning electron microscopy images. Film growth and breakdown description in terms of dissolution-precipitation from supersaturated solutions was coherent with the observed kinetics and morphologies. The relation between the film growth kinetics and Mg reactivity was discussed. From methodological point of view, the developed in-situ KRM could be easily extended to multiple processes for which in-situ measurement with local resolution can be of interest.

Introduction

Magnesium based alloys are attractive to multiple applications including automotive, aerospace, biomedical industries [1], however in contact with water or in humid atmosphere they are subject to corrosion [15]. Aqueous corrosion of active materials like magnesium and its alloys is strongly affected by chemistry and morphology of the oxide / hydroxide layer at the interface metal /solution. Multiple ex situ characterizations were published for corroded magnesium alloys [2–5,42]. From the ex-situ analyses, the surface of Mg after immersion in aqueous solutions is covered by a thin oxide (MgO) and an external Mg(OH)₂ (brucite) and

have a complex porosity [2–5,42]. The oxide/hydroxide layer is often considered as a reason of a barrier protection at the early stages of aqueous corrosion [6,7] in particular in strong alkaline solutions [43]. Localized film damage appears in neutral solutions containing chloride, sulphate, or nitrate anions [7,8] and the black color of the corroded area was previously attributed to the cracking and the detachment of small Mg particles [38,58]. The mixture of MgO/Mg(OH)₂ in the dark corroded areas was reported as well [3,14]. Magnesium hydroxycarbonates [47,154,155] and MgCl₂·6H₂O, Mg₃(OH)₅Cl·4H₂O and 5(Mg(OH)₂)·MgCl₂ were also identified after corrosion in NaCl containing aqueous solutions [8] and Cl was detected even in the inner oxide [2,44] which was ascribed as a film breakdown. Starting from the work of Vermilya [41], brucite film formation on corroding Mg is assumed by dissolution-precipitation mechanism. In multiple works the loss of barrier properties of the corrosion products films on Mg or their harmful autocatalytic effect on the hydrogen evolution reaction are attributed to dissolution-precipitation control of the film formation and breakdown [10,156,157]. The dissolution-precipitation hypothesis, even if looks very reasonable, stays speculative until the film evolution by dissolution-precipitation mechanism is proven by in-situ analysis. Moreover, one can expect that the experimental kinetics of corrosion products formation cannot be described only by precipitation from the solution bulk, the film formation rate being directly related to the corrosion rate and the local conditions at the metal surface [76]

The in-situ kinetics measurement of the surface films evolution on corroding materials and the effect of solution composition on the film growth and breakdown could be very helpful to support proposed reactivity mechanisms. Moreover, the hypotheses about the aqueous reactivity mechanisms, advanced only on the basis of the chemical and morphological characterization of the dry surface films under high vacuum can lead to incorrect interpretations because of significant chemical and morphological modifications and hence significant difference between the analyzed surface and the surface reacting in aqueous environments.

To approach the mass balance and the mechanisms of Mg corrosion, real time reactivity measurements by local electrochemistry [54,59,64,158], by coupling electrochemical techniques and chemical solution analysis [159–161] or by coupling electrochemical techniques and different types of Time Lapse Microscopy [11,61,157] or volumetric measurements [61,159,162] were reported. The effects of the alloy composition [53,163] and solution composition [85,86,159,160,164,165] on the reactivity of many Mg alloys were communicated and discussed in terms of possible modification of the surface chemistry. In contrast, the only published in-situ study of the film growth kinetics on Mg

corroding in aqueous solution reported a linear increase of the average film thickness with time measured by ellipsometry [7] without no mechanistic insight; and we did not found any in-situ chemical analysis of the corroding Mg surfaces which could prove or disprove the film formation and breakdown mechanisms.

The study of the surface films on corroding Mg is complicated by the fact that Mg reactivity is usually very inhomogeneous and the initiation of the localized processes is unpredictable. Even if some correlations were reported [82,166], the breakdown stays a stochastic process and for correct statistically valid observation the in-situ surface analysis should be able to collect information locally, with good spatial resolution and on sufficiently large surfaces.

Adapting Confocal Raman Mapping [109,121] to local kinetic measurement on large surfaces seems to be an interesting approach. In-situ Raman spectroscopy in application to corroded surfaces is developed since 1980th [110,125–133]. It is widely used to identify corrosion products formed locally during corrosion or products formed in electrochemical reactions and to survey the system evolution in semi-quantitative way [109,167]. However, most of these works were focused on the identification of corrosion products in selected locations and the quantitative film evolution is even not considered. At the same time, despite the complexity of the quantitative data treatment in Raman spectroscopy [23], it has been possible to extract the kinetics of the chemical evolution from Raman spectra [117] in case of phase transformations of polymers [118] or inorganic compounds [119,120,139], as well as to use Raman spectroscopy in biology [122,123]. These works inspired us to combine the advantage of CRM and the approaches proposed in different analytical works to achieve an in-situ kinetic study of the surface evolution in aqueous environment, namely extracting kinetics of local chemical and morphological evolution, of film growth and film breakdown.

Since Mg corrosion rate is quite fast and non-uniform and the location of future local anode or cathode cannot be easily predicted by optical microscopy, the measurement of film growth and breakdown kinetics in one point is not representative. Monitoring of the film growth requires continuous mapping with good (μm) lateral resolution, sensitive to chemical composition, and fast enough to provide in situ measurements on large surfaces which is possible with CRM. The intensity of Raman scattered light from a sample is proportional to the number of Raman active bonds in the analyzed volume [23] that allows us to provide the semi-quantitative analysis and monitor growth kinetics using the spectra normalization. Although the Raman spectra of crystals can be influenced by their size and shape (absolute scattering intensity, relative intensities and band shapes can be affected [24]), these effects usually take place only for nano-size material, 5 – 50 nm [113] and also could be turned in an

advantage in order to access morphology and crystal size. Depending on the immersion conditions, the average brucite thickness can vary from about 100 nanometers to 2-3 microns [73]. The fact that the layer thickness is smaller than the analyzed volume in Raman experiments (see the experimental details) is applied in the present work to use the signal of water, contained in the major part of the analyzed volume, to normalize in-situ spectra and to monitor the local growth kinetics.

Experimental details

Materials

Magnesium foil 99.9 % (see Table 2 for impurity content) of 0.5 mm thickness was supplied by Goodfellow. 3 cm square Mg coupons were polished with 800, 1200, 2400, 4000 SiC grinding paper, using ethanol as a lubricant, rinsed with ethanol and dried by compressed air. All electrolytes were prepared using analytical grade reagents (Sigma Aldrich) and distilled water. pH of NaCl solutions was adjusted to the required value of 9 by 0.1 M NaOH solution and to the required pH 13 by the addition of solid NaOH.

Table 2. Impurities level in studied materials.

	Element (ppm)							
	Mg	Fe	Mn	Al	Cu	Ni	Si	Zn
Mg1	Bal.	280	170	70	20	<10	50	<20
Mg2	Bal.	36	38	42	10	5	86	-

In situ Raman spectroscopy

Long distance objective Leica ($\times 50$ and $NA = 0.5$, working distance 8 mm) and green laser (532 nm, 50 mW) were used for in situ measurements. A freshly prepared Mg sample was directly mounted in a 3D printed polylactic flow cell with a glass optical window (Fig. 35). The thickness of the liquid layer on the sample was about 1 mm. Solution was

systematically renewed using a syringe pump before each map in order to remove the bubbles which affect the laser focusing. In the selected experimental conditions, the analyzed depth was estimated as 59 μm , and the laser spot diameter as 1.3 μm . For a typical experiment a selected area of 1×1 mm was scanned with a step of 50 μm in the high resolution (HR) streamline acquisition CRM mode with the exposure time of 0.2 sec for each location. The total time of each map recording was about 2 minutes. The mapping was repeated every 5-10 minutes.

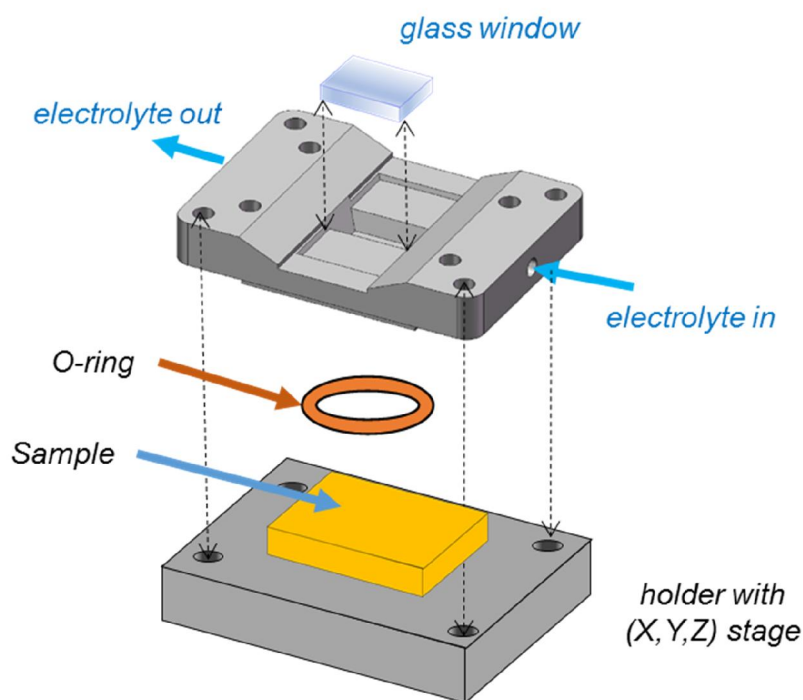


Fig. 35. Schematics of 3D printed thin layer cell for in-situ Raman mapping experiments.

The Raman spectra were pre-processed using Wire 4.2. software. The preprocessing included cosmic ray removal, noise removal, baseline subtraction and signal normalization: spectra were normalized in a way that the baseline corresponded to 0, and the maximum of the intensity of liquid water (3415 cm^{-1}) corresponded to 1. The area (A) of the peak with the Raman shift 3652 cm^{-1} corresponding to A_{1g} O-H stretch vibrations in $\text{Mg}(\text{OH})_2$ [168] was used to monitor the spatial distribution of brucite and its growth kinetics. The maps of the peak areas acquired at different times of the experiment were exported in the txt format and were treated with a homemade software. The software was able to verify for each location of the map if the peak evolution as a function of time can be described by a selected kinetics law (linear, parabolic, threshold like, etc...) and to present in the same color the points in which the film growth is described by the same kinetics law. Another mapping mode was used to

ascribe a color code to the time at which the film growth kinetics changes, mapping in such a way the film breakdown time.

Ex situ analysis

In selected locations, additional ex-situ Raman spectra were obtained after the experiment using a short distance Leica objective with NA 0.75 and longer exposure times, typically 10 sec. The morphology of corroded surfaces was also observed using scanning electron microscope (SEM-FEG Gemini 1530®) at applied voltage of 1 to 10 kV.

Results

Visual surface evolution and characteristic Raman spectra for typical morphologies

Fig. 36 shows a typical evolution of Mg surface appearance visible in optical microscope during Mg reactivity in the thin layer cell with 0.1 M NaCl solution at initial pH 9-10. One should note that after approximately 20 minutes of the experiment the downstream solution pH approaches 10 for all the experiments in which the initial solution pH was between 8 to 10. This value of pH is coherent with the pH of brucite precipitation and its buffering effect [169]. As expected from the literature [57], the black filaments of 10-20 μm width appeared randomly after approximately 20 minutes of the experiment. The propagation of the “head” of the filament was accompanied by a significant gas evolution. In Fig. 36, the gas is visible as circular shadows. The surface appearance outside the filaments did not change neither in visual observation after the experiment nor in optical images taken in situ by the microscope. In further discussion, the term “intact region” will be used for such areas. For the experiments made in strongly alkaline solutions (pH>12), during the time of the experiments black filaments did not appear.

In-situ Raman spectra in the OH-region recorded in different locations of the surface revealed small but systematic differences in the OH region as illustrated by examples in Fig. 37. All the spectra in the figure are normalized by the water signal as described in the experimental section. The presence of microcrystalline brucite is evidenced by a strong peak at 3652 cm^{-1} corresponding to A_{1g} O-H stretching mode in $\text{Mg}(\text{OH})_2$ crystals [168].

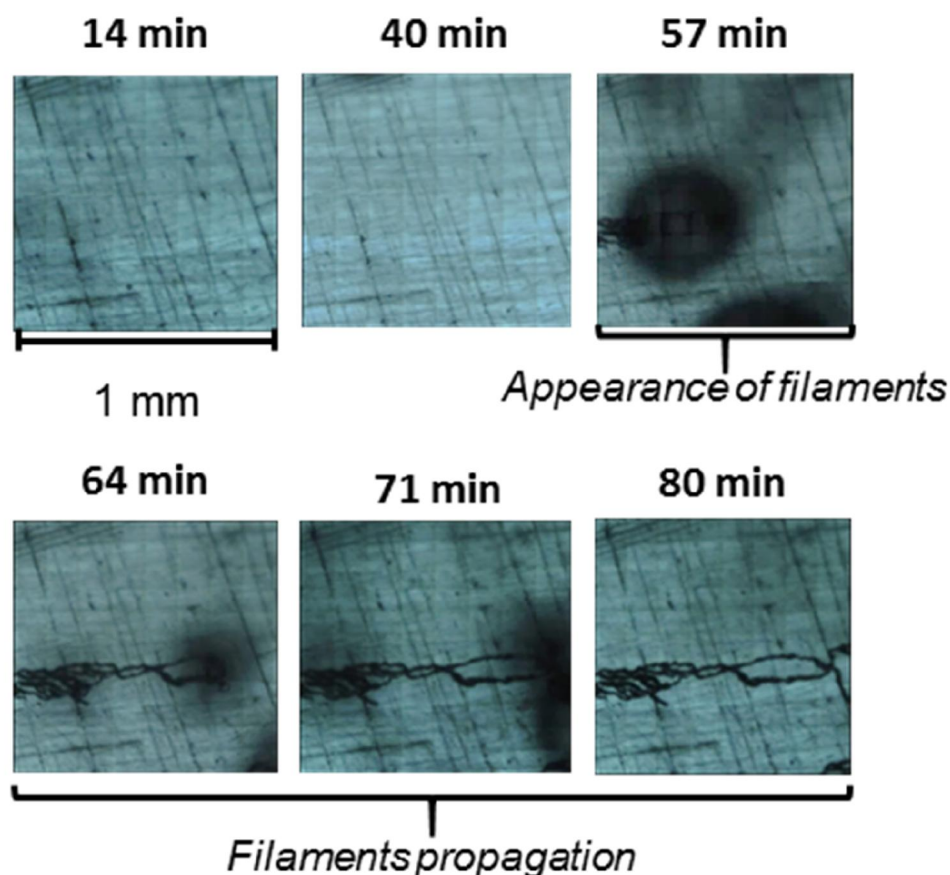


Fig. 36. Time Lapse images of Mg surface evolution in 0.1 M NaCl solution at initial pH 9.

It was also confirmed in broad scans (not shown) by peaks at 443 cm^{-1} and 280 cm^{-1} corresponding to lattice vibrations, A_{1g} and E_g respectively. More Raman spectra characteristic for different locations can be consulted in Supplementary information (Figure S1). On low purity Mg (Mg 1) at some areas the black points appeared from which the filaments did not develop. Spectra of these spots did not show the appearance of the second peak.

The figure evidences the appearance of two types of “satellites” in Raman spectra: at 3675 cm^{-1} and 3710 cm^{-1} , appearing at high pH and in black filaments at moderate pH. No satellites were detected in situ in intact areas at neutral pH. We did not find any publication reporting clearly these Raman shifts in the experimental Raman spectra of crystalline brucite. They were also not listed for nanocrystalline brucite [170]. We noted also that the appearance of these peaks was not affected by Cl^- content and that no carbonate contamination was detected (no peaks between 1000 and 1100 cm^{-1}). This argument let us tentatively interpret these peaks to specific surface vibrations of Mg-OH surface groups respectively situated at the basal plane (0001) for 3675 cm^{-1} and at the (10-10) plane for 3710 cm^{-1} peaks, as was

proposed on the basis of molecular simulations in [28]. To differentiate the “trivial” for crystalline brucite peak at 3652 cm^{-1} we will name it “bulk”. In such an interpretation, the presence of satellites can be considered as an indication of the high surface to volume ratio and can be tentatively used for the survey of the morphological evolution of the crystals [24].

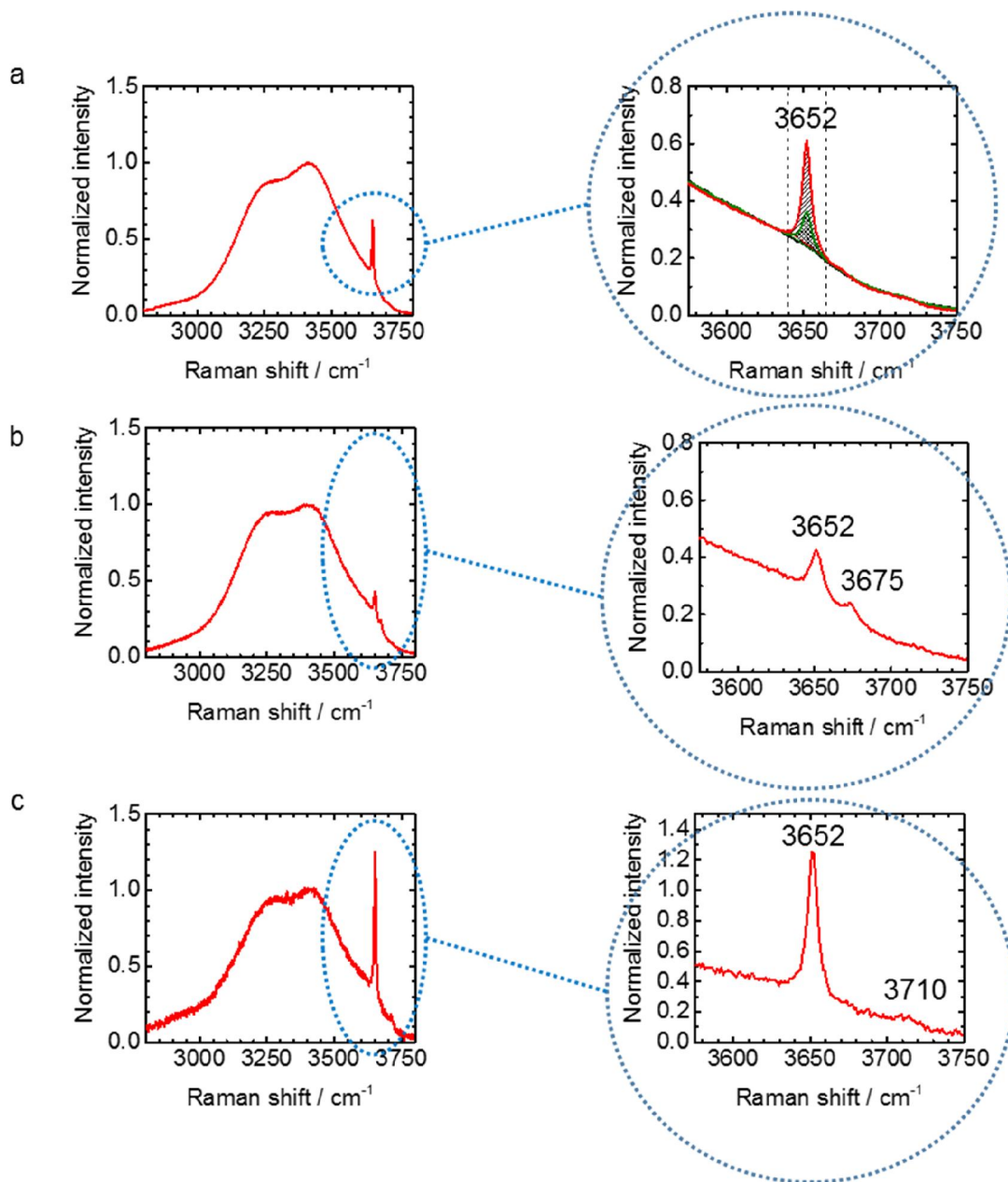


Fig. 37. Typical in-situ Raman spectra of corroding Mg in 0.1 M NaCl solution with different initial pH: (a) pH 9, intact area; (b) pH 9, black filament; (c) pH 13, intact area.

Comparison of the optical images of the surface and the in situ recorded maps representing the spatial distribution of the normalized peak area of “bulk” brucite at different pH (examples in Fig. 38) illustrates that at pH 13 the brucite film looks homogenous while at pH 9-10 the

intensity of brucite signal is significantly higher in black filaments. A statistical analysis of the surface to bulk peak areas $A(\text{surface})/A(\text{bulk})$ at different times of the experiment has shown that after an initial period at which the satellite peaks cannot be separated from the noise, the ratio $A(\text{surface})/A(\text{bulk})$ stays constant at pH 13 (around 0.17 ± 0.07 for high purity Mg2 and around 0.07 ± 0.07 for low purity Mg1).

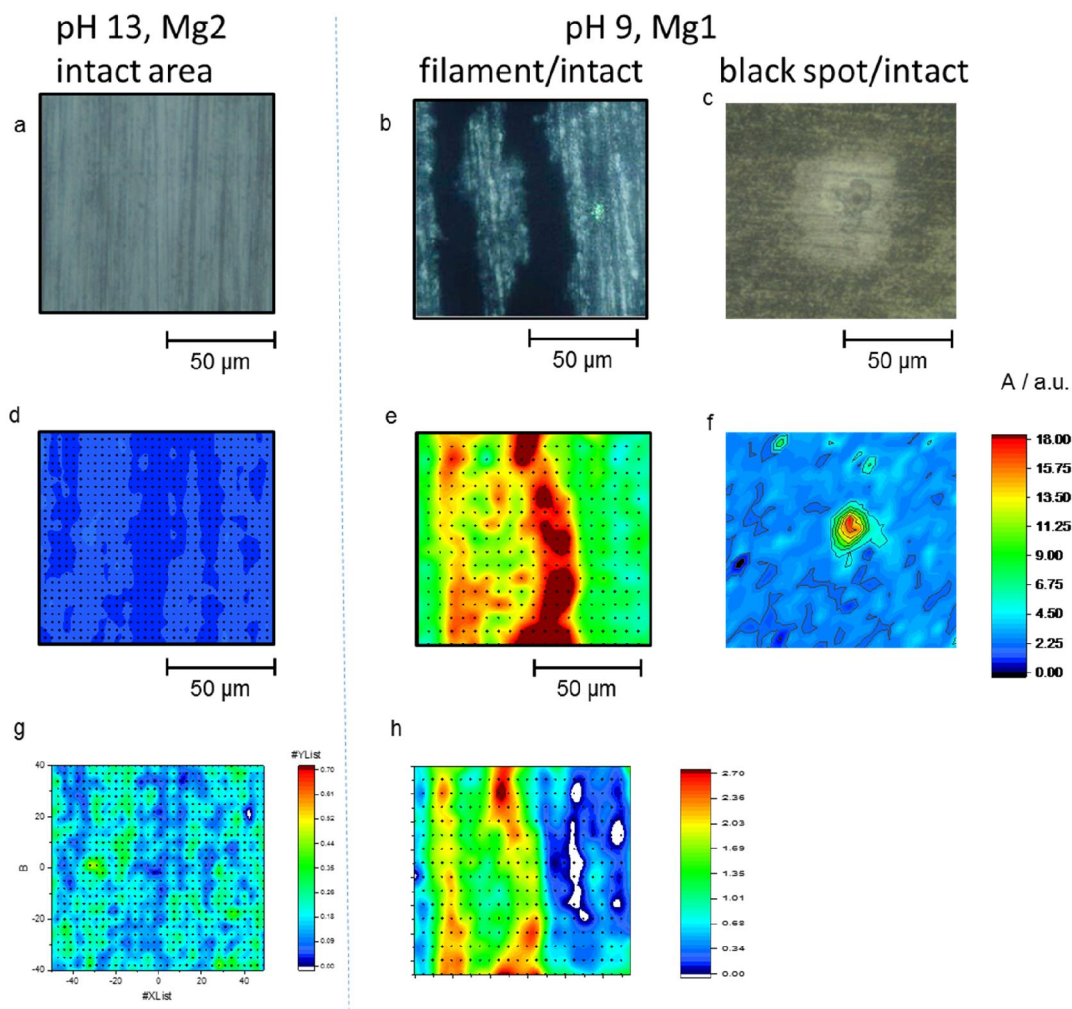


Fig. 38. Example of in-situ observed surface morphologies (a-c) typical for different pH as indicated and corresponding high resolution in-situ CRM of brucite 3652 cm^{-1} (bulk) peak area (d-f) and 3675 cm^{-1} (g) and (h) - 3710 cm^{-1} peaks).

Ex-situ morphologies of the brucite film

Ex-situ Scanning Electron Microscopy (SEM) (Fig. 39) demonstrated that brucite crystals present similar platelet-like morphology with the thickness of the platelets in order of 5-7 nm for all observed areas, while the platelet diameter varied significantly in function of local conditions. Bigger crystals were formed in intact areas and in black spots with the platelets diameter between 200 and 1000 nm. The platelet diameter was less than 50 nm inside

the filaments and below 100 nm at pH 13. The presence of satellites in in-situ Raman spectra correlated hence well with the lowering of the brucite crystal size. The EDS analysis of black spots made at 20 kV revealed the presence of nano-sized particles containing Ca or the underlying Si-rich particles of μm size (Supplementary information). A simple interpretation of the black spots with no development of filaments but high quantity of precipitated brucite can be hence in terms of silica impurities acting as crystallization centers accelerating brucite precipitation.

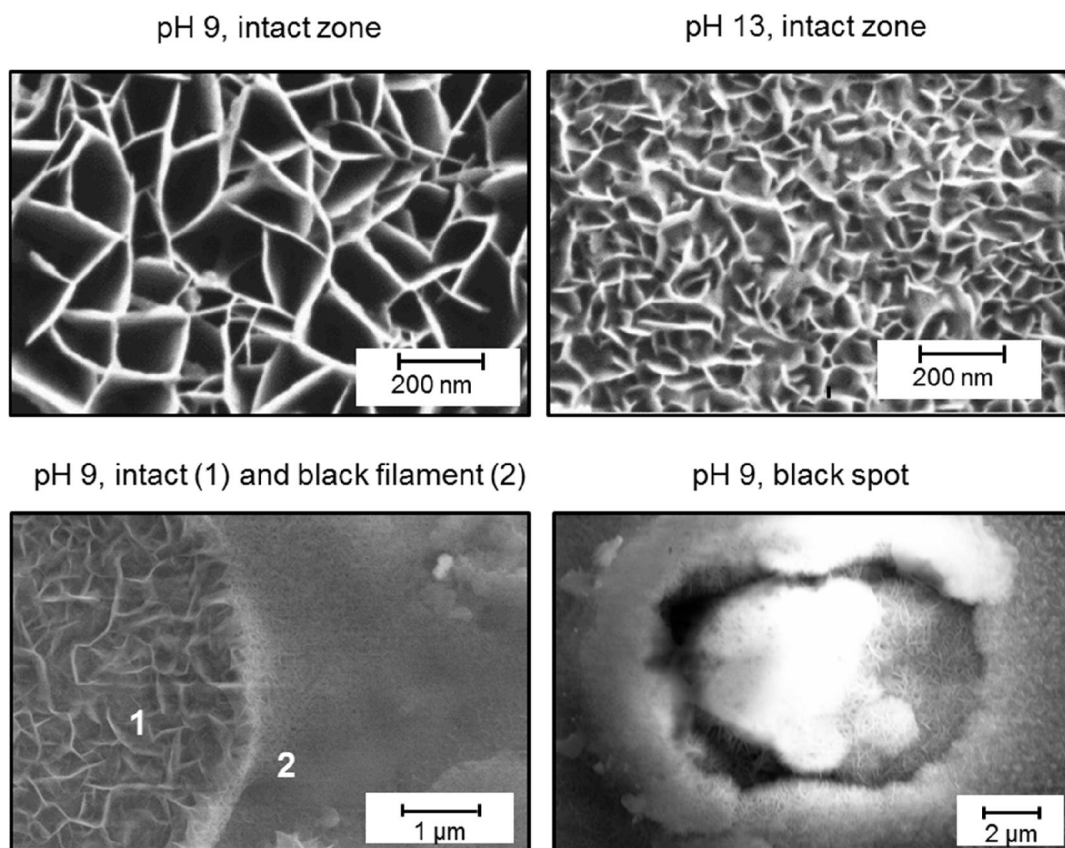


Fig. 39. Ex-situ secondary electron images of different zones defined by in-situ analysis. Accelerating voltage 1kV for intact zones and 10 kV for other images

Mg(OH)₂ growth and breakdown kinetics

Shaded areas in Fig. 37a illustrates how the evolution of the peak area (A) was evaluated for kinetic measurements. The procedure described in Experimental section was applied to plot the kinetics of brucite growth on Mg1 and Mg2 surfaces (typical size 1×1 mm) at different pH. The kinetic plots were made with different spatial resolutions to verify that the kinetic law does not depend on the resolution. At the areas in which gas bubbles were

formed they caused the defocusing of the laser beam that disturbed the local measurements. Despite systematic solution renewal it was impossible to eliminate completely the bubbles from the head of the filament. The times at which at selected locations the gas bubble disturbed the measurement were excluded from the kinetics analysis of these points.

The statistical analysis of the maps obtained on both Mg types and at different pH and Cl⁻ concentrations revealed for intact areas two typical kinetics of the brucite growth illustrated in Fig. 40a. At pH 13 the bulk brucite evolution is characterized by the kinetics which could be described by a parabolic law (the slope of the graph $\log A - \log(\text{time})$ was close to 0.5). At pH 9, Mg(OH)₂ growth in the intact region is linear with time (the slope 1 of the $\log A - \log(\text{time})$ plot). Interestingly, the increase of Cl concentration (Fig. 40b) seems to increase the quantity of the formed brucite in intact areas but doesn't seem to modify the kinetics law (slope of $\log - A \log(\text{time})$ curve stays close to 1 for different concentrations of Cl⁻). Very different film growth kinetics (Fig. 40c) was observed in the areas identified at the end of the experiment as black filaments and black points. The curve presented in Fig. 40 c initially follows the same kinetic law as an intact region and then shows a threshold like increase.

Statistical data treatment confirmed that this type of kinetics is associated with the proximity of black filaments and black spots and that that the time of the jump in the kinetics curve (Fig. 41a) coincides with the first visual observation of filament in studied zone. In Fig. 41a the color code reflects the time of the jump in the Mg(OH)₂ growth kinetics curve for the experiment presented in Fig. 36. It is clearly seen on the map that the time development of the filament in optical images (Fig. 36) correlates with the change in the brucite growth kinetics (Fig. 41a). Using the map shown in Fig. 41a, it is also possible to plot the fraction of the surface with "broken" film as a function of time (Fig. 41b). At times more than 20 minutes the breakdown kinetics could be approximated by a linear law which is coherent with the previously reported filament growth under anodic polarization [59]. The initial time period is difficult to interpret because the points considered by the software as "breakdown" points corresponds to the initial inhomogeneity of the surface.

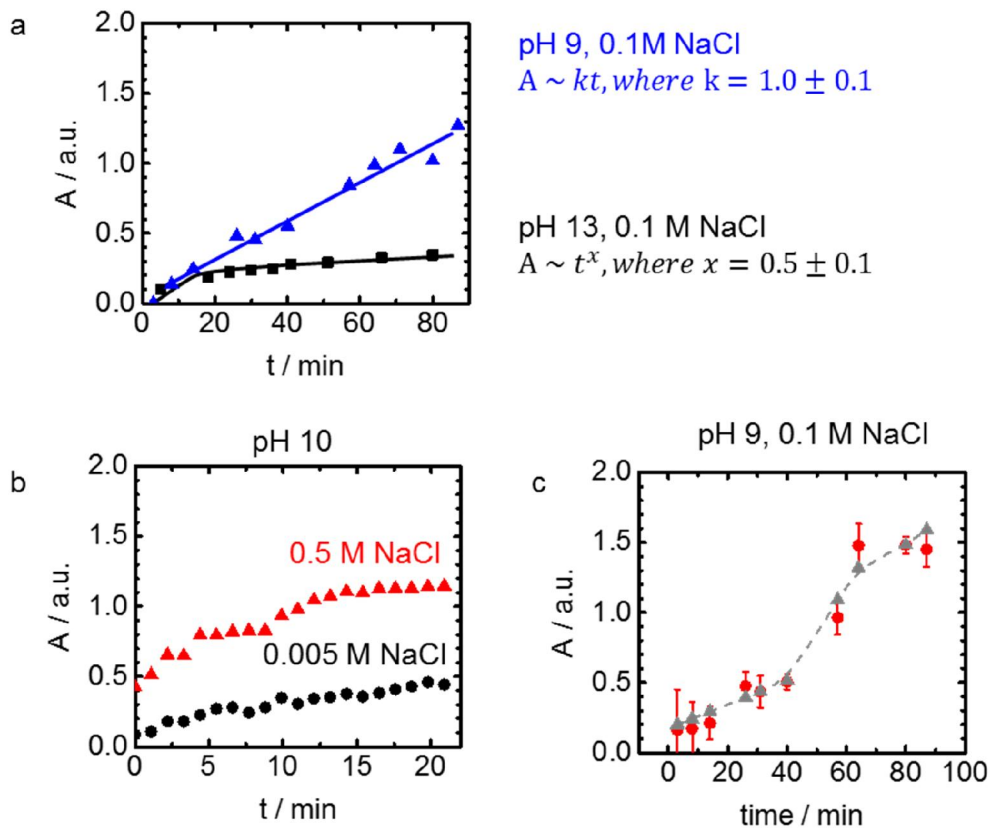


Fig. 40. Effect of solution pH and Cl⁻ concentration in the electrolyte (as indicated) on the kinetics of the brucite growth on Mg 1 immersed in different solutions as indicated: (a, b) “intact” regions, (c) black filaments. The dash line in figure (c) represents kinetics simulated from supersaturation model

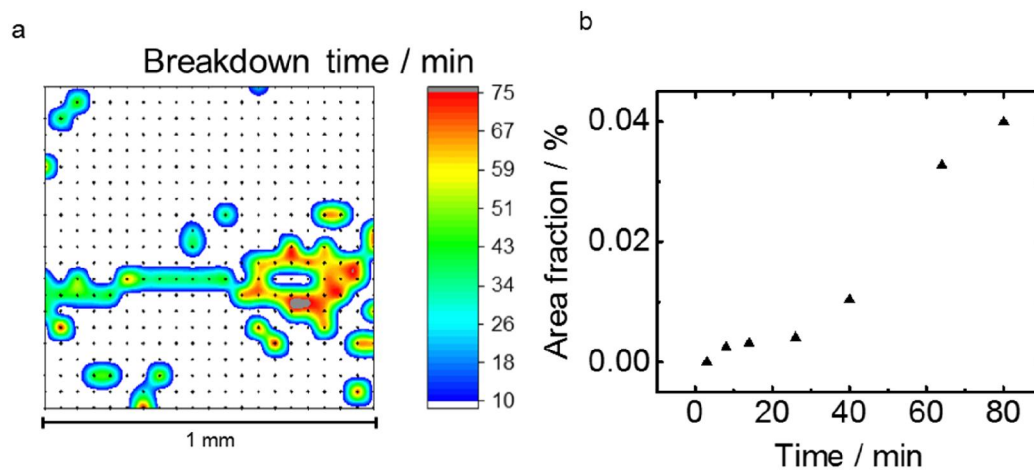


Fig. 41. Example of filiform corrosion advancement represented as (a) kinetic map (breakdown time for each point is shown by the color code), and (b) fraction of the surface with “broken” film as a function of time. Optical evolution of the surface during this experiment is shown in Fig. 36.

Discussion

Role of dissolution – precipitation processes for surface film growth and Mg reactivity

Numerous works justify the properties of the surface films on corroding Mg by dissolution-precipitation processes. The origin of the \log_{10} relationship of pitting potential with Cl^- concentration was discussed in terms of the solubility product of magnesium hydroxide [52]. Recently, enhanced hydrogen evolution at the $\text{Mg}(\text{OH})_2$ covered Mg surface compared with pristine Mg [10] was attributed to the enhancement of the self-dissociation of water on corrosion products in order to precipitate released Mg^{2+} ions from a supersaturated condition. Other authors speculated the disruption of the oxide/hydroxide film when an anodic current is available and environmental conditions can induce de-passivation [157] to explain the generation of streams of bubbles at the corrosion front. Such speculations look reasonable but could be stronger if the film evolution by dissolution-precipitation mechanism is proven in situ.

The platelet morphology typical for the precipitated $\text{Mg}(\text{OH})_2$ [2,171,172] which was observed previously in slightly alkaline solutions and in all the conditions of our work, including strongly alkaline pH and inside the filaments, is coherent with the mechanisms including precipitation and grain growth with dissolution of high energy surfaces and development of the low energy basal surface. These ex situ observations however could not be considered alone because they cannot confirm that observed crystals are formed during the experiment and not during solution drying or sample preparation and even during observation under high vacuum and in high energy beam.

The presented in situ results could reinforce the ex situ observations. First of all, considering the effect of pH and surface location on the evolution of not only the bulk brucite signal at 3652 cm^{-1} but also distribution and evolution of the “surface” signals in Raman spectra, the evolution of the crystal size and morphology can be evaluated in situ. Secondly, the kinetics of the film growth could be considered to verify the mechanism of its formation.

The in situ spectra obtained for Mg reacting in solutions with pH 13 show stable and uniformly distributed signal of the surface OH groups with a constant ratio $A(\text{surface})/A(\text{bulk})$ at different times of the experiment. This can be interpreted as the formation of a uniformly distributed hydrated layer with a relatively constant grain morphology with high surface to volume ratio which can be ascribed by high nucleation and slow crystal growth rate. Parabolic

film growth kinetics indicates diffusion limitation of the film growth typical for passive films [71,72].

For the Mg surfaces immersed in slightly alkaline conditions in situ spectra evolution before the film breakdown indicates insignificant surface contribution to the Raman signal, suggesting formation of bigger crystals. Measured linear growth kinetics in these conditions is coherent with the surface reaction limited growth [73] and the formation of bigger crystals with well-developed basal planes can be ascribed to continuous dissolution-precipitation process on a very limited number of nuclei with dissolution of the surfaces with high surface energy and development of low energy surfaces. The linear kinetics of the film growth is also coherent with the kinetics of the electrochemical precipitation of brucite from Mg^{2+} solutions under applied cathodic currents [173]. These continuous dissolution-precipitation processes and big crystal size should lead to higher porosity and easy incorporation of Cl^- in depth of the film. It should also facilitate the hydration of the inner MgO.

Brucite film evolution explained by precipitation from supersaturated solution

The effect of pH on the evolution of the crystal size and morphology, on the film growth kinetics and on its resulting properties could be hence easily attributed to the dominance of one of the processes [174]: crystal growth (in case of pH 9) or nucleation (pH 13) [175] in the film growth. Considering solution supersaturation, Π , defined as the difference between the real measured concentrations and the solubility product at a given temperature (eq. 20):

$$\Pi = \frac{[Mg^{2+}][OH^-]^2}{[Mg^{2+}]_{eq}[OH^-]_{eq}^2} \quad (20)$$

it is easy to verify that for Mg^{2+} high supersaturations are easily achieved at high pH ([169]), favoring nucleation, whereas at $pH < 11.5$, for the same quantity of leached Mg^{2+} supersaturation level will be low and the crystal growth is favored vs nucleation.

Assuming the film growth in the approach of precipitation from supersaturated solutions [75] and taking into account that in corrosion the concentration of ions in the solution evolves with corrosion process, one can explain also the threshold-like kinetics of the brucite growth and formation of small crystals observed in black filaments. Indeed, at low supersaturation levels, small changes of concentration significantly modify the precipitation rate [176]. The reactivity at the black filaments is usually described as cathodic activation with H_2 evolution and pH increase and anodic Mg^{2+} release occurring at the border between the dark and intact areas [11,64,177].

In the approach of the relaxation of supersaturated solutions [178,179] the precipitation rate is proportional to the supersaturation factor Π and the surface area of the formed precipitates. Assuming hemispheric particles for which the surface is $\propto \sqrt[3]{m^2}$ and assuming that the area of the bulk Raman peak (A) reflects the quantity of the precipitated brucite, the brucite growth rate can be expressed as

$$A = \int_0^t k'' m_{Mg(OH)_2}^{\frac{2}{3}} \Pi(t) dt \quad (21)$$

where k'' is a proportionality coefficient.

Using Eq. (21) and the experimental growth rates of the intact film at pH 9, the tree-step film growth kinetics distinguishable in Fig. 40c can be simulated (dash line):

1) initial linear growth of the film thickness is ensured by a constant Mg^{2+} release from the substrate via a low barrier surface film;

2) at 90 minutes the surface film breakdown results in the activation of local anodic and cathodic reactions and the injection of the excess Mg^{2+} and OH^- ions. Assuming the local pH increase by 1 unit (from 9 to 10) and approximating the “supplementary” precipitation by Eq.(21) a sharp increase of the growth kinetics is easily obtained;

3) once the injected ions precipitate, the film re-passivates and the reaction rate should be the same as in step 1.

The proposed schema of the filament propagation and the resulting evolution of the brucite film growth kinetics is presented in Fig. 42.

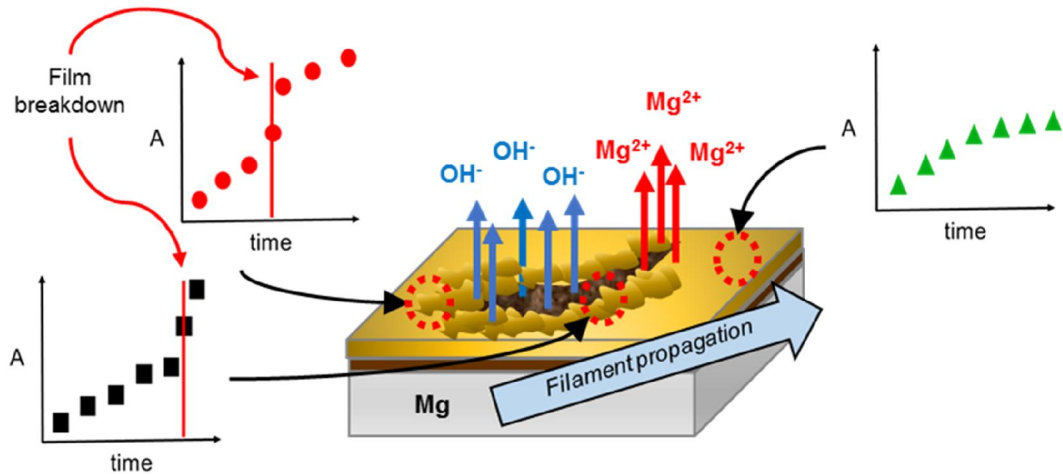


Fig. 42. Schematic representation of $Mg(OH)_2$ film growth processes in Cl^- containing solution around filament and in intact region

Conclusions

CRM in a form of in-situ kinetics Raman mapping (KRM) was used to describe the effect of solution pH on the local evolution of the surface films at initial stages of Mg corrosion in thin layer cell. Using a specific normalizing procedure, the survey of A_{1g} brucite peak (3652 cm^{-1}) evolution allowed to map the local film growth and breakdown and extract kinetics laws on mm large surfaces with about $10\text{ }\mu\text{m}$ spatial resolution within the same experiment.

On the areas, which did not evolve in optical images during immersion, brucite growth kinetics was parabolic (diffusion limited) at pH 13 but linear (surface reaction limited) at pH 7-10.5. A jump in the kinetics curve was observed in some particular locations. Statistical data treatment showed that this type of kinetics is associated with the proximity of black filaments and that the time of the steep increase in kinetics curve coincides with the first visual observation of filaments in studied zones.

The spectra were also tentatively analyzed in order to extract information about the in-situ evolution of the crystal size and morphology. Alkalinity increase favored the appearance of “satellites” peaks in Raman spectra. Bands at 3675 cm^{-1} and 3710 cm^{-1} were attributed to the vibrations of the surface Mg-OH groups situated at different crystallographically oriented planes, (0001) and (10-10) respectively [28]. The presence of “satellites” hence was considered as an evidence of high surface area and smaller $\text{Mg}(\text{OH})_2$ crystal size at high pH, which was confirmed by ex-situ Scanning Electron Microscopy (SEM). Similar kinetics of the bulk and satellite peaks growth were obtained at pH 13 after about 10 minutes of induction period indicating that the crystal morphology reaches equilibrium at this time.

The effects of pH on the kinetics of the brucite film growth, on the crystals size and morphology are coherent with a dissolution-precipitation process of the film formation. In this regard, enhanced growth of $\text{Mg}(\text{OH})_2$ in the proximity of filaments could be explained and simulated by the local film breakdown resulting in the injection of the excess Mg^{2+} and/ or OH^- ions and additional brucite precipitation.

From the methodological point of view, the developed in-situ KRM could be easily extended to multiple processes for which in-situ measurement with local resolution can be of interest.

Supplementary 1

The analyzed depth at present experimental conditions was measured by monitoring the change of intensity of the 520.5 cm^{-1} band of a silicon wafer mounted in the flow cell with water. The intensity changes of the Si peak with the z-position of the objective demonstrated a Gaussian type variation, the full width at half-maximum (FWHM) was used to calculate the focus depth [124]. The laser spot diameter (d) was calculated using the formula

$$d = \frac{1.22\lambda}{NA}, \quad (22)$$

where λ is the excitation wavelength (532 nm), NA is the numerical aperture of the objective (0.5). In our experimental conditions, the analyzed depth was $59\text{ }\mu\text{m}$, and the laser spot diameter was $1.3\text{ }\mu\text{m}$.

Supplementary 2

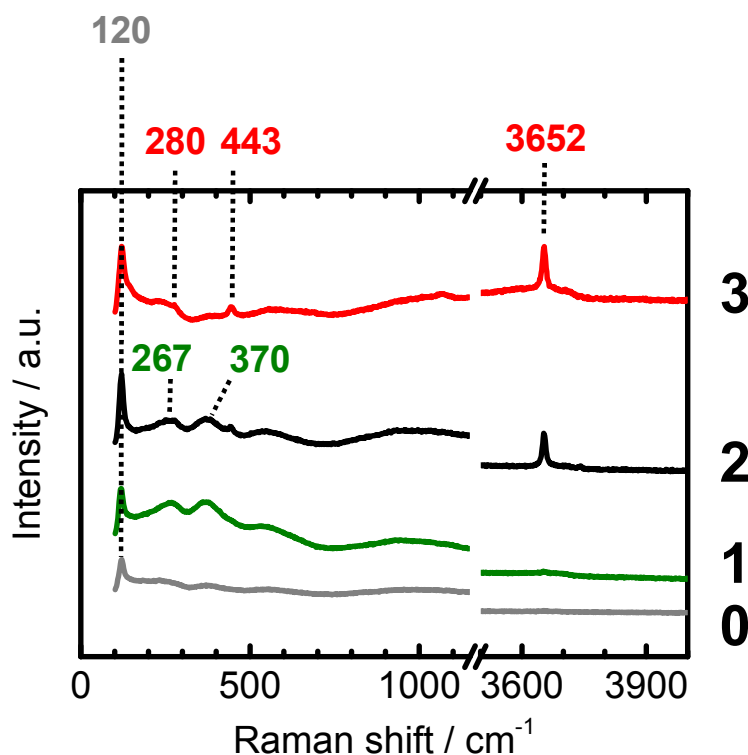


Fig. S1. Typical ex-situ Raman spectra before (0) and after (1-3) 2 hours of Mg reactivity in 0.1 M NaCl, initial pH 9. Spectra (1,2) are made in black filaments, spectrum (3) in an intact region.

The ex situ Raman spectra before and after immersion are shown in Fig. S1. Typically, before immersion only the peak at 120 cm^{-1} , which corresponds to the optical mode of Mg [180] is detected (spectrum 0) because in the absence of impurities MgO is not Raman active. After immersion, the presence of microcrystalline brucite in intact regions (spectrum 3) is evidenced by a strong peak at 3652 cm^{-1} (A_{1g} O-H stretching mode in $\text{Mg}(\text{OH})_2$) and smaller peaks at 443 cm^{-1} and 280 cm^{-1} (lattice vibrations, A_{1g} and E_g respectively) [168]. Inside the filaments (spectra 1 and 2) broad peaks at 267 and 370 cm^{-1} can be assigned to Mg salts containing crystallized water. In the literature, the bands at $\sim 360\text{ cm}^{-1}$ were previously assigned to Mg-O vibrations in Mg salts [181,182] containing crystalline water and peak at 243 cm^{-1} to the A_{1g} breathing mode of MgO_6 octahedra in the $\text{MgCl}_2 \cdot \text{H}_2\text{O}$ lattice [183,184]. As for brucite, its detection by Raman inside the filament depended on the location, in some places it was visible, which can be interpreted by the fact that the film can be broken during drying.

Supplementary 3

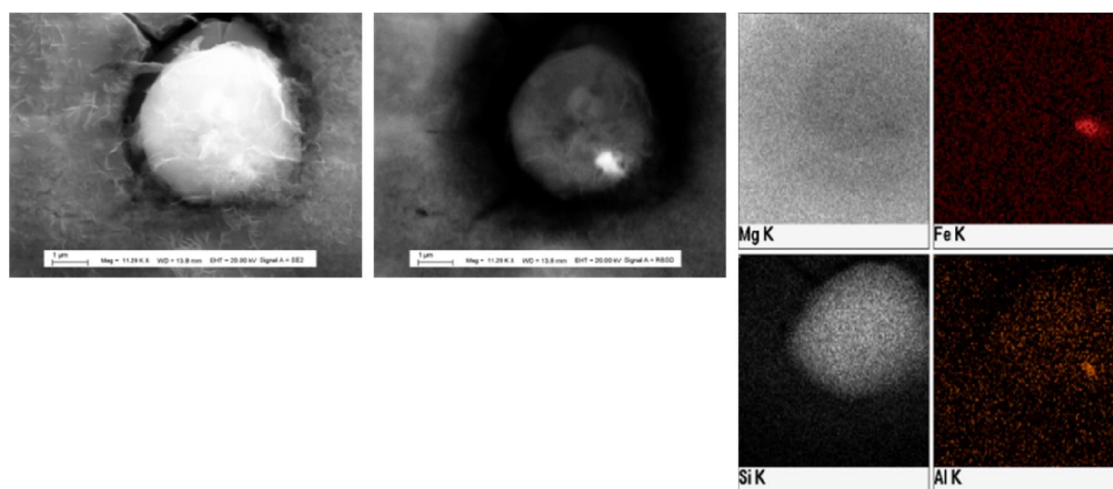


Fig. S2. Secondary (topographic contrast) and backscattered (chemical contrast) electron images of an area on corroded Mg surface with an excess brucite thickness and corresponding EDS maps evidencing the presence of Si rich particle with Al-Fe intermetallic underneath the excess of brucite.

Chapter 6

On the application of Glow Discharge Optical Emission Spectroscopy (GD-OES) for depth profiling of corroded materials: example of pH effect on Fe and Mn enrichment on corroding Mg

This chapter demonstrates the applicability of GD-OES to monitor impurities depth distribution on corroded commercial purity Mg.

(The content of the chapter represents the article in preparation for Corrosion Science)

Abstract

The applicability of glow discharge optical emission spectroscopy (GD-OES) to monitor impurities depth distribution in 99.9 % purity Mg alloys corroded in aqueous solutions with pH 9-14 was studied. Results have demonstrated that in some cases the oxide enrichment can be directly concluded from qualitative GD-OES depth profiles although the analyzed matrix differs between corroded and intact layers while in other cases a direct interpretation of depth profiles can be misleading which justifies the analytical work. The effects of solution pH and location on the surface on the observed depth profiles were interpreted using solubility considerations.

Introduction

The reactivity of Mg alloys has been extensively studied in recent decades [185–189] in relation with their interest for numerous applications [190]. For these materials corrosion is considered to be governed by hydrogen evolution which is enhanced on pre-corroded magnesium (see for instance the review [187]). The latter is often attributed to the catalytic effect of corrosion products because of the surface enrichment by more noble elements forming local cathodes [185,191,192] or due to the cathodic reactivity of the oxide-hydroxide film itself [6,159]. Thus, the chemical composition and depth distribution of impurities in corrosion products formed on Mg alloys is of great interest. The evidence of the surface enrichment in high purity Mg is not trivial due to the trace level of impurities and high thickness and porosity of corrosion products. For alloys with high impurities level (in order of 1% and more), it is commonly accepted that the surface behavior is strongly affected by the enrichment of the film by Al oxides and spinel and that Fe and Cu particles can be concentrated in the surface oxides [185,193–197]. The behavior of other elements in the oxide layer is less known; for instance, the anomalous hydrogen evolution under anodic polarization is still observed for Mg-Ca and Mg-Li alloys while their surface enrichment is not expected [198]. The methods used in the cited works are however either not sensitive enough for the trace impurities level (case of scanning electron microscopy, electron dispersion spectroscopy, X-ray diffraction) or not convenient for routine studies of isolated impurities in corrosion products of micrometric thickness (photoelectron spectroscopy, transmission

electron microscopy, etc.). Several original approaches combining magnetic field, X-ray diffraction and TEM [192] and applications of Rutherford Backscattered Spectroscopy [198], particle induced X-ray emission [191] and TOF SIMS [199] were recently used to demonstrate Fe enrichment on the surface of pure Mg. Nevertheless, a depth profiling of corrosion product is still challenging.

Radio Frequency Glow Discharge Optical Emission Spectrometry (RF GD-OES) offers a unique combination of a fast sputtering rate, high depth resolution, excellent sensitivity, multi-element capability and experimental simplicity with no requirement for an ultrahigh vacuum or special surface preparation [25,200]. It was successfully applied to study the enrichment of rare earth metals [201] and Cu [202] in the anodized layer on Mg alloys containing several wt. % of these alloying elements. However, the previously reported attempts of using GD-OES to study the impurities enrichment in corroded high purity Mg were unsuccessful [198]. Authors attributed it to the experimental difficulties to maintain the hermetic joint during sputtering of naturally formed Mg corrosion products because of their high porosity and roughness. Another critical aspect related to the application of GD-OES to corroded surfaces is that the plasma composition can be significantly affected by the presence of hydrogen in corroded layers. For our knowledge, all the works previously applying GD-OES to corrosion and surface treatment, used the interpretation of the GD OES intensities in an assumption that only the sputtering rate (SR) is different between the corroded or oxidized layer and the metallic substrate and that the plasma properties are not significantly modified during sputtering. However, the reality is different and the plasma properties can change significantly during sputtering, in particular, the presence of H in the plasma during sputtering of the corroded zone can increase or decrease the measured intensities of the element of interest [27,152,203]

The present work demonstrates that with optimized analysis conditions it is possible to achieve reliable RF-GD-OES depth profiles of corroded Mg while a direct interpretation of the depth profiles measured on corroded surfaces without taking into account the analytical aspects can be misleading and even wrong. The focus is made on the possible origins of the surface enrichment of corroded layer by some impurities present in the material or in the solution. We insist that a correlation between the enhanced cathodic reactivity of Mg and the surface enrichment stays out of the scope of the present work. The main questions we want to answer are hence

Could the enrichment of corroding Mg by low level impurities be reliably measured by a simple method without specific surface preparation and high vacuum?

What could be tricky analytical issues to take into account for such a measurement?

Which mechanisms can lead for the corroded layer enrichment by different impurities elements and what is the effect of pH on the enrichment?

A particular attention will be payed to the effect of the plasma modification by H on the depth profiles interpretation, because corroded Mg contains a high fraction of brucite (Mg(OH)₂) in the external layer, which can be a source of high content of H in plasma.

Experimental and calculation details

Materials and experimental conditions

Two types of samples of commercially pure Mg were used– 99.9 % purity Mg and MgMn with about 1 % of Mn (see Table 3 for compositions). Strips of 3 cm width cut from commercial purity Mg samples were mechanically polished (SiC paper up to P4000 grit) with ethanol as a lubricant, rinsed with ethanol and dried under N₂ gas flow. Samples were immersed in solutions prepared from solid NaOH (Prolabo, analytical grade), NaCl (Prolabo, analytical grade), and deionized water (Millipore, 18 Ω cm), rinsed with deionized water and analyzed by GD-OES. The Cl concentrations varied between 0.0 and 0.1 M and NaOH concentration between 0 (natural pH of NaCl solution was 5.8-6) and 1 M (pH up to 12.8 were measured, then only solution concentration was considered and theoretical value will be given – 13 for 0.1 M NaCl, 14 for 1.0 M NaCl). The immersion time varied in function of NaCl concentration and pH, in 0.1 M NaCl it was 2 h, without chloride in solutions – 12 hours

Table 3. Impurity level in the studied Mg alloy (ppm), used emission lines (λ /nm) and calculated from [26] H-correction coefficients, h_x (see text for explanations).

Element	Fe	Mn	Al	Cu	Ni	Si	Zn	Mg
Mg	280	170	70	20	<10	50	<20	Bal.
MgMn	80	10800	100	100	<10	100	<20	Bal.
λ /nm	371.99 9	403.454 *	396.157	324.759	352.459	288.162	481.060	285.217
h_x	2.03	0.29	1.36	0.23	not studied			no data

* studied on monochromator

GD-OES analysis was performed with a GD-Profilier 2 (HORIBA Jobin Yvon) using Quantum software. The instrument configuration included a pulsed radiofrequency (RF) generator, a standard HJY glow discharge source with an anode of 4 mm internal diameter and an automatic impedance matching system between the RF generator and the GD source.

The latter permits matching even in pulsed RF mode operation and continuous monitoring of the DC bias voltage for conducting samples.

High purity argon (99.999% minimum purity) and Ar-H₂ mixtures with volume H₂ fractions 200 ppm, 500 ppm, 1000 ppm, 2500 ppm and 10000 ppm (1 %) were supplied by Air Liquide and were employed as the discharge gas. The optical system was purged by high purity N₂ in order to detect emission lines in the VUV region. The Differential interferometry Profiling (DiP) system integrated in the instrument allowed in addition a direct depth measurement along with the elemental depth profile analysis and therefore an independent estimation of the erosion rate in different layers. The final crater depth obtained by DiP was also verified by the 2D profilometer. Prior to each analysis, the source was cleaned by 60 s of sputtering of a sacrificial Si wafer [204].

Elemental depth profiling was performed under several sets of conditions: Ar pressure of 686 Pa and 750 Pa and a constant power of 25 W or 17 W. A specific surrounding bell system filled with Ar was used for the sputtering of samples corroded at low pH to exclude air ingress through the layer porosity [205]. The emission signals of 47 elements were recorded but only the signals of the species of interest are discussed in the paper. The selected wavelength for metallic elements are reported in Table 3, other wavelengths were: O - 130.223 nm, Ca – 422.679 nm, Na – 589.600 nm, N - 149.267 nm, Cl – nm, Na - and H - 122.574 nm.

Theoretical approaches to hydrogen effect on emission yield

To take into account the H-effect it was previously proposed in the literature [206] to assume a linear relation between the inversed emission yield of the element X (noted below as R_X and calculated as (emission yield)⁻¹), and the H-signal intensity I_H with a correlation coefficient h_X :

$$R_X \approx 1 + h_X I_H \quad (23)$$

H-corrected intensity (I^{corr}) of GD-OES signal was calculated using the equation

$$I_X^{corr} = I \cdot R_X(I_H) \quad (24)$$

Using the data of works [152,207] we estimated h_X for the elements of interest in assumption that (i) the values of h_x are independent on the matrix (and hence optimized plasma conditions) and (ii) a linear function can be used for fitting even if the linear region is very narrow. The obtained h_X for Fe 273, Al 396, Cu 325 and Mn 403 lines are listed in Table 3. It is clear from the table that the H-corrected signals can be expected higher (Al, Fe, Cu) or lower (Mn) than before correction.

Results

Types of element profiles observed by GD-OES

Fig. 43a illustrates an example of a typical depth profile (intensity of the GD-OES signal of the element X, I_X , measured in V, as a function of the eroded depth, in μm , determined by DiP) for Mg, O, H and N as well as the total light (Fi) and module (Mod) and phase (Phase) values of the matching box obtained on the sample immersed at pH 9 in Ar plasma gas. First of all, it is clear from Fig. 1a that the signal of N is in an acceptable limit and shows a normal decreasing profile corresponding to the initial surface contamination. The values of Fi, Mod and Pha also vary smoothly. These observations indicate the absence of the previously reported problems of sealing the GD chamber with the sample during the measurement and confirms the validity of the recorded data. Two regions could be identified: a corroded zone with relatively high signals of O and H and the bulk metal with near constant intensities of all the signals. We do not show the periods of plasma stabilization at the extreme surface for which the instantaneous change of Mod and Pha resulted in a high reflected power (Pr) and hence nul or very low sputtering efficiency.

Fig. 43b presents depth profiles of Mg and the impurities normalized by the intensities of each element in the bulk (I_X^{bulk}). Signals of Fe, Al, Cu are clearly higher in the oxidized layer than in the metallic bulk while Mn and Mg signals are lower in the oxide layer. The signal intensity depends however on SR. The sputtering rate (SR) estimated by DiP was in order of several nm/s in the oxide and above 90 nm/s in the metal. Higher SR implies higher measured intensities, thus, the increase of the SR from the oxide to the metal correlates well with increasing intensity of Mg and Mn (Fig. 1 b). Fe, Al, Cu profiles show a contrary tendency which can be interpreted as the enrichment of the oxide by these elements. The emission signals of Ca and Na are not shown on the figure however they were systematically present in the oxide layer, indicating a possible accumulation despite they are not expected to reduce on Mg. The enrichment by Na will be discussed in the next sections. Considering the same SR for different elements in the same matrix, the ratio I_{X1}/I_{X2} , where I_{Xi} is a signal intensity of the element X_i , can be used to represent the enrichment. If X1 and X2 are the minor and the major element of an alloy, higher value of I_{X1}/I_{X2} in the oxide layer than in the metal bulk indicates the enrichment of the oxide by the element X1. Fig. 43c illustrates the evolution of I_X/I_{Mg} , where $X=\text{Fe, Al, Mn, Cu}$ confirming that the oxide seems to be enriched by Fe, Cu and Al. The depth evolution of H-corrected signals (the emission intensity expected for the same quantity of the atoms of these elements in the plasma free of H) of the elements

are presented in Fig. 43d. Comparing Fig. 43b et Fig. 43d, it is clear that the H-corrected signals are even higher than before correction. Interestingly, after H-correction the corroded layer seems to be enriched by Mn illustrating that a direct interpretation of the GD profile without taking into account analytical aspects can be completely misleading.

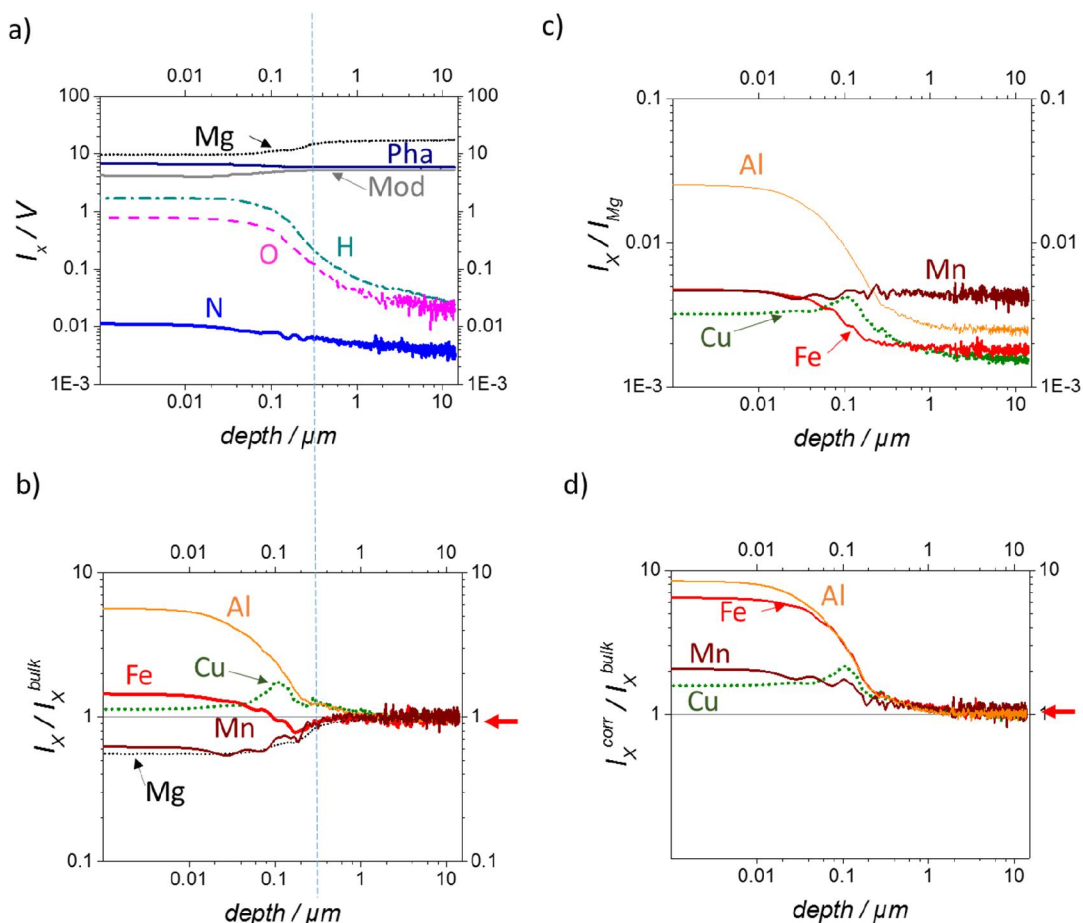


Fig. 43. Typical qualitative elemental GD-OES depth profiles of pure Mg pre-corroded in alkaline solutions. (a) Emission intensities I_X of Mg, O, H and analytical parameters (total light (Fi), module (Mod) and phase (Pha)) in function of eroded depth measured by DIP; (b) emission intensities of metallic elements normalized by their bulk values, I_X/I_X^{bulk} ; (c) Emission intensities of metallic elements normalized by the intensity of Mg, I_X/I_{Mg} ; (d) H-corrected emission intensities of selected impurities normalized by their bulk values, I_X^{corr}/I_X^{bulk} . All the profiles demonstrate the enrichment of the corroded layer by Fe, Cu, Al. the interpretation of Mn profile is difficult

Effect of H in plasma on the GD-OES intensities.

The effect of H on the Mg 285 emission was not previously documented. The effect of H on the emission efficiency in Mg matrix was not studied too. For this reason, we completed the experiments in Ar plasma by the experiments in Ar/H₂ mixtures expecting that

the presence of hydrogen in all conditions can neglect the H-content difference between the corroded and uncorroded materials and therefore provide more accurate profiles. In order to verify the effect of H in plasma on the analytical parameters of GD-OES a series of metallic standards available at Horiba JobinYvon with 50-5000 ppm of Fe and 50 – 20000 ppm of Mn were used.

Looking at the response of Mg 285 signal (Fig. 44a), one can note that at H₂ contents in plasma gas up to 1000 ppm I_{Mg} linearly decreases with I_H , however at higher H-contents it is very difficult to approximate the effect.

Mn-intensity linearly decreased with H signal (Fig. 44b) confirming the expected from the theoretical approximations (Fig. 1d) possibility of the wrong interpretation of GD-OES depth profiles obtained in Ar plasma without taking into account analytical issues.

The effect of hydrogen in plasma on the apparent Fe signal also confirmed the possibility of wrong conclusions for non-accurately made work. In Fig. 44c the evolution of the apparent Fe signal with increased H-intensity is shown for samples with Fe content as low as 50-80 ppm, below the detection limit of the Ar-H₂ plasma even for 200 ppm of H₂. With increase of the hydrogen intensity, the apparent Fe signal increases linearly. Another effect was noted (not shown here), illustrating that in presence of H₂ the detection limit of Fe significantly degraded: if in Ar plasma about several tens of ppm of Fe were detectable, in Ar-1% H₂ a strong background masked the Fe signal and the apparent GD profile from the samples containing between 50 ppm and 5000 ppm of Fe was exactly the same.

Fig. 44a-c do not present all the measured points but give the idea about the complexity of the analytical problem when analyzing corroded layers. They illustrate also the completely different behavior of plasmas containing 10000 ppm of H₂ (point encircled in all figures). The behavior in this mixture was verified in multiple experiments and the difference with other mixtures was stable in all plasma conditions. The crater observation demonstrated that this difference should be also related with the significantly slower erosion rate in this mixture than in all the other studied H₂ containing plasma gazes (up to 2500 ppm of H₂).

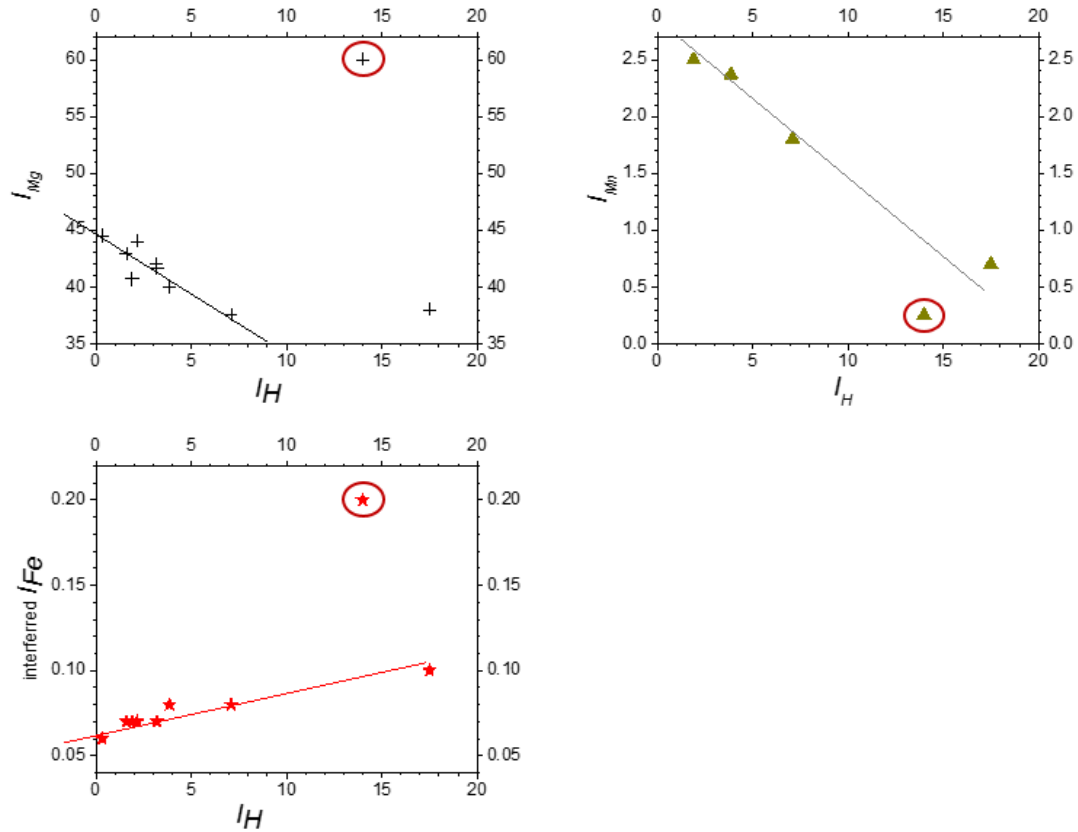


Fig. 44. Effect of hydrogen in plasma on the intensities of Mg, Mn and Fe in Mg matrix at 17 W and 750 Pa. The evolution of (a) Mg intensity (I_{Mg}), (b) Mn intensity (I_{Mn}) and (c) “interfered” Fe signal (interfered I_{Fe}) are shown as a function of the H signal intensity (I_H) in different Ar mixtures with 200 – 2500 ppm of H_2 and 10000 ppm of H_2 (the encircled point). Mg samples containing 0.5 – 1.92 wt. % of Mn and less than 80 ppm Fe (lower than detection limit) were used.

Correlation between pH and surface enrichment

Taking into account the evident effect of hydrogen in plasma on the intensity observed in depth profiles, we decided to study the effect of pH on the local surface enrichment in Ar/ H_2 plasma with the highest H_2 content (10000 ppm) expecting that this high content will level the differences in H content and that the slow sputtering rate will improve the quality of the profile at the interface.

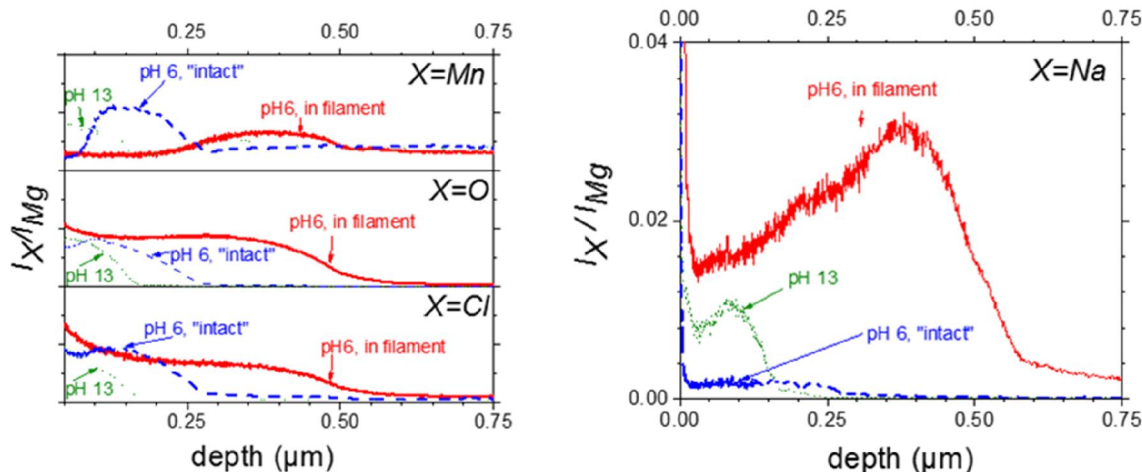


Fig. 45. Typical qualitative elemental GD-OES depth profiles measured on different locations of pure Mg pre-corroded for 2 hours in 0.1M NaCl solutions of different pH: (a) normalized emission intensities I_X/I_{Mg} for X= Mn, O and Cl as indicated in function of eroded depth measured by DIP; (b) normalized emission intensities of Na. O profile indicates the depth of the corroded layer in different conditions.

Fig. 45a illustrates the normalized by Mg intensity depth profiles for Mn, Cl, O obtained on the MgMn samples immersed for 2 hours in 0.1 M NaCl solutions at different pH.

First of all, it is clear from the presented profiles that the thickness of the oxide layer, visible from the position of the O signal, is strongly affected by the solution pH and the local conditions: higher pH results in thinner oxide, while the thickest film is formed in the area containing black filament.

The second interesting observation is that the Cl-enrichment looks uniform through the whole depth of the corroded layer and the Cl-level is independent neither from the solution pH nor from the location on the surface (intact areas or the area containing black filaments).

The third interesting observation is that even if the GD-OES is not able to detect Fe enrichment in studied conditions because of low Fe content and high H₂ content, the Mn enrichment looks different in function of both, solution pH and the location of the analyzed surface. It looks that the “intact” area at initially neutral pH is significantly enriched by Mn at the metal/oxide interface, while the area containing the black filament shows significantly lower Mn enrichment. One should also remember that the analyzed surface is large (circle of 4 mm diameter) and in the last case it contains not only black filament but also some intact surface. Taking into account that Mn is often considered as an element which decreases the harmful effect of Fe inclusions by increasing iron solubility, the local depletion of Mn in the area which corrodes preferentially looks logic. It looks also that in case of high pH the

interface has no enrichment but some depletion of Mn, while some Mn is present in the outer oxide layer.

The last effect we would note, is the variation in depth profile of Na (Fig. 45b). The profiles are extracted from the same locations and conditions as in the previous figure. GD-OES is extremely sensitive to Na and Na contamination is expected (and visible at the first 10-50 nm of the extreme surface). However, the differences observed in depth distribution in the samples immersed in NaCl and NaOH containing solutions look interesting and will be discussed in the next section.

Discussion

Interpretation of GD-OES profiles of corroded surfaces and the effect of H

The results presented in section 3 indicate that if H-effect in plasma is correctly taken into account, reliable conclusions about the surface enrichment can be made from qualitative GD OES profiles. Before going to discussion of the H effect, we would note that the use of GD OES with DiP permitted reasonable evaluation of the thickness of corrosion products (100 to 500 nm if the position at 50 % of decrease in O profile is considered as the interface) correlating with lower quantity of corrosion products at higher pH [208].

It seems that for ppm level impurities of Fe, Cu and Al the detection limits in the presence of H should be verified before any consideration of the profile. For alloys with higher content of these impurities one can expect that the H-interferences are less harmful. The use of H₂ containing plasma can solve part of analytical problems. The interpretation of GD-OES profiles of corroded samples for the chemical elements for which the effect of H on the analytical parameters was not previously studied can be completely wrong as demonstrated by both, the theoretical calculation and the experience in Ar-H₂ plasma for Mn. The direct interpretation of the profile obtained in Ar plasma implies the depletion of the corroded surface by Mn while correct interpretation taking into account the H-effect demonstrates Mn enrichment at the interface at neutral pH and in the outer layer at high pH. The use of Ar/H₂ plasma could unlevel the H-content difference between the corroded and uncorroded materials and therefore provide more accurate profiles.

The observed effects are hence important to take into account by corrosion and surface treatment scientists often routinely interpreting the depth profiles obtained in Ar plasma. Without correct analytical treatment, the direct interpretation about the enrichment of the

corroded layer can be just an interference related to the plasma modification by the H sputtered from the hydroxide or the depletion can be an effect of the reduced efficiency.... This justifies deeper analytical work and its presentation for corrosion community.

Reasons of enrichment

Numerous works discuss the surface enrichment of corroding Mg by more noble elements enrichment which is usually explained by selective dissolution of Mg while noble elements form metallic precipitates in the Mg matrix and act as local cathodes [209]. We can't prove or disprove this mechanism by our results but we would like to note that the enrichment and the cathodic activation are different phenomena which have a right to be studied independently. Pre-corroded Mg is more reactive than not pre-corroded even if the pre-corrosion was made in Cl-free solution [10], while enhanced cathodic reactivity of Mg is mainly observed in Cl-containing solutions [32]. The enrichment can hence appear independently from the enhanced cathodic reactivity and later contribute or not to this reactivity. We will focus hence only on the possible reasons of the film enrichment but not on its consequences for the reactivity of Mg.

The fact that Cl-depth distribution looks very homogenous and that the level of Cl incorporated in the corrosion products formed on similar samples immersed in different solutions is independent on the solution pH and on the surface location (in the intact area or in the area with black filaments) correlates well with previously formulated hypothesis [57] that Cl accumulates in the corroded layer but serves as a factor of localized corrosion only if another specific conditions (local pH, grain boundary, local defect in the film, etc.) are satisfied. In this perspective the fact that Na enrichment is significantly higher in the black filament looks interesting. The reason of high Na content could be just because of solution trapped in the pores of the channels under corrosion product. However, it could also be a fact in favor of the intensive cathodic reaction inside the filament [11,64] which favor migration of Na^+ ions to cathodic areas like it was previously proposed for cathodic delamination mechanisms [210]. Concerning the pH effect on Na enrichment, even if Na content is higher in the solution containing both, NaCl and NaOH, than in solution of NaCl, which could explain higher signal at pH 13 than in intact area at pH 6, the concentration is however enough high in both cases. Moreover, the effect from the solution is more expected at the external oxide/solution interface than at the interface oxide/metal. From this perspective, the increase of Na content inside the oxide/hydroxide layer and in particular in its inner part can be also an indication of higher adsorption of Na on the oxide layer than at the hydroxide layer due to lower surface charge. Indeed, at neutral pH the surface of MgO and brucite are expected to be

positively charged [169] and Na^+ should not adsorb, however at high pH both oxide and hydroxide will be charged negatively and this can result in enhanced cation adsorption.

The observed enrichment of the interface metal/oxide by Mn is expected from the values of corrosion potentials of Mg and Mn. The decrease of Mn enrichment at the interface at high pH could be understood from the speculations based on the difference in the solubility of different elements. Indeed, the impurities potential is related with the potential of corroding Mg only if the impurities are galvanically coupled with the matrix. If the matrix around a noble inclusion is dissolved or oxidized, the impurity can lose the electrical contact with it but stay accessible for the solution. In this case the dissolution of the impurity will be governed by its internal reactivity which is supposed to be very high for nanometric particles. Actually, the oxidized ions can be reduced on Mg surface if they can access it easily but the latter is less evident on the porous corrosion products. Fig. 46 illustrates the concentrations of saturated aqueous solutions containing Mg^{2+} , Mn^{2+} , Cu^{2+} and Fe^{2+} (Fe^{3+} being much less soluble than Fe^{2+}) at pH 7-14 and 30 mM CO_2 calculated by HYDRA/MEDUSA software [211].

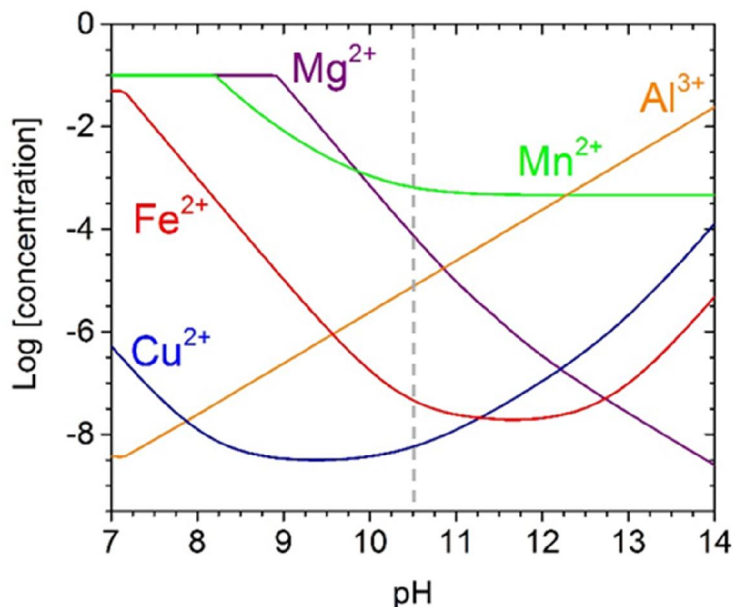


Fig. 46. **Effect of pH on the solubility of different impurities calculated by Hydra/Medusa software.** Mg(II), Mn(II), Fe(II), Al(III) and Cu(II) solution concentrations were considered as 0.1M. Fe(III) is not shown because its solubility is in orders of magnitude lower than the solubility of Fe(II). Complexes used for calculation were $\text{Al}(\text{OH})_2^+$, $\text{Al}(\text{OH})_3$, $\text{Al}(\text{OH})_4^-$, $\text{Al}_2(\text{OH})_2^{4+}$, $\text{Al}_3(\text{OH})_4^{5+}$, AlOH^{2+} , $\text{Al}(\text{OH})_3$, AlOOH , $\text{Cu}(\text{OH})_2$, $\text{Cu}(\text{OH})_3^-$, $\text{Cu}(\text{OH})_4^{2-}$, $\text{Cu}_2(\text{OH})_2^{2+}$, $\text{Cu}_2\text{OH}^{3+}$, $\text{Cu}_3(\text{OH})_4^{2+}$, CuOH^+ , $\text{Cu}(\text{OH})_2$, CuO , $\text{Fe}(\text{OH})_2$, $\text{Fe}(\text{OH})_3^-$, $\text{Fe}(\text{OH})_4^{2-}$, FeOH^+ , $\text{Fe}(\text{OH})_2$, FeAl_2O_4 , $\text{Mg}_4(\text{OH})_4^{4+}$, MgOH^+ , $\text{Mg}(\text{OH})_2$, MgAl_2O_4 , $\text{Mn}(\text{OH})_3^-$, $\text{Mn}(\text{OH})_4^{2-}$, $\text{Mn}_2(\text{OH})_3^+$, OH^- , MgO , $\text{Mn}(\text{OH})_2$.

The surface pH of corroding Mg is expected to approach rapidly pH 10.5 (buffering effect due to $\text{Mg}(\text{OH})_2$ precipitation). At pH 10-11 the solubility concentrations of Fe^{2+} , Fe^{3+}

and Cu^{2+} is much lower than the solubility concentration of Mg^{2+} and they unlikely leave the surface even in an oxidized state. Mn solubility concentration in contrast is high and with pH increase becomes in order of magnitude higher than the solubility concentration of Mg. This could explain the absence of strong Mn enrichment at the interface at high pH.

Conclusions

Despite experimental simplicity, the data interpretation of GD OES profiles of corroded surfaces is not always evident, especially for the estimation of the surface layer enrichment by low content impurities from the metal bulk. The atomic H in plasma, coming from the sample (outer hydroxide layer), can significantly modify not only the sputtering rate but also the detection limits and the emission yield for particular emission lines and cause an ambiguous interpretation of the changes in elements intensities when comparing oxide/hydroxide layers to the metal bulk. The effects of H on the analytical parameters of GD OES, the consequences of these effects for interpretation of depth profiles of corroded surfaces and the way to obtain simply interpretable qualitative profiles are discussed in the work. Thus, the proposed data treatment (H-correction), shows that the apparent Mn depletion is a result of H effect in plasma. The H correction as well as the experiments in Ar/H₂ plasma demonstrated in this condition that the surface was enriched by Mn in studied conditions. GD OES has also demonstrated that the oxide-hydroxide layer is enriched by Cl during immersion in solutions of any pH and in all locations including the areas looking intact and that Na can be accumulated in the oxide film, in particular in black filaments. Working in Ar/H₂ in place of conventional Ar gas can prevent some artefacts related to the different sputtering rate of oxide and metal and significant plasma modifications between these two layers. Unfortunately, detection limit for Fe is significantly degraded in presence of H, thus, it was not possible to confirm the ppm-level enrichment of the oxide film by Fe in Ar/H₂ plasma, however the results of theoretical H-correction taking into account the measured in Ar/H₂ plasma interferences of H signal give a way to evaluate the effect from the result in Ar plasma and limit the situations when the result cannot be interpreted. The results don't contradict the existing hypothesis about Mg incongruent dissolution accompanied by impurity enrichment however also demonstrate that only corrosion potential values are insufficient to predict systematically all the behaviors. Solubility considerations and specific adsorption can help to interpret all the observed enrichment tendencies.

Chapter 7

Inhibition Mechanisms of Mg Corrosion by Selected Carboxylates

The proposed in previous chapters analytical methods (in situ Raman spectroscopy and GD-OES depth profiling) were applied to explore the effect of several organic molecules, namely sodium salts of salicylic, 2,5-pyridine-dicarboxylic and fumaric acids, on the corrosion mechanism of Mg and the resulting corrosion inhibition effects.

(The chapter present the publication in preparation for submission to Corrosion Science)

Introduction

The reactivity of Mg and its alloys has been extensively studied in recent decades due to their potential application in numerous areas from engineering materials to bio-implants and batteries [54,212–220]. However, there is still a lot of questions concerning the mechanism of its reactivity and factors that govern its degradation. One of the most promising methods to protect the metal from corrosion attack is efficient inhibition by additives that could be embedded in conventional surface treatments. The area of Mg inhibition evolves rapidly, numerous inhibition systems are reported regularly [17,18,93,104]. However, there is a lack of a systematization of knowledge in this field. In recent review [17] the known Mg inhibitors were classified by the mechanism of action (anodic/cathodic or mixed type) and by the type of interaction with the substrate (adsorption/precipitation type). However, such a classification may be too general and not sufficient for the choice of a specific inhibitor for a particular application.

Recently, a new inhibition approach for Mg has been proposed by Lamaka et al. [81]. The main idea was based on the suppression of detrimental effect of noble inclusions (mostly, Fe) which are always present in magnesium based engineering materials and can act as local cathodes. Authors assumed that the initial corrosion process leads to the detachment of iron particles from magnesium substrate, and its further self-corrosion occurs with formation of $\text{Fe}^{2+/3+}$. These species can be reduced to metallic iron and re-precipitated on Mg substrate creating local cathodes that causes acceleration of corrosion process [80]. The prevention of the last step due to the complexing of $\text{Fe}^{2+/3+}$ is the general principle of proposed inhibition approach, which has been further extended by testing of more than 150 chemical compounds [18].

Authors reported the high inhibition efficiency of sodium salts of fumaric acid (Fum), pyridinedicarboxylic (PDCA) and derivatives of salicylic (Sal) acid with few exceptions: while PDCA and Fum demonstrated high inhibition efficiency for all tested types of pure Mg, Al- and RE-containing Mg alloys, sodium salicylate inhibited corrosion of Mg alloys and commercial purity Mg (CP-Mg) containing more than 220 ppm of Fe, but it accelerated corrosion of high purity Mg containing 51 ppm of Fe. In cited work, the high inhibition efficiency was explained by Fe-complexing effect but no direct proof was given. All of listed molecules are supposed to form the stable complexes with $\text{Fe}^{2+/3+}$, whereas Sal can complex Mg^{2+} as well. Thus, in case of HP-Mg, the positive effect of iron complexing was offset by accelerated Mg dissolution.

It should be noted that the apparent Fe-complexing effect may be not the only one key factor defining the inhibition efficiency. Thus, another authors [17,98,101] reported the positive inhibition efficiency of the molecules containing the aromatic ring and heteroatoms, such S or N. This positive effect was attributed to adsorption mechanisms due to the electron-donor properties of conjugated π -system or heteroatom. From the other side, additives in the solution could influence the $\text{Mg}(\text{OH})_2$ precipitation, changing the ratio between nucleation and crystal growth rate [221], and as a consequence the crystal size [175]. This aspect also can affect the protective properties of the film. Therefore, this article aims to verify hypotheses about the mechanism of the inhibition of Mg corrosion by sodium salts of salicylic, 2,5-pyridinedicarboxylic and fumaric acids in aqueous environment containing Cl^- . Particularly, hypotheses of Fe-complexing, physical or chemical adsorption on Mg surface [30] are considered. Surface analysis techniques such as in situ Kinetic Raman Microscopy (KRM), Attenuated Total Reflectance Fourier-Transform Infrared Spectroscopy (ATR-FTIR), Glow Discharge Optical Emission Spectroscopy (GD OES) are used in this work to estimate influence of inhibitors on the film evolution: growth kinetics, chemical composition, morphology.

Experimental details

Materials and reagents

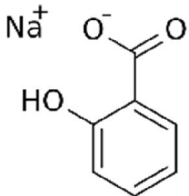
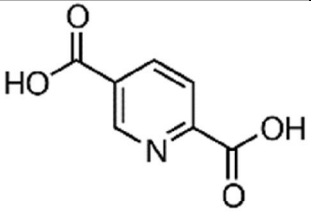
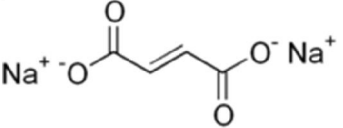
As-cast commercial purity magnesium (CP-Mg342) and high purity magnesium (HP-Mg51) were produced by Helmholtz Centrum Geestacht. The average elemental compositions determined by Spark OES (Spark analyser M9, Spectro Ametek, Germany) is presented in Table 4. Mg pieces were grinded with 800, 1200, 2400, 4000 SiC grinding paper, using ethanol as a lubricant, rinsed with ethanol and dried by compressed air.

In this work the solutions of 0.1M NaCl with and without inhibitors were studied. All electrolytes were prepared using analytical grade reagents (Sigma Aldrich) and Millipore water. The list of chemicals tested in this study is shown in Table 5. Amount of reagents necessary to prepare 0.05 M solution was added to 0.1 M NaCl solution and stirred until complete dissolution. The initial pH of sodium salicylate and fumarate were 5.3 and 6.7 respectively; PDCA was used in acidic form, thus initial pH was adjusted by NaOH to the value of 5.5.

Table 4. Chemical composition of pure Mg and alloys as analysed by spark optical emission spectroscopy. The values are in ppm or in wt. % when indicated.

	Mg	Ag	Al	Ca	Ce	Cu	Fe	La	Mn	Ni	Pb	Si	Sn	Zn	Zr
CP Mg342	99.96%	<0.5	40	<1	7	4	342	<5	24	<2	<4	<1	<3	5	<5
HP Mg51	99.98%	0.7	50	<1	<4	<1	51	<5	8	<2	<4	<1	<3	10	23

Table 5. Organic compounds studied in present work. The tests were performed with Na salts at the initial pH of the electrolyte from 5.3 to 6.7

Name	Abbreviation in article	Structural formula
Sodium Salicylate	Sal	
2,5 – Pyridine-dicarboxylic acid	PDCA	
Sodium Fumarate	Fum	

Raman spectroscopy

Ex situ Raman spectra were recorded on Renishaw Confocal Raman Microscope (CRM), using the green laser (doubled Nd:YAG, 532 nm) with power of 50 mW. Illumination and detection were performed through a microscope objective Leica of $\times 50$ magnification and numerical aperture (NA) of 0.75 with exposure time of 10 sec. Objectives with $\times 5$ and $\times 20$ magnification were used to make the optical images of the sample surface. In situ measurements were performed with Leica long working distance objective ($\times 50$, NA = 0.5).

The detailed procedure of in situ measurements and data treatment is described in Chapter 5. Shortly, a freshly prepared Mg sample was mounted in a flow cell with the glass optical window. Immersed area was 3.14 cm², the distance between the sample surface and the optical glass window was about 1 mm. In order to remove the bubbles from the corroded surface, which disturb the laser focus and hamper the in situ measurements, 25 ml of studied solution was looped, flowing through the cell with the rate of 5 ml/min. Raman mapping was performed every 7-10 minutes during 2 hours on the areas of 100×100 μm with the step of 10 μm. Two series of Raman spectra were recorded: in range of 100 - 1800 cm⁻¹ and 2500 – 3800 cm⁻¹. Exposure time was 0.2 sec for each location on the surface, the total time of each map recording was about 2 minutes.

Attenuated Total Reflectance Fourier-Transform Infrared Spectroscopy (ATR-FTIR)

Infrared spectra were measured with a Thermo Scientific Nicolet 6700 FTIR spectrometer equipped with a mercury cadmium telluride detector cooled at 77 K by liquid nitrogen. Spectral resolution was 4 cm⁻¹, and spectra were averaged from 256 scans. The ATR accessory was a horizontal ZnSe crystal coated with diamond (A = 2.54 mm²) with single reflection and an angle of incidence of 45° (Smart Miracle from PIKE). OMNIC software was used for the data collection and treatment. The ex-situ ATR spectra were collected in dry and in wet conditions. In the latest case the electrolyte spectra was used as a background.

Glow Discharge Optical Emission Spectroscopy (GD OES)

GD-OES analysis was performed with a GD-Profiler 2 (HORIBA Jobin Yvon) using Quantum software. The instrument configuration included a pulsed radiofrequency (RF) generator, a standard HJY glow discharge source with an anode of 4 mm internal diameter and an automatic impedance matching system between the RF generator and the GD source. Mixture of Ar with 10000 ppm of H₂ was prepared by Air Liquide and used as the discharge gas. The optical system was purged by high purity N₂ in order to detect emission lines in the VUV region. The Differential interferometry Profiling (DiP) system integrated in the instrument allowed in addition a direct depth measurement along with the elemental depth profile analysis. Elemental depth profiling was performed under Ar/H₂ pressure of 750 Pa and a power of 17 W. The used spectral wavelengths were: Mg - 285.217 nm, C - 156.149 nm, Cl - 134.730 nm and O 130.223 nm.

Results

Visual observation

Fig. 47 illustrates the difference in appearance of corroded surface of CP-Mg342 and HP-Mg 51 samples after 2 hours of immersion with and without the inhibitors. For CP-Mg 342, it is clear that the surface is more attacked on the sample immersed without inhibitors: the image with higher magnifications reveals the filiform-like corrosion, which looks like the black threads of about 10 μm width. The surface immersed in solutions containing the inhibitors has different color in comparison with the non-immersed area, however no filament was detected after 2 hours that suggests a partial corrosion protection. Round spots, presented even on just-polished surface, were the source of gas evolution during the immersion test. These spots could increase in diameter with time, but no filaments originated from those locations.

For HP-Mg 51, no filaments were observed in any case, at least for 2h of immersion. In presence of fumarate and 2,5-pyridin-dicarboxylate the surface looked similar to the surface of CP-Mg 342. In presence of salicylate, gas evolution was very intensive during the whole experiment, the surface looked etched, the grain boundaries became visible.

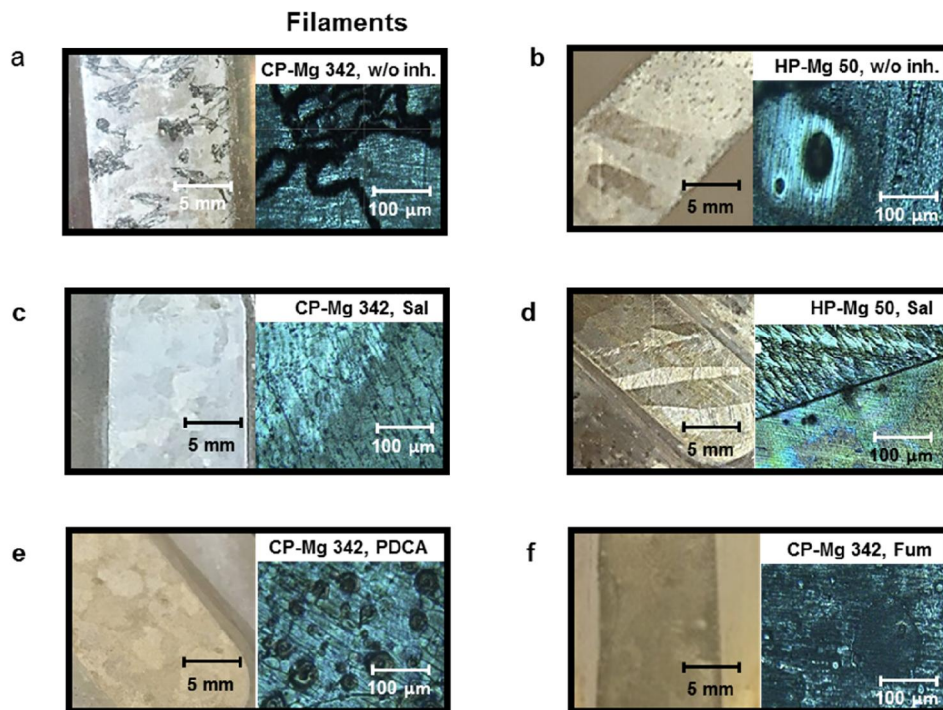


Fig. 47. Corroded CP-Mg342 and HP-Mg51 after 2h of immersion in 0.1 M NaCl solution (a,b) and with addition of 0.05 M inhibitors: sodium salicylate (c, d), 2,5-pyridin-dicarboxylate (e) and fumarate (f).

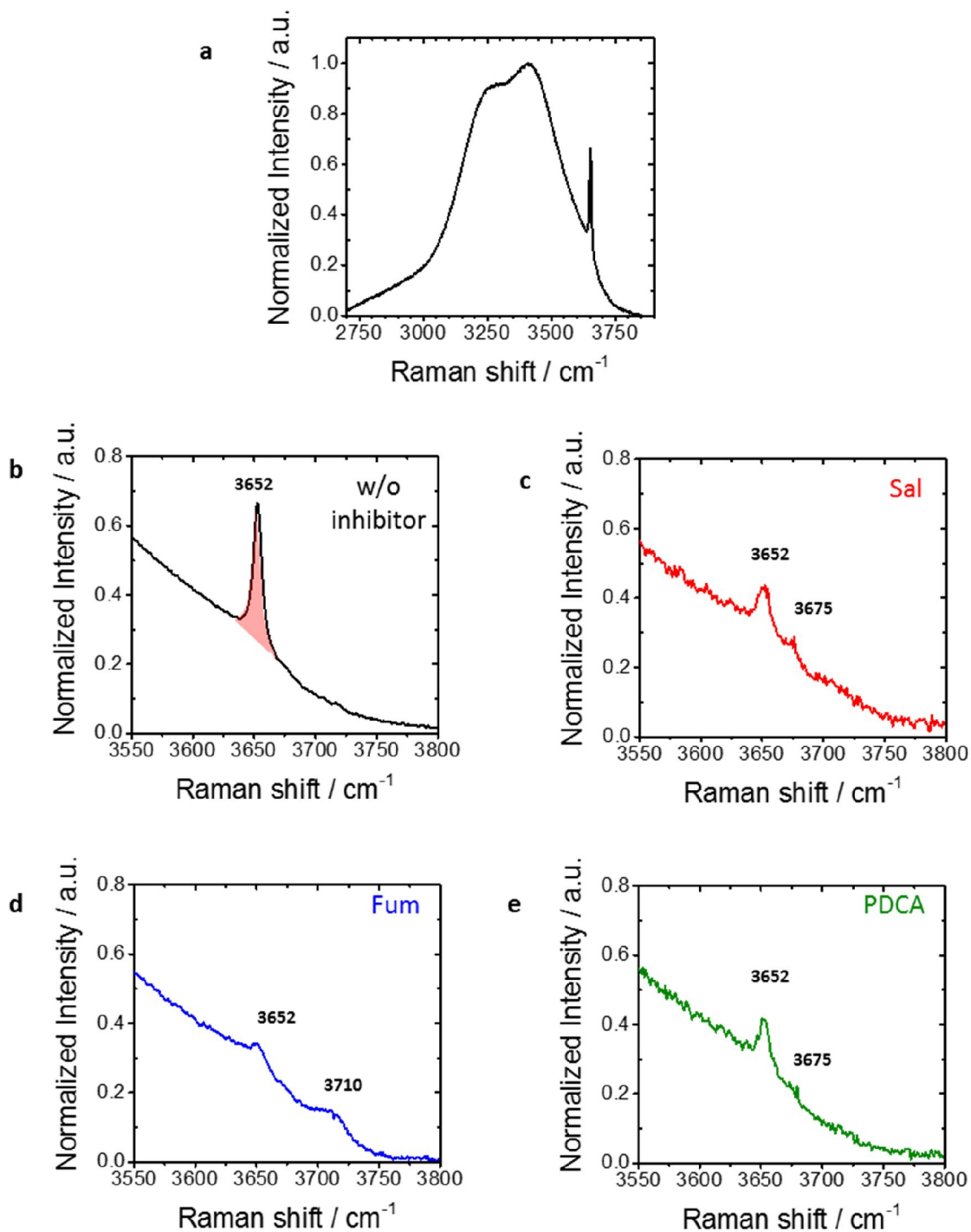


Fig. 48. (a) In situ Raman spectra in range of 2700 – 3900 cm⁻¹ recorded on CP-Mg342 in 0.1M NaCl after 2h of immersion. Zoomed Raman spectra in range of 3500 – 3800 cm⁻¹ in absence (b) and in presence of inhibitors (c-e).

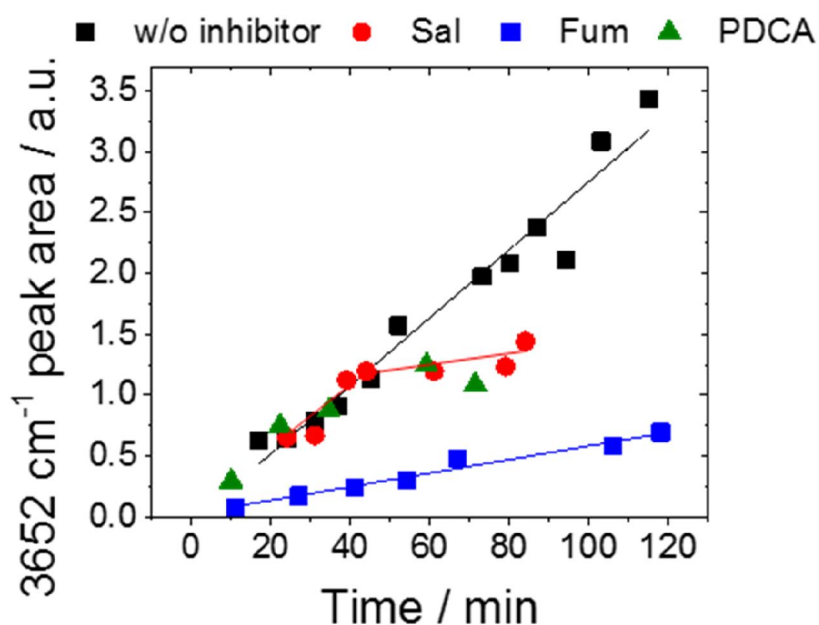


Fig. 49. Growth kinetics of $\text{Mg}(\text{OH})_2$ in 0.1 M NaCl in presence and absence of 0.05M inhibitors

$\text{Mg}(\text{OH})_2$ growth kinetics was estimated by the evolution of $\text{Mg}(\text{OH})_2$ bulk signal (3652 cm^{-1} peak area). The detailed data treatment was described in Chapter 5. Shortly, after the standard procedure of preprocessing, spectra were normalized so that the baseline corresponded to 0 and the maximum of water band (3415 cm^{-1}) corresponded to 1. The peak area was calculated as it is shown on Fig. 48b – the shaded zone between the spectrum and the line passing through 2 points on the spectrum with the abscissa 3640 and 3665 cm^{-1} . As it was described in the experimental section, the kinetics data were collected from 100 locations on the surface. Since the zone with homogeneous growth (without black filaments) was studied, the kinetics curves demonstrated the same tendency in all the locations, thus only one representative kinetics curve for each experiment is shown on Fig. 49. In absence of inhibitor, $\text{Mg}(\text{OH})_2$ growth is fitted by linear law, the growth rate is much higher than in the presence of inhibitors that is obvious from the graphs slope. Curiously, the growth tendency differs for selected inhibitors, thus, with sodium salicylate and 2,5-pyridine-dicarboxylate $\text{Mg}(\text{OH})_2$ the growth rate is the same as without inhibitors at the beginning of experiment, then after about 40 minutes it decreases notably, whereas in presence of fumarate the growth rate is lower from the very beginning of experiment. This implies the existence of an induction period for salicylate and 2,5-pyridine-dicarboxylate inhibition.

In-situ Raman spectra in the range of $750 - 1750 \text{ cm}^{-1}$ show the signal from organic inhibitors themselves (Fig. 50). In situ Raman spectra recorded on Mg samples in presence of

2.5-pyridin-dicarboxylate and fumarate solutions didn't reveal any difference as compared with spectra of inhibitors solutions (only CP-Mg342 results are shown on Fig. 50).

During the experiment in PDCA solution, the intense background was growing so that the Raman signals were impossible to observe in the end of experiment. For salicylate, the marked shifts in peak positions were discovered for CP-Mg342 compare to salicylate solution and in situ spectra on HP-Mg51, indicating the chemical interaction with the surface of CP-Mg342.

In order to understand the origin of these shifts and verify the hypothesis about the role of interaction of salicylate with Fe-containing particles, we compared in situ Raman and IR spectra (in case of IR spectra, we compared the spectra recorded on wet Mg sample just after immersion of CP-Mg342 with the synthesized reference samples). For references, we also used the wet powders of Mg(OH)_2 , Fe(OH)_3 , specially precipitated in presence of Cl^- and salicylate from the corresponding chlorides by addition of NaOH and the solution of Fe(III) complex with salicylate, as well as carbon steel immersed in salicylate solution for 2 hours. For salicylate containing conditions a lot of similarities were found for the spectra of Mg(OH)_2 and FeSal complex, as it is shown on Fig. 51, Fig. 52). Most of the peaks position on CP-Mg342 coincide with salicylate adsorbed on precipitated Mg(OH)_2 , but some of the peaks were still shifted and have the positions matching with the positions corresponding to the most intensive peaks of Fe(III)Sal complex. Detailed peaks positions and assignments are presented in Table 6.

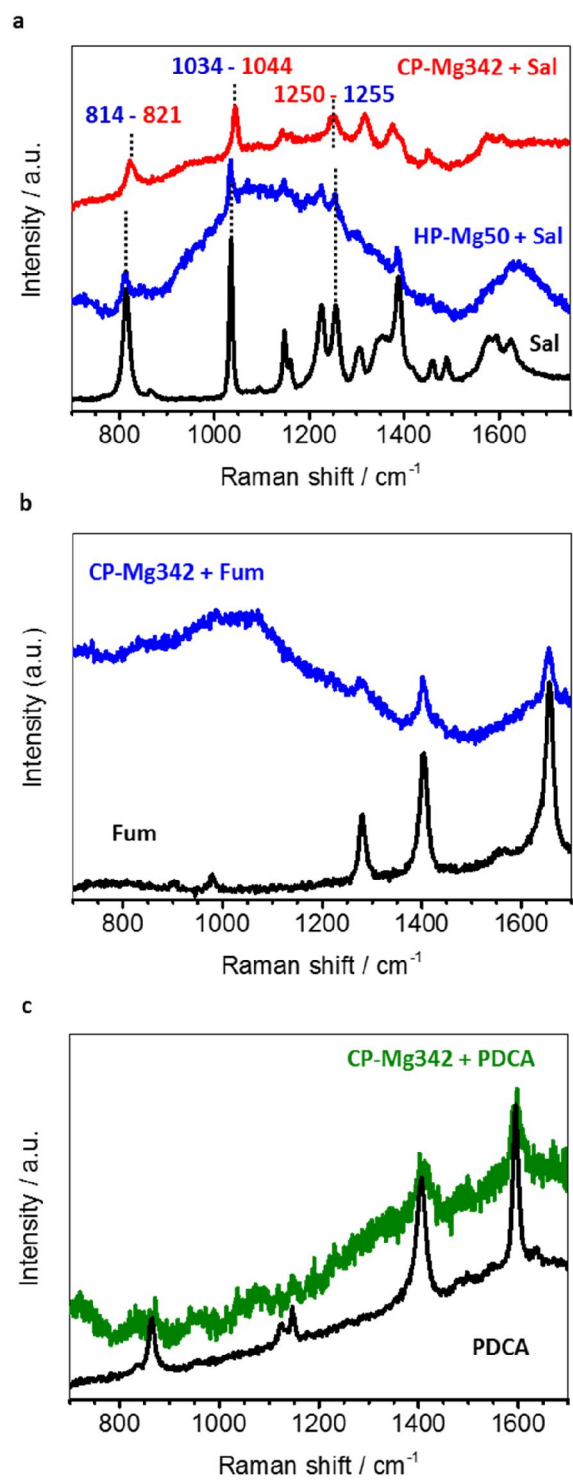


Fig. 50. Comparison of in-situ Raman spectra recorded in presence of 0.05 M inhibitors solutions with the in-situ spectra of concentrated inhibitor solutions: (a) CP-Mg342 and HP-Mg51 in salicylate, (b) CP-Mg342 in fumarate, (c) CP-Mg342 in 2,5-pyridine-dicarboxylate.

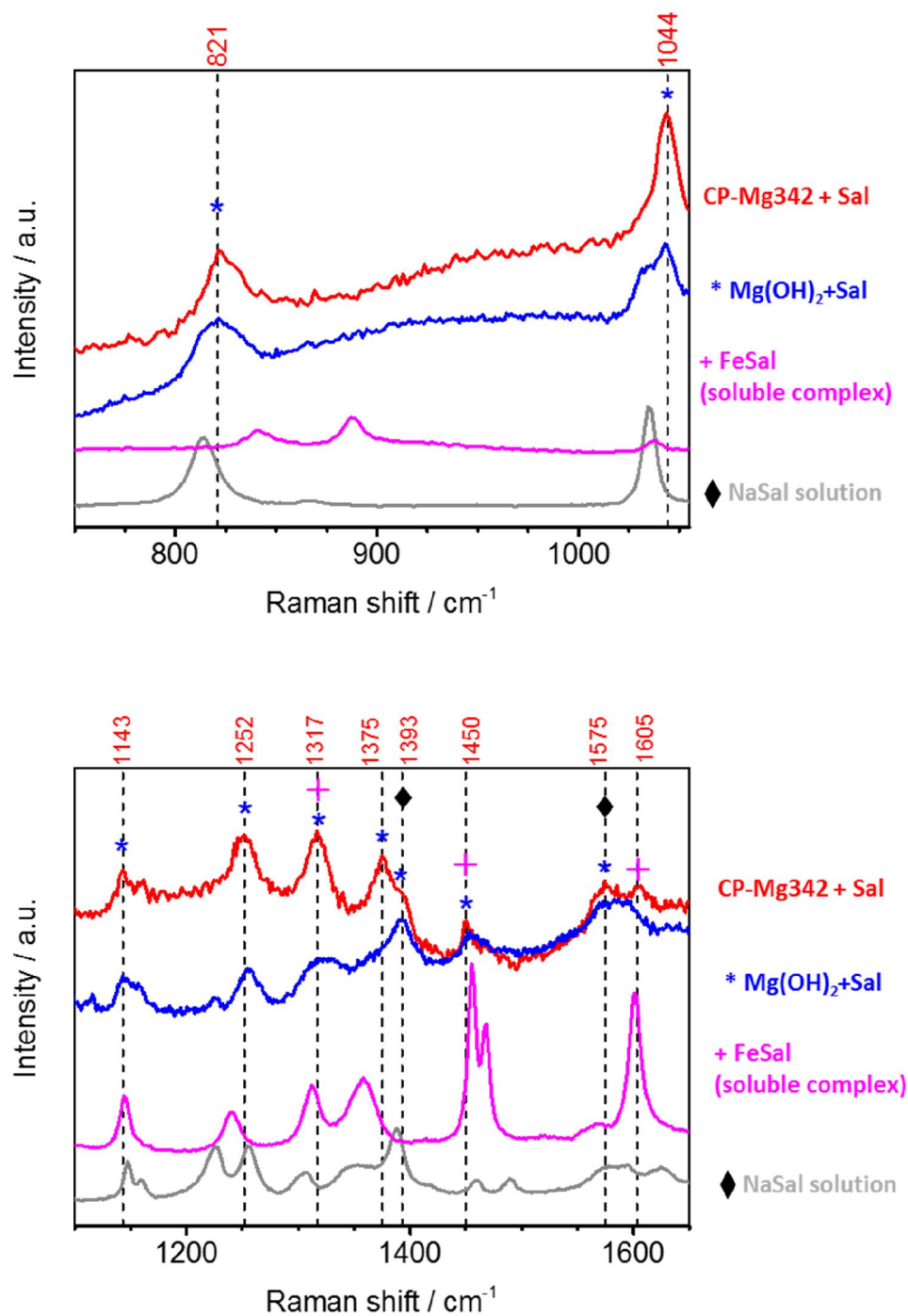


Fig. 51. In situ Raman spectra recorded on CP-Mg342 immersed in solution containing 0.05 M NaSal, (*) precipitated in presence of Sal Mg(OH)₂, (+) Fe(III) Sal solution, (◆) NaSal solution.

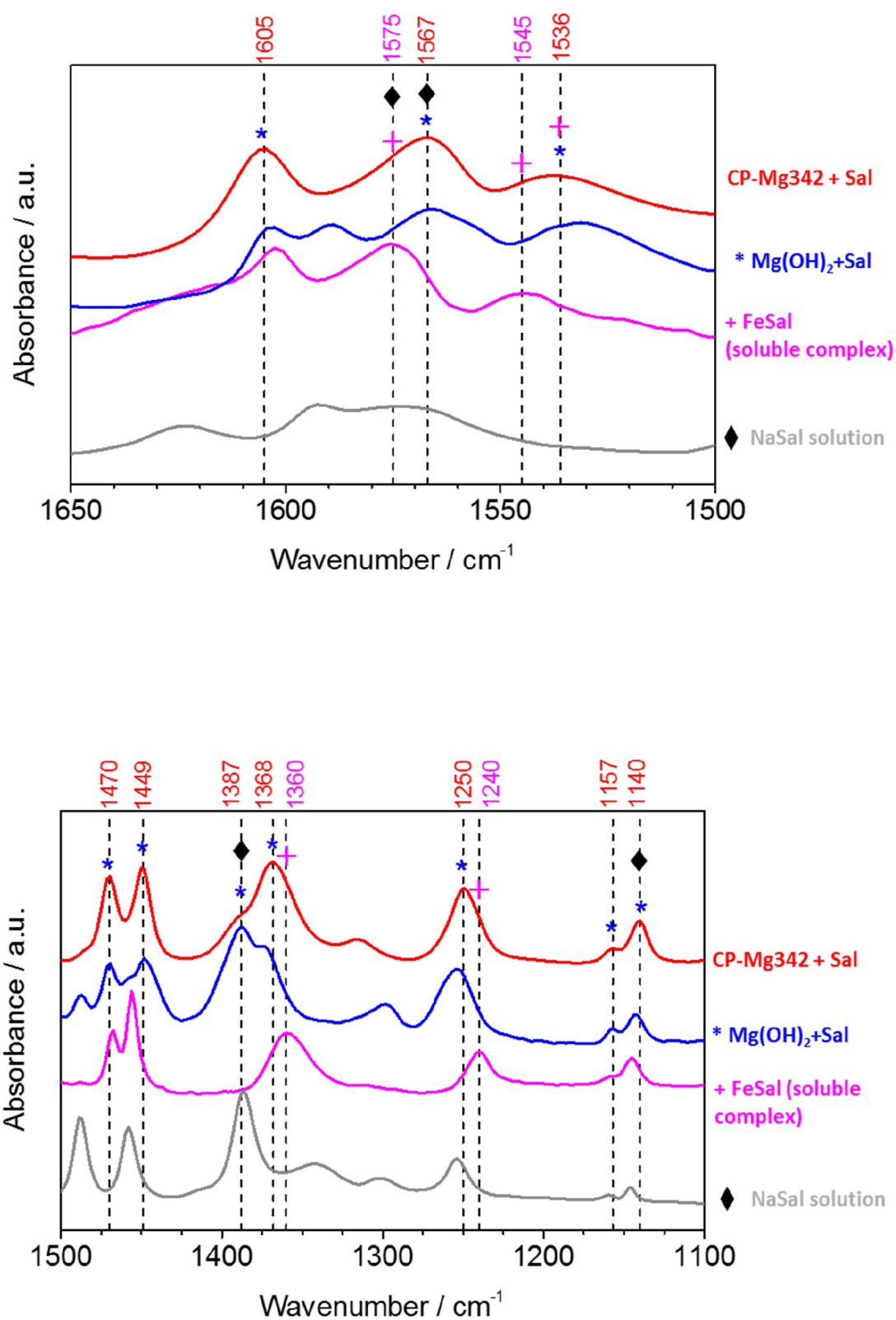


Fig. 52. IR spectra recorded on wet CP-Mg342 just after 2h immersion in solution containing 0.05 M NaSal; (*) precipitated in presence of Sal Mg(OH)₂, (+) Fe(III) Sal solution, (♦) NaSal solution.

Table 6. IR and Raman spectral data (cm⁻¹) and band assignments for NaSal solution, CP-Mg342 immersed in NaSal solution, precipitated in presence of NaSal Mg(OH)₂, soluble complex of Fe(III)Sal.

Sal Solution		CP-Mg342 surface + Sal		Mg(OH) ₂ + Sal		Fe(III)Sal		Assignment [106,223–228]
IR	Raman	IR	Raman	IR	Raman	IR	Raman	
1624, 1592	1625, 1595	1605	1605	1603, 1589	1595, br	1602	1601	v _{8b} + v(C=O)+δ(C _φ -OH)
1572	1574, br	1567 br	1575, br	1565, br	1575	1574		v (C-C) ring or v _{as} (COO ⁻)
-	-	1536, br	-	1531, br	-	1544		v _{as} (COO ⁻)
1489	1489	1470	1470, sh			1467	1468	C-C ring, (19a)
1457	1460	1449	1450	1447, s	1453, m	1455	1455	C-C ring or δ(OH)
1387	1387	1387, sh	1393, sh	1388	1392	1359	1350, s	v _s (COO ⁻)
1342	1347, br	1368, br	1375, s	1373, sh	1376, sh			v _s (COO ⁻)+ δ C _{ph} -O
1300, sh	1306	1309, br	1317, s		1317, s, br		1312, s	v (C-C) ring, 14
1254	1256	1250	1252	1254	1255	1242	1240 ,m	v (C _φ -O)
-	1225	-	-					δCH
1159	1160, vw	1157, vw	1160, vw				-	
1147	1147	1140	1143, m			1146	1144	δCC (10)
1033	1034	1045, s	1044, s	1041	1043, br		1037, vw	δCH
861	867, w	877	-	872		887	886	
810	814, s	818	821		821		840	v (C _φ -COO ⁻)+ (C _φ - OH)+δ _s (COO ⁻)

v- very; *s*-strong; *m*- medium, *w*- weak; *sh*- shoulder; *br*- broad.

v indicates a stretching mode, *δ* an in-plane bending mode

(+) in-phase movement; (-) out-of-phase movement;

C_φ – carbon of the aromatic ring

Fig. 53 shows IR spectra recorded on CP-Mg342 after immersion in NaPDC solution. It demonstrates some differences compare to spectrum of NaPDC solution (see Table 7): band

at 1724 cm^{-1} , attributed to C=O stretching vibration appears on spectra of dry sample; bands in range of 1580 – 1610 cm^{-1} attributed to asymmetric stretching modes of COO^- groups [229,230] are shifted. Nevertheless, position of symmetric modes of COO^- (stretching at 1362 and 1385, bending at 826 cm^{-1}) remains the same. Bending mode of aromatic system (1030 cm^{-1}) is shifted towards higher wavenumbers compare to solution spectrum.

Table 7. IR spectral data (cm^{-1}) and band assignments for NaPDC solution, CP-Mg342 immersed in NaPDC solution.

NaPDC Solution	CP-Mg342 surface + PDC	Assignment[229–232]
-	1724	$\nu\text{C=O}$
1652	1607	$\nu_{\text{as}}(\text{COO}^-)$
1581, br	1589	$\nu_{\text{as}}(\text{COO}^-)$; $\nu\text{CC ring} + \nu\text{CN} + \delta\text{CCH} + \delta\text{CNH}$
1480	1480, sh	$\nu(\text{CN}) + \delta\text{CCH} + \nu(\text{C-O})$
	1457, sh	$\nu_{\text{s}}(\text{COO}^-)$
1385, vs	1385, vs	$\nu_{\text{s}}(\text{COO}^-)$
1362	1362	$\nu_{\text{s}}(\text{COO}^-)$
1278	1278	$\nu\text{C-O} + \nu\text{CC ring} + \nu\text{CN}$
1178	1178	$\delta(\text{CC}) + \nu(\text{CC}) + \delta(\text{CH})$
1121	1121	
1030	1036	$\nu\text{CC ring} + \nu\text{CN} + \delta\text{CCH}$
826	826, vw	$\delta_{\text{s}}(\text{COO}^-)$

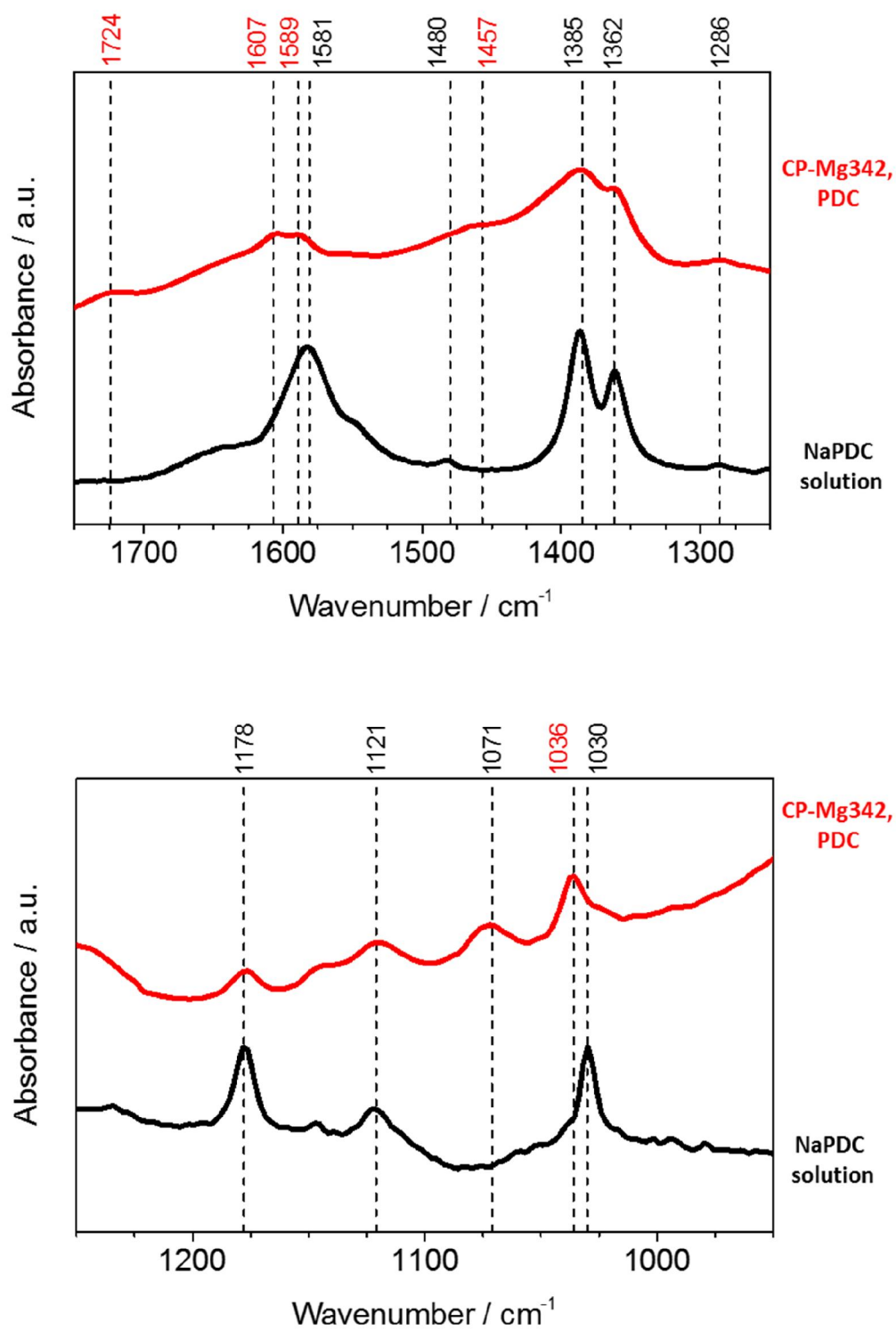


Fig. 53 IR spectra of dry CP-Mg342 sample after immersion in solutions containing 0.05 M of 2,5-pyridin-dicarboxylate (NaPDC) and Na PDC solution.

Depth profiling

Fig. 54 illustrates the elemental depth profiles of CP-Mg342 corroded in absence and in presence of the inhibitors. Generally, they demonstrate the oxide/hydroxide layer, with the interface defined as decrease of oxygen and increase of magnesium signal. For the blank solution, we had to reduce the immersion time in order to avoid the formation of rough surface, which is not suitable for GD OES analysis; therefore, the oxide/hydroxide layer seems thinner than for the other samples. The thickness of the oxide layer formed during 2 hours of the immersion in the solutions containing the inhibitors correlates well with the kinetics data obtained by in situ Raman spectroscopy: the oxide layer for fumarate is the thinnest.

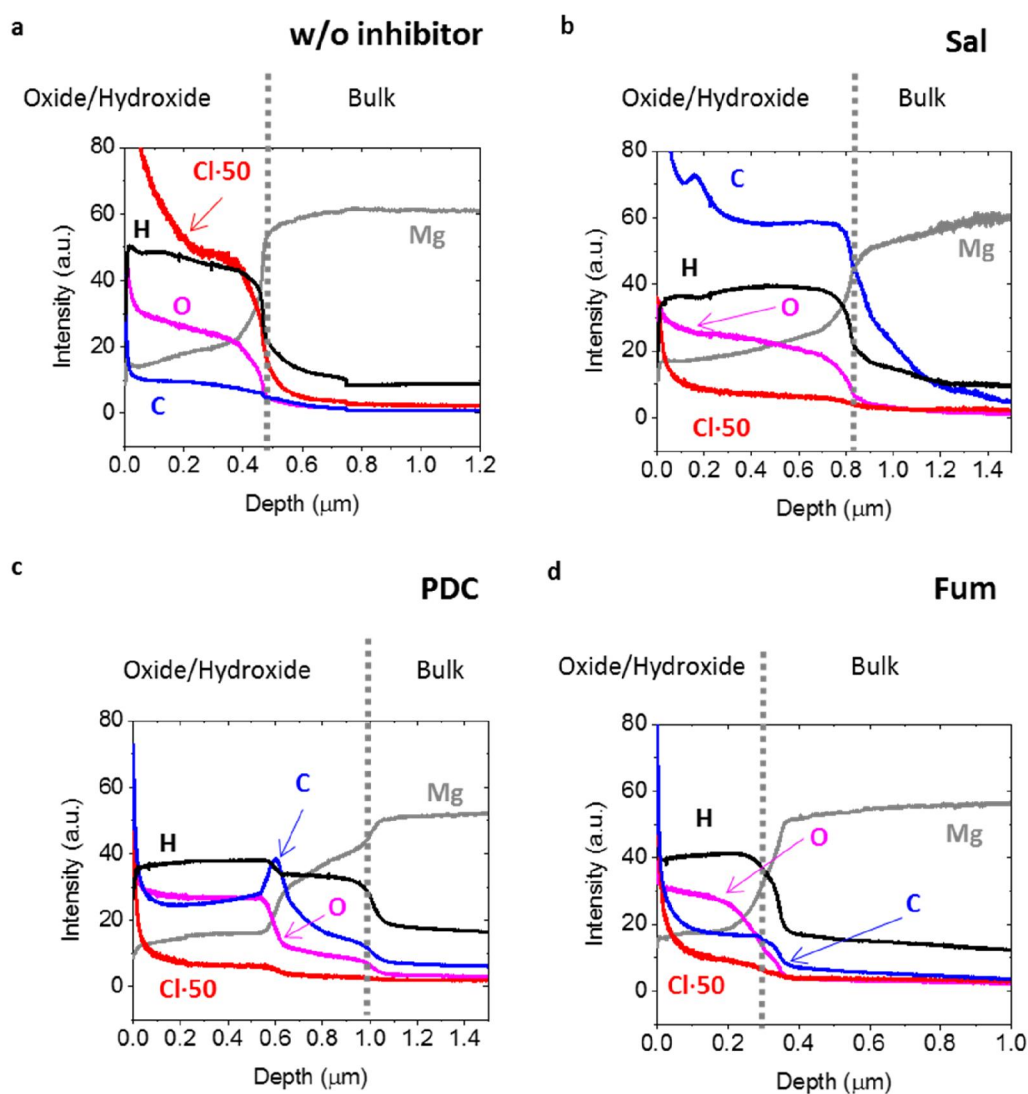


Fig. 54. Qualitative depth profiles of CP-Mg342 immersed in 0.1M NaCl solution in absence (a) and in presence of inhibitors: (b) – NaSal, (c) PDC, (d) Fum

It should be noted that the intensity of any element does not provide the information about its mass without a calibration procedure. However, for our purposes it is enough to compare the profiles of the similar samples and estimate the preferential presence of each element qualitatively. Taking into account that the intensity of Mg as the principal element is similar within the oxide layer (and in the bulk) for all the samples, we can compare the intensity of other elements between the samples. H signal cannot be used for semi-quantitative analysis in this case, because the discharge gas contained 1 % of H₂ in order to minimize the effect of H variation in plasma on the analytical parameters of GD OES (Chapter 4).

It is clear from the Figure that without inhibitors the oxide/hydroxide layer is enriched by Cl. Depth profiles of the samples with inhibitors demonstrate carbon enrichment in the oxide layer that indicates the presence of organic molecules in the surface film. Interesting that for salicylate the carbon level is much higher compared to other inhibitors. For 2,5-pyridin-dicarboxylate it seems that the two different layers exist: O and Mg signals are evolving in two steps. Probably it corresponds to the well-defined oxide and hydroxide layers. Carbon signal reaches the maximum exactly on the interface between these two layers.

Discussion

It is commonly accepted that Mg reactivity strongly depends on two factors: barrier properties of the surface film and distribution of more noble impurities in Mg matrix. Both factors are illustrated schematically in Fig. 55. In regards with the surface film itself, crystal morphology and size play an important role in barrier protection: access of water and diffusion of aggressive species to the metal substrate through the layer consisting of the large crystals with low surface area is supposed to be easier than in case of the compact layer. Thus, Raman spectra showing formation of big crystals (the band of bulk –OH groups at 3652 cm⁻¹ was much more intensive compared to bands of surface –OH groups at 3675 and 3710 cm⁻¹) and GD OES depth profiles demonstrating the Cl accumulation within the surface film, formed in blank solution, are coherent with the high reactivity of Mg in these conditions.

The second factor playing an important role in Mg reactivity – presence of Fe-rich inclusions in Mg matrix. Influence of Fe content is obvious from difference in corrosion rate for HP-Mg51 and CP-Mg342 containing 51 and 342 ppm of Fe respectively, that was reported previously [18] and was visible in this work on the photos of corroded samples **Error! Reference source not found.** Role of more noble inclusions is usually associated with the

formation of microgalvanic cell between inclusion and Mg, where inclusion act as a local cathode, accelerating H_2 evolution and material degradation rate.

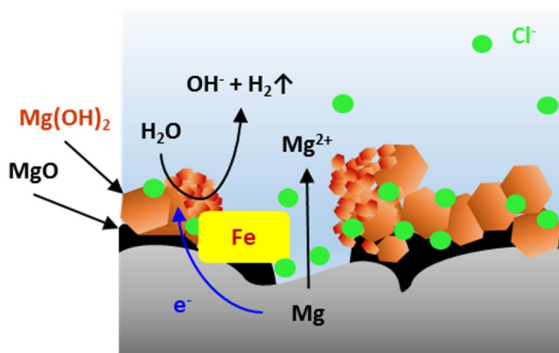


Fig. 55. Schematic representation of Mg reactivity in NaCl solution.

It is obvious from Raman spectra in range of -OH vibrations that addition of all inhibitors leads to formation of $Mg(OH)_2$ films with smaller crystals and high surface area, which limits the access of Cl^- to the interface, that was evidenced by GD OES profiles. However, the reason of such an effect, most probably, is different, according to other results (shifts of peaks position in Raman and IR spectra, $Mg(OH)_2$ growth kinetics, appearance of GD OES profile).

Thus, further discussion of inhibition mechanisms will be based on explanation of such a behavior and attribution of each inhibitor to “Fe-complexing”, “adsorption” (chemical or physical) or “precipitation” type.

Sodium salicylate (Sal)

It is likely that the inhibition efficiency of Sal is explained by both Fe-complexing and stabilization of $Mg(OH)_2$ nano-crystals due to the strong chemical interaction with the surface.

First of all, the accumulation of Sal molecules on corroded surface of CP-Mg342 sample was concluded from the high C signal in GD OES depth profile, which was significantly higher than for others inhibitors. The origin of this accumulation can be assigned as chemical interaction according to Raman and IR spectra of CP-Mg342 sample immersed in Sal solution. They revealed significant shifts in bands position as compared with Sal solution spectra, suggesting the modification of Sal molecule geometry caused by strong interactions and formation of covalent bonds between Sal and the sample. According to the shifts of COO^- ($1603, 1567, 1536, 1387, 818\text{ cm}^{-1}$) and $-OH$ (1250 cm^{-1}) bands, both of these groups participate in the interaction [106]. Comparison with the reference samples demonstrated that the most of the peaks shifts can be explained by the interaction with

Mg(OH)₂. Sal is known as an agent stabilizing the nano-particles of metals oxides or hydroxides due to the adsorption on their surface [233]. Thus, it is very probable that the inhibition efficiency of salicylate is related to the stabilization of nano-crystals of Mg(OH)₂.

Nevertheless, several shifts in spectra (1605, 1450, broad peak at 1317 for Raman spectra and broad band at 1575, 1545 shoulder, 1360 cm⁻¹ for IR spectra) were different from those observed on Mg(OH)₂. The apparent position shift of peaks maximums in many cases of vibrational studies can be explained by assuming two distinct species with fixed absorption frequencies, which vary only their population and consequently their relative intensities. This kind of spectral fluctuations can be caused by the effect of temperature or concentration [234,235]. In our case, all the measurements were done on the same instrument, at equal temperature. The effect of concentration can eventually take place, cause the surface area (area of adsorption sites) of precipitated Mg(OH)₂ might be not the same as on corroded Mg sample.

Alternative explanation of the shifts as compared with precipitated Mg(OH)₂ can be related to the presence of Fe(III) complex in the surface layer, given that the shifts coincide well with the most intensive characteristic peaks of Fe(III)Sal soluble complex (Fig. 51, Fig. 52). This suggests that besides the stabilization of Mg(OH)₂ nano-crystals, Sal inhibition efficiency can be related to the binding of Fe ions coming from dissolution of detached from Mg substrate Fe-rich particles. This prevents iron re-deposition and inhibits cathodic reaction. This mechanism is in agreement with the data reported in literature [30], suggesting the cathodic type of inhibition by Sal, as well as with the absence of the inhibiting effect on Mg-HP51 sample.

Kinetics of Mg(OH)₂ growth on CP-Mg342 in presence of Sal is described by a two steps trend: the first 40 minutes it evolves like in solution without inhibitor, and then the growth rate of Mg(OH)₂ slows down. Probably, the first 40 minutes are needed to dissolve the Fe-containing particles and stabilize pH that is suitable for the formation of Mg(OH)₂ particles with well-developed surface, so that, the inhibition effect of Sal starts only after this “induction period”.

The fact that Sal inhibits CP-Mg342 corrosion and accelerate degradation of HP-Mg51 can be explained by both factors: Fe content and initial reactivity. Sal can form stable complexes with Fe and Mg [18]. In case of HP-Mg51 with lower Fe content, the positive effect of iron complexing is offset by accelerated Mg dissolution. Another explanation is that the initial HP-Mg51 dissolution rate in 0.1 M NaCl solution is lower than the initial CP-Mg342 dissolution rate, so that the ratio between [Mg²⁺], [OH⁻] and [Sal] concentrations in the initial stage is different for these two types of Mg. In case of HP-Mg5, [Sal] is in excess compare to [OH⁻], this causes preferential formation of MgSal soluble complex, that

accelerates corrosion rate. In case of CP-Mg342, due to the high reactivity at very beginning of immersion, excess of $[\text{OH}^-]$ goes to the surface, that leads to the precipitation of $\text{Mg}(\text{OH})_2$ and its further stabilization by Sal adsorption.

To sum up, proposed inhibition mechanism by Sal includes both suppression of Fe-redeposition and stabilizing of $\text{Mg}(\text{OH})_2$ particles (Fig. 56).

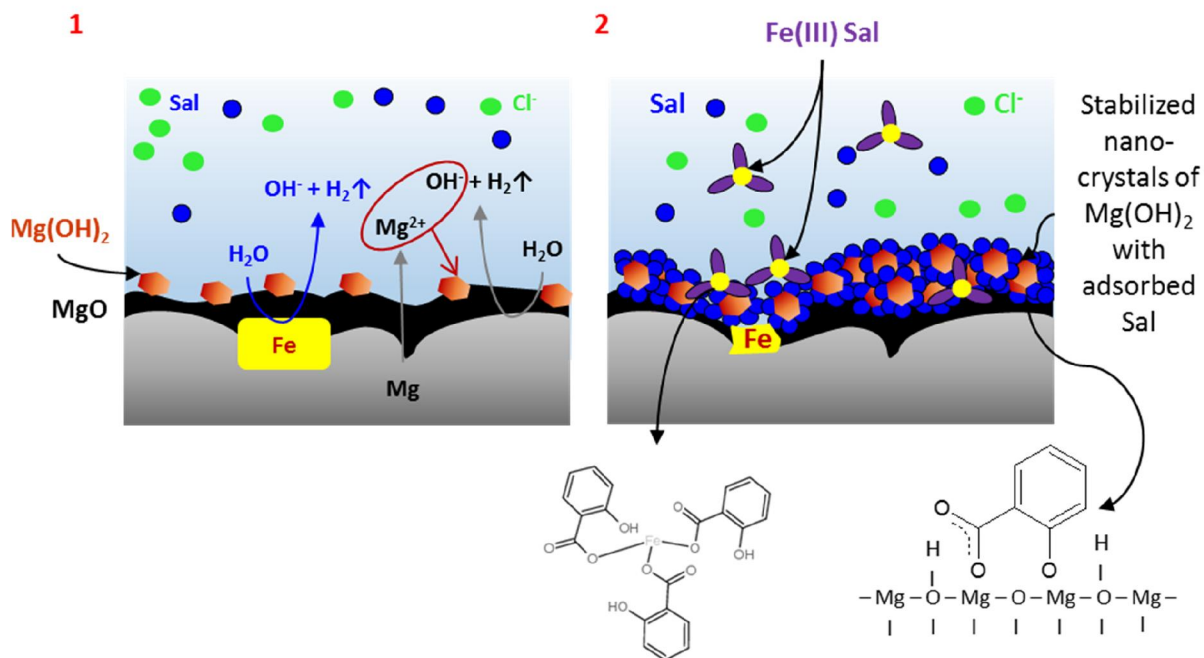


Fig. 56. Schematic representation of Sal inhibition mechanism: 1- initial stage (the first 40 minutes of immersion), 2-dissolution of Fe-rich inclusions and stabilization of $\text{Mg}(\text{OH})_2$ nano-crystals.

2,5-pyridinedicarboxylate (PDC)

Precipitation of coordination polymer consisted of long chains of with PDC molecules bonded due to the electrostatic interaction with metal cations is the possible explanation of Mg corrosion inhibition by PDC (Fig. 57).

Firstly, GD-OES profile differs significantly from those of other inhibitors. During the sputtering of the oxide/hydroxide layer, intensities of all elements evolve in two steps. This could be explained by formation of two layers with different sputtering rate. Probably, it corresponds to well defined $\text{Mg}(\text{OH})_2$ and MgO layers. Carbon intensity reaches the maximum on the interface between these two layers, suggesting the enhanced accumulation of PDC molecules there.

Secondly, the high fluorescence background appears after “induction period”. PDC molecule itself does not provide fluorescence background. However, formation of a specific network of the organic molecules which contains a chain of alternating double and single

bonds, called conjugation, or π -electron delocalization can cause fluorescence [29,236]. It was reported that PDC can form so-called coordination polymer with different dimensionality, consisting of the long chains of PDC molecules bonded due to the electrostatic interaction with metal ions [236–238]. Many of reported coordination polymers has fluorescent properties [236,239,240].

Analysis of IR spectra demonstrated that bands of carboxylates (COO^-) were shifted compared to the solution spectra ($1607 - \nu_{\text{as}}$, $1457 - \nu_{\text{s}}$ [232]). Band at 1724 corresponding to $\text{C}=\text{O}$ stretching of COOH , is absent in the PDC solution spectrum and appears in the spectrum of Mg sample, suggesting that carboxylates are partly deprotonated. $\nu(\text{C}=\text{C})$ and $\nu(\text{C}=\text{N})$ vibrations in PDC solution at 1581 and 1030 cm^{-1} are shifted to higher wavenumbers on Mg sample spectra (1589 and 1036 cm^{-1}). Therefore, most likely the coordination occurs through both, COO^- group and pyridine N [239]. Most likely, “induction period” in kinetics curve of $\text{Mg}(\text{OH})_2$ growth is related to the time period which is necessary for increasing pH [236] and formation of polymer film.

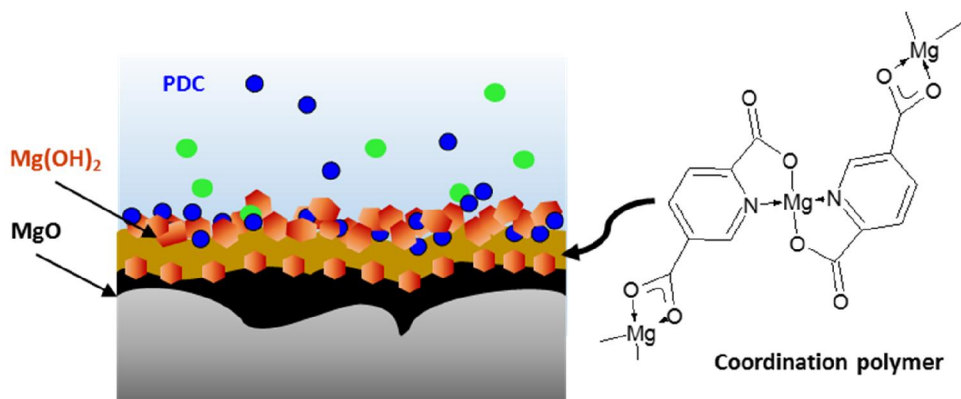


Fig. 57. Schematic representation of PDC inhibition mechanism.

Fumarate (Fum)

The most probable, the action of Fum can be attributed to physical adsorption on Mg surface Fig. 58. Despite the well-developed $\text{Mg}(\text{OH})_2$ surface area, accumulation of organic molecules is relatively low compared to other inhibitors: in depth profiles, the intensity of C within the oxide layer is lower than in the oxide layers formed in the presence of other inhibitors, but it is still higher than for the blank solution. According to in situ Raman spectra in range of $700 - 1700 \text{ cm}^{-1}$ there is no specific (chemical) interaction of Fum with the sample surface (no shifts as compared with Fum solution was noticed). Usually, the absence of difference in the spectra between the adsorbed and free molecules is associated with a weak physical adsorption due to electrostatic interactions; this should not modify significantly the

geometry of the adsorbed molecule [105]. $\text{Mg}(\text{OH})_2$ growth kinetics differs from other inhibitors by the absence of an “induction period”, hence, its inhibition effect does not depend on the formation of $\text{Mg}(\text{OH})_2$ particles, like it was in the case of Sal. This also can be the argument for instantaneous physical adsorption on Mg surface.

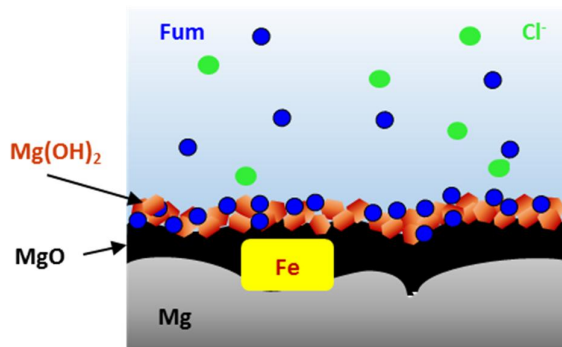


Fig. 58. Schematic representation of Fum inhibition mechanism

Conclusions

Surface analysis techniques such as in situ Raman spectroscopy in kinetic mapping mode, ATR-FTIR and GD OES were applied to study the effect of inhibitors (Sal, PDC, Fum) on the surface film formation and evolution during corrosion of pure Mg in aqueous solutions containing Cl^- . Namely, the growth kinetics of the surface film, its chemical composition, depth elemental distribution and morphology were studied.

Raman spectra in the range of OH vibrations demonstrated that addition of all of these inhibitors leads to formation of a compact $\text{Mg}(\text{OH})_2$ layer with well-developed surface area. This layer has relatively good barrier properties preventing the diffusion of Cl^- to the metal substrate, that was clearly shown by GD OES depth profiles of corroded Mg samples.

Three different mechanisms caused formation of the protective films were proposed: physical adsorption of fumarate on Mg surface, stabilization of $\text{Mg}(\text{OH})_2$ particles due to the chemical adsorption of Sal and precipitation of coordination polymer at the interface between more and less hydrated oxide layers in case of PDC. Despite the chemical adsorption on $\text{Mg}(\text{OH})_2$ nano-crystals, Fe-complexing mechanism more likely takes place in case of Sal inhibition. It was concluded from the characteristic peaks of $\text{Fe}(\text{III})\text{Sal}$ IR and Raman, found in the spectra of CP-Mg342 corroded sample. This mechanism is also consistent with the fact that Sal inhibits corrosion of only Mg with higher Fe content and cathodic inhibition type of inhibition reported previously [30].

Chapter 8

Conclusions and Perspectives

Development of new analytical approaches for investigation of Mg corrosion and protection mechanisms

The first objective of the work was analytical and consisted in the development of new approaches to study evolution of the surface films on corroding Mg. Both, in-situ and ex-situ aspects were taken into account.

Concerning in-situ evaluation, for the first time a methodology was proposed which is able to survey in-situ the kinetics of the oxide/hydroxide film evolution in aqueous solutions on significantly large surfaces and with sufficient lateral resolution (mapping mode). In-situ kinetics Raman mapping (KRM) was developed and its applicability to describe the effect of solution composition (pH, presence of Cl⁻, presence of inhibitors) on the local evolution of surface film at initial stages of Mg corrosion in thin layer cell was demonstrated. Namely, the use of a specific normalization procedure for the evolution of A_{1g} Mg(OH)₂ peak during immersion in different locations allowed extracting film growth kinetics from sufficiently large surfaces with about 10 μm spatial resolution within the same experiment. The detailed analysis of the in-situ Raman spectra modifications was also able to extract information about the evolution of the crystal shape and crystal size during reactivity. From the methodological

point of view, such a technic should be easily extended to multiple processes for which in situ measurement with local resolution can be of interest.

Concerning the ex-situ characterization, the novelty of the work is the verification of the applicability of RF GD-OES to test surface enrichment on corroded Mg surfaces as a relatively non-expensive and low time consuming alternative to high vacuum technics like XPS, ToF SIMS, etc...), testing its limits and suggestion of solutions for the found difficulties. One of the important but often neglected in corrosion research problems of applicability of GD OES is that atomic H in plasma, coming from the sample (outer hydroxide layer), can significantly modify not only the sputtering rate but also detection limits and emission yield for particular emission lines. The effects of H on the analytical parameters of GD OES were studied and it was demonstrated that not take into account the H-effect can cause an ambiguous interpretation of elements intensities changes in oxide/hydroxide layer compared to metal bulk. Two different approaches which permits take into account the effect of H were proposed. The experimental approach was to characterize the corroded layers using not conventional Ar but Ar/H₂ plasma gas, while in case of results obtained in conventional Ar gas the H-correction procedure was proposed and correlation coefficients for Mg, Mn and Fe were obtained. The results give a way to obtain simply interpretable qualitative profiles on corroded Mg surfaces. Another important conclusion from the work is that the detection limit for Fe is significantly degraded in presence of H, thus, it was not every time possible to confirm the ppm-level enrichment of the oxide film in Ar/H₂ plasma, however the results of theoretical H-correction taking into account the measured in Ar/H₂ plasma interferences of H signal on the Fe background signal can be used.

Understanding the solution chemistry effects on the evolution of oxide/hydroxide films on corroding Mg: corrosion and protection mechanisms

The main objective of the work related to Material Science was to correlate environmental composition, evolution of the surface film and Mg reactivity with help of new proposed methodologies and additional ex situ characterizations.

Among different factors, which could be taken into account, we selected the effects of solution pH, concentration of Cl⁻ ions and the presence of selected organic inhibitors on the film growth and breakdown kinetics, film enrichment and reactivity mechanisms.

1.1.1 Effect of solution pH

The direct application of the proposed in-situ **KRM** was able to distinguish the **pH effect on the brucite growth kinetics** on the areas, which did not evolve in optical images during immersion. This kinetics was parabolic (diffusion limited) at pH 13 but linear (surface reaction limited) at pH 7-10.5 (Fig. 59a). A jump in the kinetics curve was observed in particular locations on the surface (Fig. 59b) which were associated with the proximity of black filaments (Fig. 60a). **The time of the jump in kinetics curve coincides with the first visual observation of filament in studied zone and mapping of this time** (Fig. 60b). It was also shown that increase of Cl⁻ content in solution result in higher overall rates of the film growth but doesn't modify the slope of the kinetics curve, thus don't influence the film growth mechanism.

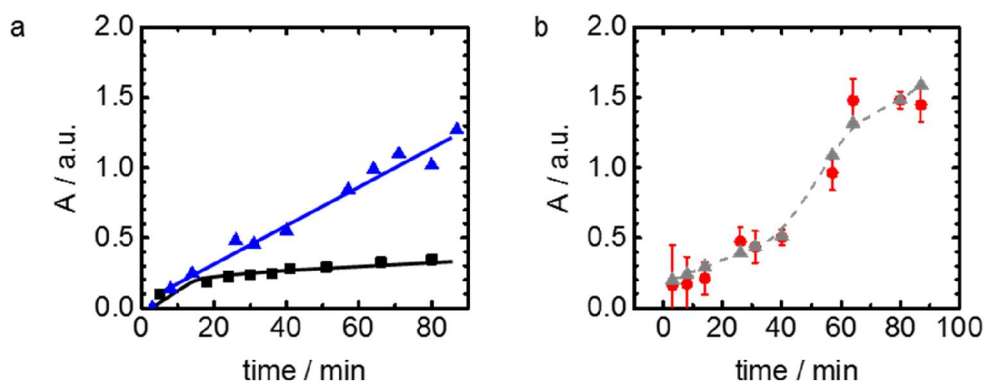


Fig. 59. Examples of localized in-situ Mg(OH)₂ growth kinetics on corroding Mg immersed in 10 mM NaCl at different pH: a) “intact” areas at pH 9 (blue triangles) and pH 13 (black squares); and b) in black filament at pH 9, experimental results (red circles) and theoretical simulation of enhanced Mg(OH)₂ precipitation due to spontaneous pH increase.

Fraction of the surface with “broken” film as a function of time was also plotted showing the linear breakdown kinetics coherent with the previously observed by Time Laps Optical Microscopy.

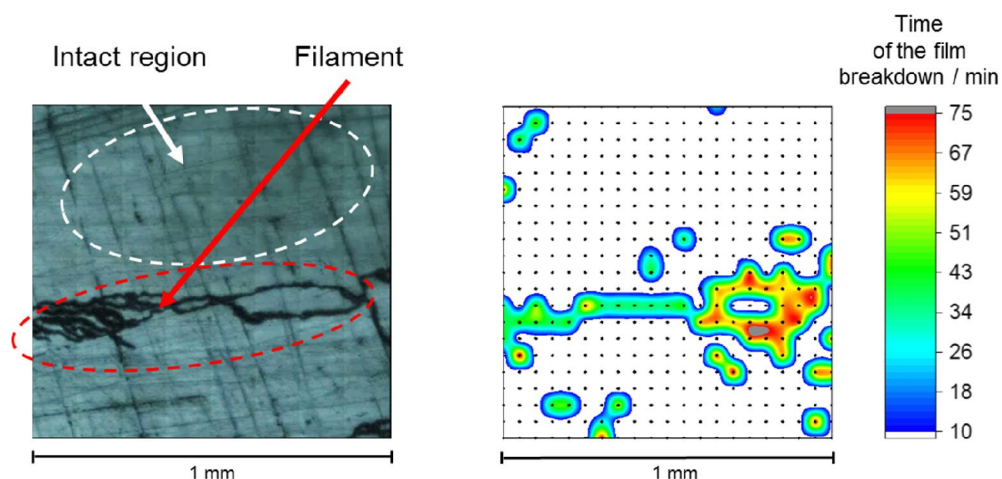


Fig. 60. (a) Example of Mg surface appearance at 80 minutes of contact with 0.1 M NaCl solution; (b) kinetic map (time of sharp growth rate increase for each point) for the same surface.

Concerning the in situ evolution of the crystal size and morphology, from the analysis of “satellites” peaks in Raman spectra **it was possible to correlate high alkalinity with decrease of brucite grain size** and the favoring of nucleation processes versus grain growth. Namely, on the basis of recently published in the literature results of quantum calculations, the bands at 3675 cm^{-1} and 3710 cm^{-1} were attributed to vibrations of surface Mg-OH groups with different crystallographic oriented planes, (0001) and (10-10) respectively the presence of “satellites” hence was considered as an evidence of high surface area and smaller $\text{Mg}(\text{OH})_2$ crystal size at high pH. This hypothesis was confirmed by ex-situ Scanning Electron Microscopy (SEM) (Fig. 61 b,d). **Similar kinetics of the bulk and satellite peaks growth were obtained at pH 13 after about 10 minutes of induction period indicating that the crystal morphology reaches equilibrium at this time.**

pH effect on the kinetics of the brucite film growth, the crystals size and morphology is coherent with dissolution-precipitation model of its formation. In this regard, enhanced growth of $\text{Mg}(\text{OH})_2$ in proximity of filaments could be explained by surface film breakdown in this locations resulting in the injection of the excess Mg^{2+} and/ or OH^- ions and causing additional brucite precipitation as schematically present in Fig. 62.

A simple calculation of film growth kinetics around the filaments using a precipitation from supersaturated solution gives results which fit well with the observed jump (simulated kinetics is shown by the grey curve in Fig. 59b).

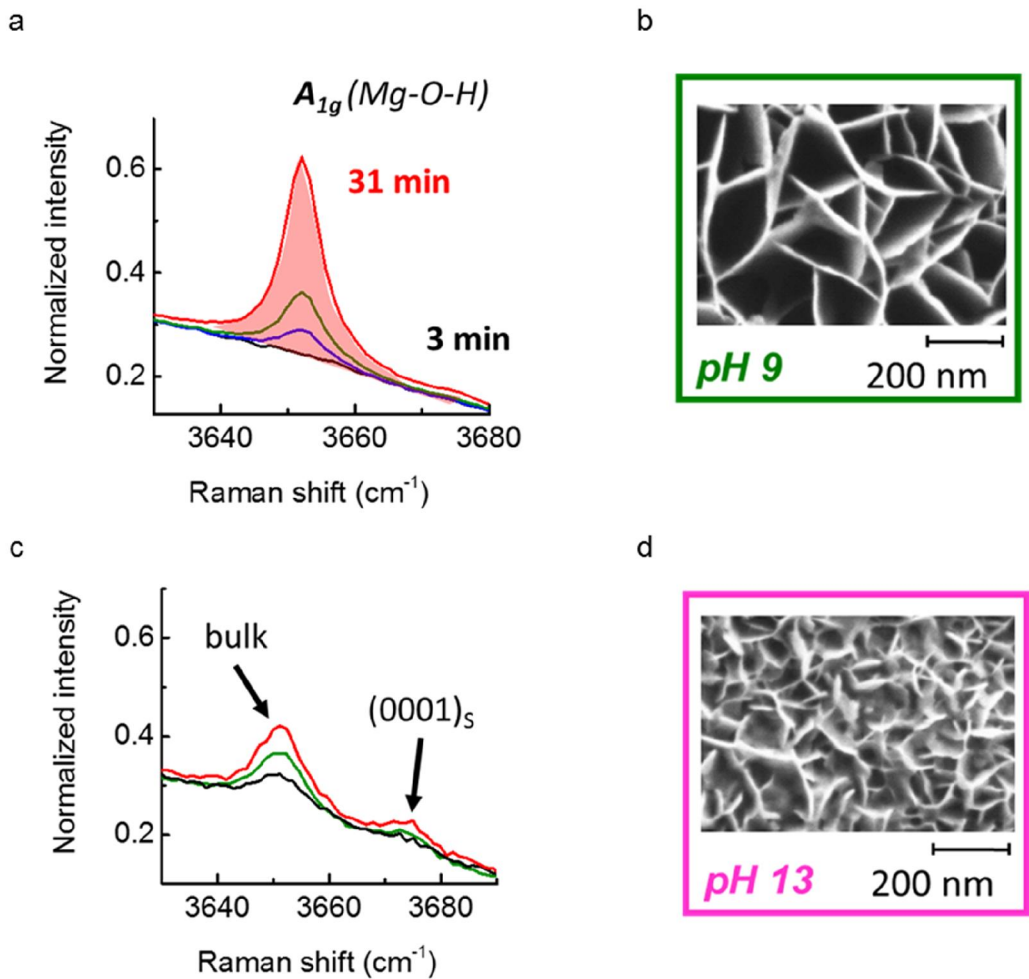


Fig. 61. Examples of in-situ Raman spectra of Mg surface in contact with 0.1 M NaCl at pH 9 (a) and 13 (b) and ex-situ SEM images of the corresponding surfaces after immersion (c,d).

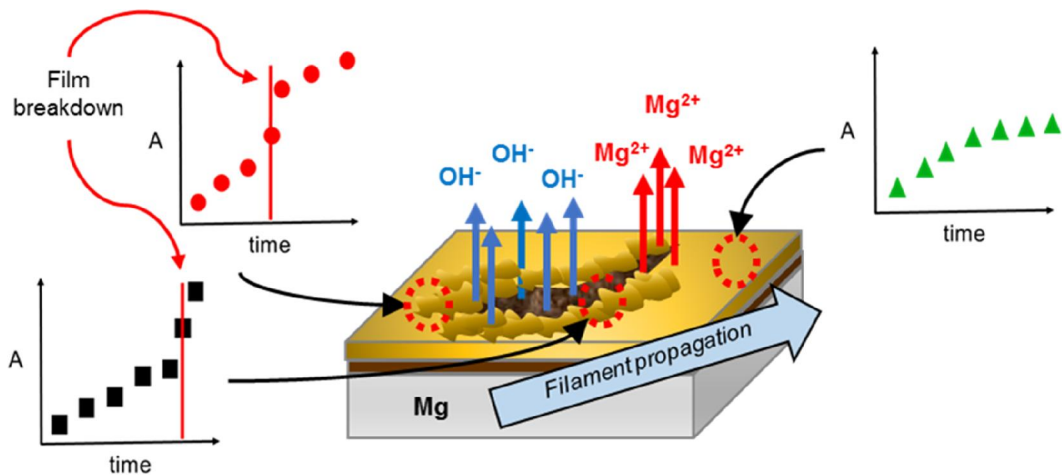


Fig. 62. Schematic representation of Mg(OH)₂ growth in Cl⁻ containing solution around

Finally, with help of in-situ kinetics measurements the importance of dissolution – precipitation processes for brucite film growth and breakdown on corroding Magnesium was demonstrated and a simple description of the related mechanisms in terms of precipitation from supersaturated solution was proposed. The effect of pH on the film stability can be hence interpreted in terms of this mechanisms and this understanding can contribute for the choice of effective anticorrosion strategy.

1.1.2 Effect of selected organic molecules

The proposed analytical methods contributed into understanding of corrosion inhibition mechanisms by selected organic molecules, namely sodium salts of salicylic (Sal), 2,5-pyridine-dicarboxylic (PDCA) and fumaric (Fum) acids (see Fig. 8)

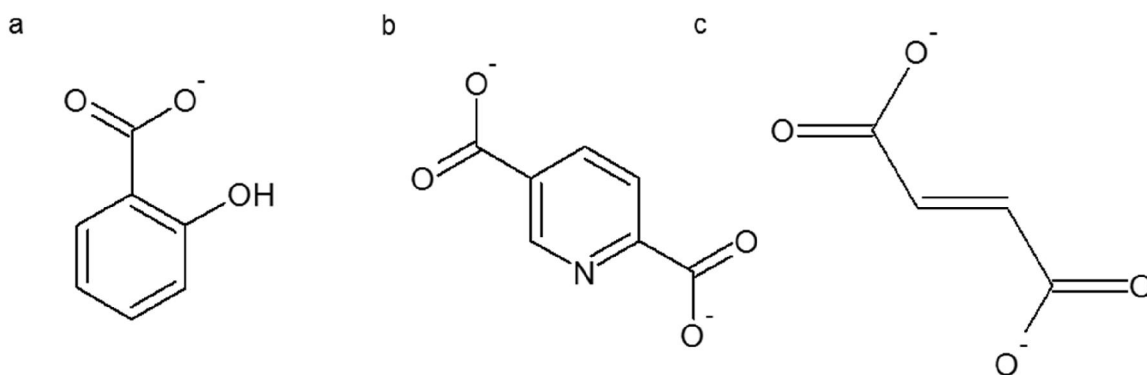


Fig. 63. Structural formula of Mg corrosion inhibitors studied in this work: (a) salicylate, (b) 2,5-pyridinedicarboxylate, (c) fumarate.

The surface evolution in 0.1 M NaCl solution with and without inhibitors was compared on two types of pure Mg. The principle difference between the Mg compositions was amount of Fe impurities, 342 and 50 ppm for commercial and high purity Mg respectively. All of inhibitors efficiently retarded Mg corrosion, except salicylate, which inhibited only Mg with higher content of Fe inclusions and, conversely, accelerated corrosion for high purity Mg.

GD-OES depth profiles after immersion of Mg in 0.1 M NaCl solutions with and w/o the inhibitors (Fig. 64) confirmed that **all inhibitors were incorporated into the oxide/hydroxide film (strong C signal) and efficiently decreased the quantity of adsorbed Cl⁻**, which is known as a film destabilizing agent responsible for the initial pitting.

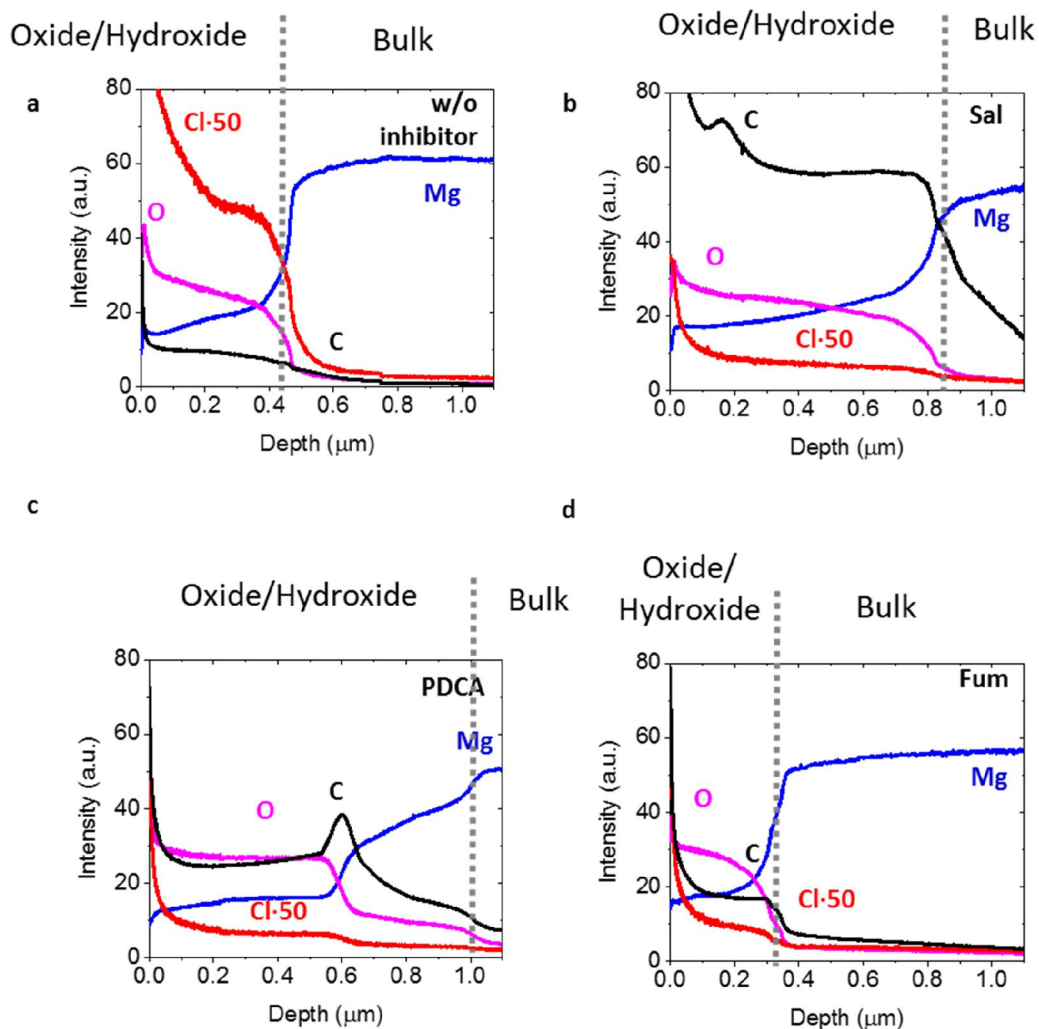


Fig. 64. Elemental GD OES depth profiles obtained on commercial purity Mg (ppm impurities) after 2 h of immersion in 0.1 M NaCl without inhibitors (a) and with addition of XM inhibitor: sodium salicylate (b), PDCA (c) or sodium fumarate obtained in Ar/H₂ plasma.

In situ Raman spectroscopy revealed **two different trends in Mg(OH)₂ growth kinetics in presence of inhibitors** (Fig. 65). For fumarate, the growth was slower as compared with 0.1 M NaCl solution. For salicylate and PDCA the growth rate evolved in 2 periods. Initially, it was similar to the growth rate evolution w/o inhibitors. After approximately 40 minutes of the surface contact with the solution, the growth was slower and looked similar to fumarate solution. In presence of all inhibitors the satellite peaks were visible, revealing smaller crystal size than in solutions w/o the inhibitors.

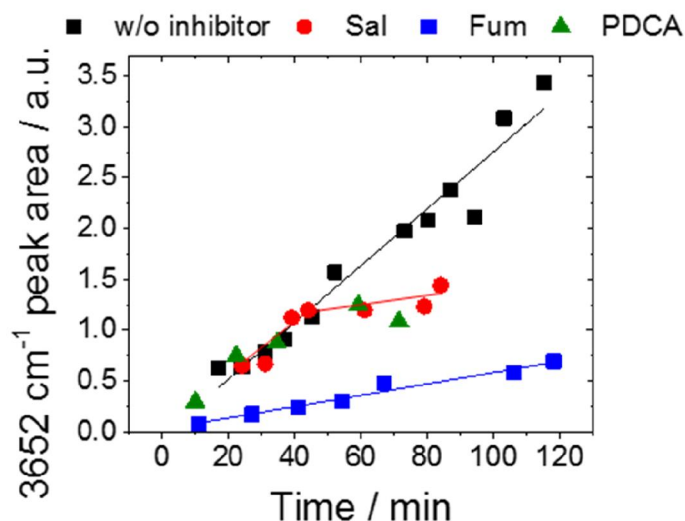


Fig. 65. Typical localized $\text{Mg}(\text{OH})_2$ growth kinetics on corroding Mg immersed in 0.1 M NaCl w/o inhibitors (black squares), with addition of 0.05 M sodium salts of fumaric (blue squares, Fum) salicylic (red circles) and 2.5-pyridindicarboxylic (green triangles, PDCA) acids.

The **interaction of the inhibitors with the surface film was also analyzed**. On the corroding Mg of commercial purity, the characteristic Raman shifts and IR bands **positions of $-\text{COO}^-$ and $-\text{OH}$ groups of salicylate were shifted as compared with the position observed for the inhibitor** (Fig. 66). This was interpreted as a specific interaction of salicylate with the surface. **For fumarate, no specific interaction was observed. For PDCA no shifts in bands position in Raman spectra were registered during first 40 minutes, and then the high fluorescence background appeared hindering the Raman signal**. This could be explained by formation of a specific set of the organic molecules which has a chain of alternating double and single bonds, called conjugation. Ex situ analysis by IR spectroscopy confirmed slight shifts of the peaks positions characteristic for aromatic ring vibrations for PDCA.

Three different types of interaction of the organic molecule with the Mg surface were proposed for studied inhibitors. Physical adsorption of fumarate, chemisorption of salicylate on $\text{Mg}(\text{OH})_2$ with probable Fe-complexation and coordinated polymer formation at the interface between more and less hydrated oxide/hydroxide layers in case of PDCA are the most probable mechanisms of the surface modification. **Concerning the inhibition mechanisms, specific interaction of salicylate with Fe is coherent with cathodic inhibition reported in the literature as well as with the absence of the inhibition effect for high purity Mg. Fumarate and PDCA form homogenous surface films that is more coherent with inhibition of anodic reactivity. All the surface films formed in the presence of inhibitors contain $\text{Mg}(\text{OH})_2$ nanocrystals with a reduced size as compared with the films**

formed w/o inhibitors and block Cl⁻ access to the surface, reducing the possibility of localized corrosion due to the film breakdown.

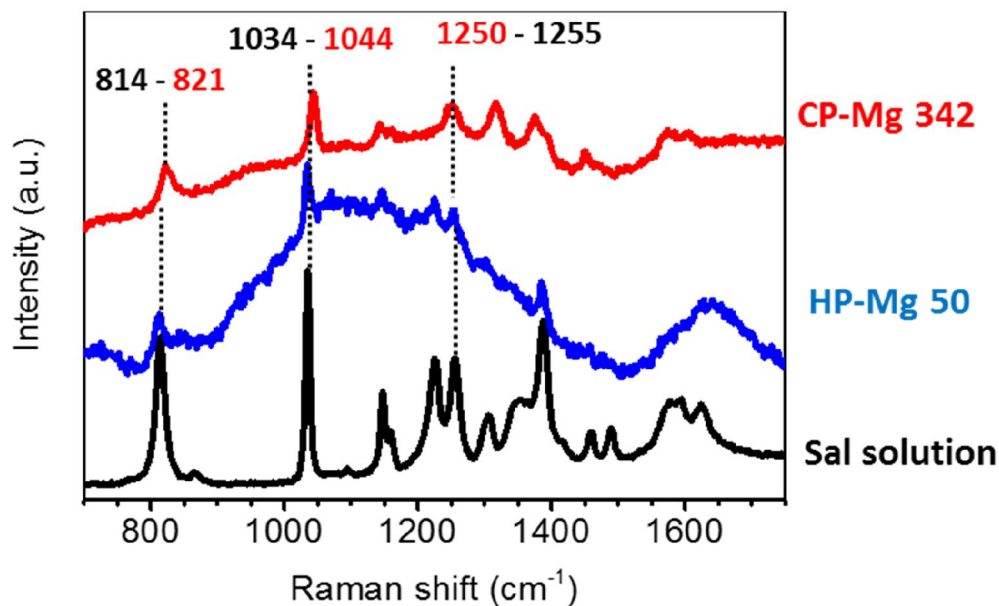


Fig. 66. Examples of in-situ Raman spectra of commercial purity Mg (CP –Mg342) and high purity Mg (HP-Mg50) in contact with 0.1 M NaCl + 0.05 M Na salicylate solution compared with Raman spectra of Na salicylate solution.

Perspectives

This work had two aspects: one of them was analytical (development/adaptation of methodologies) and another one was related to the understanding of physico-chemical processes that occur at solid/liquid interfaces. Both of these directions can be further extended.

Concerning the analytical part, in this work GD-OES analysis was carried out in a qualitative way, whereas it could be performed quantitatively with beforehand calibration procedure. It needs, however, serious analytical development, choice of the calibration standards etc. Another direction for GD-OES analysis can be related to the content of discharge gas. In current work we tested only Ar and Ar/H₂ mixtures and demonstrated that addition of H₂ changes significantly the sputtering rate, which was an advantage in case of analysis of thin oxide layers and disadvantage in terms of detection limits of minor elements. Thus, the choice of the optimal H₂ content or another additive such as N₂, could be performed in future to improve the analysis characteristics.

The application of developed techniques, in particular the kinetic analysis in mapping mode, can be further explored for investigation of multiple systems (not only Mg), for which

in situ kinetics measurement of the surface chemical evolution with local resolution can be of interest, including the problems of hydration of cements, the problems of surface treatment, etc...

In regards to Mg corrosion, the influence of alloying elements such as Li, Ca, Mn, Zn, which are extensively studied for new applications (batteries, bio-ressorbable implants), as well as the effect of different species present in the solution, for instance the presence of protein in relation to bio-application or the effect of the ionic liquids in relation to batteries research, can be studied with help of the proposed approaches. Some work in this direction, which is presented in appendices, were have already started.

Bibliography

- [1] S.N. Mathaudhu, A.A. Luo, N.R. Neelameggham, E.A. Nyberg, W.H. Sillekens, Essential Readings in Magnesium Technology, Wiley, 2014. doi:10.1002/9781118859803.
- [2] M.P. Brady, G. Rother, L.M. Anovitz, K.C. Littrell, K.A. Unocic, H.H. Elsentriecy, G.-L. Song, J.K. Thomson, N.C. Gallego, B. Davis, Film breakdown and nano-porous Mg(OH)₂ formation from corrosion of magnesium alloys in salt solutions, *J. Electrochem. Soc.* 162 (2015) C140–C149. doi:10.1149/2.0171504jes.
- [3] M. Taheri, J.R. Kish, N. Birbilis, M. Danaie, E.A. McNally, J.R. McDermid, Towards a physical description for the origin of enhanced catalytic activity of corroding magnesium surfaces, *Electrochim. Acta.* 116 (2014) 396–403. doi:10.1016/j.electacta.2013.11.086.
- [4] M. Taheri, R.C. Phillips, J.R. Kish, G.A. Botton, Analysis of the surface film formed on Mg by exposure to water using a FIB cross-section and STEM-EDS, *Corros. Sci.* 59 (2012) 222–228. doi:10.1016/j.corsci.2012.03.001.
- [5] J.H. Nordlien, S. Ono, N. Masuko, K. Nisancioglu, Morphology and structure of oxide films formed on magnesium by exposure to air and water, *J. Electrochem. Soc.* 142 (1995) 3320–3322. doi:10.1149/1.2049981.
- [6] G. Song, A. Atrens, D. Stjohn, J. Nairn, Y. Li, The electrochemical corrosion of pure magnesium in 1 N NaCl, *Corros. Sci.* 39 (1997) 855–875. doi:10.1016/S0010-938X(96)00172-2.
- [7] N. Hara, Y. Kobayashi, D. Kagaya, N. Akao, Formation and breakdown of surface films on magnesium and its alloys in aqueous solutions, *Corros. Sci.* 49 (2007) 166–175. doi:10.1016/j.corsci.2006.05.033.

- [8] G.L. Makar, J. Kruger, Corrosion of magnesium, (1993).
- [9] G.G. Perrault, The potential-pH diagram of the magnesium-water system, *Electroanalytical Chem. Interfacial Electrochem.* 51 (1974) 107–119.
- [10] S.H. Salleh, S. Thomas, J.A. Yuwono, K. Venkatesan, N. Birbilis, Enhanced hydrogen evolution on Mg (OH)₂ covered Mg surfaces, *Electrochim. Acta.* 161 (2015) 144–152. doi:10.1016/j.electacta.2015.02.079.
- [11] G. Williams, H.N. Neil McMurray, Localized Corrosion of Magnesium in Chloride-Containing Electrolyte Studied by a Scanning Vibrating Electrode Technique, *J. Electrochem. Soc.* 155 (2008) C340–C349. doi:10.1149/1.2918900.
- [12] J.D. Hanawalt, Some corrosion characteristics of high purity magnesium alloys, *J. Electrochem. Soc.* 81 (1942) 423–433.
- [13] T. Cain, S.B. Madden, N. Birbilis, J.R. Scully, Evidence of the enrichment of transition metal elements on corroding magnesium surfaces using Rutherford backscattering spectrometry, *J. Electrochem. Soc.* 162 (2015) C228–C237. doi:10.1149/2.0541506jes.
- [14] Z.P. Cano, M. Danaie, J.R. Kish, J.R. McDermid, G.A. Botton, G. Williams, Physical characterization of cathodically-activated corrosion filaments on magnesium alloy AZ31B, *Corrosion.* 71 (2015) 146–159. doi:10.5006/1384.
- [15] M. Esmaily, J.E. Svensson, S. Fajardo, N. Birbilis, G.S. Frankel, S. Virtanen, R. Arrabal, S. Thomas, L.G. Johansson, Fundamentals and advances in magnesium alloy corrosion, *Prog. Mater. Sci.* 89 (2017) 92–193. doi:10.1016/j.pmatsci.2017.04.011.
- [16] I. Giner, O. Ozcan, G. Grundmeier, In situ AFM studies of the stability of MgO(100) in aqueous electrolytes, *Corros. Sci.* 87 (2014) 51–59. doi:10.1016/j.corsci.2014.06.012.
- [17] X.-P. Guo, G.-L. Song, J.-Y. Hu, D.-B. Huang, Corrosion inhibition of magnesium (Mg) Alloys, in: *Corros. Prev. Magnes. Alloy.*, Elsevier, 2013: pp. 61–84. doi:10.1533/9780857098962.1.61.
- [18] S. V. Lamaka, B. Vaghefinazari, D. Mei, R.P. Petrauskas, D. Höche, M.L. Zheludkevich, Comprehensive screening of Mg corrosion inhibitors, *Corros. Sci.* 128 (2017) 224–240. doi:10.1016/j.corsci.2017.07.011.
- [19] T. Ohtsuka, M. Matsuda, In situ Raman spectroscopy for corrosion products of zinc in humidified atmosphere in the presence of sodium chloride precipitate, *Corrosion.* 59 (2003) 407–413. doi:10.5006/1.3277572.
- [20] M.C. Bernard, A. Hugot-Le Goff, D. Massinon, N. Phillips, Underpaint corrosion of zinc-coated steel sheet studied by in situ raman spectroscopy, *Corros. Sci.* 35 (1993) 1339–1349. doi:10.1016/0010-938X(93)90356-L.

- [21] X. Zhang, K. Xiao, C. Dong, J. Wu, X. Li, Y. Huang, In situ Raman spectroscopy study of corrosion products on the surface of carbon steel in solution containing Cl- and SO₄²⁻, *Eng. Fail. Anal.* 18 (2011) 1981–1989. doi:10.1016/j.engfailanal.2011.03.007.
- [22] S. Simard, M. Odziemkowski, D.E. Irish, L. Brossard, H. Ménard, In situ micro-Raman spectroscopy to investigate pitting corrosion product of 1024 mild steel in phosphate and bicarbonate solutions containing chloride and sulfate ions, *J. Appl. Electrochem.* 31 (2001) 913–920. doi:10.1023/A:1017517618191.
- [23] M.J. Pelletier, Quantitative Analysis Using Raman Spectrometry, *Appl. Spectrosc.* 57 (2003) 20A–42A. doi:DOI: 10.1366/000370203321165133.
- [24] G. Goudec, P. Colomban, Raman Spectroscopy of nanomaterials : How spectra relate to disorder, particle size and mechanical properties, *Prog. Cryst. Growth Charact. Mater.* 53 (2007) 1–56. doi:10.1016/j.pcrysgrow.2007.01.001.
- [25] J. Angeli, A. Bengtson, A. Bogaerts, V. Hoffmann, V.-D. Hodoroaba, E. Steers, Glow discharge optical emission spectrometry: moving towards reliable thin film analysis - a short review, *J. Anal. At. Spectrom.* 18 (2003) 670–679. doi:10.1039/b301293j.
- [26] V.-D. Hodoroaba, Hydrogen Effect and Analysis in GDS – Applications in Material Science, Technische Universität Dresden, 2002.
- [27] V.D. Hodoroaba, E.B.M. Steers, V. Hoffmann, W.E.S. Unger, W. Paatsch, K. Wetzig, Influence of hydrogen on the analytical figures of merit of glow discharge optical emission spectroscopy - friend or foe?, *J. Anal. At. Spectrom.* 18 (2003) 521–526. doi:10.1039/b301326j.
- [28] T.R. Zeitler, J.A. Greathouse, J.D. Gale, R.T. Cygan, Vibrational analysis of brucite surfaces and the development of an improved force field for molecular simulation of interfaces, *J. Phys. Chem. C.* 118 (2014) 7946–7953. doi:10.1021/jp411092b.
- [29] V. Masilamani, H.M. Ghaithan, M.J. Aljaafreh, A. Ahmed, R. Thagafi, S. Prasad, M.S. Alsalmi, Using a Spectrofluorometer for Resonance Raman Spectra of Organic Molecules, 2017 (2017). doi:10.1155/2017/4289830.
- [30] J. Yang, C. Blawert, S.V. Lamaka, K.A. Yasakau, L. Wang, D. Laipple, M. Schieda, I. Di, M.L. Zheludkevich, Corrosion inhibition of pure Mg containing a high level of iron impurity in pH neutral NaCl solution, *Corros. Sci.* Accepted (2018).
- [31] W. Beetz, XXXIV. On the development of hydrogen from the anode, *Philos. Mag. Ser.* 4. 32 (1866) 269–278. doi:10.1080/14786446608644179.
- [32] M. Esmaily, J.E. Svensson, S. Fajardo, N. Birbilis, G.S. Frankel, S. Virtanen, R. Arrabal, S. Thomas, L.G. Johansson, Fundamentals and advances in magnesium alloy corrosion, *Prog. Mater. Sci.* 89 (2017) 92–193. doi:10.1016/j.pmatsci.2017.04.011.

- [33] S. Thomas, N.V. Medhekar, G.S. Frankel, N. Birbilis, Corrosion mechanism and hydrogen evolution on Mg, *Curr. Opin. Solid State Mater. Sci.* 19 (2015) 85–94. doi:10.1016/j.cossms.2014.09.005.
- [34] R.L. Petty, A.W. Davidson, J. Kleinberg, The Anodic Oxidation of Magnesium Metal: Evidence for the Existence of Unipositive Magnesium, *J. Am. Chem. Soc.* 76 (1954) 363–366. doi:10.1021/ja01631a013.
- [35] B. Guang, L. Song, A. Atrens, G.L. Song, A. Atrens, B. Guang, L. Song, Corrosion Mechanisms of Magnesium Alloys, *Adv. Eng. Mater.* 1 (1999) 11–33. doi:10.1002/(SICI)1527-2648(199909)1:1<11::AID-ADEM11>3.3.CO;2-E.
- [36] G. Song, A. Atrens, Recent insights into the mechanism of magnesium corrosion and research suggestions, *Adv. Eng. Mater.* 9 (2007) 177–183. doi:10.1002/adem.200600221.
- [37] A. Atrens, W. Dietzel, The negative difference effect and unipositive Mg, *Adv. Eng. Mater.* 9 (2007) 292–297. doi:10.1002/adem.200600275.
- [38] M.E. Straumanis, B.K. Bhatia, Disintegration of Magnesium While Dissolving Anodically in Neutral and Acidic Solutions, *J. Electrochem. Soc.* 110 (1963) 357–360. doi:10.1149/1.2425763.
- [39] E. Gulbrandsen, Anodic Behavior of Mg in Hc03-/Co23- Buffer Solutions, Quasi-Steady Measurements, *Electrochim. Acta.* 37 (1992) 1403–1412.
- [40] J.H. Nordlien, Morphology and structure of oxide films formed on MgAl alloys by exposure to air and water, *J. Electrochem. Soc.* 143 (1996) 2564. doi:10.1149/1.1837048.
- [41] D.A. Vermilyea, C.F. Kirk, Studies of Inhibition of Magnesium Corrosion, *J. Electrochem. Soc.* 116 (1969) 1487–1492. doi:10.1149/1.2411579.
- [42] J.H. Nordlien, S. Ono, N. Masuko, K. Nisancioglu, A TEM investigation of naturally formed oxide films on pure magnesium, *Corros. Sci.* 39 (1997) 1397–1414. doi:10.1016/S0010-938X(97)00037-1.
- [43] G.L. Song, Corrosion electrochemistry of magnesium (Mg) and its alloys, Woodhead Publishing Limited, 2011. doi:http://dx.doi.org/10.1533/9780857091413.1.3.
- [44] J.R. Kish, Y. Hu, J. Li, W. Zheng, J.R. McDermid, Technical note: Examination of focused ion beam-sectioned surface films formed on am60b mg alloy in an aqueous saline solution, *Corrosion.* 68 (2012) 468–474. doi:10.5006/i0010-9312-68-6-468.
- [45] S. Feliu Jr, M.C. Merino, R. Arrabal, A.E. Coy, E. Matykina, XPS study of the effect of aluminium on the atmospheric corrosion of the AZ31 magnesium alloy, *Surf. Interface Anal.* 41 (2009) 143–150. doi:10.1002/sia.3004.

- [46] S. Feliu, A. Pardo, M.C. Merino, A.E. Coy, F. Viejo, R. Arrabal, Correlation between the surface chemistry and the atmospheric corrosion of AZ31, AZ80 and AZ91D magnesium alloys, *Appl. Surf. Sci.* 255 (2009) 4102–4108. doi:10.1016/j.apsusc.2008.10.095.
- [47] L. Wang, B.-P. Zhang, T. Shinohara, Corrosion behavior of AZ91 magnesium alloy in dilute NaCl solutions, *Mater. Des.* 31 (2010) 857–863. doi:10.1016/j.matdes.2009.07.049.
- [48] M. Curioni, The behaviour of magnesium during free corrosion and potentiodynamic polarization investigated by real-time hydrogen measurement and optical imaging, *Electrochim. Acta.* 120 (2014) 284–292. doi:10.1016/j.electacta.2013.12.109.
- [49] G. Williams, R. Grace, Chloride-induced filiform corrosion of organic-coated magnesium, *Electrochim. Acta.* 56 (2011) 1894–1903. doi:10.1016/j.electacta.2010.09.005.
- [50] N. Birbilis, G. Williams, K. Gusieva, A. Samaniego, M.A. Gibson, H.N. McMurray, Poisoning the corrosion of magnesium, *Electrochem. Commun.* 34 (2013) 295–298. doi:10.1016/j.elecom.2013.07.021.
- [51] H. Wang, Y. Song, J. Yu, D. Shan, H. Han, Characterization of Filiform Corrosion of Mg–3Zn Mg Alloy, *J. Electrochem. Soc.* 164 (2017) C574–C580. doi:10.1149/2.1221709jes.
- [52] G. Williams, H.A. Llwyd Dafydd, R. Subramanian, H.N. McMurray, The influence of Chloride Ion Concentration on Passivity Breakdown in Magnesium, *Corrosion.* 73 (2017) 471–481.
- [53] K. Gusieva, C.H.J. Davies, J.R. Scully, N. Birbilis, Corrosion of magnesium alloys: the role of alloying, *Int. Mater. Rev.* 60 (2015) 169–194. doi:10.1179/1743280414Y.0000000046.
- [54] M.L.Z. Sviatlana V. Lamaka, Jorge Gonzalez, Di Mei, Frank Feyerabend, Regine Willumeit-Römer, Local pH and its Evolution near Mg Alloy Surfaces Exposed to Simulated Body Fluids, *Adv. Mater. Interfaces.* 1800169 (2018) 1–6. doi:10.1002/admi.201800169.
- [55] Z.P. Cano, J.R. McDermid, J.R. Kish, Cathodic Activity of Corrosion Filaments Formed on Mg Alloy AM30, *J. Electrochem. Soc.* 162 (2015) C732–C740. doi:10.1149/2.0381514jes.
- [56] G.S. Frankel, S. Fajardo, M. Lynch, Introductory lecture on corrosion chemistry: a focus on anodic hydrogen evolution on Al and Mg, *Faraday Discuss.* 180 (2015) 11–33. doi:10.1039/C5FD00066A.

- [57] G. Williams, N. Birbilis, H.N. McMurray, Controlling factors in localised corrosion morphologies observed for magnesium immersed in chloride containing electrolyte, *Faraday Discuss.* 180 (2015). doi:10.1039/C4FD00268G.
- [58] G.R. Hoey, M. Cohen, Corrosion of Anodically and Cathodically Polarized Magnesium in Aqueous Media, *J. Electrochem. Soc.* 105 (1958) 245. doi:10.1149/1.2428817.
- [59] G. Williams, N. Birbilis, H.N. McMurray, The source of hydrogen evolved from a magnesium anode, *Electrochem. Commun.* 36 (2013) 1–5. doi:10.1016/j.elecom.2013.08.023.
- [60] S. Fajardo, G.S. Frankel, Effect of impurities on the enhanced catalytic activity for hydrogen evolution in high purity magnesium, *Electrochim. Acta.* 165 (2015) 255–267. doi:10.1016/j.electacta.2015.03.021.
- [61] M. Curioni, F. Scenini, T. Monetta, F. Bellucci, Correlation between electrochemical impedance measurements and corrosion rate of magnesium investigated by real-time hydrogen measurement and optical imaging, *Electrochim. Acta.* 166 (2015) 372–384. doi:10.1016/j.electacta.2015.03.050.
- [62] S. Fajardo, C.F. Glover, G. Williams, G.S. Frankel, The evolution of anodic hydrogen on high purity magnesium in acidic buffer solution, *Corrosion.* 73 (2017) 482–493. doi:10.5006/2247.
- [63] K.S. Williams, J.P. Labukas, V. Rodriguez-Santiago, J.W. Andzelm, First Principles Modeling of Water Dissociation on Mg(0001) and Development of a Mg Surface Pourbaix Diagram, *Corrosion.* 71 (2015) 209–223. doi:doi.org/10.5006/1322.
- [64] S. V. Lamaka, O. V. Karavai, A.C. Bastos, M.L. Zheludkevich, M.G.S. Ferreira, Monitoring local spatial distribution of Mg²⁺, pH and ionic currents, *Electrochem. Commun.* 10 (2008) 259–262. doi:10.1016/j.elecom.2007.12.003.
- [65] A. Seyeux, V. Maurice, P. Marcus, Oxide Film Growth Kinetics on Metals and Alloys: I. Physical Model, *J. Electrochem. Soc.* 160 (2013) C189–C196. doi:10.1149/2.036306jes.
- [66] C. Wagner, Contribution to the Theory of the Tarnishing Process, *J. Phys. Chem.* B21 (1933) 25–41.
- [67] N. Cabrera, N.F. Mott, Theory of the oxidation of metals, *Reports Prog. Phys.* 12 (1949) 163–184. doi:10.1088/0034-4885/12/1/308.
- [68] F.P. Fehlner, N.F. Mott, Low-temperature oxidation, *Oxid. Met.* 2 (1970) 59–99. doi:10.1007/BF00603582.
- [69] C.Y. Chao, L.F. Lin, D.D. Macdonald, A Point Defect Model for Anodic Passive Films.

- I. Film Growth Kinetics, *J. Electrochem. Soc.* 128 (1981) 1981. doi:10.1149/1.2127592.
- [70] D.D. Macdonald, S.R. Biaggio, H. Song, Steady State Passive Films Interfacial Kinetic Effects and Diagnostic Criteria, *J. Electrochem. Soc.* 139 (1992) 170–177. doi:10.1149/1.2069165.
- [71] A.T. Fromhold, Kinetics of oxide film growth on metal crystals - I. Formulation and numerical solutions, *J. Phys. Chem. Solids.* 24 (1963) 1081–1092. doi:10.1016/0038-1098(63)90400-9.
- [72] A.T. Fromhold, Fundamental Theory of the Growth of Thick Oxide Films on Metals, *J. Phys. Soc. Japan.* 48 (1980) 2022–2030. doi:10.1143/JPSJ.48.2022.
- [73] E. Ghali, Corrosion Resistance of Aluminum and Magnesium Alloys: Understanding, Performance and Testing, John Wiley, 2010.
- [74] J. Robertson, J.E. Forrest, Corrosion of carbon steels in high temperature acid chloride solutions, *Corros. Sci.* 32 (1991) 521–540. doi:10.1016/0010-938X(91)90105-X.
- [75] A.E. Nielsen, Kinetics of Precipitation, Pergamon P, New York, 1964.
- [76] W. Sun, S. Nescic, Basics revisited: kinetics of iron carbonate scale precipitation in CO₂ corrosion, in: NACE, NACE International, San Diego, California, 2006: pp. 1–26.
- [77] J. Robertson, The mechanism of high temperature aqueous corrosion of stainless steels, *Corros. Sci.* 32 (1991) 443–465. doi:10.1016/0010-938X(91)90125-9.
- [78] L. Yin, Y. Jin, C. Leygraf, N. Birbilis, J. Pan, Numerical Simulation of Micro-Galvanic Corrosion in Al Alloys: Effect of Geometric Factors, *J. Electrochem. Soc.* 164 (2017) C75–C84. doi:10.1149/2.1221702jes.
- [79] M. Bartosch, S. Schubert, F. Berger, Magnesium stents-fundamentals, biological implications and applications beyond coronary arteries, *BioNanoMaterials.* 16 (2015) 3–17. doi:10.1515/bnm-2015-0004.
- [80] D. Höche, C. Blawert, S. V. Lamaka, N. Scharnagl, C. Mendis, M.L. Zheludkevich, The effect of iron re-deposition on the corrosion of impurity-containing magnesium, *Phys.Chem.Chem.Phys.* 18 (2015) 1279–1291. doi:10.1039/c5cp05577f.
- [81] S. V. Lamaka, D. Höche, R.P. Petruskas, C. Blawert, M.L. Zheludkevich, A new concept for corrosion inhibition of magnesium : Suppression of iron re-deposition, *Electrochem. Commun.* (2015). doi:10.1016/j.elecom.2015.10.023.
- [82] D. Mercier, J. Światowska, S. Zanna, A. Seyeux, P. Marcus, Role of Segregated Iron at Grain Boundaries on Mg Corrosion, *J. Electrochem. Soc.* 165 (2018) C42–C49. doi:10.1149/2.0621802jes.
- [83] N. Birbilis, T. Cain, J.S. Laird, X. Xia, J.R. Scully, a. E. Hughes, Nuclear Microprobe

- Analysis for Determination of Element Enrichment Following Magnesium Dissolution, *ECS Electrochem. Lett.* 4 (2015) C34–C37. doi:10.1149/2.0081510eel.
- [84] F. El-Taib Heakal, A.M. Fekry, M.Z. Fatayerji, Influence of halides on the dissolution and passivation behavior of AZ91D magnesium alloy in aqueous solutions, *Electrochim. Acta.* 54 (2009) 1545–1557. doi:10.1016/j.electacta.2008.09.055.
- [85] L. Wang, T. Shinohara, B.P. Zhang, Influence of chloride, sulfate and bicarbonate anions on the corrosion behavior of AZ31 magnesium alloy, *J. Alloys Compd.* 496 (2010) 500–507. doi:10.1016/j.jallcom.2010.02.088.
- [86] G. Wu, Y. Fan, A. Atrens, C. Zhai, W. Ding, Electrochemical behavior of magnesium alloys AZ91D, AZCe2, and AZLa1 in chloride and sulfate solutions, *J. Appl. Electrochem.* 38 (2008) 251–257. doi:10.1007/s10800-007-9433-y.
- [87] M.M. Antonijevic, M.B. Petrovic, Copper Corrosion Inhibitors . A review, *Rev. Lit. Arts Am.* 3 (2008) 1–28. doi:10.1016/j.ijengsci.2004.12.001.
- [88] B.E.A. Rani, B.B.J. Basu, Green inhibitors for corrosion protection of metals and alloys: An overview, *Int. J. Corros.* 2012 (2012). doi:10.1155/2012/380217.
- [89] K. Khanari, M. Finšgar, M. Knez Hrnčič, U. Maver, Ž. Knez, B. Seiti, Green corrosion inhibitors for aluminium and its alloys: A review, *RSC Adv.* 7 (2017) 27299–27330. doi:10.1039/c7ra03944a.
- [90] J. Hu, D. Zeng, Z. Zhang, T. Shi, G.L. Song, X. Guo, 2-Hydroxy-4-methoxyacetophenone as an environment-friendly corrosion inhibitor for AZ91D magnesium alloy, *Corros. Sci.* 74 (2013) 35–43. doi:10.1016/j.corsci.2013.04.005.
- [91] N. Dinodi, A.N. Shetty, Alkyl carboxylates as efficient and green inhibitors of magnesium alloy ze41 corrosion in aqueous salt solution, *Corros. Sci.* 85 (2014) 411–427. doi:10.1016/j.corsci.2014.04.052.
- [92] I.A. Kartsonakis, S.G. Stanciu, A.A. Matei, E.K. Karaxi, R. Hristu, A. Karantonis, C.A. Charitidis, Evaluation of the protective ability of typical corrosion inhibitors for magnesium alloys towards the Mg ZK30 variant, *Corros. Sci.* 100 (2015) 194–208. doi:10.1016/j.corsci.2015.07.028.
- [93] G. Williams, R. Grace, R.M. Woods, Inhibition of the localized corrosion of mg alloy AZ31 in chloride containing electrolyte, *Corrosion.* 71 (2015) 184–198. doi:10.5006/1376.
- [94] J. Hu, D. Huang, G.L. Song, X. Guo, The synergistic inhibition effect of organic silicate and inorganic Zn salt on corrosion of Mg-10Gd-3Y magnesium alloy, *Corros. Sci.* 53 (2011) 4093–4101. doi:10.1016/j.corsci.2011.08.017.
- [95] D. Huang, J. Hu, G.L. Song, X. Guo, Inhibition effect of inorganic and organic

- inhibitors on the corrosion of Mg-10Gd-3Y-0.5Zr alloy in an ethylene glycol solution at ambient and elevated temperatures, *Electrochim. Acta.* 56 (2011) 10166–10178. doi:10.1016/j.electacta.2011.09.002.
- [96] S. Thirugnanaselvi, S. Kuttirani, A.R. Emelda, Effect of Schiff base as corrosion inhibitor on AZ31 magnesium alloy in hydrochloric acid solution, *Trans. Nonferrous Met. Soc. China (English Ed.* 24 (2014) 1969–1977. doi:10.1016/S1003-6326(14)63278-7.
- [97] J. Hu, D. Huang, G. Zhang, G.L. Song, X. Guo, Research on the inhibition mechanism of tetraphenylporphyrin on AZ91D magnesium alloy, *Corros. Sci.* 63 (2012) 367–378. doi:10.1016/j.corsci.2012.06.021.
- [98] J. Lei, L. Li, F. Pan, Environmental Friendly Corrosion Inhibitors for Magnesium Alloys, *Magnes. Alloy. - Corros. Surf. Treat.* (2010) 47–64. doi:10.5772/13824.
- [99] D. Landolt, *Corrosion and surface chemistry of metals*, 2007. doi:10.1016/S1369-7021(07)70081-0.
- [100] E. Slavcheva, G. Schmitt, Screening of new corrosion inhibitors via electrochemical noise analysis, *Mater. Corros.* 53 (2002) 647–655.
- [101] N.H. Helal, W.A. Badawy, Environmentally safe corrosion inhibition of Mg-Al-Zn alloy in chloride free neutral solutions by amino acids, *Electrochim. Acta.* 56 (2011) 6581–6587. doi:10.1016/j.electacta.2011.04.031.
- [102] A. Frignani, V. Grassi, F. Zanotto, F. Zucchi, Inhibition of AZ31 Mg alloy corrosion by anionic surfactants, *Corros. Sci.* 63 (2012) 29–39. doi:10.1016/j.corsci.2012.05.012.
- [103] D. Huang, Y. Tu, G. Song, X. Guo, E.T. Al, Inhibition Effects of Pyrazine and Piperazine on the Corrosion of Mg-10Gd-3Y-0.5Zr Alloy in an Ethylene Glycol Solution, 2013 (2013) 36–38.
- [104] N. Dang, Y.H. Wei, L.F. Hou, Y.G. Li, C.L. Guo, Investigation of the inhibition effect of the environmentally friendly inhibitor sodium alginate on magnesium alloy in sodium chloride solution, *Mater. Corros.* 66 (2015) 1354–1362. doi:10.1002/maco.201408141.
- [105] R.P. Eischens, W.A. Pliskin, The Infrared Spectra of Adsorbed Molecules, *Adv. Catal.* 10 (1958) 1–56. doi:10.1016/S0360-0564(08)60403-4.
- [106] W. Stumm, M. V. Blber, An In-Situ ATR-FTIR Study: The Surface Coordination of Salicylic Acid on Aluminum and Iron(III) Oxides, *Environ. Sci. Technol.* 28 (1994) 763–768. doi:10.1021/es00054a004.
- [107] A. Davantès, G. Lefèvre, In situ real time infrared spectroscopy of sorption of (poly)molybdate ions into layered double hydroxides, *J. Phys. Chem. A.* 117 (2013)

12922–12929. doi:10.1021/jp408885k.

- [108] V. Shkirskiy, P. Keil, H. Hintze-Bruening, F. Leroux, P. Vialat, G. Lefèvre, K. Ogle, P. Volovitch, Factors Affecting MoO_4^{2-} Inhibitor Release from Zn_2Al Based Layered Double Hydroxide and Their Implication in Protecting Hot Dip Galvanized Steel by Means of Organic Coatings, *ACS Appl. Mater. Interfaces*. 7 (2015) 25180–25192. doi:10.1021/acsami.5b06702.
- [109] A. Zoubir, *Raman Imaging Techniques and Applications*, 1st ed., Springer, Verlag Berlin Heidelberg, 2012. doi:10.1007/978-3-642-28252-2.
- [110] P. Colomban, Potential and Drawbacks of Raman (Micro)Spectrometry for the Understanding of Iron and Steel Corrosion, *New Trends Dev. Automot. Syst. Eng.* (2011) 567–584. doi:10.5772/13436.
- [111] A. Quentmeier, Glow Discharge Optical Emission Spectroscopy (GD-OES), in: H. Bubert, H. Jenett (Eds.), *Surf. Thin Film Anal. Princ. Instrumentation, Appl.*, Wiley-VCH Verlag GmbH, 2002. doi:10.1002/3527600167.
- [112] D. Wei, S. Chen, Q. Liu, Review of fluorescence suppression techniques in Raman spectroscopy, *Appl. Spectrosc. Rev.* 50 (2015) 387–406. doi:10.1080/05704928.2014.999936.
- [113] I.A.N.M. Clegg, N.J. Everall, B. King, H. Melvin, C. Norton, On-Line Analysis Using Raman Spectroscopy for Process Control during the Manufacture of Titanium Dioxide, *Appl. Spectrosc.* 55 (2001) 1138–1150.
- [114] W.A. England, S.N. Jenny, D.A. Greenhalgh, Chromium Oxide Film Thickness Measurements Using Spontaneous Raman Scattering, *J. Raman Spectrosc.* 15 (1984) 156–159. doi:10.1002/jrs.1250150305.
- [115] E.J. Hutchinson, D. Shu, F. Laplant, Measurement of Fluid Film Thickness on Curved Surfaces by Raman Spectroscopy, *Appl. Spectrosc.* 49 (1995) 1275–1278.
- [116] L. Black, G.C. Allen, P.C. Frost, Quantification of Raman Spectra for the Primary Atmospheric Corrosion Products of Lead, *Appl. Spectrosc.* 49 (1995) 1299–1304. doi:10.1366/0003702953965227.
- [117] M. Assirelli, W. Xu, W. Chew, Reactor kinetics studies via process raman spectroscopy, multivariate chemometrics, and kinetics modeling, *Org. Process Res. Dev.* 15 (2011) 610–621. doi:10.1021/op100337v.
- [118] E. Dropsit, D. Chapron, P. Bourson, S. Hoppe, A. Durand, On the exploitation of optical signal from Raman spectroscopy for in-situ conversion monitoring of emulsion polymerization, *AIP Conf. Proc.* 1914 (2017). doi:10.1063/1.5016752.
- [119] D. De Waal, A.M. Heyns, K.J. Range, A Raman spectroscopic determination of the

- kinetics of decomposition of ammonium chromate $(\text{NH}_4)_2\text{CrO}_4$, *J. Solid State Chem.* 80 (1989) 170–177. doi:10.1016/0022-4596(89)90076-5.
- [120] L.J. Bonales, V. Muñoz-Iglesias, D. Santamaría-Pérez, M. Cáceres, D. Fernández-Remolar, O. Prieto-Ballesteros, Quantitative Raman spectroscopy as a tool to study the kinetics and formation mechanism of carbonates, *Spectrochim. Acta - Part A Mol. Biomol. Spectrosc.* 116 (2013) 26–30. doi:10.1016/j.saa.2013.06.121.
- [121] A. Tomandl, M. Wolpers, K. Ogle, The alkaline stability of phosphate coatings II: In situ Raman spectroscopy, *Corros. Sci.* 46 (2004) 997–1011. doi:10.1016/S0010-938X(03)00183-5.
- [122] R. Rodríguez, S. Vargas, M. Estevez, F. Quintanilla, A. Trejo-Lopez, A.R. Hernández-Martínez, Use of Raman spectroscopy to determine the kinetics of chemical transformation in yogurt production, *Vib. Spectrosc.* 68 (2013) 133–140. doi:10.1016/j.vibspec.2013.06.004.
- [123] S.-S. Li, Q.-Y. Guan, G. Meng, X.-F. Chang, J.-W. Wei, P. Wang, B. Kang, J.-J. Xu, H.-Y. Chen, Revealing chemical processes and kinetics of drug action within single living cells via plasmonic Raman probes, *Sci. Rep.* 7 (2017) 2296. doi:10.1038/s41598-017-02510-9.
- [124] N.J. Overall, Modeling and Measuring the Effect of Refraction on the Depth Resolution of Confocal Raman Microscopy, *Appl. Spectrosc.* 54 (2000) 772–782.
- [125] M.C. Bernard, A. Hugot-Le Goff, D. Massinon, N. Phillips, Underpaint corrosion of zinc-coated steel sheet studied by in situ raman spectroscopy, *Corros. Sci.* 35 (1993). doi:10.1016/0010-938X(93)90356-L.
- [126] P. Delichere, A. Hugot Le Goff, S. Joiret, Study of thin corrosion films by in situ Raman spectroscopy combined with direct observation of nuclear reactions, *Surf. Interface Anal.* 12 (1988) 419–423.
- [127] D. Abourazzouk, A.H. Goff, Corrosion of Ni-Cr dental alloys studied by in situ Raman spectroscopy: role of beryllium, *Corros. Sci.* 35 (1993) 809–815.
- [128] N. Boucherit, A. Hugot-Le Goff, S. Joiret, Raman studies of corrosion films grown on iron and iron-molybdenum (Fe-6Mo) in pitting conditions, *Corros. Sci.* 32 (1991) 497–507.
- [129] R.L. Farrow, A.S. Nagelberg, Raman spectroscopy of surface oxides at elevated temperatures, *Appl. Phys. Lett.* 36 (1980) 945–947. doi:10.1063/1.91659.
- [130] A.H. Goff, C. Pallotta, In Situ Raman Spectroscopy for the Study of Iron Relation to Solution Composition Passivity in A., *J. Electrochem. Soc.* 132 (1985) 2805–2806.
- [131] T. Ohtsuka, K. Kubo, N. Sato, Raman Spectroscopy of Thin Corrosion Films on Iron

- At 100 To 150 C in Air., *Corrosion*. 42 (1986) 476–481. doi:10.5006/1.3583054.
- [132] D. Thierry, D. Persson, C. Leygraf, In-Situ Raman Spectroscopy Combined with X-Ray Photoelectron Spectroscopy and Nuclear Microanalysis for Studies of Anodic Corrosion Film Formation on Fe-Cr Single Crystals, *J. Electrochem. Soc.* 135 (1988) 305. doi:10.1149/1.2095605.
- [133] J. Weissenrieder, C. Leygraf, In Situ Studies of Filiform Corrosion of Iron, *J. Electrochem. Soc.* 151 (2004) B165. doi:10.1149/1.1645263.
- [134] L. Kouisni, M. Azzi, M. Zertoubi, F. Dalard, S. Maximovitch, Phosphate coatings on magnesium alloy AM60 part 1: Study of the formation and the growth of zinc phosphate films, *Surf. Coatings Technol.* 185 (2004) 58–67. doi:10.1016/j.surfcoat.2003.10.061.
- [135] J. Zhang, C. Dai, J. Wei, Z. Wen, S. Zhang, C. Chen, Degradable behavior and bioactivity of micro-arc oxidized AZ91D Mg alloy with calcium phosphate/chitosan composite coating in m-SBF, *Colloids Surfaces B Biointerfaces*. 111 (2013) 179–187. doi:10.1016/j.colsurfb.2013.05.040.
- [136] A.A. Zuleta, E. Correa, C. Villada, M. Sepúlveda, J.G. Castaño, F. Echeverría, Comparative study of different environmentally friendly (Chromium-free) methods for surface modification of pure magnesium, *Surf. Coatings Technol.* 205 (2011) 5254–5259. doi:10.1016/j.surfcoat.2011.05.048.
- [137] D. Iqbal, A. Sarfraz, M. Stratmann, A. Erbe, Solvent-starved conditions in confinement cause chemical oscillations excited by passage of a cathodic delamination front, *Chem. Commun.* 51 (2015) 16041–16044. doi:10.1039/C5CC06468F.
- [138] R. Posner, A.M. Jubb, G.S. Frankel, M. Stratmann, H.C. Allen, Simultaneous in situ Kelvin probe and Raman spectroscopy analysis of electrode potentials and molecular structures at polymer covered salt layers on steel, *Electrochim. Acta.* 83 (2012) 327–334. doi:10.1016/j.electacta.2012.08.042.
- [139] D. Iqbal, A. Sarfraz, A. Erbe, Gradient in defect density of ZnO nanorods grown by cathodic delamination, a corrosion process, leads to end-specific luminescence, *Nanoscale Horizons*. 3 (2018) 58–65. doi:10.1039/c7nh00111h.
- [140] E.S.M. Sherif, R.M. Erasmus, J.D. Comins, In situ Raman spectroscopy and electrochemical techniques for studying corrosion and corrosion inhibition of iron in sodium chloride solutions, *Electrochim. Acta.* 55 (2010) 3657–3663. doi:10.1016/j.electacta.2010.01.117.
- [141] J.D. Ramsey, R.L. McCreery, In Situ Raman Microscopy of Chromate Effects on Corrosion Pits in Aluminum Alloy, *J. Electrochem. Soc.* 146 (1999) 4076.

doi:10.1149/1.1392594.

- [142] P. Cao, R. Gu, Z. Tian, Electrochemical and surface-enhanced raman spectroscopy studies on inhibition of iron corrosion by benzotriazole, *Langmuir*. 18 (2002) 7609–7615. doi:10.1021/la025570m.
- [143] F. Zhang, T. Brinck, B.D. Brandner, P.M. Claesson, A. Dedinaite, J. Pan, In situ confocal Raman micro-spectroscopy and electrochemical studies of mussel adhesive protein and ceria composite film on carbon steel in salt solutions, *Electrochim. Acta*. 107 (2013) 276–291. doi:10.1016/j.electacta.2013.05.078.
- [144] A. Samaniego, B.L. Hurley, G.S. Frankel, On the evidence for univalent Mg, *J. Electroanal. Chem.* 737 (2015) 123–128. doi:10.1016/j.jelechem.2014.04.013.
- [145] A. Bengtson, S. Hanstrom, in: *Proc. Fifth Int. Conf. Prog. Anal. Chem. Steel Met. Ind.*, 1999: pp. 47–54.
- [146] P.L. Larkins, The effect of water vapour on atom production by glow-discharge sputtering, *Spectrochim. Acta Part B At. Spectrosc.* 46 (1991) 291–299. doi:10.1016/0584-8547(91)80030-7.
- [147] T.J. Loving, W.W. Harrison, Simultaneous analysis of an abnormal glow discharge by atomic absorption spectrometry and mass spectrometry, *Anal. Chem.* 55 (1983) 1523–1526. doi:10.1021/ac00260a017.
- [148] K.R. Hess, W.W. Harrison, The Role of Metastable Atoms in Glow Discharge Ionization Processes, *Anal. Chem.* 60 (1988) 691–696. doi:10.1021/ac00158a019.
- [149] P.H. Ratliff, W.W. Harrison, The effects of water vapor in glow discharge mass spectrometry, *Spectrochim. Acta Part B At. Spectrosc.* 49 (1994) 1747–1757. doi:10.1016/0584-8547(94)80145-2.
- [150] A. Bogaerts, R. Gijbels, Effects of adding hydrogen to an argon glow discharge: overview of relevant processes and some qualitative explanations, *J. Anal. At. Spectrom.* 15 (2000) 441–449. doi:10.1039/a909779a.
- [151] V.-D. Hodoroaba, V. Hoffmann, E.B.M. Steers, K. Wetzig, Investigations of hydrogen in an argon glow discharge, *J. Anal. At. Spectrom.* 15 (2000) 1075–1080. doi:10.1039/b002367l.
- [152] V.-D. Hodoroaba, E.B.M. Steers, V. Hoffman, K. Wetzig, The effect of small quantities of hydrogen on a glow discharge in neon. Comparison with the argon case, *J. Anal. At. Spectrom.* 16 (2001) 43–49. doi:10.1039/b007527m.
- [153] R. Payling, M. Aeberhard, D. Delfosse, Improved quantitative analysis of hard coatings by radiofrequency glow discharge optical emission spectrometry (rf-GD-OES), *J. Anal. At. Spectrom.* 16 (2001) 50–55. doi:10.1039/b007543o.

- [154] T.W. Cain, I. Gonzalez-Afanador, N. Birbilis, J.R. Scully, The Role of Surface Films and Dissolution Products on the Negative Difference Effect for Magnesium: Comparison of Cl⁻ versus Cl⁻ Free Solutions, *J. Electrochem. Soc.* 164 (2017) C300–C311. doi:10.1149/2.1371706jes.
- [155] S. Feliu Jr, M.C. Merino, R. Arrabal, A.E. Coy, E. Matykina, XPS study of the effect of aluminium on the atmospheric corrosion of the AZ31 magnesium alloy, *Surf. Interface Anal.* 41 (2009) 143–150. doi:10.1002/sia.3004.
- [156] E.C.S. Transactions, T.E. Society, Chloride Ion Concentration Effects on Passivity Breakdown in Magnesium G. Williams, *Corrosion.* 58 (2014) 23–34. doi:10.5006/2328.
- [157] Y. Yang, F. Scenini, M. Curioni, A study on magnesium corrosion by real-time imaging and electrochemical methods: Relationship between local processes and hydrogen evolution, *Electrochim. Acta.* 198 (2016) 174–184. doi:10.1016/j.electacta.2016.03.043.
- [158] P. Dauphin-ducharme, J. Mauzeroll, Surface Analytical Methods Applied to Magnesium Corrosion, (n.d.). doi:10.1021/ac504576g.
- [159] S. Lebouil, O. Gharbi, P. Volovitch, K. Ogle, Mg dissolution in phosphate and chloride electrolytes : Insight into the mechanism of the negative difference effect ., *Corrosion.* 71 (2015) 234–241.
- [160] J. Światowska, P. Volovitch, K. Ogle, The anodic dissolution of Mg in NaCl and Na₂SO₄ electrolytes by atomic emission spectroelectrochemistry, *Corros. Sci.* 52 (2010) 2372–2378. doi:10.1016/j.corsci.2010.02.038.
- [161] O. Gharbi, N. Birbilis, Clarifying the Dissolution Mechanisms and Electrochemistry of Mg 2 Si as a Function of Solution pH, *J. Electrochem. Soc.* 165 (2018) C497–C501. doi:10.1149/2.1061809jes.
- [162] G.S. Frankel, A. Samaniego, N. Birbilis, Evolution of hydrogen at dissolving magnesium surfaces, *Corros. Sci.* 70 (2013) 104–111. doi:10.1016/j.corsci.2013.01.017.
- [163] D.S. Gandel, N. Birbilis, M.A. Easton, M.A. Gibson, The Influence of Mn on the Corrosion of Al-Free Mg Alloys, *18th Int. Corros. Cong.* 8 (2011) 1–9.
- [164] G. Baril, N. Pébère, Corrosion of pure magnesium in aerated and deaerated sodium sulphate solutions, *Corros. Sci.* 43 (2001) 471–484. doi:10.1016/S0010-938X(00)00095-0.
- [165] G. Baril, G. Galicia, C. Deslouis, N. Pébère, B. Tribollet, V. Vivier, An Impedance Investigation of the Mechanism of Pure Magnesium Corrosion in Sodium Sulfate

- Solutions, *J. Electrochem. Soc.* 154 (2007) C108. doi:10.1149/1.2401056.
- [166] L.G. Bland, K. Gusieva, J.R. Scully, Effect of Crystallographic Orientation on the Corrosion of Magnesium: Comparison of Film Forming and Bare Crystal Facets using Electrochemical Impedance and Raman Spectroscopy, *Electrochim. Acta.* 227 (2017) 136–151. doi:10.1016/j.electacta.2016.12.107.
- [167] R. Baddour-Hadjean, J.P. Pereira-Ramos, Raman microspectrometry applied to the study of electrode materials for lithium batteries, *Chem. Rev.* 110 (2010) 1278–1319. doi:Doi 10.1021/Cr800344k.
- [168] B. Downs, S. Robinson, H. Yang, P. Mooney, RRUFF Project, Dep. Geosci. Univ. Arizona. (2015). <http://rruff.info/>.
- [169] O.S. Pokrovsky, J. Schott, Experimental study of brucite dissolution and precipitation in aqueous solutions: Surface speciation and chemical affinity control, *Geochim. Cosmochim. Acta.* 68 (2004) 31–45. doi:10.1016/S0016-7037(03)00238-2.
- [170] S.R. Soniya, V.M. Nair, Synthesis and Characterization of Nanostructured Mg(OH)₂ and MgO, *Int. J. Sci. Res.* 5 (2016) 197–203. doi:10.1179/174328409X415020.
- [171] C. Henrist, J.P. Mathieu, C. Vogels, A. Rulmont, R. Cloots, Morphological study of magnesium hydroxide nanoparticles precipitated in dilute aqueous solution, *J. Cryst. Growth.* 249 (2003) 321–330. doi:10.1016/S0022-0248(02)02068-7.
- [172] B. Dabir, R.W. Peters, J.D. Stevens, Precipitation Kinetics of Magnesium Hydroxide in a Scaling System, *Ind. Eng. Chem. Fundam.* 21 (1982) 298–305. doi:10.1021/i100007a018.
- [173] K. Zeppenfeld, Electrochemical removal of calcium and magnesium ions from aqueous solutions, *Desalination.* 277 (2011) 99–105. doi:10.1016/j.desal.2011.04.005.
- [174] C.S. Grove, R. V. Jelinek, H.M. Schoen, Crystallization from Solution, *Adv. Chem. Eng.* 3 (1962) 1–60. doi:10.1016/S0065-2377(08)60057-5.
- [175] J.A. Dirksen, T.A. Ring, Fundamentals of Crystallization: Kinetic Effects on Particle Size Distributions and Morphology, *Chem. Eng. Sci.* 46 (1991) 2389–2427. doi:10.1016/0009-2509(91)80035-W.
- [176] O.S. Pokrovsky, J. Schott, Experimental study of brucite dissolution and precipitation in aqueous solutions: Surface speciation and chemical affinity control, *Geochim. Cosmochim. Acta.* 68 (2004) 31–45. doi:10.1016/S0016-7037(03)00238-2.
- [177] G. Williams, H.A.L. Dafydd, R. Grace, The localised corrosion of Mg alloy AZ31 in chloride containing electrolyte studied by a scanning vibrating electrode technique, *Electrochim. Acta.* 109 (2013) 489–501. doi:10.1016/j.electacta.2013.07.134.
- [178] G. Lefèvre, V. Pichot, M. Fédoroff, Controlling particle morphology during growth of

- bayerite in aluminate solutions, *Chem. Mater.* 15 (2003) 2584–2592. doi:10.1021/cm0310059.
- [179] H.A. Straten, P.L. Bruyn, Precipitation from Supersaturated Aluminate Solutions, *J. Colloid Interface Sci.* 102 (1984) 260–277.
- [180] J.H. Parker, D.W. Feldman, M. Ashkin, Raman Scattering by Optical Modes of Metals, in: G.B. Wright (Ed.), *Light Scatt. Spectra Solids Proc. Int. Conf. Held New York Univ. New York, Sept. 3--6, 1968*, Springer Berlin Heidelberg, Berlin, Heidelberg, 1969: pp. 389–397. doi:10.1007/978-3-642-87357-7_42.
- [181] J.R. Ferraro, *Low-Frequency Vibrations of Inorganic and Coordination Compounds*, Springer US, 2012. <https://books.google.fr/books?id=BbrSBwAAQBAJ>.
- [182] J. Kapitán, M. Dračínský, J. Kaminský, L. Benda, P. Bouř, Theoretical modeling of magnesium Ion imprints in the Raman scattering of water, *J. Phys. Chem. B.* 114 (2010) 3574–3582. doi:10.1021/jp9110508.
- [183] E.S. Gnanakumar, R.R. Gowda, S. Kunjir, T.G. Ajithkumar, P.R. Rajamohan, D. Chakraborty, C.S. Gopinath, MgCl₂·6CH₃OH: A simple molecular adduct and its influence as a porous support for olefin polymerization, *ACS Catal.* 3 (2013) 303–311. doi:10.1021/cs300730j.
- [184] R.J. Capwell, Raman spectra of crystalline and molten MgCl₂, *Chem. Phys. Lett.* 12 (1972) 443–446.
- [185] M. Taheri, J.R. Kish, N. Birbilis, M. Danaie, E.A. Mcnally, J.R. Mcdermid, Electrochimica Acta Towards a Physical Description for the Origin of Enhanced Catalytic Activity of Corroding Magnesium Surfaces, *Electrochim. Acta.* 116 (2014) 396–403. doi:10.1016/j.electacta.2013.11.086.
- [186] A. Atrens, G.-L. Song, F. Cao, Z. Shi, P.K. Bowen, Advances in Mg corrosion and research suggestions, *J. Magnes. Alloy.* 1 (2013) 177–200. doi:10.1016/j.jma.2013.09.003.
- [187] G.S. Frankel, S. Fajardo, M. Lynch, Introductory lecture on corrosion chemistry: a focus on anodic hydrogen evolution on Al and Mg, *Faraday Discuss.* 180 (2015) 11–33. doi:10.1039/C5FD00066A.
- [188] G. Baril, G. Galicia, C. Deslouis, N. Pébère, B. Tribollet, V. Vivier, An Impedance Investigation of the Mechanism of Pure Magnesium Corrosion in Sodium Sulfate Solutions, *J. Electrochem. Soc.* 154 (2007) C108. doi:10.1149/1.2401056.
- [189] S. Thomas, N.V. Medhekar, G.S. Frankel, N. Birbilis, Corrosion mechanism and hydrogen evolution on Mg, *Curr. Opin. Solid State Mater. Sci.* 19 (2015) 85–94. doi:10.1016/j.cossms.2014.09.005.

- [190] S.N. Mathaudhu, A.A. Luo, N.R. Neelameggham, E.A. Nyberg, W.H. Sillekens, Essential readings in magnesium technology, John Wiley, 2014. doi:10.1002/9781118859803.
- [191] N. Birbilis, T. Cain, J.S. Laird, X. Xia, J.R. Scully, a. E. Hughes, Nuclear Microprobe Analysis for Determination of Element Enrichment Following Magnesium Dissolution, ECS Electrochem. Lett. 4 (2015) C34–C37. doi:10.1149/2.0081510eel.
- [192] D. Höche, C. Blawert, S. V. Lamaka, N. Scharnagl, C. Mendis, M.L. Zheludkevich, The effect of iron re-deposition on the corrosion of impurity-containing magnesium, Phys.Chem.Chem.Phys. 18 (2015) 1279–1291. doi:10.1039/c5cp05577f.
- [193] M. Liu, S. Zanna, H. Ardelean, I. Frateur, P. Schmutz, G. Song, A. Atrens, P. Marcus, A first quantitative XPS study of the surface films formed, by exposure to water, on Mg and on the Mg-Al intermetallics: Al₃Mg₂ and Mg₁₇Al₁₂, Corros. Sci. 51 (2009) 1115–1127. doi:10.1016/j.corsci.2009.02.017.
- [194] Z.P. Cano, M. Danaie, J.R. Kish, J.R. McDermid, G.A. Botton, G. Williams, Physical characterization of cathodically-activated corrosion filaments on magnesium alloy AZ31B, Corrosion. 71 (2015) 146–159. doi:10.5006/1384.
- [195] K.A. Unocic, H.H. Elsentriecy, M.P. Brady, H.M. Meyer, G.L. Song, M. Fayek, R.A. Meisner, B. Davis, Transmission Electron Microscopy Study of Aqueous Film Formation and Evolution on Magnesium Alloys, J. Electrochem. Soc. 161 (2014) C302–C311. doi:10.1149/2.024406jes.
- [196] L. Yang, X. Zhou, M. Curioni, S. Pawar, H. Liu, Z. Fan, G. Scamans, G. Thompson, Corrosion Behavior of Pure Magnesium with Low Iron Content in 3.5 wt% NaCl Solution, J. Electrochem. Soc. 162 (2015) C362–C368. doi:10.1149/2.1041507jes.
- [197] L. Yang, X. Zhou, S.M. Liang, R. Schmid-Fetzer, Z. Fan, G. Scamans, J. Robson, G. Thompson, Effect of traces of silicon on the formation of Fe-rich particles in pure magnesium and the corrosion susceptibility of magnesium, J. Alloys Compd. 619 (2015) 396–400. doi:10.1016/j.jallcom.2014.09.040.
- [198] T. Cain, S.B. Madden, N. Birbilis, J.R. Scully, Evidence of the enrichment of transition metal elements on corroding magnesium surfaces using Rutherford backscattering spectrometry, J. Electrochem. Soc. 162 (2015) C228–C237. doi:10.1149/2.0541506jes.
- [199] D. Mercier, A. Seyeux, S. Zanna, J. Swiatowska, P. Marcus, Chemical surface analyses: towards the understanding of magnesium corrosion, in: Eurocorr, Montpellier, 2016.
- [200] R. Payling, J. Delwyn, A. Bengston, Glow Discharge Optical Emission Spectrometry, John Wiley, Chichester, 1997.

- [201] J.M. Hernández-López, A. Nemcova, X.L. Zhong, H. Liu, M.A. Arenas, S.J. Haigh, M.G. Burke, P. Skeldon, G.E. Thompson, Formation of barrier-type anodic films on ZE41 magnesium alloy in a fluoride/glycerol electrolyte, *Electrochim. Acta.* 138 (2014) 124–131. doi:10.1016/j.electacta.2014.05.147.
- [202] M.S. Palagonia, A. Nemcova, I. Kubena, M. Smid, S. Gao, H. Liu, X.L. Zhong, S.J. Haigh, M. Santamaria, F.D. Quarto, H. Habazaki, P. Skeldon, G.E. Thompson, Behavior of Alloying Elements during Anodizing of Mg-Cu and Mg-W Alloys in a Fluoride/Glycerol Electrolyte, *J. Electrochem. Soc.* 162 (2015) C487–C494. doi:10.1149/2.0761509jes.
- [203] A. Martín, A. Menéndez, R. Pereiro, N. Bordel, A. Sanz-Medel, Modifying argon glow discharges by hydrogen addition: Effects on analytical characteristics of optical emission and mass spectrometry detection modes, *Anal. Bioanal. Chem.* 388 (2007) 1573–1582. doi:10.1007/s00216-007-1291-2.
- [204] I.S. Molchan, G.E. Thompson, P. Skeldon, N. Trigoulet, P. Chapon, A. Tempez, J. Malherbe, L. Lobo Revilla, N. Bordel, P. Belenguer, T. Nelis, A. Zahri, L. Therese, P. Guillot, M. Ganciu, J. Michler, M. Hohl, The concept of plasma cleaning in glow discharge spectrometry, *J. Anal. At. Spectrom.* 24 (2009) 734–741. doi:10.1039/b818343k.
- [205] S. Cremel, E. Gadatek, P. Chapon, Breakthrough on GDOES Analysis Applied to Rough Metal Surfaces, in: *GD Day 2016*, 2016: p. 38. www.gd-day.com.
- [206] R. Payling, M. Aeberhard, D. Delfosse, Improved quantitative analysis of hard coatings by radiofrequency glow discharge optical emission spectrometry (rf-GD-OES), *J. Anal. At. Spectrom.* 16 (2001) 50–55. doi:10.1039/b007543o.
- [207] V.-D. Hodoraba, Wasserstoffeffekt und -analyse in der GDS - Anwendungen in der Werkstoffforschung (Hydrogen Effect and Analysis in GDS – Applications in Material Science), Technischen Universität Dresden, 2002.
- [208] L. Rossrucker, A. Samaniego, J. Grote, A.M. Mingers, C.A. Laska, N. Birbilis, G.S. Frankel, K.J.J. Mayrhofer, The pH Dependence of Magnesium Dissolution and Hydrogen Evolution during Anodic Polarization, *J. Electrochem. Soc.* 162 (2015) C333–C339. doi:10.1149/2.0621507jes.
- [209] N. Birbilis, G. Williams, K. Gusieva, A. Samaniego, M.A. Gibson, H.N. McMurray, Poisoning the corrosion of magnesium, *Electrochem. Commun.* 34 (2013) 295–298. doi:10.1016/j.elecom.2013.07.021.
- [210] W. Fürbeth, M. Stratmann, The delamination of polymeric coatings from electrogalvanised steel – a mechanistic approach., *Corros. Sci.* 43 (2001) 207–227.

doi:10.1016/S0010-938X(00)00047-0.

- [211] I. Puigdomenech, MEDUSA (Chemical Equilibrium Diagrams), (2010).
- [212] D. Schloffer, S. Bozorgi, P. Sherstnev, C. Lenardt, B. Gollas, Manufacturing and characterization of magnesium alloy foils for use as anode materials in rechargeable magnesium ion batteries, *J. Power Sources*. 367 (2017) 138–144. doi:10.1016/j.jpowsour.2017.09.062.
- [213] H. Hornberger, S. Virtanen, A.R. Boccaccini, Biomedical coatings on magnesium alloys - A review, *Acta Biomater.* 8 (2012) 2442–2455. doi:10.1016/j.actbio.2012.04.012.
- [214] Y. Zhang, J. Xu, Y.C. Ruan, M.K. Yu, M. O’Laughlin, H. Wise, D. Chen, L. Tian, D. Shi, J. Wang, S. Chen, J.Q. Feng, D.H.K. Chow, X. Xie, L. Zheng, L. Huang, S. Huang, K. Leung, N. Lu, L. Zhao, H. Li, D. Zhao, X. Guo, K. Chan, F. Witte, H.C. Chan, Y. Zheng, L. Qin, Implant-derived magnesium induces local neuronal production of CGRP to improve bone-fracture healing in rats, *Nat. Med.* 22 (2016) 1160–1169. doi:10.1038/nm.4162.
- [215] J. Gonzalez, R.Q. Hou, E.P.S. Nidadavolu, R. Willumeit-Römer, F. Feyerabend, Magnesium degradation under physiological conditions – Best practice, *Bioact. Mater.* 3 (2018) 174–185. doi:10.1016/j.bioactmat.2018.01.003.
- [216] M.A. Deyab, Decyl glucoside as a corrosion inhibitor for magnesium-air battery, *J. Power Sources*. 325 (2016) 98–103. doi:10.1016/j.jpowsour.2016.06.006.
- [217] F.W. Richey, B.D. McCloskey, A.C. Luntz, Mg Anode Corrosion in Aqueous Electrolytes and Implications for Mg-Air Batteries, *J. Electrochem. Soc.* 163 (2016) A958–A963. doi:10.1149/2.0781606jes.
- [218] M. Deng, D. Höche, S. V. Lamaka, D. Snihirova, M.L. Zheludkevich, Mg-Ca binary alloys as anodes for primary Mg-air batteries, *J. Power Sources*. 396 (2018) 109–118. doi:10.1016/j.jpowsour.2018.05.090.
- [219] D. Höche, S. V. Lamaka, B. Vaghefinazari, T. Braun, R.P. Petruskas, M. Fichtner, M.L. Zheludkevich, Performance boost for primary magnesium cells using iron complexing agents as electrolyte additives, *Sci. Rep.* 8 (2018) 1–9. doi:10.1038/s41598-018-25789-8.
- [220] M. Yuasa, X. Huang, K. Suzuki, M. Mabuchi, Y. Chino, Discharge properties of Mg-Al-Mn-Ca and Mg-Al-Mn alloys as anode materials for primary magnesium-air batteries, *J. Power Sources*. 297 (2015) 449–456. doi:10.1016/j.jpowsour.2015.08.042.
- [221] A. Alamdari, M.R. Rahimpour, N. Esfandiari, E. Nourafkan, Kinetics of magnesium hydroxide precipitation from sea bittern, *Chem. Eng. Process. Process Intensif.* 47

- (2008) 215–221. doi:10.1016/j.cep.2007.02.012.
- [222] W.F. Murphy, H.J. Bernstein, Raman Spectra and an Assignment of the Vibrational Stretching Region of Water, *J. Phys. Chem.* 76 (1971) 1147–1152.
- [223] B. Humbert, M. Alnot, F. Quilès, Infrared and Raman spectroscopical studies of salicylic and salicylate derivatives in aqueous solution, *Spectrochim. Acta - Part A Mol. Biomol. Spectrosc.* 54 (1998) 465–476. doi:10.1016/S1386-1425(97)00239-4.
- [224] M.C. Alvarez-Ros, S. Sánchez-Cortés, J. V. García-Ramos, Vibrational study of the salicylate interaction with metallic ions and surfaces, *Spectrochim. Acta - Part A Mol. Biomol. Spectrosc.* 56 (2000) 2471–2477. doi:10.1016/S1386-1425(00)00328-0.
- [225] D. Philip, A. John, C.Y. Panicker, H.T. Varghese, FT-Raman, FT-IR and surface enhanced Raman scattering spectra of sodium salicylate, *Spectrochim. Acta - Part A Mol. Biomol. Spectrosc.* 57 (2001) 1561–1566. doi:10.1016/S1386-1425(01)00395-X.
- [226] M.A. Elbagerma, G. Azimi, H.G.M. Edwards, A.I. Alajtal, I.J. Scowen, In situ monitoring of pH titration by Raman spectroscopy, *Spectrochim. Acta - Part A Mol. Biomol. Spectrosc.* 75 (2010) 1403–1410. doi:10.1016/j.saa.2010.01.008.
- [227] P.J. Goulet, R.F. Aroca, Chemical adsorption of salicylate on silver - A systematic approach to the interpretation of surface-enhanced vibrational spectra, *Can. J. Chem.* 82 (2004) 987–997. doi:10.1139/v04-075.
- [228] E.C. Yost, M.I. Tejedortejedor, M.A. Anderson, In situ cir-ftir characterization of salicylate complexes at the goethite aqueous-solution interface, *Environ. Sci. Technol.* 24 (1990) 822–828.
- [229] G. Świdorski, M. Kalinowska, I. Rusinek, M. Samsonowicz, Z. Rzączyńska, W. Lewandowski, Spectroscopic (IR, Raman) and thermogravimetric studies of 3d-metal cinchomerates and dinicotinates, *J. Therm. Anal. Calorim.* 126 (2016) 1521–1532. doi:10.1007/s10973-016-5818-7.
- [230] M. Karabacak, S. Bilgili, A. Atac, Molecular structure investigation of neutral, dimer and anion forms of 3,4-pyridinedicarboxylic acid: A combined experimental and theoretical study, *Spectrochim. Acta - Part A Mol. Biomol. Spectrosc.* 135 (2015) 270–282. doi:10.1016/j.saa.2014.06.130.
- [231] L. Wasylina, E. Kucharska, Z. Weglinski, A. Puszko, *Chemistry of Heterocyclic Compounds*, Vol.35, No. 2, 1999, *Chem. Heterocycl. Compd.* 35 (1999) 210–218.
- [232] Y. Song, X. Wang, S. Zhang, J. Wang, S. Gao, S. Chen, Lanthanide-Coordination Polymers with Pyridinedicarboxylic Acids : Syntheses , Structures , and Luminescent Properties, *c* (2016) 681–691. doi:10.1002/zaac.201600135.
- [233] I.L. Ardelean, L.B.N. Stoencea, D. Ficai, A. Ficai, R. Trusca, B.S. Vasile, G. Nechifor,

- E. Andronescu, Development of Stabilized Magnetite Nanoparticles for Medical Applications, *J. Nanomater.* 2017 (2017). doi:10.1155/2017/6514659.
- [234] S.R. Ryu, I. Noda, Y.M. Jung, Positional Fluctuation of IR Absorption Peaks: Frequency Shift of a Single Band or Relative Intensity Changes of Overlapped Bands, *Am. Lab.* 43 (2011) 40–43.
- [235] S.O.O.R. Ryu, I. Noda, Y.M.E.E. Jung, What is the Origin of Positional Fluctuation of Spectral Features : True Frequency Shift or Relative Intensity Changes of Two Overlapped Bands ?, 64 (2010) 1017–1021.
- [236] L. Pan, T. Frydel, M.B. Sander, X. Huang, J. Li, The Effect of pH on the Dimensionality of Coordination Polymers, (2001) 1271–1283.
- [237] M.C. Das, S.K. Ghosh, E.C. Sañudo, P.K. Bharadwaj, Coordination polymers with pyridine-2,4,6-tricarboxylic acid and alkaline-earth/lanthanide/transition metals: Synthesis and X-ray structures, *J. Chem. Soc. Dalt. Trans.* (2009) 1644–1658. doi:10.1039/b814066a.
- [238] B. Ay, N. Doğan, E. Yildiz, I. Kani, A novel three dimensional samarium(III) coordination polymer with an unprecedented coordination mode of the 2,5-pyridinedicarboxylic acid ligand: Hydrothermal synthesis, crystal structure and luminescence property, *Polyhedron.* 88 (2015) 176–181. doi:10.1016/j.poly.2014.12.035.
- [239] S. Caglar, E. Dilek, S.H. Alisir, B. Caglar, New copper (II) complexes including pyridine-2 , 5- dicarboxylic acid : synthesis , spectroscopic , thermal properties , crystal structure and how these complexes interact with purified PON 1 enzyme, 8972 (2016). doi:10.1080/00958972.2016.1188295.
- [240] R.K. Vakiti, B.D. Garabato, N.P. Schieber, M.J. Rucks, Y. Cao, C. Webb, J.B. Maddox, A. Celestian, W. Pan, B. Yan, Synthesis and Characterization of Two- and Three-Dimensional Calcium Coordination Polymers Built with Benzene-1 , 3 , 5-tricarboxylate and / or Pyrazine-2-carboxylate, (2012).

Appendices

This part of dissertation presents complementary results which were obtained during PhD study.

Appendix 1

Investigating the surface film on a corrosion resistant Mg-Li(-Al-Y-Zr) alloy

Y. Yan^{1,2}, O. Gharbi¹, A. Maltseva², X.B. Chen^{1,3}, Z.R. Zeng¹, S.W. Xu⁴, P. Volovich², M. Ferry⁵ and N. Birbilis^{*, 1}

¹*Department of Materials Science and Engineering, Monash University, VIC 3800, Australia.*

²*Chimie ParisTech, PSL Research University, CNRS, Institut de Recherche de Chimie Paris (IRCP), F-75005 Paris, France*

³*School of Engineering, RMIT University, Carlton, VIC 3053, Australia*

⁴*Research Institute (R & D Centre), Baosteel Group Corporation, Shanghai, China*

⁵*School of Materials Science and Engineering, The University of New South Wales, NSW 2052, Australia*

*Corresponding author: nick.birbilis@monash.edu (N. Birbilis) / Tel: +61 39905 4941.

Abstract

The surface film formed on an ultra-lightweight Mg-Li(-Al-Y-Zr) alloy was investigated. The high Li content (10.3 wt%) of this alloy led to the formation of a homogeneous body center cubic (bcc) crystal structure. Previous research reported that this bcc Mg-Li(-Al-Y-Zr) alloy demonstrated high corrosion resistance that was associated with the formation of a protective lithium carbonate (Li₂CO₃) surface film. Herein, the surface film that forms upon the bcc Mg-Li(-Al-Y-Zr) alloy following exposure to aqueous chloride containing electrolyte and ambient air was comprehensively studied by complementary methods, to provide a holistic representation of the alloy surface. In addition to scanning electron microscopy and transmission electron microscopy of focused ion beam prepared surface cross sections, the composition of the surface film was studied by grazing incidence

x-ray diffraction and Raman spectroscopy, both of which clearly showed Li_2CO_3 formation on the surface. The surface film structure was also investigated by glow discharge optical emission spectroscopy. The results indicated a complex and multi-layer surface film is formed upon Mg-Li(-Al-Y-Zr).

Keywords: Magnesium, Mg-Li alloy, lithium carbonate, surface film, scanning TEM, GIXRD, GDOES, Raman spectroscopy.

1. Introduction

Magnesium (Mg) alloys are the lightest structural metal available; however, owing to their intrinsic shortage on room temperature ductility and high corrosion susceptibility, the use of Mg alloys in industrial applications is still limited [1]. By alloying Mg with lithium (Li), the density of Mg alloys can be further reduced; moreover, the improvement in room temperature ductility can be significant as well [2-5]. Except for the low density and high ductility, Mg-Li alloys can also achieve many desirable properties such as high specific strength, high elastic modulus, weak anisotropy and good damping property etc. [6-9]. However, despite all the benefits, the poor corrosion resistance and creep resistance have restrained the development of Mg-Li alloys for industrial applications [10].

The structure of Mg-Li alloy is dictated by the Li content [11]. In fact, when Li content is lower than 5.7 wt%, hexagonal close-packed (hcp) α Mg-Li matrix forms; if Li content is between 5.7 wt% and 10.3 wt%, hcp α phase and bcc β phase coexist in the system and form a dual phase Mg-Li alloy. Furthermore, if Li exceeds 10.3 wt%, β phase bcc Mg-Li matrix becomes the predominant phase. To date, there are many studies investigated the impact of Li addition on the susceptibility of Mg alloys. Haferkamp et al. [4] reported that a small amount of Li addition (to obtain single-phase hcp Mg-Li alloys) could reduce the corrosion rate of pure Mg. Conversely, Song et al. [12] indicated that the corrosion resistance of a dual phase Mg-Li alloys (with 8 wt% of Li) was deteriorated through an accelerated cathodic reaction. On the other hand, Frost et al. [13] observed good corrosion resistance on single phase bcc Mg-Li alloys. In a research of bcc Mg-Li alloy, Xu et al. [14] reported the development of a Mg-Li(-Al-Y-Zr) alloy with 10.3 wt% of Li that possesses both good corrosion resistance and specific strength. Xu attributed the improvement in corrosion resistance of the Mg-Li(-Al-Y-Zr) alloy to the homogeneous bcc microstructure and, more importantly, the formation of a protective surface film.

The dissolution and surface film formation of Mg alloys have been largely documented and it is well known that Mg in neutral and chloride containing environments is not able to form a compact protective film [15, 16]. When Mg is exposed to an aqueous environment (in neutral or alkaline conditions), a Mg hydroxide surface film rapidly forms on the surface. However, because the Pilling-Bedworth ratio of Mg is less than 1, which means the volume of the oxide/hydroxide of Mg is smaller than the original volume of the Mg matrix, the surface film formed on Mg is usually highly defective [17]. In addition, Mg(OH)₂ surface film is not stable except in highly alkaline environment (pH > 10.5); which means Mg alloys are lack of protection from the aggressive environment in most of the common conditions. In Mg-Li

alloys, on the other hand, a more protective surface film was reported by many researchers [18-21]. In the study of Zeng et al. [18], carbonates and hydroxides (e.g. MgCO_3 and LiOH) formed on the surface of an air-exposed Mg-9.29Li-0.88Ca alloy sample were proposed to jam the cracks on the surface film and to limit further corrosion. In the study of Mg-Li-Al-Zn alloys, Lin et al. [19] attributed the improvement in corrosion resistance mainly to the formation of Al-Li particles that helped to form a more compact $\text{Mg}(\text{OH})_2$ surface film. In addition, Lin also reported the increase in Li^+ cation concentration in MgCl_2 test solution improved the corrosion resistance of Mg-Li-Al-Zn alloys. In the study of Witte et al. [20], the improvement in corrosion resistance of Li-containing Mg alloys was attributed to the increased alkalinity caused by the lithium dissolution, triggering faster $\text{Mg}(\text{OH})_2$ precipitation. During the open circuit exposure of a bcc Mg-Li(-Al-Y-Zr) alloy in 0.01 M NaCl, Hou et al. [21] observed a relatively low dissolution rate of Li (comparing with Mg) using an inductively coupled plasma mass spectroscopy (ICP-MS) coupled with an electrochemical flow cell. Hou reported a Mg/Li dissolution ratio of 3.4 : 1, which is much larger than the nominated compositional Mg/Li ratio of 2 : 1. Such a low dissolution rate of Li was attributed to the formation of a Li containing protective film that caused Li retention on the surface. In one study, Song et al. [22] characterised the composition of surface film on a dual phase Mg-8Li(wt%) alloy formed in ambient atmosphere using X-ray photoelectron spectroscopy (XPS). A four-layer structure was proposed by Song, that contains: a Li_2O and $\text{Mg}(\text{OH})_2$ out layer; a $\text{Mg}(\text{OH})_2$, Li_2O and MgO second layer; a $\text{Mg}(\text{OH})_2$, Li_2O , MgO and LiOH third layer; a MgO and Li_2O bottom layer. Note Song also observed high carbon concentration on surface film which was attributed to the adventitious hydrocarbons from the environment. In the study of Zeng et al. [18], a four-layer structure of surface film was also proposed that contains: an out layer of Li_2O , LiOH and Li_2CO_3 ; a second layer of LiOH , Li_2CO_3 , Li_2O_2 , MgCO_3 and LiH ; a third layer of Li_2O_2 , Li_2O , MgO and CaO ; a bottom layer includes matrix phases and oxides. However, both Song and Zeng studied dual phase Mg-Li alloys with intermediate Li content using X-ray photoelectron spectroscopy (XPS), in which the combination of α and β phases could make the accurate interpretation of surface film structure difficult. In the study on the bcc single-phase Mg-Li(-Al-Y-Zr) alloy of Xu et al. [14], the XPS results showed a relatively simple structure of surface film, which contains a Li_2CO_3 out layer, a compact $\text{Li}_2\text{O}/\text{MgO}$ intermediate layer and the Li depleted Mg matrix as bottom layer. This Li_2CO_3 -containing surface film formed on Mg-Li(-Al-Y-Zr) alloy was proposed to be similar to the passive film formed on Al or steel which can form spontaneously and can self-repair after damage. However, to date, accurate characterisation of Li distribution is still proved to be challenging. The conventional characterisation methods such as energy

dispersive x-ray spectroscopy (EDXS) cannot be used to directly characterise Li and the detailed structure of surface film formed on Mg-Li alloys remains undetermined. Herein, the morphology of the surface film formed on a bcc Mg-Li(-Al-Y-Zr) alloy after immersion and air-exposure was observed by scanning electron microscopy (SEM). The composition of the surface film was characterised by Raman spectroscopy and grazing incidence X-ray diffraction (GIXRD). Glow discharge optical emission spectroscopy (GDOES) was used to determine the elemental depth profile of alloy surface. Scanning transmission electron microscopy (STEM) was applied on carefully prepared surface film lamella to characterise the distribution of elements and the layered structure of the surface film. Even though Li cannot be detected by conventional EDXS, the maps of other elements in the system were collected, which could help to determine the structure of the surface film and to locate the proposed Li_2CO_3 film.

2. Experimental

2.1. Materials

An Mg-Li(-Al-Y-Zr) alloy with the following composition of 30.3% Li, 2.34% Al, 0.128% Y and 0.039% Zr (at%) was used. The alloy was extruded following casting, the details of which are also provided elsewhere [14]. The extruded billet was cold-rolled into 3 mm sheet. Then, the rolled sheet was solution treated at 380 °C for 5 min and subsequently water quenched. After 3 hours of ageing at 70 °C, the quenched alloy sheet was cold-rolled to a final thickness of 1 mm. Pristine samples were prepared as 30 mm × 100 mm × 1 mm rolled sheets.

2.2. Microstructure and surface morphology characterisation

Elemental composition prior to immersion as well as surface topography after immersion and air-exposure were characterised using a FEI Quanta 3D FEG scanning electron microscope (SEM) coupled with an energy dispersive X-ray spectrometer (EDXS). An acceleration voltage of 30 kV was used for the morphology characterisation using secondary electron (SE) mode; while the voltage used for acquiring EDXS maps and back scattered electron (BSE) images was 15 kV. SEM samples were ground to a 4000 grit finish using silicon carbide (SiC) under ethanol, followed by polishing (diamond paste) to 0.25 µm, before a final polish using 0.05 µm colloidal silica suspension.

2.3. Compositional characterisation of surface film

The composition of surface film was investigated by X-ray diffraction (XRD) using a Bruker D8 Advance X-ray diffractometer operating at 40 kV and 25 mA with copper target. A 2θ range of 15°-63° was used. The surface film composition was also characterised using grazing incidence X-ray diffraction (GIXRD) with an incidence angle of 0.2° and 1°. Mg-Li(-Al-Y-Zr) sample used for XRD and GIXRD spectra acquisition was prepared to a 0.05 µm colloidal silica suspension finish as per SEM specimens. After polishing, the sample was cleaned with ethanol and exposed in ambient environment for 4 hours.

Raman spectroscopy was also used for characterising the surface composition of Mg-Li(-Al-Y-Zr). Raman spectra were collected from the surface of two immersed then air-exposed samples using an InVia confocal Raman microscope (Renishaw). Scanning was performed using 532 nm laser, 50% power under 50× objective lens through 1800 l/mm visible grating. The broad scan spectra ranging from 100 to 4000 cm^{-1} Raman shifts were collected so that to observe the Li_2CO_3 peak at around 1090 cm^{-1} and the $\text{Mg}(\text{OH})_2$ peak at

3652 cm⁻¹ Raman shifts according to the RRUFF project database [23]. The spectra were collected with exposure time of 10 s under standard mode. The samples for Raman spectroscopy were ground to a 4000 grit finish using SiC paper under ethanol. The polished samples were immersed in 0.1 M NaCl at 25 °C for 24 hours, then one sample was exposed in ambient environment for 60 hours and the other sample was air-exposed for 60 days.

2.4. Characterisation of surface film structure

Glow discharge optical emission spectroscopy (GDOES) equipped with a Differential Interferometry Profiling (DiP) system able to monitor in real time the sputtered depth was used to obtain elemental depth profile on the surface of Mg-Li(-Al-Y-Zr) samples. In DiP system, a laser source is separated into two beams: the reference one is directed on the intact surface of the sample, while the depth sensing one is directed on the middle of the GD measured area. The interference between the two reflected beams permits a direct measurement of the crater depth in case of homogenous craters and flat surfaces. In case strongly rough material and/or very inhomogeneous erosion the measured depth can be not representative for the whole surface and the absolute values obtained in such cases should be taken with caution. The samples were sputtered using a GD-Profilier 2TM Glow discharge optical emission spectrometer (Horiba Jobin Yvon) at power of 17 W in argon atmosphere of 750 Pa and anode diameter of 4 mm. The spectral wavelengths (nm) used for detection are: Mg 285, Li 671, Al 396, Y 371, Zr 360, C 156 and O 130. Mg-Li(-Al-Y-Zr) samples were first ground to a 4000 grit finish using SiC paper under ethanol. Two different exposure conditions were applied to the ground sample before GDOES analysis: 1. immersed in 0.1 M NaCl at 25 °C for 24 hours then air-exposed for 60 hours in ambient environment; 2. immersed in 0.1 M NaCl at 25 °C for 24 hours then air-exposed for 60 days in ambient environment.

Scanning transmission electron microscopy (STEM) characterisation of surface film was performed using a FEI Tecnai G2 F20 S-TWIN FEG operating at an acceleration voltage of 200 kV. Bright field (BF) image, high angle annular dark field (HAADF) image, selected area diffraction (SAD) pattern and EDXS maps were collected. The electron transparent cross-section foil was extracted from the surface of the immersed then air-exposed SEM sample using a focused ion beam (FIB) system coupled in the FEI Quanta 3D FEG SEM. For preparing the foil, a thin layer of Pt was deposited on the area of interest to protect the surface film before sectioning with Ga ion beams. The sectioned foils were subsequently welded to Cu grids using Pt deposition through micro-manipulation (designated as “lift-out” process). Fine polishing was applied using Ga ion to reduce the final thickness of foils to about 100 nm.

3. Results

3.1. Initial microstructure of Mg-Li(-Al-Y-Zr) sample

The general microstructure and elemental composition of the surface prior immersion test are shown in SEM images (**Figure 1**).

The backscattered electron (BSE) images show a relatively homogeneous microstructure with the presence of several micrometre-size bright particles sporadically distributed on the surface of the polished Mg-Li(-Al-Y-Zr) sample (**Figure 1a**). Comparing with the SEM images of dual phase Mg-Li alloys [24], the absence of contrast indicates the formation of a relatively homogeneous bcc microstructure. However, the higher magnification image shows some bright points on the surface which may be formed by the reaction between the sample surface and the aqueous colloidal suspension polishing media used during sample preparation. The SEM-EDXS maps (**Figure 1b**) indicate the presence of Y, Zr and Al-rich particles. These observed particles should be the grain refiners in the system as Y and Zr are conventionally added into Mg alloys for grain refinement and strengthening purpose [25]. Note that, from the EDXS maps, the compositions of these observed particles are not identical.

The XRD spectrum collected on the Mg-Li(-Al-Y-Zr) sample surface without using grazing incidence angle is shown in **Figure 2**.

Except for the intense signal of bcc Mg-Li matrix, small signals of Al_2Y phase and Al_3Zr_5 phase are also observed; which confirms the observed Y, Zr and Al-rich particles are Al_2Y and Al_3Zr_5 grain refiners. Interestingly, there are small signals of hcp Mg-Li matrix that can be observed in the XRD spectrum, which means small volume of hcp Mg-Li structure was also formed in the proposed homogeneous bcc Mg-Li matrix.

3.2. Surface morphology after immersion

In previous studies [14, 21], the superior corrosion resistance of bcc Mg-Li(-Al-Y-Zr) alloy was attributed to the homogeneous microstructure and, more importantly, to the formation of a Li-rich surface film. Therefore, in this study, the specimen was immersed and air-exposed to sufficiently trigger the film formation then analysed via SEM (**Figure 3**).

The surface after exposure includes two distinct surface morphologies where the presence of localised attack is clearly illustrated by the interconnected trenches on the surface as well as quite significant proportion of relatively unaffected region, which are designated as “Type 1” and “Type 2” regions respectively. A large population of the bright surface particles are observed in the vicinity of the unaffected region and have no sign of localised corrosion,

which suggests these grain refiners would not induce localised attack in the Mg-Li(-Al-Y-Zr) alloy.

The SEM images of the immersed then air-exposed surface with higher magnifications are shown in **Figure 4** and **Figure 5** for the “Type 1” region and “Type 2” region respectively.

Even though the “Type 1” region covers large proportion of the surface, it can be observed that the damage to the alloy surface is superficial. Obvious fissures can be observed at the bottom of the trench-like attacked region, which are most likely caused by the dehydration of the surface corrosion product. The general structure inside the attacked region suggests the presence of porosity, which contains a large number of needle-shape objects of several hundred nm in length (**Figure 4**). The needle-like shape and the wide distribution of these objects are typical to $\text{Mg}(\text{OH})_2$ that can precipitate on the corroded surface of Mg alloys [26]. Although these objects are observed to cover the majority of the attacked regions, they do not form a compact film and, therefore, should not contribute much to protect the underlying matrix.

In contrast, on the “Type 2” relatively unaffected region, a film can be readily observed (**Figure 5**). The needle-shape objects can also be found in this region. However, they are mostly covered and connected by the film. The surface film in this region provides good surface coverage without obvious sign of crack or fissure.

3.3. Chemical composition of the surface film

The composition of the surface film was characterised using GIXRD and Raman spectroscopy. The GIXRD spectra acquired from the air exposed Mg-Li sample are shown in **Figure 2**.

From the air-exposed sample, GIXRD clearly identifies the presence of Li_2CO_3 on surface. Since the sample used for GIXRD was not immersed before air-exposure, almost no $\text{Mg}(\text{OH})_2$ signal can be observed (only visible at small 2θ angles). Moreover, it is interesting to notice that signal intensity of hcp and bcc Mg-Li phase changes dramatically with different incidental angles. When increasing the incidental angle from 0.2° to 1° , the hcp Mg-Li signal decreases dramatically comparing with the signal from the bcc Mg-Li phase. Moreover, the signal of hcp Mg-Li phase in conventional XRD spectrum is very weak while it is much stronger in the GIXRD spectra. (Note the extremely high intensity of bcc Mg-Li signal at large 2θ angles (around 52°) in XRD spectrum may be attributed to the influence of texture induced by cold rolling.) This change in the signal intensity of hcp and bcc Mg-Li phase represents a higher amount of hcp Mg-Li phase present near the surface.

Raman spectra collected on the immersed then air-exposed samples are displayed in **Figure 6**.

The presence of Li_2CO_3 and $\text{Mg}(\text{OH})_2$ are evidenced by the strong band at 1090 cm^{-1} and the band at 3652 cm^{-1} respectively. Comparing the samples with different air exposure duration, one can see that Li_2CO_3 signal increases significantly with air exposure time while $\text{Mg}(\text{OH})_2$ signal decreases. It can also be noted that the increasing fluorescent background between 1000 to 4000 cm^{-1} , which was attributed to the accumulation of magnesium hydroxycarbonates like dypingite [23].

3.4. Structure and distribution of chemical elements of surface film.

The GIXRD and Raman spectroscopy results indicate the presence of Li_2CO_3 and $\text{Mg}(\text{OH})_2$ on the surface of Mg-Li(-Al-Y-Zr) alloy at different exposure conditions. However, their distribution and the detailed structure of surface film still need to be determined. Therefore, GDOES elemental depth profiles were obtained for Mg-Li(-Al-Y-Zr) samples after different exposure conditions which are shown in **Figure 7**.

For the sample immersed for 24 hours then air-exposed for 60 hours, the spectrum clear indicates the formation of a surface film which seems to be rich in Mg and depleted of Li. The total thickness of the film is estimated at about $1.3\text{ }\mu\text{m}$ and it shows a bi-layer structure: at about $0.5\text{ }\mu\text{m}$ depth, there is an obvious change in Mg, Al and Li content, where the Mg signal starts to decrease with increasing depth while the Al and Li start to appear in the film. This change in Mg, Al and Li signals may suggest the existence of at least two different layers in the surface film: the outer layer that is rich in Mg but depleted with Al and Li; the inner layer that contains a bit less Mg but have small amount of Al and Li. O and C can be observed all over the surface film. It is also noted that small amount of Li can be observed at the outermost region.

For the sample immersed for 24 hours then air-exposed for 60 days, the total film thickness is estimated to be about $1.75\text{ }\mu\text{m}$. Comparing with the sample that was air-exposed for 60 hours, the spectrum shows the existence of an outer layer that is rich in Li. The outer layer (about $0.25\text{ }\mu\text{m}$ of surface film) contains only Li, O, and C which is logically to attribute to Li_2CO_3 . The content of Li decreases after $0.9\text{ }\mu\text{m}$ in depth indicating the presence of a relatively Li-lean inner layer. Comparing with the outer layer, the inner layer contains less Li but more Mg, Al and Y. No detectable Zr signal can be observed on any sample which may be caused by the low concentration of Zr in the Mg-Li(-Al-Y-Zr) ($0.039\text{ at}\%$). However, it is worth a notice that the thickness measurement of surface film by GDOES is not very accurate for the strongly corroded surfaces because the DiP result can be significantly influenced by

the surface roughness. Therefore, to obtain the more accurate thickness values and to observe the morphology of each layer, STEM experiments were performed.

STEM characterisation was conducted on foils of the surface film sectioned and “lift-out” using FIB from the “Type 2” region of the immersed then air-exposed sample surface given a film was observed by SEM in this region. The maps of the major elements in the system (except Li) together with the corresponding BF and HAADF images are shown in **Figure 8**.

From the BF and HAADF images, the structure of surface film can be roughly divided into two major layers. The outer layer (except the Pt film which was deposited for sample preparation process) is a porous layer containing needle-shape objects. Judging by the shape and distribution of these objects, they are proposed to be the same needle-shape objects observed by SEM. The EDXS elemental maps confirm the presence of Mg and O in these objects which, together with the results of Raman spectroscopy, further corroborate that these objects are $\text{Mg}(\text{OH})_2$ (H cannot be detected by EDXS). In previous study, it was reported that the dissolution-precipitation process could result in the formation of a porous and platelet outer layer of $\text{Mg}(\text{OH})_2$ when immersing Mg in water [27]. The high porosity and the shape of $\text{Mg}(\text{OH})_2$ objects suggest this porous outer layer was also formed by the re-precipitation process of Mg during immersion. Under the porous outer layer, a more compact inner layer can be found. The inner layer exhibits a more complex composition, mostly comprise of Mg, C, O and Al. It can be clearly observed that the Al is present in the inner layer but not in the outer layer of surface film, which correlates with GDOES (**Figure 7a**). While it is not shown here, Y and Zr were not detected by the EDXS, probably due to the relatively low concentration of these alloying elements and their segregation at large grain refiners.

Except for the relatively thick outer layer and inner layer, at the boundary between the inner and outer layers of surface film, relatively strong Al signals can be observed in many discontinuous particles in a thin intermediate layer. The intermediate Al-rich layer is about 30 nm in thickness and it also contains signals of O, C and Mg which are overlapping with the signal of Al. In addition to the Al-rich intermediate layer, another thin layer can be observed through the O map, where a thin layer with a thickness of around 15 nm to 30 nm can be observed on top of the porous outer layer. Judging by the morphology, this thin layer may correspond to the surface film observed by SEM that covers the needle-shape $\text{Mg}(\text{OH})_2$ objects. There are only O and C while no Y, Zr, Al nor Mg in this thin layer. Therefore, it is proposed that the thin layer of O signal observed by STEM is actually originated from a layer of Li_2CO_3 given the Li cannot be detected by EDXS. Moreover, GDOES also observed small amount of Li at the outer most part of the surface film on the sample even with relatively short

air exposure time of 60 hours (**Figure 7a**). Therefore, it can be confirmed that there is a layer of Li_2CO_3 formed on top of the proposed out porous layer. In addition, by careful comparison of Mg, O and C maps, small amount of the Mg lean but O and C rich region can also be found near the needle-shape $\text{Mg}(\text{OH})_2$ objects, which may suggest some Li_2CO_3 also presents in the porous outer layer.

To confirm the existence of Li_2CO_3 , SAD was also performed on a surface film lamella. A SAD pattern collected at the outer layer of surface film and the corresponding TEM image are shown in **Figure 9**.

In the SAD pattern, the presence of MgO can be clearly identified, which should mainly be found at the inner layer of surface film formed on the immersed Mg surface [28]. In addition, small cellular structures can be clearly observed at the inner layer in the STEM image. In the study of Nordlien et al. [27, 29] the formation of this kind of cellular structure was proposed to be formed by the decomposition of hydroxides during electron microscopy characterisation. Therefore, it is proposed that the intense signal of MgO observed at the outer layer of surface film is also caused by the decomposition of $\text{Mg}(\text{OH})_2$. Except for the intense diffraction ring of MgO, the SAD pattern also exhibits a single but weak ring that is agreed well with (001) plane of Li_2CO_3 .

4. Discussion

The STEM visual inspection, coupled with the analytical GDOES and GIXRD results, indicates the surface film formed on Mg-Li(-Al-Y-Zr) after 24 hours of immersion in 0.1 M NaCl then 7 days of air-exposure may be composed of four layers: I . the outer most Li_2CO_3 layer; II . the porous outer layer that contains needle-shape $\text{Mg}(\text{OH})_2$ objects; III . the thin Al-rich intermediate layer; IV . the relatively compact inner layer.

In the study of Xu et al. [14], a similar outer most Li_2CO_3 layer was observed by XPS on a Mg-Li(-Al-Y-Zr) sample which is propose to be protective to the underlying matrix. However, in the study of Zeng et al. [18] and Song et al. [22], the outermost layer of surface films formed on Mg-Li alloys were observed to contain Li_2O or a combination of Li_2O , LiOH and Li_2CO_3 . Since the standard enthalpy of Li_2CO_3 is much lower than the LiOH and Li_2O , the formation of Li_2CO_3 would be more stable and favoured [18]. Therefore, the observation of Li_2O or LiOH on the surface film should be attributed to the insufficient air-exposure time that limited the contact of CO_2 to the alloy surface.

As shown in the Raman spectrum in **Figure 6b**, very intense signal of $\text{Mg}(\text{OH})_2$ was observed on sample that was immersed in 0.1 M NaCl for 24 hours then air-exposed for 60 hours. However, the $\text{Mg}(\text{OH})_2$ signal decreased dramatically after 60 days of air exposure. Since the standard enthalpy of MgCO_3 is lower than $\text{Mg}(\text{OH})_2$ and MgO , the $\text{Mg}(\text{OH})_2$ on the surface of Mg-Li alloys may react with CO_2 in air and form carbonate [22]. In Mg alloys, the formation of MgCO_3 in the surface film is also proposed to be protective to the alloy matrix [30]. However, the Raman spectroscopy did not detect any signal of MgCO_3 on the surface. On the other hand, a hug florescence between 1000 cm^{-1} and 4000 cm^{-1} Raman shifts can be observed on the spectra, especially for the sample that was air-exposed for 60 days. This florescence is similar to the florescence created by dypingite ($\text{Mg}_5(\text{CO}_3)_4(\text{OH})_2 \cdot 5\text{H}_2\text{O}$) from RRUFF database [23]. Since the dypingite is one of the possible product when $\text{Mg}(\text{OH})_2$ reacts with CO_2 [31], the decrease of $\text{Mg}(\text{OH})_2$ signal after long air-exposure time may be attributed to the reaction of $\text{Mg}(\text{OH})_2$ with CO_2 in air that formed dypingite. Just like the formation of Li_2CO_3 , the formation of dypingite is also limited by the amount of CO_2 in environment and should progress slowly in air.

Between the inner and outer layer of surface film, an Al-rich layer was observed by STEM but not by GDOES, which may be caused by the low concentration of Al and the small thickness (about 30 nm) of the Al-rich layer. In previous studies, Al-rich layer could be easily observed in the surface film of Mg alloys with high Al content (like in Mg alloys AZ80 or AZ91) [32, 33]. This kind of Al-rich layer was observed to form at the inner-most part of

surface film and was thought to help preventing dissolution of the underlying matrix. However, such Al-rich layer was not readily observed in Mg-Al alloys with relatively low Al content like AZ31 [33, 34]. In the case of the Mg-Li(-Al-Y-Zr) alloy, the Al concentration is relatively low (2.34 at%) and the formation of a thick Al-rich oxide/hydroxide layer was not observed. Moreover, the presence of C, O and Mg in the Al-rich layer may indicate the formation of MgCO₃ (or dypingite) as well as Al(OH)₃ in this layer. However, from the study of Al alloys, Li was proposed to be able to easily react with Al hydroxide and form Li layered double hydroxide (LDH) [35, 36]. The Li-LDH (Li₂[Al₂(OH)₆]₂·CO₃·nH₂O) is proposed to be able to form as particles with very small grain size on the surface [37]; which is in accordance with the small and segregated Al-rich particles observed by STEM. Therefore, it is proposed that the relatively intense signal of Al observed in the thin Al-rich layer comes from the small Li-LDH (Li₂[Al₂(OH)₆]₂·CO₃·nH₂O) particles. In the study of Visser et al. [37], the Li-LDH was also proposed to be able to form a compact protective layer. However, the low Al content in the Mg-Li(-Al-Y-Zr) alloy could limit the protective ability of Li-LDH which is corroborated by the discontinuous nature of the LDH particles. In a recent research of binary Mg-Li systems, Li et al. [38] demonstrated that the single phase bcc Mg-Li alloy (with 14 wt% Li) possesses better corrosion resistance than hcp Mg-Li alloy (with 4 wt% Li) and dual phase Mg-Li alloy (with 7.5 wt% Li). The results obtained by Li indicate the dissolution protection ability of bcc Mg-Li alloy does not necessitate other alloying elements. Therefore, the influence of the observed Al in the surface film to the dissolution protection ability of the Mg-Li(-Al-Y-Zr) may be limited and merits further study.

In the study of Xu et al. [14], a depletion of Li was reported in the matrix near the surface film of a Mg-Li(-Al-Y-Zr) alloy. Herein, GDOES clearly observed similar depletion of Li near the surface film after exposure (**Figure 7**). Moreover, GIXRD showed higher hcp Mg-Li signal when using smaller incidental angle. Given the sample used for GIXRD was only air-exposed for 4 hours without immersion, the oxidation to the sample surface should be limited and very superficial and the selective oxidation/dissolution of bcc Mg-Li phase should be limited. Therefore, the observed high intensity hcp Mg-Li signal in the GIXRD spectra may suggest the bcc Mg-Li matrix near the surface film transferred into hcp Mg-Li structure during exposure. Since the hcp Mg-Li phase is a relatively Li lean phase comparing with the bcc Mg-Li phase, the depletion of Li may also indicate the formation of Li lean phase near the surface. From previous study, a combination of hcp Mg-Li phase and bcc Mg-Li phase was proposed to be very detrimental to the corrosion resistance of the alloy owing to the galvanic coupling between different phases [18, 38, 39]. The formation of the hcp Mg-Li

phase near the surface can disturb the homogeneity of the microstructure and may be potentially harmful to the corrosion resistance of the alloy.

A schematic that illustrates the structure of surface film formed on the Mg-Li(-Al-Y-Zr) alloy is proposed in **Figure 10**.

5. Conclusions

The surface composition, structure and elemental distribution of the protective film formed upon Mg-Li(-Al-Y-Zr) after immersion in aqueous chloride electrolyte and air-exposure was studied by complementary characterisation methods. The utilisation of a number of methods was necessitated to provide a holistic interpretation of the alloy surface – which included the need for physical observation and chemical analysis through the surface film. Furthermore, the requirement to determine lithium concentration (not possible by EDXS) was possible by techniques with no imaging but spectroscopic capability. From the results herein, the following conclusions may be drawn:

1. A surface film that provides good surface coverage was observed by SEM. There were superficial regions of ‘attack’ on the Mg-Li(-Al-Y-Zr) alloy surface, with features that do not correspond to significant visual corrosion to the eye. Such regions were seen to contain a higher proportion of surface film relative to the unaffected regions of surface.
2. The cross section of the surface film as revealed by STEM, indicate a multilayered structure, including a well-defined outer porous and inner compact layer. When coupling visual inspection with analytical spectroscopic methods, the surface film upon Mg-Li(-Al-Y-Zr) was characterised as having four layers: the outermost Li_2CO_3 layer; a porous layer that is also comprised of needle-shaped $\text{Mg}(\text{OH})_2$ objects; a thin intermediate layer that contains a relatively intense signal of Al; and a more compact inner layer that may contain $\text{Mg}(\text{OH})_2$, MgO , as well as Li_2CO_3 and dypingite ($\text{Mg}_5(\text{CO}_3)_4(\text{OH})_2 \cdot 5\text{H}_2\text{O}$). In addition, the sub-outer-surface depletion of Li was detected by GDOES and the formation of hcp Mg-Li phase was observed via GIXRD. This may suggest a phase transformation occurs during exposure as Li is selectively dissolved from the bulk alloy – locally transforming the Li-rich bcc Mg-Li matrix near the surface to the Li-lean hcp Mg-Li phase. This phenomenon merits future, focused study.
3. A film that contains only Li_2CO_3 was observed at the outermost area of the surface film. This film of Li_2CO_3 was relatively thin with short air-exposure time (around 15 to 30 nm after 7 days of air-exposure, measured by STEM) but could grow to a much larger thickness after longer air-exposure (around 250 nm after 60 days of air-exposure, measured by GDOES).
4. Dypingite florescence was observed by Raman spectroscopy after air-exposure for 60 hours and became more intense after air-exposure for 60 days. It is proposed that

the $\text{Mg}(\text{OH})_2$ in the surface film gradually transformed into dypingite by reacting with CO_2 in air.

5. The thin Al-rich intermediate layer may contain Li-LDH ($\text{Li}_2[\text{Al}_2(\text{OH})_6]_2 \cdot \text{CO}_3 \cdot n\text{H}_2\text{O}$) particles. However, judging by the morphology of the proposed LDH particles and the low Al content in the alloy, the protection ability of this Al-rich layer is unknown.

Acknowledgements

NB is supported by Woodside Energy. We acknowledge financial support from the Australian Research Council and Baosteel Group. The Monash Centre for Electron Microscopy and the Monash X-ray Platform were utilised for this work.

References

- [1] T.B. Abbott, Magnesium: Industrial and Research Developments Over the Last 15 Years, *Corrosion*, 71 (2015) 120-127.
- [2] F.W. Bach, M. Schaper, C. Jaschik, Influence of Lithium on hcp Magnesium Alloys, *Materials Science Forum*, 419-422 (2003) 1037-1030.
- [3] R. Ninomiya, K. Miyake, A study of superlight and superplastic Mg-Li based alloys, *Journal of Japan Institute of Light Metals*, 51 (2001) 509-513.
- [4] H. Haferkamp, R. Boehm, U. Holzkamp, C. Jaschik, V. Kaese, M. Niemeyer, Alloy Development, Processing and Applications in Magnesium Lithium Alloys, *Materials Transactions*, 42 (2001) 1160-1166.
- [5] A.M. Russell, L.S. Chumbley, V.B. Gantovnik, K. Xu, Y. Tian, F.C. Laabs, Anomalously high impact fracture toughness in B.C.C. Mg-Li between 4.2K and 77K, *Scripta Materialia*, 39 (1998) 1663-1667.
- [6] D.K. Xu, T.T. Zu, M. Yin, Y.B. Xu, E.H. Han, Mechanical properties of the icosahedral phase reinforced duplex Mg-Li alloy both at room and elevated temperatures, *Journal of Alloys and Compounds*, 582 (2014) 161-166.
- [7] C.-W. Yang, T.-S. Lui, L.-H. Chen, H.-E. Hung, Tensile mechanical properties and failure behaviors with the ductile-to-brittle transition of the $\alpha+\beta$ -type Mg-Li-Al-Zn alloy, *Scripta Materialia*, 61 (2009) 1141-1144.
- [8] W.A. Counts, M. Friák, D. Raabe, J. Neugebauer, Using ab initio calculations in designing bcc Mg-Li alloys for ultra-lightweight applications, *Acta Materialia*, 57 (2009) 69-76.
- [9] J.-M. Song, T.-X. Wen, J.-Y. Wang, Vibration fracture properties of a lightweight Mg-Li-Zn alloy, *Scripta Materialia*, 56 (2007) 529-532.
- [10] E. Ghali, W. Dietzel, K.-U. Kainer, General and localized corrosion of magnesium alloys: A critical review, *J. of Materi Eng and Perform*, 13 (2004) 7-23.
- [11] A.A. Nayeb-Hashemi, J.B. Clark, in: A.A. Nayeb-Hashemi, J.B. Clark (Eds.) *Phase diagrams of binary magnesium alloys*, ASM International, Metals Park, OH, 1988, pp. 184-194.
- [12] Y. Song, D. Shan, R. Chen, E.H. Han, Corrosion characterization of Mg-8Li alloy in NaCl solution, *Corrosion Science*, 51 (2009) 1087-1094.
- [13] P.D. Frost, F.W. Fink, H.A. Pray, J.H. Jackson, Results of Some Marine Atmosphere Corrosion Tests on Magnesium-Lithium Alloys, *Journal of The Electrochemical Society*, 102 (1955) 215-218.

- [14] W. Xu, N. Birbilis, G. Sha, Y. Wang, J.E. Daniels, Y. Xiao, M. Ferry, A high-specific-strength and corrosion-resistant magnesium alloy, *Nature Materials*, 14 (2015) 1229-1235.
- [15] K. Gusieva, C.H.J. Davies, J.R. Scully, N. Birbilis, Corrosion of magnesium alloys: the role of alloying, *International Materials Reviews*, 60 (2015) 169-194.
- [16] M. Esmaily, J.E. Svensson, S. Fajardo, N. Birbilis, G.S. Frankel, S. Virtanen, R. Arrabal, S. Thomas, L.G. Johansson, Fundamentals and advances in magnesium alloy corrosion, *Progress in Materials Science*, 89 (2017) 92-193.
- [17] R.W. Revie, H.H. Uhlig, *Corrosion and corrosion control: an introduction to corrosion science and engineering*, 4th ed., John Wiley & Sons, Inc., Hoboken, 2008.
- [18] R.C. Zeng, L. Sun, Y.F. Zheng, H.Z. Cui, E.H. Han, Corrosion and characterisation of dual phase Mg-Li-Ca alloy in Hank's solution: The influence of microstructural features, *Corrosion Science*, 79 (2014) 69-82.
- [19] M.C. Lin, C.Y. Tsai, J.Y. Uan, Electrochemical behaviour and corrosion performance of Mg-Li-Al-Zn anodes with high Al composition, *Corrosion Science*, 51 (2009) 2463-2472.
- [20] F. Witte, V. Kaese, H. Haferkamp, E. Switzer, A. Meyer-Lindenberg, C.J. Wirth, H. Windhagen, In vivo corrosion of four magnesium alloys and the associated bone response, *Biomaterials*, 26 (2005) 3557-3563.
- [21] L. Hou, M. Raveggi, X.-B. Chen, W. Xu, K.J. Laws, Y. Wei, M. Ferry, N. Birbilis, Investigating the Passivity and Dissolution of a Corrosion Resistant Mg-33at.%Li Alloy in Aqueous Chloride Using Online ICP-MS, *Journal of The Electrochemical Society*, 163 (2016) C324-C329.
- [22] Y. Song, D. Shan, R. Chen, E.H. Han, Investigation of surface oxide film on magnesium lithium alloy, *Journal of Alloys and Compounds*, 484 (2009) 585-590.
- [23] B. Lafuente, R.T. Downs, H. Yang, N. Stone, The power of databases: The RRUFF project, in: T. Armbruster, R.M. Danisi (Eds.) *Highlights in Mineralogical Crystallography*, De Gruyter, Inc., Berlin, 2015.
- [24] M.V. Kral, B.C. Muddle, J.F. Nie, Crystallography of the bcc/hcp transformation in a Mg-8Li alloy, *Materials Science and Engineering: A*, 460 (2007) 227-232.
- [25] B. Liu, M. Zhang, R. Wu, Effects of Nd on microstructure and mechanical properties of as-cast LA141 alloys, *Materials Science and Engineering: A*, 487 (2008) 347-351.

[26] C. Ke, Y. Wu, Y. Qiu, J. Duan, N. Birbilis, X.-B. Chen, Influence of surface chemistry on the formation of crystalline hydroxide coatings on Mg alloys in liquid water and steam systems, *Corrosion Science*, 113 (2016) 145-159.

[27] J.H. Nordlien, S. Ono, N. Masuko, K. Nisancioglu, A TEM investigation of naturally formed oxide films on pure magnesium, *Corrosion Science*, 39 (1997) 1397-1414.

[28] M. Taheri, R.C. Phillips, J.R. Kish, G.A. Botton, Analysis of the surface film formed on Mg by exposure to water using a FIB cross-section and STEM-EDS, *Corrosion Science*, 59 (2012) 222-228.

[29] J.H. Nordlien, K. Nisancioglu, S. Ono, N. Masuko, Morphology and Structure of Water-Formed Oxides on Ternary MgAl Alloys, *Journal of The Electrochemical Society*, 144 (1997) 461-466.

[30] M. Shahabi-Navid, M. Esmaily, J.-E. Svensson, M. Halvarsson, L. Nyborg, Y. Cao, L.-G. Johansson, NaCl-Induced Atmospheric Corrosion of the MgAl Alloy AM50-The Influence of CO₂, *Journal of The Electrochemical Society*, 161 (2014) C277-C287.

[31] A. Botha, C.A. Strydom, Preparation of a magnesium hydroxy carbonate from magnesium hydroxide, *Hydrometallurgy*, 62 (2001) 175-183.

[32] R.C. Phillips, J.R. Kish, Nature of Surface Film on Matrix Phase of Mg Alloy AZ80 Formed in Water, *Corrosion*, 69 (2013) 813-820.

[33] A. Pardo, M.C. Merino, A.E. Coy, R. Arrabal, F. Viejo, E. Matykina, Corrosion behaviour of magnesium/aluminium alloys in 3.5 wt.% NaCl, *Corrosion Science*, 50 (2008) 823-834.

[34] J.H. Nordlien, K. NişancioĖu, S. Ono, N. Masuko, Morphology and Structure of Oxide Films Formed on MgAl Alloys by Exposure to Air and Water, *Journal of The Electrochemical Society*, 143 (1996) 2564-2572.

[35] G.R. Williams, D. O'Hare, A Kinetic Study of the Intercalation of Lithium Salts into Al(OH)₃, *The Journal of Physical Chemistry B*, 110 (2006) 10619-10629.

[36] P. Visser, Y. Gonzalez-Garcia, J.M.C. Mol, H. Terryn, Mechanism of Passive Layer Formation on AA2024-T3 from Alkaline Lithium Carbonate Solutions in the Presence of Sodium Chloride, *Journal of The Electrochemical Society*, 165 (2018) C60-C70.

[37] P. Visser, Y. Liu, X. Zhou, T. Hashimoto, G.E. Thompson, S.B. Lyon, L.G.J. van der Ven, A.J.M.C. Mol, H.A. Terryn, The corrosion protection of AA2024-T3 aluminium alloy by leaching of lithium-containing salts from organic coatings, *Faraday Discussions*, 180 (2015) 511-526.

[38] C.Q. Li, D.K. Xu, X.-B. Chen, B.J. Wang, R.Z. Wu, E.H. Han, N. Birbilis, Composition and microstructure dependent corrosion behaviour of Mg-Li alloys, *Electrochimica Acta*, 260 (2018) 55-64.

[39] Y.W. Song, D.Y. Shan, R.S. Chen, E.H. Han, Corrosion resistance of Mg-8.8Li alloy compared with AZ91, *Corrosion Engineering, Science and Technology*, 46 (2011) 719-723.

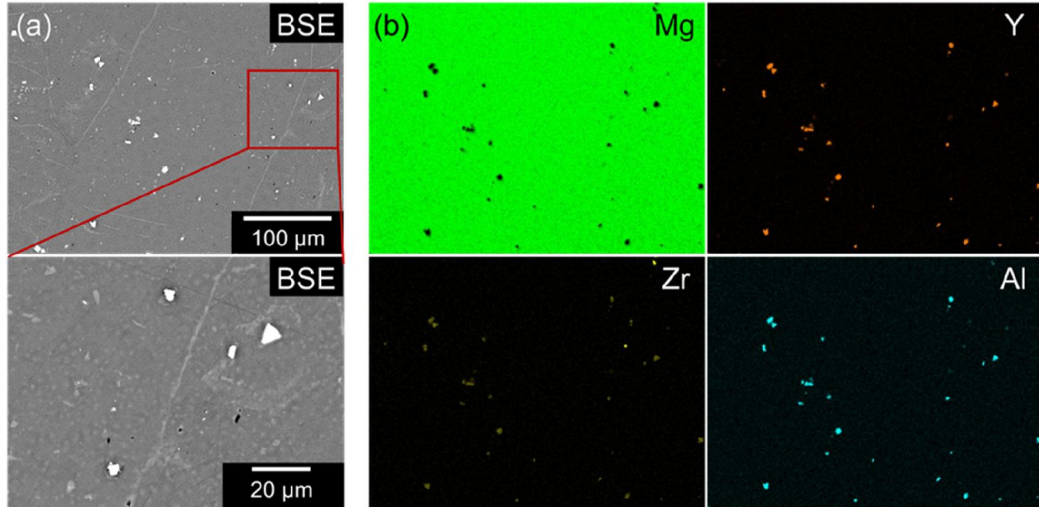


Figure 1. (a) Backscattered electron images of polished Mg-Li(-Al-Y-Zr) alloy sample and (b) corresponding EDXS maps.

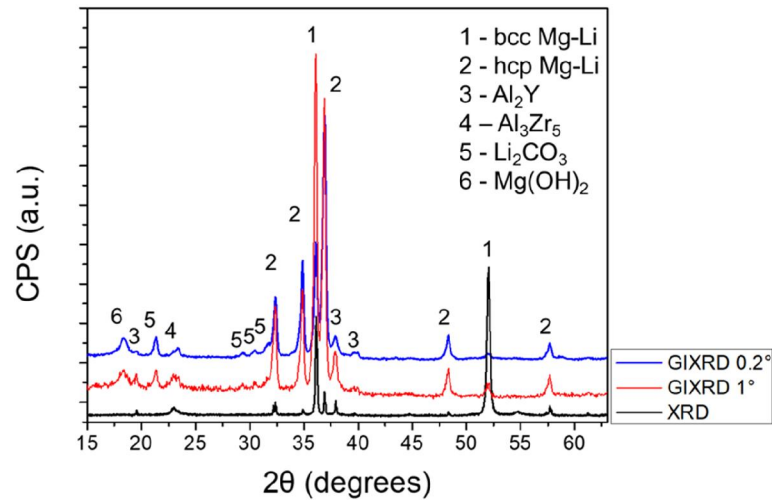


Figure 2. XRD spectra of the Mg-Li(-Al-Y-Zr) alloy after air-exposure for 4 hours. GIXRD spectra were obtained with incidental angles of 0.2° and 1° . An XRD spectrum without using small incidental angle was also acquired.

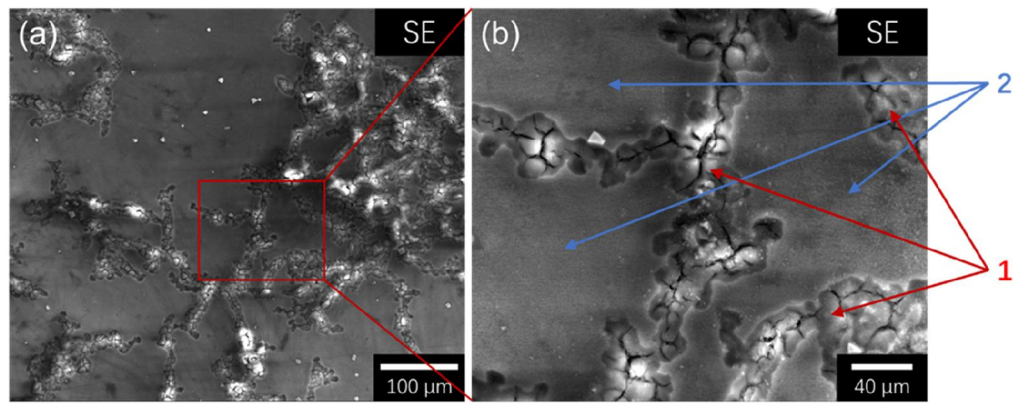


Figure 3. Secondary electron images of Mg-Li(-Al-Y-Zr) alloy sample after immersion in 0.1 M NaCl at 25 °C for 24 hours then air-exposed for 7 days: (a) image at low magnification, (b) image at higher magnification. Two types of surface morphology can be observed on sample surface, with “Type 1” be the region of surface attack and “Type 2” be the relatively unaffected region.

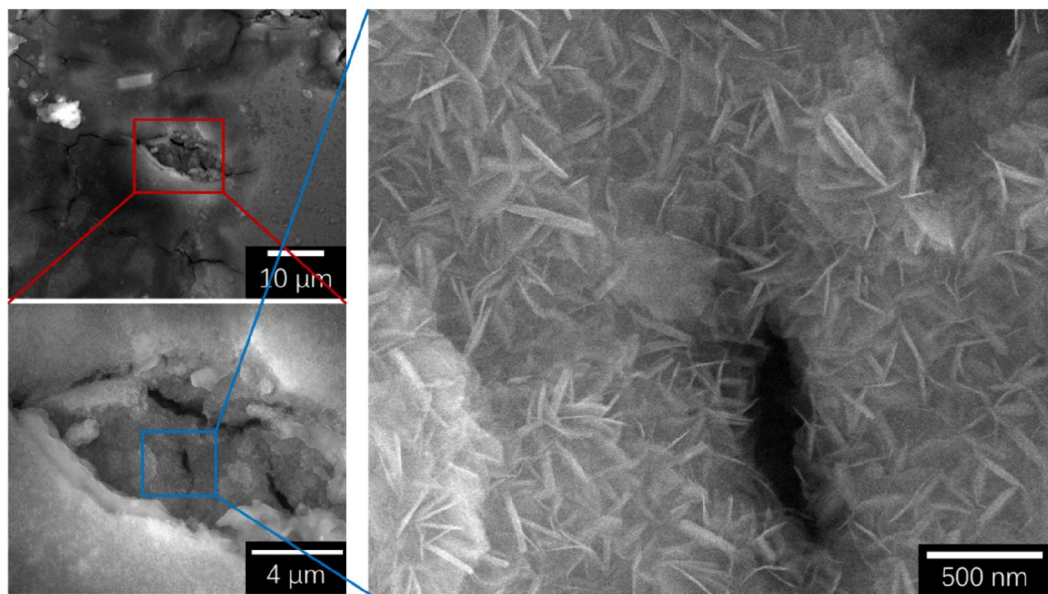


Figure 4. Secondary electron imaging of the “Type 1” region (in **Figure 3**) showing visible surface modification of a Mg-Li(-Al-Y-Zr) alloy sample after immersion in 0.1 M NaCl at 25 °C for 24 hours then air-exposed for 7 days.

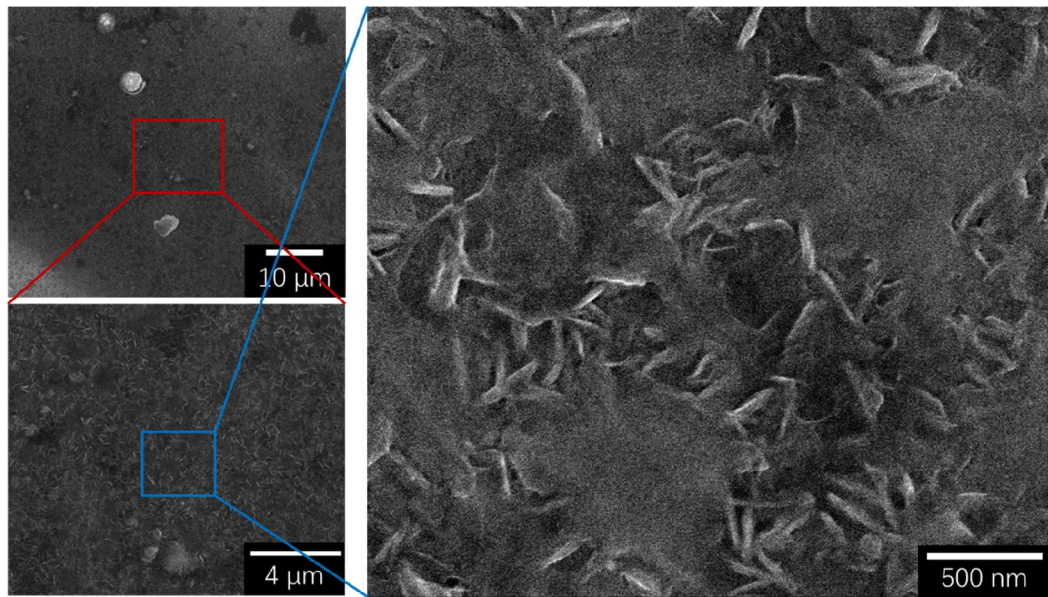


Figure 5. Secondary electron imaging of the “Type 2” region (in **Figure 3**) showing a relatively unaffected surface of a Mg-Li(-Al-Y-Zr) alloy sample after immersion in 0.1 M NaCl at 25 °C for 24 hours then air-exposed for 7 days.

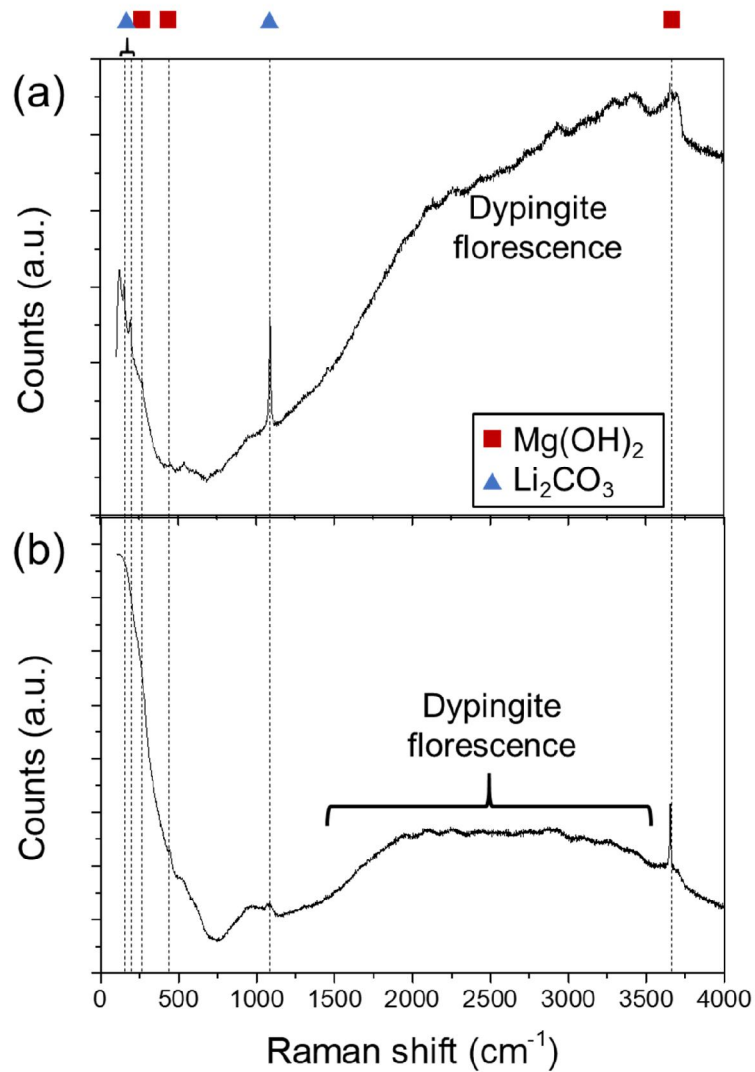


Figure 6. Raman spectra acquired on the Mg-Li(-Al-Y-Zr) alloy sample surface after immersion in 0.1M NaCl at 25 °C for 24 hours then: (a) air-exposed for 60 days, (b) air-exposed for 60 hours. Li₂CO₃ peak is more intense on the sample that was air-exposed for 60 days while the Mg(OH)₂ peak is more obvious on the sample that was air-exposed for 60 hours. Big florescence can be found between 1000 to 4000 cm⁻¹ on both samples which is proposed to be the florescence created by dypingite [23].

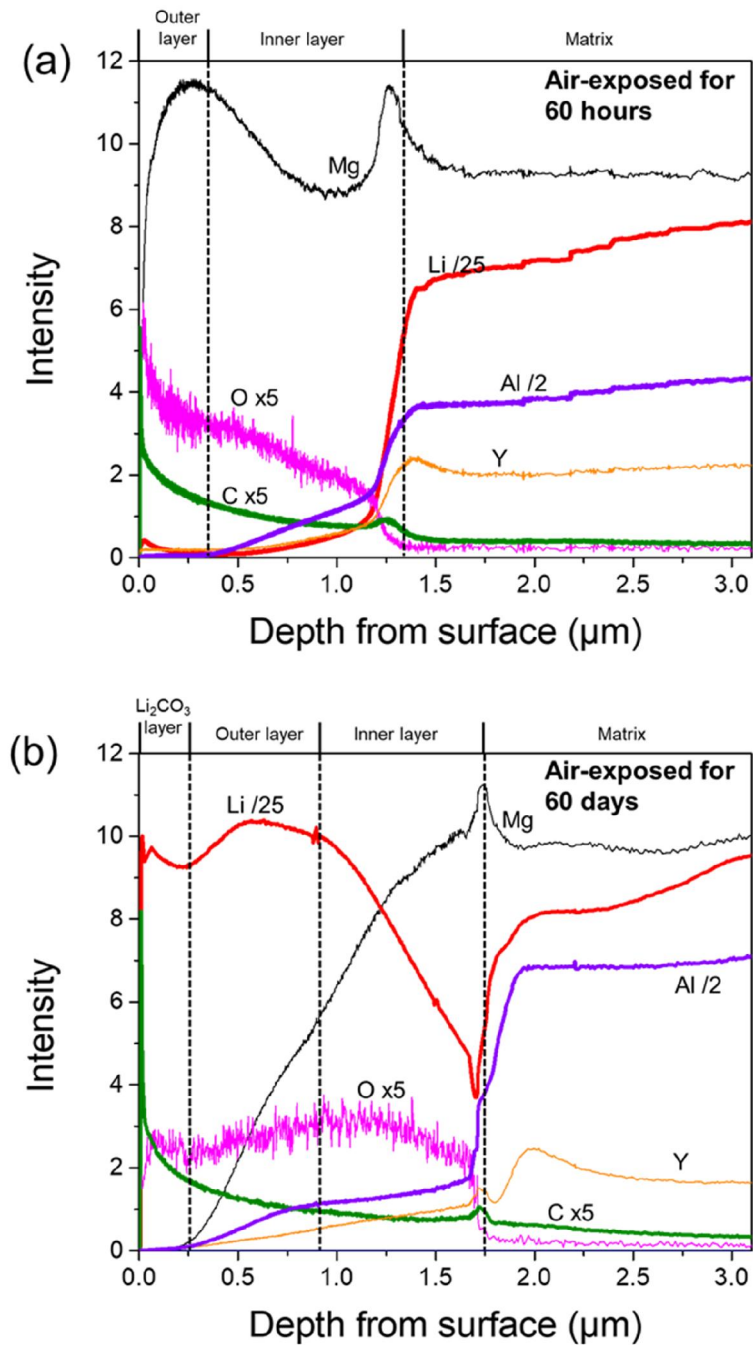


Figure 7. The GDOES depth profile obtained on Mg-Li(-Al-Y-Zr) alloy samples: (a) immersed in 0.1 M NaCl for 24 hours then air-exposed for 60 hours, (b) immersed in 0.1M NaCl for 24 hours then air-exposed for 60 days. The evolution of Li and Mg content suggests the presence of two major layers in the surface film of both samples. The outermost 250 nm of the surface film on sample that was air-exposed for 60 days contains only Li, O and C, which is proposed to be a layer of Li_2CO_3 .

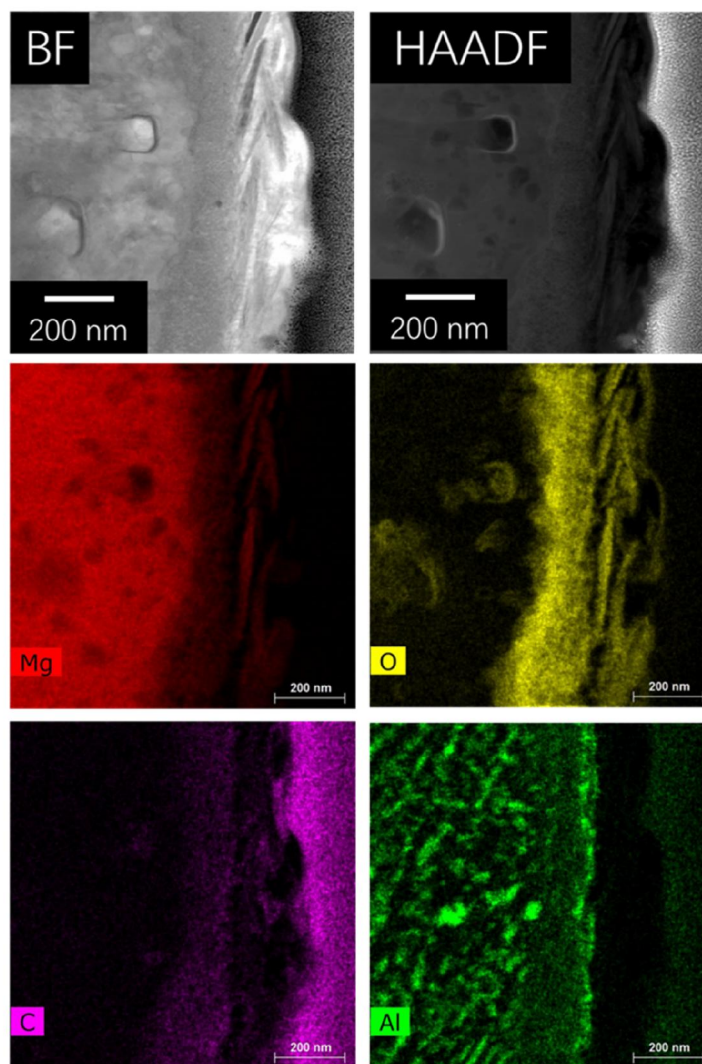


Figure 8. Scanning transmission electron micrographs and corresponding EDXS maps for Mg, O, C and Al of the surface film formed on Mg-Li(-Al-Y-Zr) alloy sample after immersion in 0.1M NaCl at 25 °C for 24 hours then air-exposed for 7 days. Y and Zr were not detected in this area.

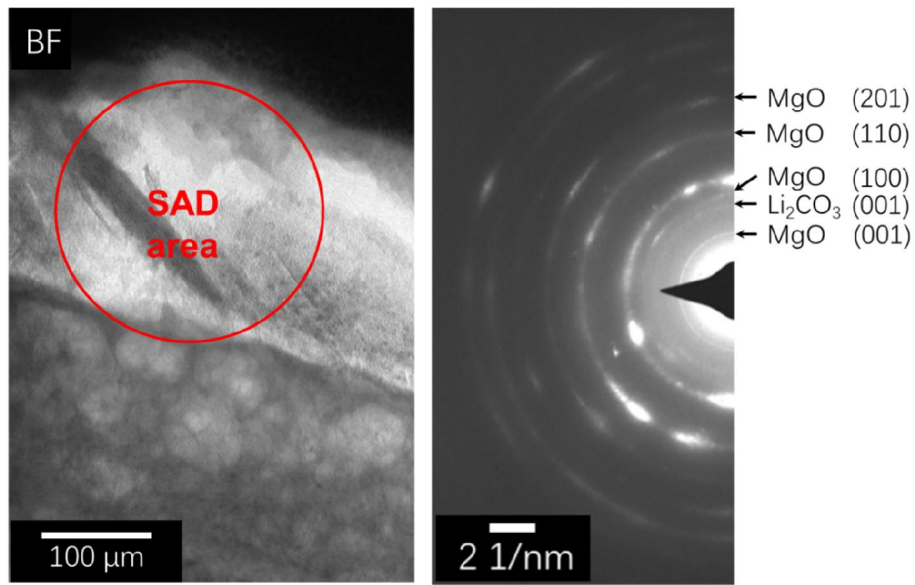


Figure 9. Scanning transmission electron micrographs and corresponding SAD pattern of the outer layer of the surface film formed upon Mg-Li(-Al-Y-Zr) after immersion in 0.1 M NaCl for 24 hours at 25 °C then exposed in air for 7 days.

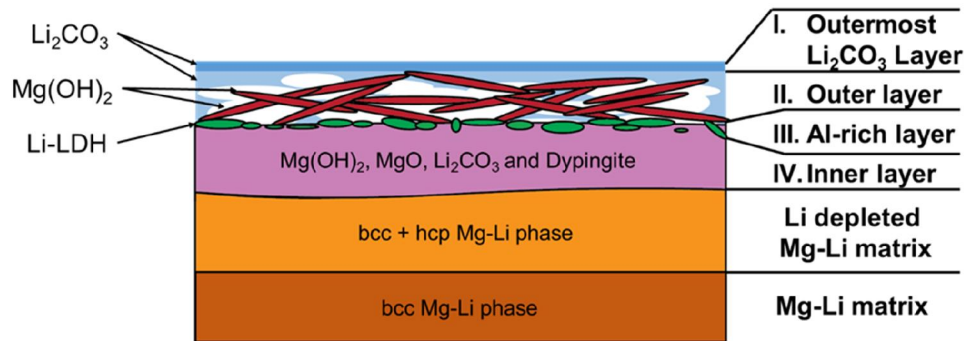
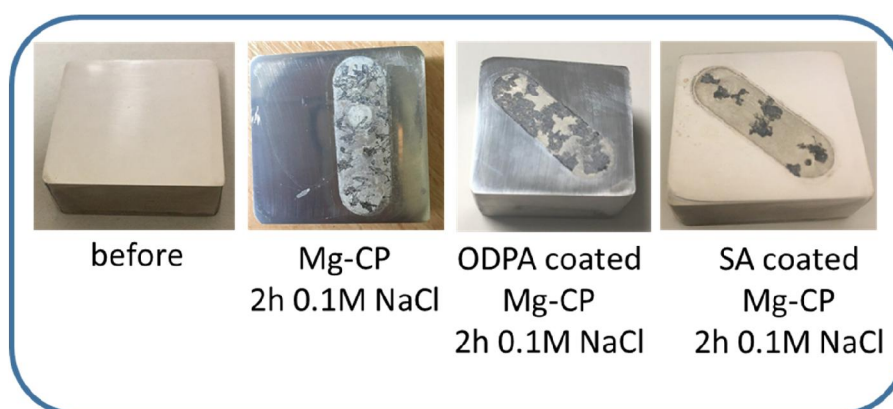


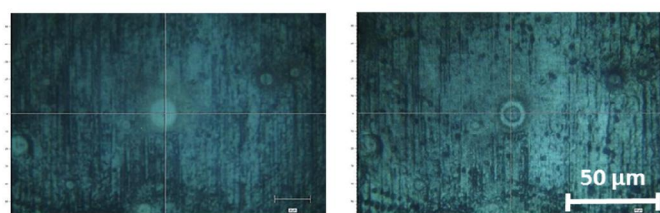
Figure 10. The proposed structure of surface film formed on the Mg-Li(-Al-Y-Zr) alloy sample after 24 hours of water immersion and 7 days of air-exposure. The surface film can be divided into four layers: I . the outermost Li_2CO_3 layer; II . The outer layer that mainly consist of $\text{Mg}(\text{OH})_2$ objects; III. the Al-rich intermediate layer that contains Li-LDH; IV. the more compact inner layer that mainly consist of $\text{Mg}(\text{OH})_2$ along with possible dypingite ($\text{Mg}_5(\text{CO}_3)_4(\text{OH})_2 \cdot 5\text{H}_2\text{O}$), MgO and Li_2CO_3 . The under-lying matrix near the surface is relatively depleted with Li and contains some hcp Mg-Li phase.

Appendix 2

On the application of in situ Raman spectroscopy to investigation of effect of self-assembling monolayers on the film growth kinetics

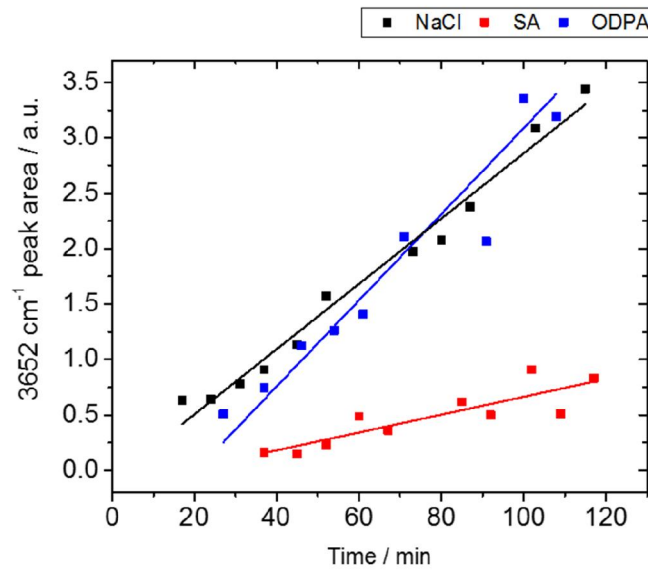


Area observed in Raman - 100 X 100 μm
1 Spectrum each 10 μm
No black filament were in observed area – all the kinetics curve were measured in “intact region”



Mg-CP 0.1M NaCl

Mg(OH)₂ growth kinetics in intact region



- Linear law for all the samples
- The Mg(OH)₂ growth rate is the same for non-coated and ODPa coated samples, for SA-coated sample the rate is lower
- The growth rate correlates with visual observation: SA-coated samples demonstrates less filaments – less corroded sample.

Appendix 3

Environmental effects on selective dissolution from ZnAlMg alloy under low frequency alternating current perturbations

This Appendix presents the text of published work V. Shkirskiy, A. Maltseva, K. Ogle, P. Volovitch, Environmental effects on selective dissolution from ZnAlMg alloy under low frequency alternating current perturbations, *Electrochim. Acta.* 238 (2017) 397–409. doi:10.1016/j.electacta.2017.03.210.



Environmental effects on selective dissolution from ZnAlMg alloy under low frequency alternating current perturbations



V. Shkirskiy*, A. Maltseva, K. Ogle, P. Volovitch*

Chimie ParisTech, PSL Research University, CNRS, Institut de Recherche de Chimie Paris (IRCP), F-75005 Paris, France

ARTICLE INFO

Article history:

Received 13 November 2016
Received in revised form 25 March 2017
Accepted 27 March 2017
Available online 29 March 2017

Keywords:

ZnMgAl coating
selective dissolution
atomic emission spectroelectrochemistry (AESEC)
corrosion products
AC - AESEC coupling

ABSTRACT

Real time measurement of elemental dissolution rates by atomic emission spectroelectrochemistry under alternating current (AC) perturbations of ZnAlMg alloy was used to precise mechanisms controlling selective dissolution as a function of pH in chloride containing solutions in the presence of NH_4^+ . At pH values of 8.5 and 10.5 Zn and Mg dissolution currents (j_{Zn} , j_{Mg}) followed the total current j_e^* respecting the stoichiometry of Zn_2Mg at the maximum of anodic current in solution at pH 8.5. Al dissolution current (j_{Al}) followed j_e^* at pH 10.5 and 8.5 with a phase shift of 180° further called cathodic Al dissolution. No correlation between AC perturbations and Al dissolution was seen at pH 8.5. At pH 13 anodic Zn dissolution, cathodic Al dissolution and no Mg dissolution were observed. The elemental dissolution rates of Al at pH 8.5 and Mg at pH 13 did not vary with AC perturbations. The detected concentrations of Al at pH 8.5 and Mg at pH 13 correlated well with the saturation concentrations of Al^{3+} and Mg^{2+} in studied electrolytes expected from solubility constants. Thus, their dissolution was controlled by the solubility of the surface films observed by infrared and Raman spectroscopy. The finding implies the separation of cathodic Al dissolution, and anodic Zn and Mg dissolution in the appropriate equivalent circuit for an adequate analysis of conventional EIS data.

© 2017 Elsevier Ltd. All rights reserved.

1. Introduction

The response of metallic materials on the alternating current (AC) perturbations in Electrochemical Impedance Spectroscopy (EIS) measurements, used to access corrosion mechanisms of complex materials [1–5], depends on both, material and solution composition [6–9], which are equivalently important for the formation of oxide films, precipitation and other factors modifying interface dynamics. In this work we illustrate how the real time analysis of the chemical evolution of the system under AC perturbations can bring an additional insight into selective dissolution of multicomponent ZnMgAl coating on steel.

The choice of ZnMgAl alloy was based on both applied and fundamental interests of this material. On one hand, growing commercial application of these materials in hot dip galvanization process [10–14] is related with their superior corrosion resistance in accelerated tests [15–17]. On another hand, these are multiphase materials: Mg alloying in Zn matrix results in the formation of

Zn-Mg intermetallics such as Zn_2Mg , $\text{Zn}_{11}\text{Mg}_2$, and binary Zn/Zn-Mg eutectics [18], Al alloying results in the formation of ternary Zn/Al/Zn-Mg or binary Zn/Al eutectics [13,14,19]. As a result, the material is susceptible to microgalvanic coupling and selective dissolution phenomena [8,9,19,20], in particular Zn-Mg intermetallics due to their anodic polarization when coupled with Zn dendrites [13,15,19]. The dissolution of Zn_2Mg and $\text{Zn}_{11}\text{Mg}_2$ intermetallics in aqueous NaCl was demonstrated to occur in two steps [21,22]: initial selective Mg dissolution and the dissolution of the remaining Zn at potentials close to a standard Zn corrosion potential. Depending on selective dissolution and electrolyte composition, different corrosion products form on the surface modifying reactivity of the underlying metal [9,23,24]. In particular, the formation of self-repairing isolating Mg(II) oxide films [13,25,26], the modification of the electronic properties of ZnO by doping it with Mg(II) [22,27]; the pH buffering effects due to Mg $(\text{OH})_2$ precipitation [17,28–31] and the formation of Zn_2Al -layered double hydroxides (LDH) with low permeability for oxygen [12,13,17,19,31–33] were reported as benefits decreasing the corrosion rate. The formation and stability of these products are highly influenced by the presence of CO_2 gas and by the presence of ammonium ions (typical pollutants in industrial atmospheres [24,34]). The NH_4^+ and HCO_3^- ions should play an important role in

* Corresponding authors.

E-mail addresses: viacheslav@shkirskiy.org (V. Shkirskiy), polina.volovitch@chimie-paristech.fr, volovitch@yahoo.com (P. Volovitch).

Table 1
Solutions used in the work and the saturated concentrations of Zn^{2+} , Al^{3+} and Mg^{2+} in ammonium/carbonate buffer solutions and 0.1 M NaCl solutions at 25 °C calculated by Hydra Medusa software. The cases of low solubility are marked. The following species of standard software database were taken into account: Zn^{2+} , $Zn(CO_3)_2^{2-}$, $Zn(NH_3)_2^{2+}$, $Zn(NH_3)_3^{2+}$, $Zn(NH_3)_4^{2+}$, $ZnNH_3^{2+}$, $Zn(OH)_2$, $Zn(OH)_3^-$, $Zn(OH)_4^{2-}$, $Zn_2(OH)_6^{2-}$, Zn_2OH^{3+} , $Zn_4(OH)_4^{4+}$, $ZnCl^+$, $ZnCl_2$, $ZnCl_3^-$, $ZnCl_4^{2-}$, $ZnClOH$, $ZnCO_3$, $ZnHCO_3^+$, $ZnOH^+$, $Al(OH)_2^+$, $Al(OH)_3$, $Al(OH)_4^-$, $Al_2O_4(OH)_{24}^{7-}$, $Al_2(OH)_2^{4+}$, $Al_3(OH)_4^{5+}$, $Al(OH)^{2+}$, $Mg(NH_3)^{2+}$, $Mg_4(OH)_4^{4+}$, $MgCO_3$, $MgHCO_3^+$, $MgNH_3^{2+}$, $MgOH^+$.

Case name	Electrolyte composition	Expected Log (saturated concentration / mol L ⁻¹)		
		Zn ²⁺	Al ³⁺	Mg ²⁺
Case (I) – buffered	0.1 M NH ₄ ⁺ /0.09 M NH ₃ + 0.01 M HCO ₃ ⁻ , initial pH 10.5	-3.35	-4.11	-3.81
Case (II) – buffered, precipitation of Mg(II)	0.1 M NH ₄ ⁺ /0.09 M NH ₃ + 0.01 M HCO ₃ ⁻ , initial pH 13	-3.73	-1.55	-7.48
Case (III) – buffered, precipitation of Al(III)	0.1 M NH ₄ ⁺ /0.09 M NH ₃ + 0.01 M HCO ₃ ⁻ , initial pH 8.5	-2.78	-6.12	-2.45
Case (IV) – unbuffered, precipitation of Zn(II)	0.1 M NaCl, initial pH 10.5 or 8.5	-5.18	-4.11	-4.07

corrosion mechanisms of Zn based materials. Taking into account the commonly accepted importance of Cl⁻ anions in corrosion studies, we have chosen for this work 0.1 M Cl⁻ aqueous solutions, containing or not NH₄⁺ and HCO₃⁻ ions. The choice to vary the pH between 8 and 13 was motivated by different saturation concentrations of Al³⁺, Zn²⁺ and Mg²⁺ cations in this pH range and hence different surface films formation that can influence ZnMgAl dissolution mechanisms (see Table 1).

The methodology chosen for this work is a combination of an electrochemical measurement with the real time analysis of the elemental dissolution rates in the flow electrochemical cell (atomic emission spectroelectrochemistry – AESEC, [35]) and the following surface analysis by vibrational spectroscopy. In the recent work, a coupling of EIS and AESEC was proposed [36]. In this way, the frequency response of the anodic and cathodic reactions was decoupled allowing the quantitative determination of kinetic parameters for each half reaction independently. In this work, we apply this approach to a ZnMgAl alloy under AC perturbations in order to precise the mechanisms controlling selective dissolution in this alloy as a function of pH in solutions containing or not NH₄⁺ and HCO₃⁻ ions.

2. Experimental

2.1. Materials

Samples of 0.7 mm thick cold rolled steel with model 20 μm thick coatings (93.3 wt. % Zn, 3.7 wt. % Al and 3.0 wt. % Mg) produced by galvanizing process were cut in 2 cm x 8 cm plates for testing. The microstructure of the model samples contained Zn dendrites, binary eutectic of Zn/Zn₂Mg and ternary eutectic Zn/Al/Zn₂Mg [24]. Prior to the experiments, the samples were degreased in an ether solution at room temperature during 20 min.

The experiments were performed in naturally aerated ammonium/carbonate solutions (0.1 M NH₄Cl/0.09 M NH₃ + 0.01 M HCO₃⁻) at the initial pH of 8.5, at the initial pH of 10.5 (natural pH) and 13, and in 0.1 M NaCl at the initial solution pH 10.5 and 8.5 (Table 1). The electrolytes were prepared in the purified water (Millipore™ system, 18.2 MΩ cm) using NH₃ solution (25 wt. % solution in water, VMR Prolabo), NH₄Cl (analytical grade, VWR Prolabo), NaHCO₃ (analytical grade, VWR Prolabo) and NaCl (analytical grade, VWR Prolabo). The initial pH values were adjusted by 0.1 M HCl for pH 8.5 or by 0.1 M NaOH for pH 10.5 and by the addition of solid NaOH to reach pH 13.

2.2. AESEC technique

2.2.1. Measurement principle

Low frequency AC perturbations coupled with online measurement of partial elements dissolution were performed on Zn3.7Al3.0Mg alloy (see Table 2 for notations) by means of atomic emission spectroelectrochemistry (AESEC) technique described elsewhere [35]. Briefly, it consists of an electrochemical flow cell connected with an inductively coupled plasma atomic emission spectrometer (ICP-AES). In the flow cell a reaction between the sample (ZnAlMg) and an aggressive electrolyte occurs, leading to the production of dissolved cations and/or slightly soluble species. Then, the electrolyte is transported downstream to the ICP-AES, where its composition is continuously analyzed. The ICP-AES analysis shows only the concentrations of the released Zn, Al and Mg species present in a soluble form, while the low soluble products or surface films are not directly detected. This flux of soluble species of X, i.e. metal cations X^{N+} (where X = Zn²⁺, Al³⁺ or Mg²⁺), away from the metal surface through the diffusion layer to the solution bulk, J_X , can be expressed as the dissolution rate of the element X (J_X) calculated from its instantaneous concentration in the solution bulk (C_o^X):

$$J_X = \frac{f C_o^X}{A} \quad (1)$$

The units, used in calculations of numerical values in this work, as well as the definitions of symbols and notations, are given in Table 2. The normalization of J_X by the geometric surface area was done only for convenience and does not imply that the flux of cations was uniformly distributed on the surface. Using the Faraday's law, J_X can be expressed as the metal dissolution current density (j_X):

$$j_X = n_X F J_X \quad (2)$$

2.2.2. Experimental protocol

The AC/AESEC experiments were performed as follows:

1. Measurement of the ICP-AES background signals of Zn, Al and Mg in the tested electrolyte was carried out for 5 min prior to the AESEC experiment. At this step the solution went directly to ICP-AES.
2. At t=0 s the valve of the flow system was switched so that the electrolyte passed through the electrochemical cell and contacted the surface of the working electrode.

Table 2
Notations.

Symbol	Description	Units
ZnAlMg	Zn based alloy with Al and Mg	–
Zn _x Al _y Mg	Zn based alloy with <i>x</i> wt. % of Al and <i>y</i> wt. % Mg	–
<i>X</i>	metal component of an alloy	–
<i>X</i> ^{<i>N</i>+}	cation of metal <i>X</i> with a charge of <i>N</i> + in solution	–
<i>X</i> (<i>N</i>)	slightly soluble product containing element <i>X</i> in oxidation state + <i>N</i>	–
<i>j</i> _{<i>X</i>}	current density associated with dissolution of metal <i>X</i> to soluble species	mA cm ⁻²
<i>J</i> _{<i>X</i>} ^{total}	total current density of dissolution of metal <i>X</i>	mA cm ⁻²
<i>j</i> _{<i>e</i>}	total or electrical current density	mA cm ⁻²
<i>j</i> _{<i>e</i>} [*]	convoluted <i>j</i> _{<i>e</i>}	mA cm ⁻²
<i>j</i> _{<i>X</i>} ^{sol}	<i>j</i> _{<i>X</i>} where metal dissolution is limited by the solubility of metal <i>X</i>	mA cm ⁻²
<i>J</i> _{<i>X</i>}	dissolution rate of metal <i>X</i> (or flux of cations away from the metal surface through the diffusion layer)	mole s ⁻¹ cm ⁻²
<i>E</i>	electrode potential	V vs Ag/AgCl
<i>E</i> _{oc}	<i>E</i> at open circuit	V vs Ag/AgCl
<i>f</i>	flow rate of electrolyte	cm ³ s ⁻¹
<i>F</i>	Faraday's constant	mC mol ⁻¹
<i>C</i> _o ^{<i>X</i>}	concentration of specie <i>X</i> in the solution bulk	mole L ⁻¹
<i>C</i> _{<i>X</i>} ^{<i>X</i>}	concentration of specie <i>X</i> in the diffusion layer near the working electrode	mole L ⁻¹
<i>A</i>	area of working electrode	cm ²
<i>n</i> _{<i>X</i>}	number of electrons consumed for the reduction of metal <i>X</i>	–
δ	diffusion layer thickness on the working electrode	cm
<i>D</i> _{<i>X</i>}	diffusion coefficient of <i>X</i> specie	cm ² s ⁻¹
<i>R</i> _{<i>p</i>}	polarization resistance	ohm cm ²
<i>h</i>	residence time distribution or transfer function	–
τ	parameter of <i>h</i>	s
β	parameter of <i>h</i>	–
<i>t</i>	Time	s

- The solution of 1 M HCl was used as the first electrolyte for 5 s in order to eliminate the natural oxides that improved the reproducibility of AC experiments [34].
- Then the tested electrolyte started to flow through the cell and the open circuit (OC) reactivity was measured for approximately 10 min until the signals of metal dissolution and open circuits potential were stable (the OC variation less than 10 mV in 10 minutes).
- Potentiostatic AC perturbations with ± 10 mV root mean square (rms) around OC potential were applied.
- The OC reactivity was measured for 3 min.
- During the 1 – 6, the solution coming after the cell was analyzed in real time by AESEC. In steps 1, 4–6 the solution pH after the cell was measured as described below.
- The valve of the flow system was switched so that the tested solution went directly to ICP-AES without contacting the sample surface in order to verify that the background signals of Zn, Al and Mg were identical to the background signals in period 1.
- To calibrate the signal, standard solutions of 0.5 ppm, 1 ppm and 5 ppm Zn(NO₃)₂, Al(NO₃)₃ and Mg(NO₃)₂ in the same electrolyte were measured.

The downstream solution was accumulated every 3 minutes and the pH was measured for each portion in order to survey the pH evolution in the bulk solution during the experiment.

2.2.3. AESEC parameters

The dissolution was surveyed by monitoring the emission intensities of Zn, Al and Mg at 213.86 nm, 167.08 nm and 285.21 nm

Table 3

Analytical parameters of AESEC experiments: detection limits (DLs) of Zn, Al and Mg under the conditions of the experiments, expressed in units of concentration and current density.

	DL / ppb	DL / mAcm ⁻²
Zn	6.9 ± 0.7	(2.0 ± 0.2) × 10 ⁻³
Mg	3.2 ± 0.9	(9.4 ± 0.3) × 10 ⁻⁴
Al	8.7 ± 0.5	(3.8 ± 0.2) × 10 ⁻³

consequently. The detection limits of Zn, Al and Mg in used electrolytes calculated as the three times standard deviation of the signal of blank solution expressed in the units of concentration and current density are shown in Table 3.

The reactive surface area was 0.51 ± 0.01 cm², the flow rate of the electrolyte was fixed at 0.050 ± 0.002 cm³ s⁻¹ and the temperature was 25 ± 1 °C (298 ± 1 K). The residence time distribution of the flow electrochemical cell obeyed an empirical function in the form of a log-normal distribution [35]:

$$h(t) = \begin{cases} \sqrt{\frac{\beta}{\pi\tau^2}} \cdot e^{-\frac{1}{4\beta}} \cdot e^{-\beta \ln^2 \frac{t}{\tau}} & \text{if } t > 0 \\ 0 & \text{if } t = 0 \end{cases} \quad (3)$$

The parameters of log-normal distribution ($\beta = 0.99 \pm 0.02$ and $\tau = 10.2 \pm 0.2$ s) were taken from our previous work [36] where it was measured under identical flow conditions. The time offset of *C*_o^{*X*} detection due to the transport of electrolyte through the capillaries was 12.0 ± 0.3 s.

The electrochemical tests were performed with a Gamry Reference 600TM potentiostat with Ag/AgCl (in saturated KCl) reference electrode and a Pt mesh counter electrode. AC perturbations were applied around the open circuit potential from 100 kHz to 5 mHz with 10 points per decade and 4 or 3 cycles per frequency with the voltage amplitude of 10 mV rms. The analog signals of potential and current were routed into the measuring circuit of the ICP-AES to guarantee the same time scale for acquisition of *j*_{Zn}, *j*_{Mg}, *j*_{Al}, *j*_{*e*} and *E* signals. All signals from ICP-AES were collected with the sampling rate of 1 point per second.

The measures of *j*_{*e*} and *E* are essentially instantaneous whereas *j*_{*X*} values are affected by the hydrodynamics of the flow cell, described previously. Therefore, *j*_{*e*} and *j*_{*X*} cannot be directly compared due to their different time scale. To overcome this difficulty, the numerical convolution [35] of *j*_{*e*} signal was systematically applied to total currents using the residence time distribution (*h*) defined above:

$$j_e^* = \sum_{i=0}^t j_e(i)h(t-i) \quad (4)$$

Table 4
Solution pH, E_{oc} vs Ag/AgCl of Zn_{3.7}Al_{1.3}Mg dissolution before and after AC application along with R_p defined at the lowest 0.0046 Hz frequency in Figs. 1–5. In case of unbuffered NaCl solution with the initial pH 8.5 the AESEC and electrochemical responses were similar to obtained in unbuffered NaCl solution with the initial pH 10.5.

	E_{oc} vs (Ag/AgCl)/V		Solution pH		R_p /ohm cm ²
	before	after	before	after	
Case (I) – 0.1 M NH ₄ ⁺ /0.09 M NH ₃ + 0.01 M HCO ₃ ⁻	-1.22	-1.23	10.5	10.2	261
Case (II) – 0.1 M NH ₄ ⁺ /0.09 M NH ₃ + 0.01 M HCO ₃ ⁻	-1.47	-1.45	13	13	1217
Case (III) – 0.1 M NH ₄ ⁺ /0.09 M NH ₃ + 0.01 M HCO ₃ ⁻	-1.12	-1.12	8.5	8.3	227
Case (IV) – 0.1 M NaCl adjusted to pH 10.5 by NaOH	-1.06	-1.04	10.5	9.8	666

2.2.4. Analysis of low frequency AC experiments by AC/AESEC method

The approach, used in this work is to explore the relationship between j_e^* and j_X ($X=Zn, Al$ or Mg), i.e. the total current consumed to oxidize the material and the current associated with the formation of soluble species of X , to access rate limiting steps (RDS) of the dissolution as was previously illustrated on the example of Zn dissolution under alternating AC perturbations [36]. For instance, in the absence of adsorbed or low soluble intermediates (the life time of any adsorbed or insoluble species is less than the time of the charge transfer, necessary to form these species), an oxidation of a single metal X is simultaneous with the formation of soluble species of X implying that j_X evolves in phase with j_e^* under AC perturbations. If insoluble species are present at the surface but the diffusion through them is quicker than the charge transfer, it can generate a phase shift between j_X and j_e^* responses on AC perturbations. Finally, for the case when the diffusion is slower than the charge transfer, j_X will not depend on the potential evolution and hence will not respond on AC perturbations. In this work we will also try to explore the ratio between metal dissolution currents at their maximum under AC perturbations to verify stoichiometry of the dissolution and the selective dissolution of some specific phases.

Note that unstable insoluble products with the life time less than the time constant of the flow cell ($\tau=10.2$ s) cannot be detected in this methodology. Moreover, the formation of a surface film and the precipitation because of solubility limitations cannot be distinguished if the precipitation equilibrium is reached faster than $\tau=10.2$ s.

2.3. Analysis of surface oxides/hydroxides after AC/AESEC

The surface of ZnAlMg after AC/AESEC experiments was characterized using Fourier-transform infrared spectroscopy in the attenuated total reflection mode (ATR – FTIR) and Raman spectroscopy.

Infrared spectra were measured with a Thermo Scientific Nicolet 6700 FTIR spectrometer equipped with a mercury cadmium telluride detector cooled at 77 K by liquid nitrogen. Spectral resolution was 4 cm⁻¹, and spectra were averaged from 256 scans. The ATR accessory was a horizontal ZnSe crystal coated with diamond (surface area = 2.54 mm²) with single reflection and an angle of incidence of 45° (Smart Miracle from PIKE). OMNIC software was used for the data collection and treatment.

Raman spectra were recorded using Renishaw InVia confocal Raman microscope with the Nd: YAG laser source (532 nm, 100 mW) and objectives x20, x50 and x100. The typical spectral acquisition time was in the range of 1 to 10 s. Spectra in one point and mapping of the surface were recorded and treated with WIRE4 software.

3. Results

3.1. Elemental dissolution under AC perturbation in different electrolytes

Solution pH and open circuit potential, E_{oc} , of ZnMgAl alloy in different electrolytes before and after AC application as well as R_p defined at 0.0046 Hz frequency in each solution are summarized in Table 4. One should note that the values in Table 4 called herein R_p present an impedance of the system determined at frequency 0.0046 Hz using Eq. (5):

$$R_p = \frac{\Delta E}{\Delta j_e} \quad (5)$$

3.1.1. Case I: NH₄⁺/HCO₃⁻ buffer at pH 10.5

Fig. 1 demonstrates j_e^* , j_{Zn} , j_{Al} and j_{Mg} variation during AC application to ZnMgAl in ammonium/carbonate buffer at pH of 10.5. The solution pH did not change after the reaction in the electrochemical cell (Table 4). It should be underlined that the decrease of j_{Zn} , j_{Al} and j_{Mg} and convoluted current j_e^* with the frequency increase is the result of the influence of the flow hydrodynamics in the cell (or convolution procedure) and does not reflect the electrochemical behavior. For the AC frequencies close and higher than $1/\tau=0.1$ Hz the system does not have enough time to clear away all dissolved cations from the cell that results in the smoothing of the elemental dissolution currents. More details about the relationship between j_e^* and j_e can be found in Appendix A (Fig. A1). Oscillations of j_e^* at frequencies less than 0.1 Hz result in the appearance of oscillations of all j_{Zn} , j_{Al} and j_{Mg} metal currents. Note that the high frequency variations (> 0.1 Hz) of j_e^* , j_{Zn} , j_{Al} and j_{Mg} currents cannot be reliably detected from the dissolution profiles due to $\tau=10.2$ s (or 0.1 Hz) time constant value of the residual time distribution of the electrochemical flow cell. Further focus will be addressed only on the low frequency (< 0.1 Hz) AC perturbations.

Illustrated on the example for the lowest 0.0046 Hz frequency in the inset of Fig. 1, j_{Zn} and j_{Mg} vary in phase with j_e^* whereas j_{Al} is shifted by 180°. Such a correlation between j_{Zn} and j_{Mg} and j_e^* indicates that the transport of the released cations was not limited by diffusion. The ratio of the amplitudes of j_{Zn} and j_{Mg} during the whole AC/AESEC experiment was about 10 (Table 5) which is much higher than the value of 2 expected from the selective dissolution of Zn₂Mg phase as often reported for this type of alloys [19,20].

Despite the fact that the dissolution of Al under high cathodic over potentials is a well-known process [37–41], the 180° phase shift between j_{Al} and j_e^* variation near the open circuit potential of ZnMgAl alloy ($E_{oc}=-1.2$ V vs Ag/AgCl electrode, Table 4) was observed for the first time. It can be explained by the fact that because of high open circuit potential $E_{oc}=-0.69$ V vs Ag/AgCl of

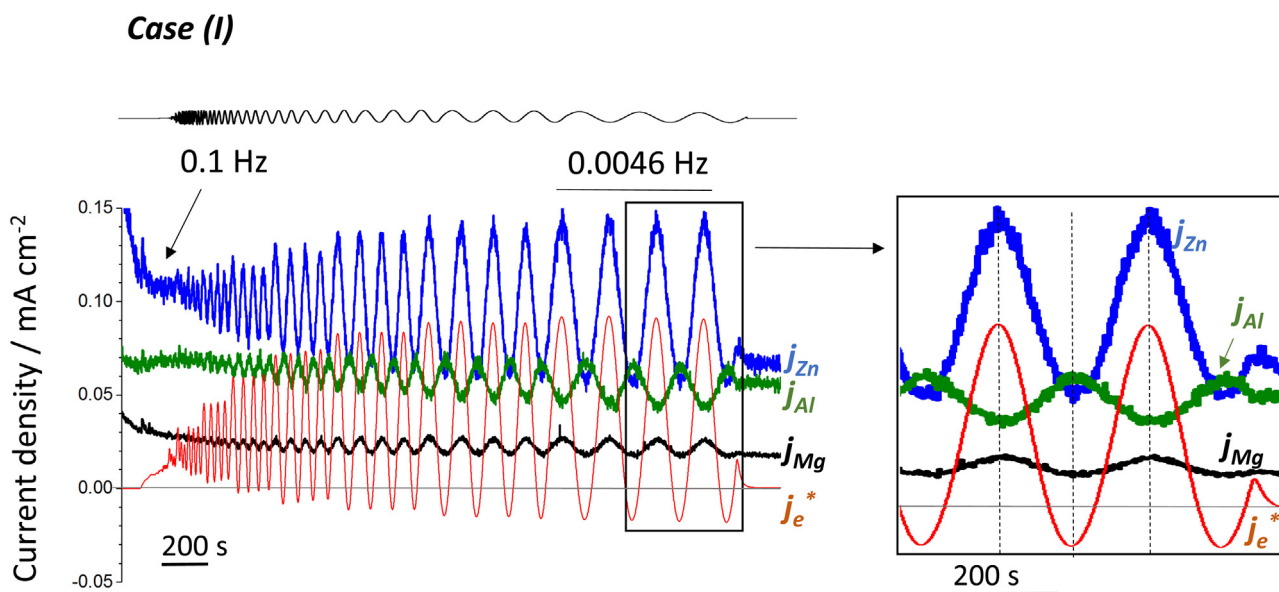


Fig 1. Evolution of elemental leaching rates of Zn, Al and Mg (j_{Zn} , j_{Al} and j_{Mg}) and total convoluted current (j_e^*) in AC/AESEC experiment in 0.1 M NH_4^+ /0.09 M NH_3 + 0.01 M HCO_3^- electrolyte, pH 10.5 (case I). AC perturbation parameters (schematically presented by the upper line): frequency decreased from 10^5 Hz to 0.0046 Hz, 10 mV amplitude, 10 points per decade.

Table 5

Stoichiometry of dissolution response on applied 10 mV AC perturbations (0.046 Hz) in $NH_4^+/HCO_3^-/Cl^-$ solutions at different pH as presented in Table 1. Measured amplitudes of dissolution current oscillations Δj_X ($X=Zn, Mg, Al$) and amplitudes of the calculated cathodic current Δj_c are presented. The evolution of j_c was calculated for the 1st and 2nd case using an approximation $j_c = j_e^* - j_{Zn} - j_{Mg} - j_{Al}$, because only in these cases all elements were dissolved. No data are presented for unbuffered NaCl solutions because $\Delta j_X = 0$ for all elements (no j_X response on AC perturbation).

Amplitudes Δj_X «peak to peak» ($mA cm^{-2}$) and their ratios (unitless)						
			Case (1) – pH 10.5			
Δj_{Zn}	Δj_{Mg}	Δj_{Al}	$\Delta j_{Zn}/\Delta j_{Mg}$	$\Delta j_{Zn}/\Delta j_{Al}$	Δj_c	$\Delta j_{Al}/\Delta j_c$
0.085	0.008	0.02	10.625	4.25	0.039	1.95
			Case (2) – pH 13			
Δj_{Zn}	Δj_{Mg}	Δj_{Al}		$\Delta j_{Zn}/\Delta j_{Al}$	Δj_c	$\Delta j_{Al}/\Delta j_c$
0.015	0	0.023		0.65	0.03	0.77
			Case (3) – pH 8.5			
Δj_{Zn}	Δj_{Mg}	Δj_{Al}	$\Delta j_{Zn}/\Delta j_{Mg}$			
0.01	0.006	0	1.666667			

pure Al [41], it is strongly cathodically polarized in the alloy which potential is defined by the active dissolution of Zn and Zn_2Mg intermetallic.

Assuming that all oxidized species are present in a soluble form, one can try to estimate the evolution of the cathodic current, j_c as

$$j_c = j_e^* - j_{Zn} - j_{Mg} - j_{Al} \quad (6)$$

and evaluate the stoichiometry of the soluble Al complex as previously proposed [37,40,41]. The calculated in this way ratio of the amplitudes of $\Delta j_c/\Delta j_{Al}$ at the maximum of cathodic perturbation presented in Table 5 differs from the values reported for cathodic dissolution of pure Al and high content Al alloys [37,40,41].

3.1.2. Case (II): NH_4^+/HCO_3^- solution at pH 13

Fig. 2 shows the dissolution profiles of ZnMgAl during AC application in ammonium/carbonate electrolyte at the solution pH 13. The measured value of bulk solution pH was identical before and after the experiment (Table 4). In contrast, the open circuit potential was more anodic after the experiment indicating the surface passivation during the experiment. One should note that

the open circuit potential variation was only about 20 mV, however, it was detectable and reproducible. The combination of the high R_p of 1217 Ohm cm^{-2} (Table 4), the slight shift of the potential in the anodic direction, the absence of the response of j_{Mg} on AC perturbation at pH 13 and its low absolute value (close to the detection limit) (Fig. 2) can be interpreted as the formation of a stable surface film containing magnesium oxy-hydroxides. This hypothesis is also coherent with the behavior of pure Mg in strong alkaline conditions [42] and will be verified in Section 3.1.5.

j_{Zn} and j_{Al} variations at pH 13 show the same tendencies as the tendencies observed at pH 10.5 (compare insets in Fig. 2 and Fig. 1): j_{Zn} oscillates with j_e^* indicating anodic Zn dissolution forming soluble species, whereas j_{Al} variations demonstrates close to 180° phase shift. However, some differences are still visible between the results. First, a small but detectable phase shift between j_{Zn} and j_e^* is present, indicating the delayed dissolution response on the AC perturbation which is also consistent with some transport limitations probably because of the surface film. Secondly, the j_{Al} at open circuit potential is significantly higher at strongly alkaline pH which correlates with the favored “chemical” Al dissolution without any external current due to the formation of

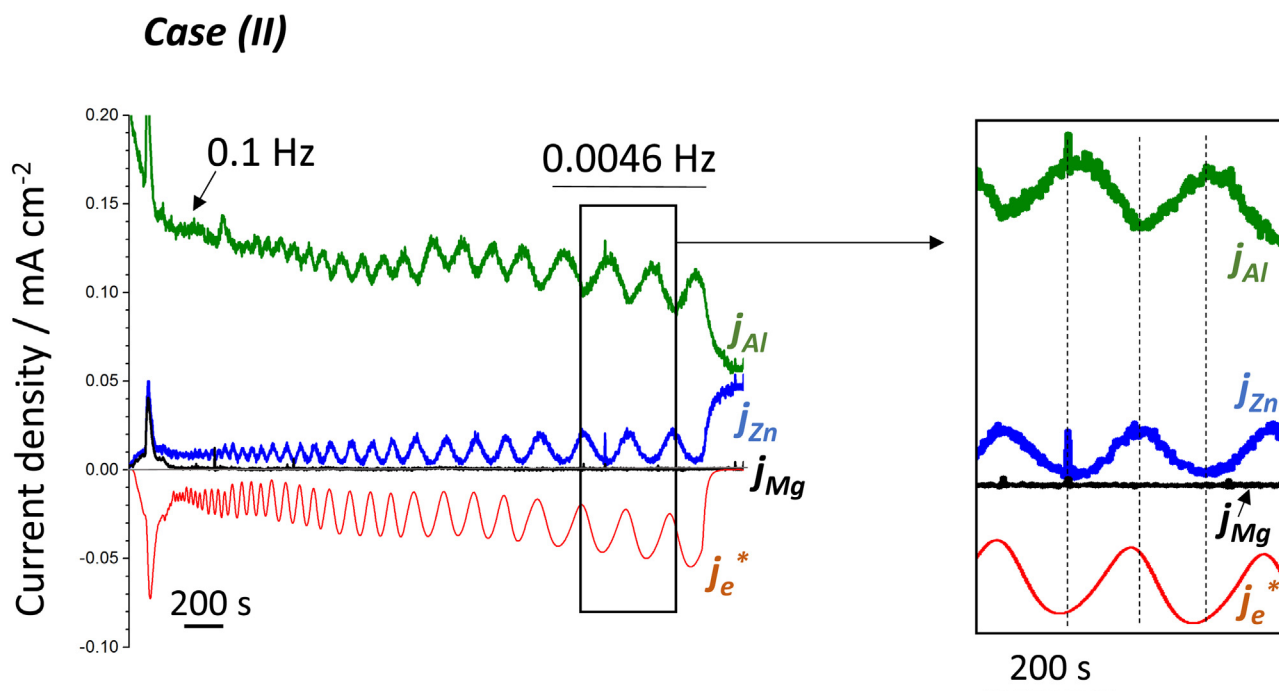


Fig. 2. Evolution of elemental leaching rates of Zn, Al and Mg (j_{Zn} , j_{Al} and j_{Mg}) and total convoluted current (j_e^*) in AC/AESEC experiment in 0.1 M NH_4^+ /0.09 M NH_3 + 0.01 M HCO_3^- electrolyte, pH 13 (case II). AC perturbation parameters: frequency varied from 10^5 Hz to 0.0046 Hz, amplitude 10 mV rms, 10 points per decade.

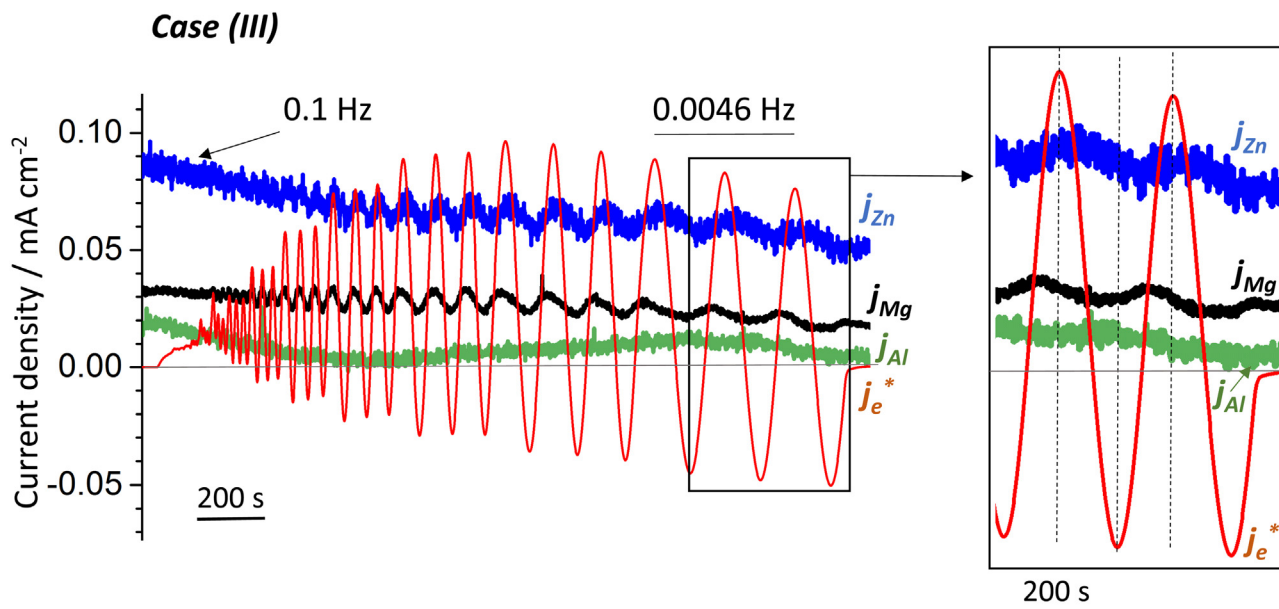


Fig. 3. Evolution of elemental leaching rates of Zn, Al and Mg (j_{Zn} , j_{Al} and j_{Mg}) and total convoluted current (j_e^*) in AC/AESEC experiment in 0.1 M NH_4^+ /0.09 M NH_3 + 0.01 M HCO_3^- electrolyte, pH 8.5 (case III). AC perturbation parameters: frequency varied from 10^5 Hz to 0.0046 Hz, amplitude 10 mV rms, 10 points per decade.

soluble complexes destabilizing the oxide layer in the areas containing Al species. And finally, the amplitude of j_{Zn} under applied AC decreases with pH (see Table 5) which can be related to the film formation at higher pH, which increases the OC potential with time.

3.1.3. Case (III): NH_4^+/HCO_3^- buffer at pH 8.5

The dissolution profile of ZnMgAl during AC application in ammonium/carbonate buffer with the solution pH of 8.5 is shown in Fig. 3. The pH and E_{oc} values were similar before and after this experiment (Table 4). In contrast with the data at pH 10.5 (Fig. 1

and 13 (Fig. 2), j_{Al} does not follow oscillations of j_e^* . This assumes that the Al dissolution is limited by the solubility of the oxide film. An interesting observation from Fig. 3 is a “sigmoidal” evolution (initial decrease and following increase) of the AC independent Al signal at long time scales. Concerning the response of other elements j_e^* , j_{Zn} and j_{Mg} evolve in correlation with the AC perturbation, however, some shift between the peak maximums is visible. As in the case of the Al response, which is time or frequency dependent, the phase shift between j_{Zn} , j_{Mg} and j_e^* as well as the amplitude of j_{Mg} variation seems to decrease at lower frequencies which were applied the last. This decrease of the

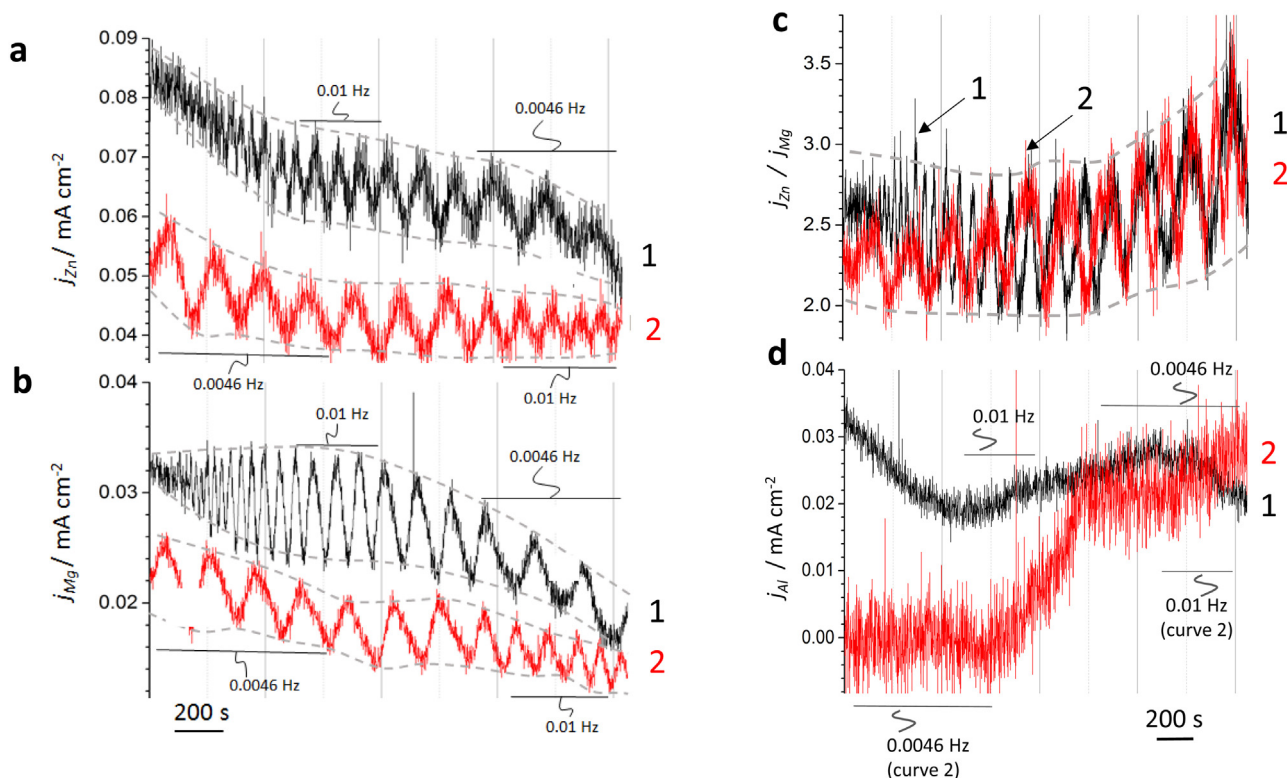


Fig. 4. Responses of ZnMgAl in experiments for AC frequencies decreasing with time from 10^5 Hz to 0.0046 Hz (curves 1) and AC frequencies increasing with time from 0.0046 Hz to 10^5 Hz (curves 2). Figure (a), (b) and (d) show Zn, Mg and Al dissolution currents (j_{Zn} , j_{Mg} , j_{Al}), figure (c) represents the ratios j_{Zn}/j_{Mg} . Electrolyte: 0.1 M NH_4^+ /0.09 M NH_3 + 0.01 M HCO_3^- , pH 8.5.

internal dynamics can indicate either the film growth or increasing diffusion limitation.

In order to distinguish the effect of the time duration of the experiment and the applied AC frequency, the experiment was repeated with the reverse order of AC frequencies application. In Fig. 4 a-d the results of the experiment 1, in which the AC was applied in descending order of frequencies, are presented by curves 1; the results of the experiment 2, when the frequencies were applied in the ascending order of frequencies, are presented by curves 2. Note, that only the results corresponding to the frequencies 0.01 Hz till 0.0046 Hz are presented, since, as discussed in Section 3.1.1., at higher frequencies the results cannot be interpreted correctly because of the cell hydrodynamics. Several observations can be drawn from the figure.

- 1) Fig. 4b shows no correlation between the AC frequency and the amplitude of j_{Mg} oscillations. Some decrease of the mean j_{Mg} signal with longer experiment time is detected.
- 2) The values of j_{Mg} (Fig. 4b) and j_{Zn} (Fig. 4a) are twice higher in the experiment 1, in which the AC was applied in descending order of frequencies than in the experiment 2 when the frequencies were applied in the inverse order from lower to higher.
- 3) Even though the poor reproducibility of the absolute values of j_{Zn} and j_{Mg} , the j_{Zn}/j_{Mg} ratios show a similar behavior in both experiments (Fig. 4c). The ratio j_{Zn}/j_{Mg} corresponding to the maximum of the anodic impulse on AC perturbation (negative peaks values on the curves in Fig. 4c) is very close to 2 in the initial time period indicating the stoichiometry of the dissolution typical for Zn_2Mg intermetallic under anodic polarization in this solution. The increase of this ratio with time indicates either the formation of Mg-rich film or activation of the anodic dissolution of Zn phase because of the surface enrichment by Zn dendrites because of the selective dissolution of Zn_2Mg .

- 4) The sigmoidal form of the j_{Al} background signal is related to the time and not frequency evolution. The origin of this oscillations is difficult to determine exactly but it could be periodical film formation and dissolution or the film modification due to local changes of the solution chemistry.

3.1.4. Case (IV): unbuffered NaCl

For comparison, the last experiments were made in unbuffered NaCl solutions at initial pH 10.5 and 8.5. In both experiments the OCP value was very close to -1.02 V vs. Ag/AgCl and the solution pH decreased after the AC experiment till pH 9.8 from the initial pH

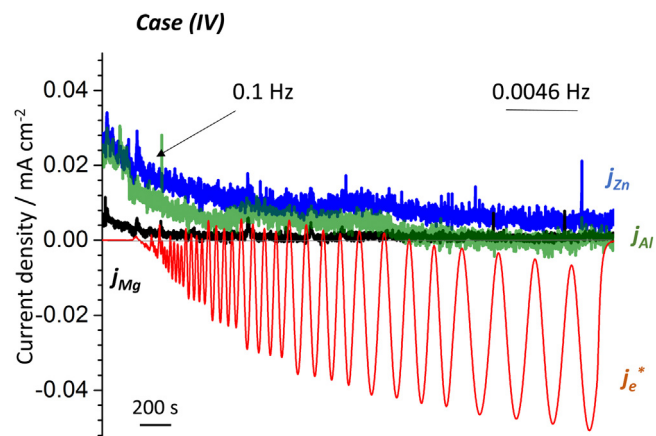


Fig. 5. Evolution of elemental leaching rates of Zn, Al and Mg (j_{Zn} , j_{Al} and j_{Mg}) and the total convoluted current (j_e^*) in AC/AESEC experiment in 0.1 M NaCl, initial pH 10.5 or 8.5 (case IV). AC perturbation parameters: frequency varied from 10^5 Hz to 0.0046 Hz, amplitude 10 mV rms, 10 points per decade.

10.5 and to pH 7 from the initial pH 8.5 (Table 4), which can be explained by the hydrolysis of the dissolved Al^{3+} , Mg^{2+} and Zn^{2+} cations and precipitation of Zn oxides. The buffer properties of ammonium and carbonate solutions can be responsible for the stable pH value in the previous experiments shown in Figs. 1–4.

The AESEC response of ZnMgAl in both cases was similar. Fig. 5 presents an example of dissolution profiles during AC application in 0.1 M NaCl at the initial solution pH of 10.5.

None of j_{Zn} , j_{Mg} and j_{Al} follows the variations of j_e^* during AC application Fig. 5 and the values of j_{Al} and j_{Mg} decrease rapidly with

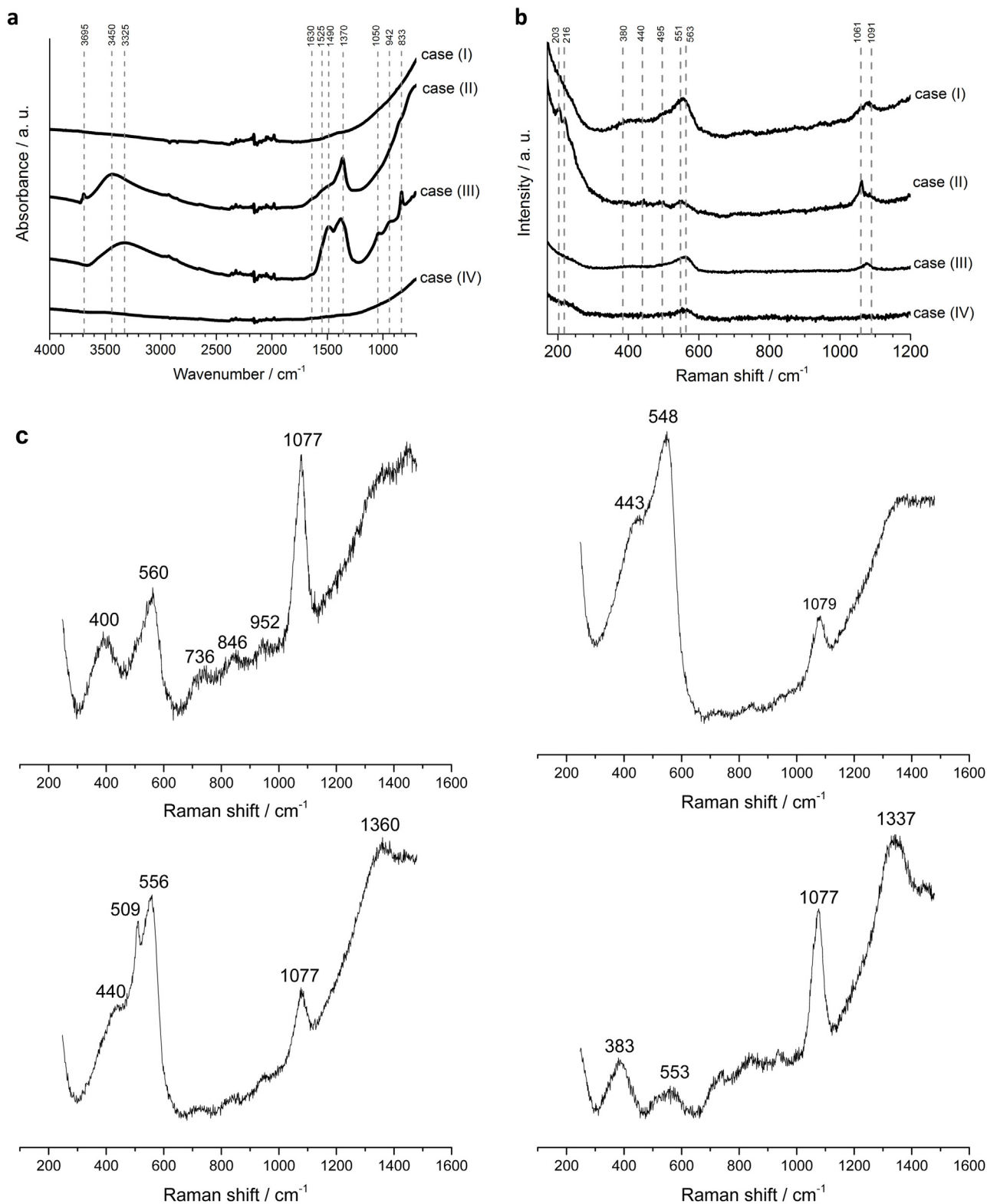


Fig. 6. Infrared (a) and Raman (b, c) spectra of samples after the experiments shown in in Figs. 1–5 (electrolytes 1–4 in Table 1). Fig. 6a and b represent general spectra evidencing the main compounds present all over the surface while Fig. 6c illustrates several local points for case III, demonstrating local formation of spinels and sodium aluminate along with carbonates and hydroxycarbonates. The peaks identification is explained in the text and in Table 6.

time approaching zero for the last half of the experiment within the limits of the technique, indicating the passivation of the surface. The absence of j_{Zn} oscillations and the stabilization of Zn dissolution rate suggest diffusion limited dissolution. These results as well as the R_p value of 666 ohm cm^2 (Table 4) are in favor of the film formation. Note, that the R_p value in this case is twice less than in the case (II) when the passivation is related to the formation of Mg oxy-hydroxide film.

3.1.5. Surface state after AC/AESEC experiments

Fig. 6 shows typical (a) infrared (IR) and (b) Raman spectra of ZnMgAl surface after AC/AESEC experiments. The range of 2700 – 3800 cm^{-1} in Raman spectra was not representative and it is not shown. The main information from this region was the absence of the characteristic narrow peaks of microcrystalline magnesium hydroxide (brucite, $Mg(OH)_2$) at 3652 cm^{-1} [43] and simonkolleite ($Zn_5(OH)_8Cl_2 \cdot H_2O$) at 3480 cm^{-1} [44]. The IR signal irregularity in the region 2000 cm^{-1} –2400 cm^{-1} (Fig. 6a) is a consequence of the presence of CO_2 from the air. The most important peak positions are labeled and their detailed assignment are given in Table 6 (data from [18,43–52] as well as from the mineralogical database RRUFF [53]). The results presented in Fig. 6 can be summarized as follow:

1) Case (I): none of species are detected in IR spectrum whereas the Raman spectrum reveals the presence of wurtzite (ZnO – 440 cm^{-1} , 563 cm^{-1}), the partially reduced Zn oxide with $Zn_{1+x}O$ composition (551 cm^{-1} , [48]) and Mg-Zn-Al hydroxalcalites ($Mg_xZn_{6-x}Al_2(OH)_{16}CO_3 \cdot 4H_2O$, 495 cm^{-1}). CO_3^{2-} symmetric stretching modes are observed at 1077 cm^{-1} were previously ascribed to the CO_3^{2-} units bonded to one OH^- in ZnAl hydroxalcalite ($x=0$ for Mg in the stoichiometric formula shown before) [52]. The peak is very broad and can also be a convolution of the band at 1092 cm^{-1} which is due to the CO_3^{2-} units bonded to two OH^- and 1061 cm^{-1} for Mg-Zn-Al hydroxalcalites or/and hydrozincite ($Zn_5(CO_3)_2(OH)_6$).

2) Case (II): IR spectrum clearly shows the presence of brucite $Mg(OH)_2$ (a narrow peak at 3695 cm^{-1}) and Mg-Zn-Al hydroxalcalites; weak peaks at 1445 cm^{-1} and 1525 cm^{-1} could be attributed to a mixture of amorphous Mg carbonates (magnesite $MgCO_3$ and nesquehonite $MgCO_3 \cdot 3H_2O$). The Raman spectra confirms the formation of Mg-Zn-Al hydroxalcalites but also suggests the presence of ZnO. More complete information was found in the frequency region of Raman spectra (not shown in Fig. 6) – despite the absence of the narrow peak at 3652 cm^{-1} , the spectra presented a broad peak around 2930 cm^{-1} previously assigned to nanocrystalline brucite [54] corroborating the results of IR analysis which is insensitive to such microstructural variations.

3) Case (III): IR spectrum looks like a fingerprint of hydrozincite [18]. ZnO, Mg-Zn-Al hydroxalcalites and magnesite are observed in Raman spectra. Relatively intense peak at 563 cm^{-1} in Raman spectrum and the absence of peak at 440 cm^{-1} is coherent with the presence of defective zinc oxide or amorphous alumina, which should also appear at 563 cm^{-1} . More detailed analysis by μ Raman mapping permitted to identify other characteristic peaks to complete this information (Fig. 6c). Firstly, hydrozincite was also observed. Secondly, in several deeply attacked zones we observed a relatively narrow peak at around 505–515 cm^{-1} which can be assigned to isolated (or surface) AlO_6 octahedra from sodium aluminates [55] in particular taking into account that a broad peak around 560 cm^{-1} is usually explained by condensed AlO_6 [49,55]. The presence of sodium aluminates is coherent with higher values of local pH which could explain oscillations of the soluble Al in the solution. Peak at 400 cm^{-1} is characteristic for $MgAl_2O_4$ spinel.

4) Case (IV): no peaks appeared in IR spectrum after background correction of adsorbed water and carbon dioxide whereas Raman spectrum reveals defective zinc oxides and probably amorphous alumina.

Table 6

Assignment of peaks in (a) IR and (b) Raman spectra presented in Fig. 6. The references complementary to the RRUFF database are presented.

(a) Infrared spectra		
	Wavenumber, cm^{-1}	References
Hydrozincite ($Zn_5(CO_3)_2(OH)_6$)	833	[18]
	942	
	1040	
	1384	
	1490	
	3325	
Brucite ($Mg(OH)_2$)	3695	[18]
Mg-Zn-Al hydroxalcalites ($Mg_xZn_{6-x}Al_2(OH)_{16}CO_3 \cdot 4H_2O$)	1370	[43,45]
	1630	
	3450	
Nesquehonite ($MgCO_3 \cdot 3H_2O$)	1525	[18]
Magnesite ($MgCO_3$)	1445	[18]
(b) Raman spectra		
	Raman shift, cm^{-1}	References
Wurtzite (ZnO)	204	[44,46]
	380	
	440	
	563	
Partially reduced wurtzite ($Zn_{1+x}O$)	551	[48]
Amorphous alumina (Al_2O_3)	563	[49]
Hydrozincite ($Zn_5(CO_3)_2(OH)_6$)	380	[44]
	1061	
Mg-Zn-Al hydroxalcalites ($(Mg_xZn_{6-x}Al_2(OH)_{16}CO_3 \cdot 4H_2O)$)	495	[43,45,52,53]
	1061	
Magnesite ($MgCO_3$)	216	[50]
	1091	
AlO_6-groups in gels	505-515	[55]

4. Discussion

4.1. Stability of the system

AC/AESEC coupling gives a unique tool to verify if the system can approach the essential conditions needed for the interpretation of conventional EIS data in terms of the system stability. The general trends of j_{Zn} , j_{Al} and j_{Mg} in all figures Fig. 1–5 clearly demonstrate that the dissolution is not stable as can be seen, for instance, from the 40% difference between the initial and the final j_X values in Figs. 1–5. At the same time validation of the conventional EIS spectra by Kramers-Kronig transformation demonstrated less than 5% error for all experiments which were presented in Figs. 1–5. Hence, it seems that the Kramers-Kronig transformation is not as sensitive to the variations of partial metal current dissolution as AESEC technique.

Variations of the open circuit potentials (E_{oc}) values before and after the AC experiments (Table 4) were small but reproducible. The interpretation of the general trends of j_e^+ variation in Fig. 1–3, 5 during potentiostatic AC application based on the mixed potential theory was coherent with the observed selective dissolution behavior and the surface state. For the experiment in Fig. 1 (Case I) E_{oc} decreased from -1.22 V vs Ag/AgCl to -1.23 V vs Ag/AgCl after AC application. Since the potential variation during AC test was performed ± 10 mV rms around the initial value of -1.22 V vs Ag/AgCl, the contribution of anodic current to j_e^+ increased (Fig. 1). Similarly, the supremacy of cathodic currents in Fig. 2 (Case II) and Fig. 5 (Case IV) can be explained by the increase of the E_{oc} before and after the AC application due to the surface film formation (Table 4).

Comparing the R_p values summarized in Table 4 with the dissolution responses presented in Figs. 1–3 and 5 one can note that the dissolution behavior cannot be predicted from the R_p values. For example, the highest R_p values are measured at pH 13, for which the dissolution rate of Al is the highest, as shown in Fig. 2. This illustrates that the system cannot be considered as homogeneous and it is therefore necessary to draw individual equivalent circuits for some alloying elements or phases, the idea which was previously proposed in the literature [4,5] but is not generally used in practice.

To summarize, the studied system is fundamentally unstable and the interpretation of the conventional EIS data from the experiments presented in Figs. 1–5 appears impossible and is not provided in the present work. In a general case, the conventional EIS data about the dissolution of ZnAlMg alloys should be interpreted with caution. Along with the careful examination of the stability of j_e , j_{Zn} , j_{Al} and j_{Mg} currents one must distinguish the anodic dissolution of Zn and Mg from the cathodic dissolution of Al in the appropriate equivalent circuit or/and kinetic model of the system.

4.2. Mechanisms of reactivity in different electrolytes

General trends of the ZnMgAl dissolution in $\text{NH}_4\text{Cl}/\text{NaHCO}_3$ mixtures observed in AC/AESEC experiments (Figs. 1–3) correlate well with the behavior expected from the saturation concentrations of Zn^{2+} , Al^{3+} and Mg^{2+} in selected electrolytes calculated by Hydra Medusa software [56] (see Table 1).

Case (I). The results suggest that the dissolution of freshly prepared surface of ZnMgAl in ammonium/carbonate buffer at pH 10.5 is controlled by the charge transfer processes and suggest no ion transport limitation. The results are coherent with the absence of detectable by IR thick layers of surface hydroxides and basic salts and the localized corrosion products detected locally “in depth” of the material suggesting very rapid transformation of the oxides in contact with the electrolyte.

Case (II). rapid formation of low soluble brucite and hydroxaltes at pH 13.0 decreased surface reactivity in 10 times compared with the previous case. The film continuously improves its barrier properties because both, the total current and the elemental dissolutions, decrease with time. However, the localized character of Mg distribution in the microstructure and the rapid film formation result in non-blocked reactivity of Zn dendrites at least at the times scales we used. High pH favor Al reactivity.

Case (III). the detection by vibration spectroscopy of sodium aluminates and several mixed Mg–Al compounds confirms the hypothesis of the Mg rich film formation on ZnMgAl surface after the contact with the $\text{NH}_4\text{Cl}/\text{NaHCO}_3$ solution at pH 8.5 expected from the AESEC data. Hydrozincite could be formed after the experiment from the soluble Zn^{2+} ions which were complexed by ammonium.

Case (IV). In unbuffered slightly alkaline NaCl j_{Mg} and j_{Al} approach their detection limits (Fig. 5) whereas Zn forms ZnO film confirmed by Raman data in Fig. 6b. The barrier properties of this film are usually considered to be poor [19,22,29] which correlates with the low R_p value (Table 4). Since Zn is the major component of the alloy and is present in all phases, formed ZnO film can block the diffusion of ejected Mg^{2+} and Al^{3+} . Therefore, j_{Zn} will be determined by the saturated concentration of Zn^{2+} under local conditions with $j_{Al}=0$ and $j_{Mg}=0$.

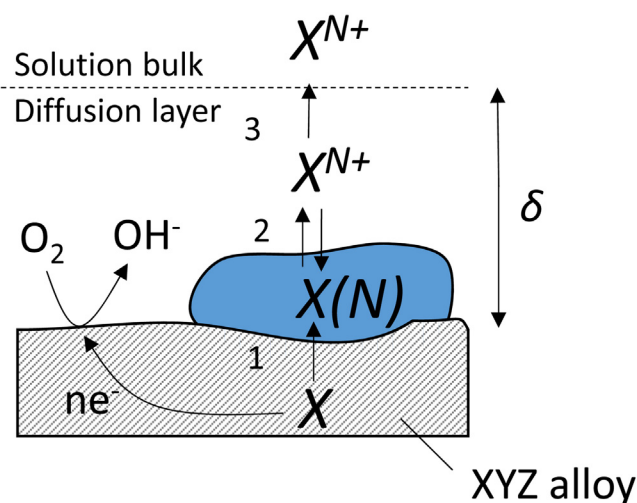


Fig. 7. Schematic representation of the processes considered to estimate a correlation of elemental dissolution in AC/AESEC experiment and solubility of selected species. The model includes: 1–electrochemical dissolution of metal X with the formation of low soluble products $X(N)$; 2–dissolution/precipitation processes, equilibrium between $X(N)$ and X^{N+} ; 3–diffusion of X^{N+} to the bulk through a diffusion layer with the diffusion thickness δ .

4.3. Solubility control of partial metal dissolution

A simple schema presented in Fig. 7 describes the dissolution process by 3 steps: (1) oxidation of the metal with formation of an insoluble or adsorbed species of $X(N)$ at the interface, (2) release of X^{N+} in the solution close to the surface (in equilibrium with re-precipitation) and (3) diffusion of X^{N+} to the bulk solution. In such a schema, diffusion limited dissolution (AC perturbation does not affect dissolution rate) should furnish the surface concentration of species of X (C_s^X) at steady state. Indeed, a flux of cations X^{N+} from the surface (J_X) to the solution bulk through the diffusion layer of a thickness δ can be described by the 1st Fick’s law:

$$J_X = D_X \frac{C_s^X - C_o^X}{\delta} \quad (7)$$

where the concentration of X^{N+} in the solution bulk (C_o^X) can be calculated from the AESEC data. Combining Eqs. (1), (2) and (7)

$$C_s^X = C_o^X \left(\frac{f\delta}{AD_X} + 1 \right) \quad (8)$$

The calculated by Eq. (8) surface concentrations C_s^X of Zn^{2+} , Mg^{2+} and Al^{3+} after the application of AC perturbations in different electrolytes are presented by spots in Fig. 8 a and b. The experimental bulk concentrations were taken from the results of the experiments presented in Figs. 1–3 and 5. The used diffusion coefficients for Zn^{2+} , Al^{3+} and Mg^{2+} are listed in Table 7 (from [57]), δ was approximated as 0.01 mm [58,59], $A=0.51 \text{ cm}^2$ and $f=0.05 \text{ cm}^3 \text{ s}^{-1}$ in AESEC experiment. The saturated concentrations presented by solid lines in Fig. 8 were calculated using the Hydra Medusa software [56] in solutions relevant for this work. Fig. 8 demonstrates a clear correlation between the ratio of C_s^X and C_o^X and the behavior of the system. For the cases (II), (III) and (IV) where measured concentrations of Mg, Al and Zn coincided with the saturated concentrations, low soluble species modified the response on AC perturbation. No evolution of Mg dissolution is visible in Fig. 2 because of formation of hydroxaltes, Al(III) (compare with Fig. 3) and Zn(II) (compare with Fig. 5). In all other

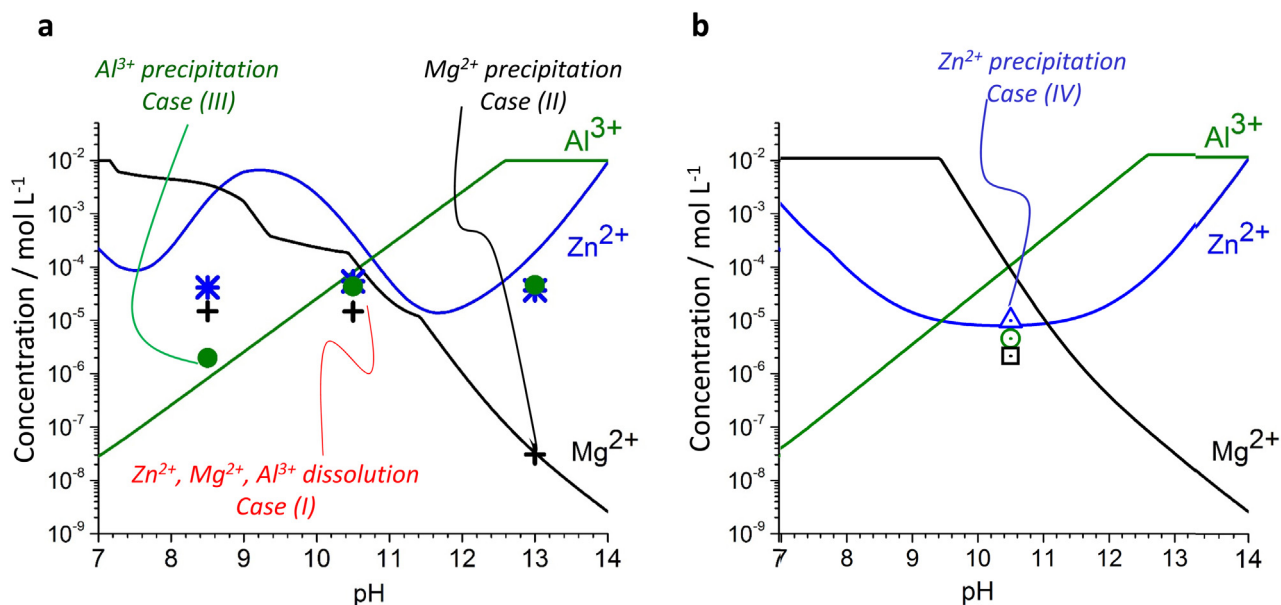


Fig. 8. Correlation between the surface concentrations (point results) of Zn (blue, *) , Al (green, ●) and Mg (black, ×) calculated by Eq. (11) from the experimental data after AC application shown in Fig. 1–3 and 5 and saturation concentration of Zn^{2+} , Al^{3+} and Mg^{2+} cations at 25 °C in (a) 0.1 M NH_4^+ /0.09 M NH_3 + 0.01 M HCO_3^- and (b) 0.1 M NaCl solutions as a function of pH calculated by Hydra Medusa software [56], the species considered in calculation are listed in the legend for Table 1.

Table 7

Diffusion coefficients D_X of Zn^{2+} , Al^{3+} and Mg^{2+} ions in water at 25 °C [57].

Cation	Al^{3+}	Zn^{2+}	Mg^{2+}
$(D/10^{-5}) / cm^2s^{-1}$	0.541	0.703	0.706

cases $C_s^X < C_X^{sol}$ and the AESEC data show direct dissolution of X to X^{N+} . This result is interesting because the expected tendencies in the AESEC response on AC perturbations from the solubility considerations promises a useful approach for optimizing the experimental conditions of AC/AESEC coupling for other alloys.

5. Conclusions

- 1) Real time measurement of elemental dissolution rates by atomic emission spectroelectrochemistry under AC perturbations of Zn3.5%Al3%Mg alloy was used to precise the mechanisms controlling selective dissolution as a function of pH in chloride containing solutions with and without the presence of NH_4^+ . The surface state after the experiment was characterized by ATR IR and Raman spectroscopy.
- 2) At pH values of 8.5 and 10.5 Zn and Mg dissolution currents (j_{Zn} and j_{Mg}) followed the total current j_e^* respecting the stoichiometry of Zn_2Mg at the maximum of anodic current at pH 8.5. Al dissolution current (j_{Al}) followed the AC oscillations with the phase shift 180° relative to j_e^* at pH 10.5 (cathodic Al dissolution). No correlation with AC perturbation and j_{Al} was at pH 8.5.
- 3) Al dissolution from ZnMgAl alloy near its open circuit was controlled by the cathodic reaction. The cathodic dissolution of Al is widely known phenomenon, however, in this work it was observed for the first time at so anodic potentials and for the low amplitude (10 mV) AC perturbation for ZnAlMg alloy. The phenomenon was explained by the strong cathodic polarization of Al component in ZnMgAl matrix.

- 4) In strong alkaline solutions faradaic anodic Zn dissolution, cathodic Al dissolution and no Mg dissolution was observed.
- 5) In all the cases where the elemental dissolution did not depend on the AC perturbation or presented a phase shift, the results demonstrated the formation of low soluble products: $Mg(OH)_2$, Mg-Zn-Al hydrotalcites, etc. in the solution with pH 13; magnesium carbonates, hydrozincite, presumably amorphous Al_2O_3 and spinel based compounds in ammonium/bicarbonate buffer at pH of 8.5; and defective $Zn_{1+x}O$ in unbuffered 0.1 M NaCl with initially alkaline pH.
- 6) In studied cases when insoluble product controlled the dissolution, the expected from the thermodynamics saturated concentrations of Zn^{2+} , Al^{3+} and Mg^{2+} in the selected electrolytes correlated well with the measured in real time metal dissolution rates.
- 7) The results suggest that until the surface is not completely passivated by the surface oxides, the response in AC/AESEC experiment is controlled by the saturated concentration of cations ejected from the metal surface in chosen electrolyte, which can help to optimize the experimental conditions for any other alloy.
- 8) Variations of Zn, Al and Mg elemental currents in all experiments did not permit to interpret the conventional EIS spectra. Even though the validation by the Kramers-Kronig transformation demonstrated less than 5% error, elemental currents varied approximately 40% relative to its initial values before AC application. In application to ZnMgAl, the finding implies the separation of cathodic Al dissolution, and anodic Zn and Mg dissolution in the appropriate equivalent circuit for the adequate analysis of the conventional EIS data.

Acknowledgment

The authors acknowledge Dr. Grégory Lefèvre for the help in the operation of ATR-FTIR analysis. We would like to thank the European Commission, Research Fund for Coal and Steel (RFCs) for partial support of this work, grant agreement RFSR-CT-2015-00011.

Appendix A.

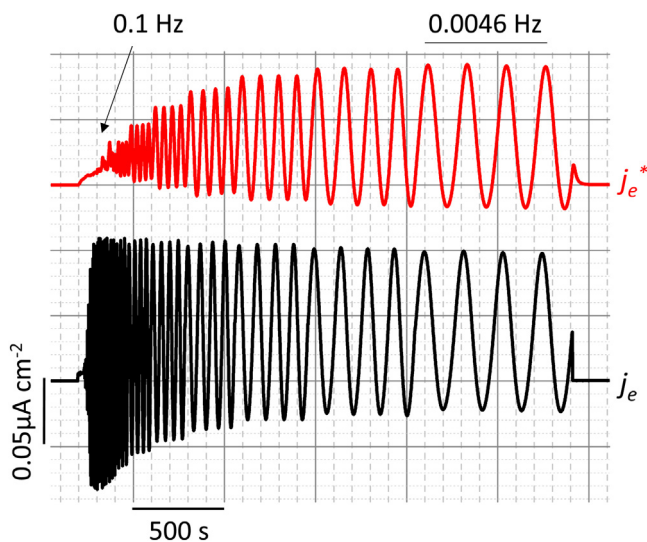


Fig. A1. An example of the original signal of current (j_e) from AESEC and the current signal after the numerical convolution (j_e^*) illustrating the effect of the cell hydrodynamics.

The presented data correspond to the EIS experiment shown in Fig. 2. Clearly, the decrease of j_e^* with the frequency increase is the result of the flow hydrodynamics of the cell and does not reflect the electrochemical behavior of dissolved elements.

References

- [1] N. Benzekri, M. Keddou, H. Takenouti, AC response of a rotating ring-disk electrode: application to 2-D and 3-D film formation in anodic processes, *Electrochim. Acta.* 34 (1989) 1159–1166.
- [2] T.T.M. Tran, B. Tribollet, E.M.M. Sutter, New insights into the cathodic dissolution of aluminium using electrochemical methods, *Electrochim. Acta.* 216 (2016) 58–67, doi:http://dx.doi.org/10.1016/j.electacta.2016.09.011.
- [3] A.D. King, N. Birbilis, J.R. Scully, Accurate Electrochemical Measurement of Magnesium Corrosion Rates: a Combined Impedance, Mass-Loss and Hydrogen Collection Study, *Electrochim. Acta.* 121 (2014) 394–406, doi:http://dx.doi.org/10.1016/j.electacta.2013.12.124.
- [4] G. Galicia, N. Pèbère, B. Tribollet, V. Vivier, Local and global electrochemical impedances applied to the corrosion behaviour of an AZ91 magnesium alloy, *Corros. Sci.* 51 (2009) 1789–1794, doi:http://dx.doi.org/10.1016/j.corsci.2009.05.005.
- [5] B. Tribollet, M.E. Orazem, *Electrochemical Impedance Spectroscopy*, John Wiley & Sons, 2008.
- [6] G. Baril, N. Pebere, The corrosion of pure magnesium in aerated and deaerated sodium sulphate solutions, *Corros. Sci.* 43 (2001) 471–484.
- [7] S. Thomas, N. Birbilis, M.S. Venkatraman, I.S. Cole, Corrosion of Zinc as a Function of pH, *Corrosion* 68 (2012) 015009-1–015009-9, doi:http://dx.doi.org/10.5006/1.3676630.
- [8] L. Jiang, P. Volovitch, M. Wolpers, K. Ogle, Activation and inhibition of Zn-Al and Zn-Al-Mg coatings on steel by nitrate in phosphoric acid solution, *Corros. Sci.* 60 (2012) 256–264, doi:http://dx.doi.org/10.1016/j.corsci.2012.03.028.
- [9] J. Rodriguez, L. Chenoy, A. Roobroeck, S. Godet, M. Olivier, Effect of the electrolyte pH on the corrosion mechanisms of Zn-Mg coated steel, *Corros. Sci.* 108 (2016) 47–59, doi:http://dx.doi.org/10.1016/j.corsci.2016.02.041.
- [10] S. Tanaka, K. Honda, Y. Takahashi, Y. Morimoto, M. Kurosaki, H. Shindo, K. Nishimura, M. Sugiyama, The performance of Zn-Al-Mg-Si hot-dip galvanized steel sheet, *Proc Galvatech '01*, Int. Conf. Zinc Zinc Alloy Coat. Steel, Brussels, Belgium, 2001, pp. 153–160.
- [11] K. Nishimura, H. Shindo, K. Kato, Y. Morimoto, Microstructure and corrosion behavior of Zn-Mg-Al hot dip galvanized steel sheet, *Proc Galvatech '98*, Int. Conf. Zinc Zinc Alloy Coat. Steel, Chiba, Japan, 1998, pp. 437–442.
- [12] T. Tsujimura, A. Komatsu, A. Andoh, Influence of Mg content in coating layer and coating structure on corrosion resistance of hot-dip Zn-Al-Mg alloy coated steel sheet, *Proc Galvatech '01*, Int. Conf. Zinc Zinc Alloy Coat. Steel (2001) 145–152.
- [13] S. Schürz, G.H. Luckeneder, M. Fleischanderl, P. Mack, H. Gsaller, A.C. Kneissl, G. Mori, Chemistry of corrosion products on Zn-Al-Mg alloy coated steel, *Corros. Sci.* 52 (2010) 3271–3279, doi:http://dx.doi.org/10.1016/j.corsci.2010.05.044.
- [14] M. Dutta, A.K. Halder, S.B. Singh, Morphology and properties of hot dip Zn-Mg and Zn-Mg-Al alloy coatings on steel sheet, *Surf. Coatings Technol.* 205 (2010) 2578–2584, doi:http://dx.doi.org/10.1016/j.surfcoat.2010.10.006.
- [15] S. Schuerz, M. Fleischanderl, G.H. Luckeneder, K. Preis, T. Haunschmied, G. Mori, A.C. Kneissl, Corrosion behaviour of Zn-Al-Mg coated steel sheet in sodium chloride-containing environment, *Corros. Sci.* 51 (2009) 2355–2363, doi:http://dx.doi.org/10.1016/j.corsci.2009.06.019.
- [16] P. Volovitch, C. Allely, K. Ogle, Understanding corrosion via corrosion product characterization: I. Case study of the role of Mg alloying in Zn-Mg coating on steel, *Corros. Sci.* 51 (2009) 1251–1262, doi:http://dx.doi.org/10.1016/j.corsci.2009.03.005.
- [17] D. Persson, D. Thierry, N. LeBozec, T. Prosek, In situ infrared reflection spectroscopy studies of the initial atmospheric corrosion of Zn-Al-Mg coated steel, *Corros. Sci.* 72 (2013) 54–63, doi:http://dx.doi.org/10.1016/j.corsci.2013.03.005.
- [18] T. Prosek, A. Nazarov, U. Bexell, D. Thierry, J. Serak, Corrosion mechanism of model zinc-magnesium alloys in atmospheric conditions, *Corros. Sci.* 50 (2008) 2216–2231, doi:http://dx.doi.org/10.1016/j.corsci.2008.06.008.
- [19] M. Salgueiro Azevedo, C. Allély, K. Ogle, P. Volovitch, Corrosion mechanisms of Zn(Mg,Al) coated steel: 2. The effect of Mg and Al alloying on the formation and properties of corrosion products in different electrolytes, *Corros. Sci.* 90 (2015) 482–490, doi:http://dx.doi.org/10.1016/j.corsci.2014.07.042.
- [20] T. Prosek, J. Hagstrom, D. Persson, N. Fuertes, F. Lindberg, O. Chocholaty, C. Taxen, J. Serak, D. Thierry, Effect of the microstructure of Zn-Al and Zn-Al-Mg model alloys on corrosion stability, *Corros. Sci.* (2016), doi:http://dx.doi.org/10.1016/j.corsci.2016.04.022 (in press).
- [21] M. Morishita, K. Koyama, Y. Mori, Inhibition of anodic dissolution of zinc-plated steel by electro-deposition of magnesium from a molten salt, *ISIJ Int.* 95 (2004) 447–455.
- [22] R. Hausbrand, M. Rohwerder, M. Stratmann, C. Scherd, B. Schuhmacher, G. Grundmeier, Model study on the corrosion of magnesium-containing zinc coating on steel sheets, *Proc Galvatech '01*, Int. Conf. Zinc Zinc Alloy Coat. Steel, Brussels, Belgium, 2001, pp. 161–167.
- [23] T. Prosek, D. Persson, J. Stouil, D. Thierry, Composition of corrosion products formed on Zn-Mg, Zn-Al and Zn-Al-Mg coatings in model atmospheric conditions, *Corros. Sci.* 86 (2014) 231–238, doi:http://dx.doi.org/10.1016/j.corsci.2014.05.016.
- [24] M. Salgueiro Azevedo, C. Allély, K. Ogle, P. Volovitch, Corrosion mechanisms of Zn(Mg, Al) coated steel in accelerated tests and natural exposure: 1. The role of electrolyte composition in the nature of corrosion products and relative corrosion rate, *Corros. Sci.* 90 (2015) 472–481, doi:http://dx.doi.org/10.1016/j.corsci.2014.05.014.
- [25] F. Thébault, B. Vuillemin, R. Oltra, C. Allely, K. Ogle, O. Heintz, Influence of magnesium content on the corrosion resistance of the cut-edges of Zn-Mg-coated steel, *vol. 97*(2015), pp. 100–106, doi:http://dx.doi.org/10.1016/j.corsci.2015.04.019.
- [26] S.O. Klemm, J.-C. Schauer, B. Schuhmacher, A.W. Hassel, High throughput electrochemical screening and dissolution monitoring of Mg-Zn material libraries, *Electrochim. Acta.* 56 (2011) 9627–9636, doi:http://dx.doi.org/10.1016/j.electacta.2011.05.065.
- [27] E. Diler, S. Rioual, B. Lescop, D. Thierry, B. Rouvellou, Chemistry of corrosion products of Zn and Mg/Zn pure phases under atmospheric conditions, *Corros. Sci.* 65 (2012) 178–186, doi:http://dx.doi.org/10.1016/j.corsci.2012.08.014.
- [28] R. Krieg, M. Rohwerder, S. Evers, B. Schuhmacher, J. Schauer-Pass, Cathodic self-healing at cut-edges: The effect of Zn²⁺ and Mg²⁺ ions, *Corros. Sci.* 65 (2012) 119–127, doi:http://dx.doi.org/10.1016/j.corsci.2012.08.008.
- [29] N. LeBozec, D. Thierry, M. Rohwerder, D. Persson, G. Luckeneder, L. Luxem, Effect of carbon dioxide on the atmospheric corrosion of Zn-Mg-Al coated steel, *Corros. Sci.* 74 (2013) 379–386, doi:http://dx.doi.org/10.1016/j.corsci.2013.05.011.
- [30] N.C. Hosking, M.A. Ström, P.H. Shipway, C.D. Rudd, Corrosion resistance of zinc-magnesium coated steel, *Corros. Sci.* 49 (2007) 3669–3695, doi:http://dx.doi.org/10.1016/j.corsci.2007.03.032.
- [31] P. Volovitch, T.N. Vu, C. Allély, A. Abdel, K. Ogle, Understanding corrosion via corrosion product characterization: II. Role of alloying elements in improving the corrosion resistance of Zn-Al-Mg coatings on steel, *Corros. Sci.* 53 (2011) 2437–2445, doi:http://dx.doi.org/10.1016/j.corsci.2011.03.016.
- [32] T. Ishikawa, M. Ueda, K. Kandori, T. Nakayama, Air permeability of the artificially synthesized Zn-Al-Mg alloy rusts, *Corros. Sci.* 49 (2007) 2547–2556, doi:http://dx.doi.org/10.1016/j.corsci.2006.12.008.
- [33] J. Duchoslav, R. Steinberger, M. Arndt, T. Keppert, G. Luckeneder, K.H. Stellnberger, J. Hagler, G. Angeli, C.K. Riener, D. Stifter, Evolution of the surface chemistry of hot dip galvanized Zn-Mg-Al and Zn coatings on steel during short term exposure to sodium chloride containing environments, *Corros. Sci.* 91 (2015) 311–320, doi:http://dx.doi.org/10.1016/j.corsci.2014.11.033.
- [34] M. Salgueiro Azevedo, C. Allely, K. Ogle, P. Volovitch, Corrosion mechanisms of Zn(Mg,Al) coated steel: The effect of HCO₃⁻ and NH₄⁺ ions on the intrinsic reactivity of the coating, *Electrochim. Acta.* 153 (2015) 159–169, doi:http://dx.doi.org/10.1016/j.electacta.2014.09.140.
- [35] K. Ogle, S. Weber, Anodic Dissolution of 304 Stainless Steel Using Atomic Emission Spectroelectrochemistry, *J. Electrochem. Soc.* 147 (2000) 1770, doi:http://dx.doi.org/10.1149/1.1393433.
- [36] V. Shkirskiy, K. Ogle, A novel coupling of electrochemical impedance spectroscopy with atomic emission spectroelectrochemistry: Application to the open circuit dissolution of zinc, *Electrochim. Acta.* 168 (2015) 167–172, doi:http://dx.doi.org/10.1016/j.electacta.2015.03.171.

- [37] K. Ogle, M. Serdechnova, M. Mokaddem, P. Volovitch, The cathodic dissolution of Al, Al₂Cu, and Al alloys, *Electrochim. Acta* 56 (2011), doi:<http://dx.doi.org/10.1016/j.electacta.2010.09.058>.
- [38] S.M. Moon, S.-I. Pyun, The corrosion of pure aluminium using cathodic polarization in aqueous solutions, *Corros. Sci.* 39 (1997) 399–408.
- [39] B.P. Caldwell, V.J. Alano, Rates of solution of zinc and aluminum while cathodic, *Trans. Electrochem. Soc.* 76 (1939) 271.
- [40] M. Serdechnova, P. Volovitch, F. Brisset, K. Ogle, On the cathodic dissolution of Al and Al alloys, *Electrochim. Acta.* (2013), doi:<http://dx.doi.org/10.1016/j.electacta.2013.09.145>.
- [41] M. Mokaddem, P. Volovitch, F. Rechou, R. Oltra, K. Ogle, The anodic and cathodic dissolution of Al and Al-Cu-Mg alloy, *Electrochim. Acta* 55 (2010) 3779–3786, doi:<http://dx.doi.org/10.1016/j.electacta.2010.01.079>.
- [42] S. Thomas, N.V. Medhekar, G.S. Frankel, N. Biribilis, Corrosion mechanism and hydrogen evolution on Mg, *Curr. Opin. Solid State Mater. Sci.* 19 (2015) 85–94, doi:<http://dx.doi.org/10.1016/j.cossms.2014.09.005>.
- [43] J.T. Kloprogge, L. Hickey, R.L. Frost, FT-Raman and FT-IR spectroscopic study of synthetic Mg/Zn/Al-hydroxalcalites, *J. Raman Spectrosc.* 35 (2004) 967–974, doi:<http://dx.doi.org/10.1002/jrs.1244>.
- [44] M.C. Bernard, A. Hugot-Le Goff, D. Massinon, N. Phillips, Underpaint corrosion of zinc-coated steel sheet studied by in situ raman spectroscopy, *Corros. Sci.* 35 (1993) 1339–1349, doi:[http://dx.doi.org/10.1016/0010-938X\(93\)90356-L](http://dx.doi.org/10.1016/0010-938X(93)90356-L).
- [45] S. Xu, M.-C. Liao, H.-Y. Zeng, X.-J. Liu, J.-Z. Du, P.-X. Ding, W. Zhang, Surface modification and dissolution behavior of Mg-Al hydroxalcalite particles, *J. Taiwan Inst. Chem. Eng.* 56 (2015) 174–180, doi:<http://dx.doi.org/10.1016/j.jtice.2015.04.013>.
- [46] O.F. Lopes, V.R. de Mendonça, A. Umar, M.S. Chuahan, R. Kumar, S. Chauhan, C. Ribeiro, Zinc hydroxide/oxide and zinc hydroxy stannate photocatalysts as potential scaffolds for environmental remediation, *New J. Chem.* (2015) 4624–4630, doi:<http://dx.doi.org/10.1039/c5nj00324e>.
- [47] V. Russo, M. Ghidelli, P. Gondoni, C.S. Casari, A. Li Bassi, Multi-wavelength Raman scattering of nanostructured Al-doped zinc oxide, *J. Appl. Phys.* 115 (2014) 1–10, doi:<http://dx.doi.org/10.1063/1.4866322>.
- [48] Y. Chen, P. Schneider, B.-J. Liu, S. Borodin, B. Ren, A. Erbe, Electronic structure and morphology of dark oxides on zinc generated by electrochemical treatment, *Phys. Chem. Chem. Phys.* 15 (2013) 9812–9822, doi:<http://dx.doi.org/10.1039/c3cp44714f>.
- [49] P.V. Thomas, V. Ramakrishnan, V.K. Vaidyan, Oxidation studies of aluminum thin films by Raman spectroscopy, *Thin Solid Films.* 170 (1989) 35–40, doi:[http://dx.doi.org/10.1016/0040-6090\(89\)90619-6](http://dx.doi.org/10.1016/0040-6090(89)90619-6).
- [50] D. Wang, L.M. Hamm, R.J. Bodnar, P.M. Dove, Raman spectroscopic characterization of the magnesium content in amorphous calcium carbonates, *J. Raman Spectrosc.* 43 (2012) 543–548, doi:<http://dx.doi.org/10.1002/jrs.3057>.
- [51] N.S. Azmat, K.D. Ralston, B.C. Muddle, I.S. Cole, Corrosion of Zn under acidified marine droplets, *Corros. Sci.* 53 (2011) 1604–1615, doi:<http://dx.doi.org/10.1016/j.corsci.2011.01.044>.
- [52] R.L. Frost, W.N. Martens, K.L. Erickson, Thermal decomposition of the hydroxalcalite: Thermogravimetric analysis and hot stage Raman spectroscopic study, *J. Therm. Anal. Calorim.* 82 (2005) 603–608, doi:<http://dx.doi.org/10.1007/s10973-005-0940-y>.
- [53] B. Lafuente, R.T. Downs, H. Yang, N. Stone, The power of databases: The RRUFF project, (2016), doi:<http://dx.doi.org/10.1515/9783110417104-003>.
- [54] S.R. Soniya, V.M. Nair, Synthesis and Characterization of Nanostructured Mg(OH)₂ and MgO, *Int. J. Sci. Res.* 5 (2016) 197–203, doi:<http://dx.doi.org/10.1179/174328409x415020>.
- [55] S.F. Agnew, J.R. Schoonover, Microstructural Properties of High Level Waste Concentrates and Gels with Raman and Infrared Spectroscopies, (1996) .
- [56] I. Puigdomenech, Hydra/Medusa Chemical Equilibrium Database and Plotting Software KTH Royal Institute of Technology, <https://sites.google.com/site/chemdiagr/download>, Consulted 07/05/2015.
- [57] R.L. David, Handbook of Chemistry and Physics, CRC Press, 2003.
- [58] K. Ogle, A. Tomandl, N. Meddahi, In situ monitoring of dissolution-precipitation mechanisms using coupled quartz crystal microbalance/atomic emission spectroelectrochemistry, in: L. Fedrizzi, H. Terry, A. Simoes (Eds.), *Innov. Pre-Treatment Tech. to Prev. Corros. Met. Surfaces*, CRC Press, 2007, pp. 158–172.
- [59] E. Samson, J. Marchand, K.A. Snyder, Calculation of ionic diffusion coefficients on the basis of migration test results, *Mater. Struct. Constr.* 36 (2003) 156–165, doi:<http://dx.doi.org/10.1617/14002>.

Résumé

La réactivité des alliages de Mg est fortement influencée par la formation et la stabilité des films de surface, rendant primordiale leur compréhension fondamentale pour une stratégie anticorrosion. En général, ils sont analysés par des techniques ex situ qui peuvent modifier la chimie et la morphologie de surface. Dans ce travail, la spectroscopie Raman a été adaptée pour cartographier in situ la cinétique de l'évolution du film de surface lors des étapes initiales de corrosion de Mg grâce à une cellule en circulation. De plus, la spectroscopie à décharge lumineuse a été appliquée à l'analyse des surfaces corrodées, démontrant qu'elle peut rapidement et précisément déterminer la distribution en profondeur des éléments, y compris les impuretés présentes à des concentrations entre 10 et 100 ppm. L'approche analytique développée a été appliquée à la compréhension de l'effet du pH, des ions chlorure et de plusieurs inhibiteurs organiques dans les mécanismes de dégradation de Mg.

Mots Clés

Produits de corrosion, Inhibiteurs de corrosion, Magnésium, Spectroscopie Raman in situ, Spectroscopie à Décharge Luminescente

Abstract

The reactivity of Mg alloys is strongly affected by formation and stability of surface films making their fundamental understanding primordial for intelligent anticorrosion strategy. In general, their chemistry and morphology are approached by ex-situ technics, which can modify the chemistry and morphology of the surface. In the present work in-situ confocal Raman spectroscopy was adapted to map the local kinetics of surface film evolution at initial stages of Mg corrosion in thin layer cell. Additionally, the applicability of Glow Discharge Optical Emission Spectroscopy (GD OES) for corroded surfaces was analyzed demonstrating that it provides a fast and robust way to obtain elemental depth distribution within the surface film thickness for major elements and minor impurities (10 to 100 ppm). Developed analytical approach was applied to understand the effect of pH, Cl⁻ content and several organic inhibitors on the mechanisms of Mg degradation.

Keywords

Corrosion products, corrosion inhibitors, Magnesium, In situ Raman spectroscopy, Glow Discharge Optical Emission Spectroscopy